Carnegie Mellon University
MELLON COLLEGE OF SCIENCE

THESIS

SUBMITTED IN PARTIAL FULFILLMENT OF THE REQUIREMENTS
FOR THE DEGREE OF

DOCTOR OF PHILOSOPHY IN THE FIELD OF PHYSICS

TITLE: **"**Tilt-Dependent Analysis of Diffuse X-ray Scattering from Oriented Stacks of Fluid Phase Lipid Bilayers.*"*

PRESENTED BY: Michael Jablin

ACCEPTED BY THE DEPARTMENT OF PHYSICS

John Nagle	09/14/15
JOHN NAGLE, CHAIR PROFESSOR	DATE

Stephen Garoff	09/14/15
STEPHEN GAROFF, DEPT HEAD	DATE

APPROVED BY THE COLLEGE COUNCIL

Fred Gilman	09/14/15
FRED GILMAN, DEAN	DATE

Tilt-Dependent Analysis of Diffuse X-ray Scattering from Oriented Stacks of Fluid Phase Lipid Bilayers

by

Michael Stephen Jablin

Submitted in partial fulfillment of the
requirements for the degree of
Doctor of Philosophy
at
Carnegie Mellon University
Department of Physics
Pittsburgh, Pennsylvania

Advised by Professor John F. Nagle

September 4, 2015

Abstract

Recent simulations have indicated that the traditional Helfrich-Canham model for topographical fluctuations in fluid phase biomembranes should be enriched to include molecular tilt. Experimental evidence supporting the aforementioned enrichment is reported. The current work is a tilt-dependent analysis of the X-ray scattering from oriented stacks of fluid phase lipid bilayers. By analyzing several X-ray exposures from different DOPC samples, final single membrane mechanical moduli values of $K_c = 8.4 \pm 0.6 \times 10^{-13}$ ergs and $K_\theta = 90 \pm 7$ mN/m are determined at 30 °C. The tilt-dependent K_c-value is $\sim$20% greater than its tilt-independent analog, and therefore, it compares more favorably with K_c-values reported for some of the other experimental techniques as well as values determined from molecular dynamics simulations. The experimentally determined K_θ-value is between 10 and 20% greater than values reported from molecular dynamics simulations, more consistent than the corresponding K_c-values. As of yet, there is no other experimental technique that has determined the value of K_θ. The determined tilt-dependent and tilt-independent form factors are consistent, but the interpretation of the form factor within the tilt-dependent and -independent models is not identical.

First, a tilt-dependent stacked bilayer free energy functional is hypothesized, based on a recent single membrane tilt-dependent free energy. Then, a tilt-dependent stacked bilayer electron density is posited, and a novel form factor / structure factor separation is derived. The height-height correlation function remains the most important statistical quantity for predicting the X-ray scattering from stacked bilayers. The tilt-dependent height-height correlation function is derived as well as an approximate analytic form for long in-plane length scales. Importantly, both the tilt-dependent and tilt-independent analytic approximations logarithmicly diverge for increasing in-plane length scales; both theories predict quasi-long range order of the height-height correlations. The theoretically predicted intensity is modified by several sample concerns including domain sizes and mosaicity and several experimental issues such as X-ray beam coherence, geometric broadening, and absorption of the incident and scattered X-rays. Measured scattering intensity from stacked DOPC bilayers are analyzed using both tilt-dependent and -independent models. The tilt-dependent model is shown to better account for the measurements, supporting the extension of the classic Helfrich-Canham model to include a tilt degree of freedom.

Acknowledgments

I would like to thank my advisor Professor John F. Nagle for being a patient source of consistent constructive criticism. Also, I would like to thank my committee for attending my annual reviews and thesis defense and providing insightful feedback.

This research was supported by the National Institute of General Medical Sciences of the National Institutes of Health under Grant No. R01GM44976.

Contents

1 Introduction **1**

1.1 Fluid Phase Lipid Bilayers 1

1.1.1 Motivation to Extend Helfrich-Canham Model 3

1.2 X-ray Scattering Methodologies and Analyses 5

1.3 Brief Summary of Thesis Content 6

2 Experimental Methods **8**

2.1 Oriented Samples 8

2.2 Flightpath Components 9

2.2.1 X-ray optics 9

2.2.2 Beam Stop 10

2.2.3 CCD Detector 10

2.3 Sample Chamber 11

2.4 Low Angle X-ray Scattering 13

2.5 Background Subtraction 14

2.5.1 Light Background 14

2.5.2 Water Background 19

3 Tilt-Dependent Membrane Model **25**

3.1 Membrane Model Relevant to X-ray Scattering 25

3.2 Theoretical Scattering Intensity 28

3.2.1 Membrane Electron Density 28

3.2.2 Separation of the Structure and Form Factors 31

3.3 Determining Statistical Quantities 37

3.3.1 Free energy in Fourier Space 37

3.3.2 Height Fluctuation Spectrum 40

3.3.3 Height-height Correlation Function 42

4 Calculating the Height-Height Correlation Function 47

4.1 Tabling $h_j(\rho, \ell, \tau)$ 49

4.1.1 Considering the Finite Upper Limit τ 49

4.2 Analytic Approximation of $h_j(\rho, \ell, \tau)$ 53

4.3 Difference of Tilt-dependent and -independent Height-Height Correlations 63

4.4 Corresponding Caillé Exponents 64

5 Predicted Experimental Scattering Intensity 66

5.1 Structure Factor for Cylindrical Subvolumes 67

5.1.1 Gaussian Subvolume Distributions 71

5.1.2 Exponential Subvolume Distributions 71

5.2 Mosaicity 72

5.3 Experimental Details 73

5.3.1 Scattering Geometry 74

5.3.2 Coherence Effects 76

5.3.3 Beam Size Effects 86

5.3.4 Absorption Correction 95

5.3.5 CCD Integral 96

5.4 Calculating the Final Structure Factor 101

6 Survey of Predicted Structure Factors 105

6.1 Primary Structure Factor Parameters 110

6.1.1 K_c, B, and K_θ 110

6.1.2 $\mathscr{L}_r$ 113

6.1.3 $\mathscr{L}_z$ 116

6.1.4 Minimum In-plane Length: a 119

6.2 Gaussian vs Exponential Distributions 123

6.3 Finite-sized Domains 123

6.4 Second Experimental Structure Factor 128

7 Data Analysis 132

7.1 Comparing Tilt-dependent and -independent Models 137

7.2 Limiting Long Length Scale Correlations . . . 142
7.3 Fitted q_x, q_z-Region . . . 146
7.3.1 q_z-Range . . . 146
7.3.2 q_x-Range . . . 149
7.4 Comparing $I^{\mathrm{F}}_{\mathrm{CCD},1}$ and $I^{\mathrm{F}}_{\mathrm{CCD},2}$ . . . 153
7.4.1 Modeling F_Δ . . . 153
7.4.2 Fitting Measured Intensity . . . 155
7.5 Form Factor . . . 159
7.6 Uncertainty in Primary Fitted Parameters . . . 163

8 Results for Many DOPC Samples **166**
8.1 K_c and K_θ . . . 169
8.1.1 Future Work . . . 175
8.2 B . . . 179
8.2.1 Fluctuation Free Energy: $\Delta\mathcal{F}_{\mathrm{fl}}$ . . . 181
8.2.2 Hamaker Parameter . . . 181

9 Conclusions **185**

Appendices **187**

A Chapter 3: Some Details in Theoretical Derivations **188**
A.1 Free Energy Involving a Hermitian Matrix . . . 188
A.2 $\Psi_j(\mathbf{r})$ . . . 189
A.2.1 Reformulation . . . 190
A.2.2 Variance . . . 191
A.2.3 Implications . . . 192

B Cartesian Structure Factor **196**

C Form Factor Details **201**
C.1 Fluctuations in Electron Density . . . 201
C.1.1 Removing Fluctuations . . . 203
C.1.2 Bilayer Model . . . 204
C.1.3 Leaflets Model . . . 206
C.2 Undulation Correction . . . 209

C.2.1 $\Psi_{\rm UC}$ Evaluated 212
C.2.2 Averages of Quantities Dominated by Short Length Scales . . 214

D Miscellaneous **221**
D.1 a-Dependence of Structure Factor 221
D.2 Computational Precision of $S^{\rm F}_{\rm CCD,1}$ 223
D.3 Numerical Integration Issue 223
D.4 Deriving Tilt-Dependent Fluctuation Free Energy: $\Delta\mathcal{F}_{\rm fl}$ 225

E Vesicle Undulation Correction **228**
E.1 Spherical Geometry 229
E.1.1 $\left\langle |u_\theta|^2 \right\rangle$ 230
E.1.2 $\left\langle |u_\phi|^2 \right\rangle$ 232
E.1.3 Spherical UC 233
E.2 Planar Geometry 234
E.3 Spherical and Planar UCs Compared 235

F Relating the Tilt Field and the Order Parameter **238**
F.1 Single Membrane Free Energy 239
F.1.1 Order Parameter Relations 239
F.2 $\left\langle |\hat{\mathbf{m}}_j|^2 \right\rangle$ of Membrane Stack 244

Glossary

Acronyms

CHESS	Cornell High Energy Synchrotron Source	9
DOPC	1,2-dioleoyl-*sn*-glycero-3-phosphatidylcholine	8
FWHM	full-width at half maximum	92
GUV	giant unilamellar vesicles	172
kLB	kludged light background	15
LAXS	low angle X-ray scattering	13
LB	light background	14
LC	liquid crystal	5
QLRO	quasi-long range order	5
MD	molecular dynamics	1
MLV	multilamellar lipid vesicle	6
UC	undulation correction	228
ULV	unilamellar vesicle	228

Greek letters

γ_{m}	FWHM of mosaicity distribution	72
$\Delta\gamma_x$	angular divergence of the beam in the x-direction	77
$\Delta\gamma_z$	angular divergence of the beam in the z-direction	77
η	dimensionless multiplicative prefactor of $h_j(\rho,\ell,\tau)$	45
2θ	angle between the scattered and direct X-ray beams	73
λ	X-ray wavelength	74
$\Delta\lambda/\lambda$	energy dispersion of incident X-ray beam	77
$\xi_{\mathrm{T}x}$	transverse beam coherence in x-direction	77
$\xi_{\mathrm{T}z}$	transverse beam coherence in z-direction	77
μ	X-ray absorption length in sample	95
ξ	bending dependent length scale : $\sqrt[4]{K_c/B}$	41
ξ_θ	tilt-dependent length scale : $\sqrt{K_c/K_\theta}$	40
ξ_{L}	longitudinal beam coherence	77
ρ	dimensionless in-plane variable in $h_j(\rho,\ell,\tau)$	45
$\rho(\mathbf{R})$	electron density of bilayer stack	31
$\rho_{\mathrm{s}}(\mathbf{r},z)$	electron density of single bilayer along membrane normal	29

$\rho_{\mathrm{w}}(\mathbf{R})$	electron density of water	29
$\rho_j(\mathbf{r}, z)$	electron density of the jth bilayer in the stack	30
σ_{e}	estimated standard deviation of measured intensity	133
τ	dimensionless upper integration limit of $h_j(\rho, \ell, \tau)$	45
ϕ	angle between equator and scattered beam measured on detector	73
Ψ_{UC}	undulation correction	162
$\Psi_j(\mathbf{r})$	geometric factor for deviations from $\rho_{\mathrm{s}}(\mathbf{r}, z)$	30
ω	angle between incident X-ray beam and substrate	13
$\omega_{\mathrm{C}}(p_z)$	minimum incident angle where p_z is blocked by substrate	90

Latin letters

a	shortest real space length scale for continuum theory	43
$\tilde{a}$	longest real space length scale	212
A_{p}	area considered for calculating free energy	27
B	bulk modulus	28
b_x	width of beam in millimeters	86
b_z	height of beam in millimeters	15
D	bilayer stack repeat distance in the z-direction	29
$F(q_z)$	form factor	35
F_Δ	variance of form factor	36
$\mathcal{F}_{\mathrm{u}}$	free energy of membrane stack	28
$F_r(x)$	area overlap of two circles with centers separated by x	68
$\mathcal{F}_{\mathrm{s}}$	free energy of single membrane	27
G	pair scattering correlation function	67
$\tilde{h}_j(\rho, \ell, \tau)$	$\rho \gg 1$ analytic approximation of $h_j(\rho, \ell, \tau)$	47
$h_j(\rho, \ell, \tau)$	height-height correlation function	45
h	index of out-of-plane lamellar scattering peaks	10
$H_r(r)$	effective in-plane finite-size factor	70
$H_z(z)$	effective out-of-plane finite-size factor	70
I	theoretical scattering intensity	31
I_{bf}	intensity due to single bilayer fluctuations with a bilayer stack	35
I_{c}	intensity commonly associated with scattering from stacked bilayers	35
$I^{\mathrm{F}}_{\mathrm{CCD}}$	final theoretical intensity on CCD	96
I_{m}	scattering intensity measured by CCD	14
J	number of bilayers in the stack	37
j	stacked bilayer index	28
K_A	bilayer lateral compressibility modulus	202
k_{B}	Boltzmann constant	40
K_c	bilayer bending modulus	27
$\mathbf{k}_f$	outgoing wavevector	74
$\mathbf{k}_i$	incoming wavevector	74
K_θ	bilayer tilt modulus	27

$\mathcal{L}_r$	in-plane sample coherence length	85
$\mathcal{L}_x$	sample coherence in x-direction (sample centered coordinates)	79
$\mathcal{L}_y$	sample coherence in y-direction	79
$\mathcal{L}_z$	sample coherence in z-direction	79
L_r	diameter of cylindrical domain	67
$\mathfrak{L}_r$	characteristic in-plane length of subvolume distribution	70
$L_{\rm s}$	width of sample along primary beam propagation direction	15
$\mathfrak{L}_z$	characteristic out-of-plane length of subvolume distribution	70
$\hat{\mathbf{m}}(\mathbf{r})$	tilt fluctuation field averaged over upper and lower leaflets	26
$\mathbf{m}^{(\alpha)}$	monolayer tilt	27
$\mathbf{N}^{(\alpha)}$	unit vector normal to headgroup/hydrocarbon interface	27
$\mathbf{n}^{(\alpha)}$	unit vector pointing from headgroup to hydrocarbon tails	27
$P_j(\mathbf{r})$	single effective peristaltic mode	30
$P_r(L_r)$	in-plane domain distribution	70
$p_{\rm s}$	size in millimeters of 1 pixel	88
p_x	x-position on X-ray detector	10
$P_z(L_z)$	out-of-plane domain distribution	71
p_z	z-position on X-ray detector	10
$\mathbf{q}$	wavevector transfer; describes scattering Fourier space	31
$\mathbf{Q}$	Fourier space of the thermal fluctuations	37
$\mathcal{R}$	scaled residuals; proportional to (data - theory)/uncertainty	133
$\mathbf{r}$	independent in-plane variable $\mathbf{r} = (x, y)$	26
$\mathbf{R}$	indepedent spatial variable : $\mathbf{R} = (\mathbf{r}, z) = (x, y, z)$	28
$\mathcal{S}$	distance from sample to detector in millimeters	88
$S(\mathbf{q})$	structure factor of the bilayer stack	35
s	distance from sample to detector in pixels	75
$S_0(\mathbf{q})$	structure factor of single bilayers within the stack	35
$S^{\rm F}_{\rm CCD,1}$	final theoretical structure factor for stacked bilayers	103
$S^{\rm F}_{\rm CCD,2}$	final theoretical structure factor for single bilayer in a stack	104
$c(p_z)$	linear offset to model remaining background scattering	104
$S_{\rm MD}$	many domain (MD) structure factor	69
$S_{\rm SD}$	single domain (SD) structure factor	67
T	temperature	40
$t_{\mathbf{s}}$	thickness of sample	95
$\mathbb{U}$	Hermitian matrix involved in Fourier representation of $F_{\rm u}$	39
$z^+(\mathbf{r})$	out-of-plane bilayer fluctuations	26
$\left\langle \lvert z^+_{\mathbf{Q}}\rvert^2 \right\rangle$	height fluctuation spectrum	40
$z^{(\alpha)}$	headgroup/hydrocarbon interface	27

Symbols

ℓ	$2\xi_\theta^2/\xi^2$: dimensionless parameter in $h_j(\rho, \ell, \tau)$	45

List of Tables

2.1 Intensity of several common scattering features in panel (a) of Fig. 2.2 11

5.1 Typical experimental parameter values and ranges of q for analysis. . 85

6.1 Default parameter values used to calculate examples of $S^{\mathrm{F}}_{\mathrm{CCD},1}$ and $S^{\mathrm{F}}_{\mathrm{CCD},2}$ 108

7.1 Sample and experimental parameter values for 2015 DOPC exposure. 135
7.2 Parameter values for tilt-dependent and tilt-independent models. . . 137
7.3 Parameter values for scaled residual distributions plotted in Fig. 7.6. 141
7.4 Fitted parameter values for different initial values of $\mathscr{L}_r$ and $\mathscr{J} \equiv \mathscr{L}_z/D$ ($D = 63.8$ Å). 143
7.5 Parameter values for scaled residual distributions plotted in Fig. 7.8. 145
7.6 Parameter values for cyan and magenta bounded fitting regions in Fig. 7.1 ($D = 63.8$ Å). 147
7.7 Parameter values for various $q_{x,\mathrm{min}}$-values of the fitting range. 150
7.8 Possible $q_{x,\mathrm{max}}$-values based on length scales of the continuum model. 150
7.9 Parameter values for cyan bounded fitting region in Fig. 7.1 ($D = 63.8$ Å). 152
7.10 Sets of fitted parameter values used to determine $\Phi(q_z)$. 159
7.11 Parameter values and associated uncertainties based on a $\Delta\chi^2$-value of 1. 164
7.12 Fitted parameter values for fits in Table 7.11 for which $\Delta\chi^2 < 0$. . . . 165

8.1 Experimental parameter values for 2013 - 2015 DOPC exposures. . . 167
8.2 Tilt-dependent and -independent fitted parameter values for DOPC exposures measured between 2013 and 2015. * 168
8.3 Average K_c- and K_θ-values for DOPC samples from 2013 - 2015. . . . 170
8.4 Values of $K_c/(k_{\mathrm{B}}T)$ determined from various experimental procedures and molecular dynamics simulation. Values were adjusted to 30 °C. . 172

8.5 Values of K_θ determined from experiments and MD simulations. . . . 173
8.6 Fitted parameter values for K_θ fixed to MD simulation determined value of 66 mN/m. 174
8.7 Tilt-dependent and -independent values of λ_{fl} and H. 183

C.1 Contributions to Ψ_{UC} and Ψ_{UC} using values from Table C.2. 210
C.2 Parameter values from [1] and Section 7.1. 211

List of Figures

1.1 A cartoon of a lipid is shown with labeled vectors illustrating the definition of tilt **m** Eq. (1.1). The blue dashed line indicates the surface dividing the headgroup from the hydrocarbon tails. 4

2.1 A simplified schematic of the flightpath is shown. Two pairs of horizontal and vertical slits define the beam's cross section. The Molybdenum beam stop attenuates the direct beam and is placed close to the sample chamber (about 1 mm) to block the detector from background scattering. The sizes and distances between flightpath elements are not to scale. 9

2.2 DOPC sample and direct beam exposures are shown in (a) and (b), respectively. The attenuated direct beam is visible through the beam stop centered at about $(490, 75)$. Intensity is indicated by the linear grayscale where white corresponds to most intense. The dark rectangular feature in the lower left corner is the shadow of the beam stop. The bright feature to the right of the beam stop shadow is the beam's splash. The beam and several out-of-plane orders are identified by the cyan text. 10

2.3 The intensity of the beam through the beam stop, see panel (b) in Fig. 2.2, is plotted as a function of p_z (left-hand side) and p_x (right-hand side). Ideal beam profiles are a boxcar and a Gaussian in the p_z- and p_x-directions, respectively. 11

2.4 A top view of the sample chamber is shown. Substrate and chamber dimensions are drawn to scale. The dash-dot lines are the 1.5-6 μm thick mylar windows. The blue arrows indicate entrance and exit holes for He. The X-rays propagate from right to left. 12

2.5 The simplified sample rotation as a function of time is plotted, where τ is the cycle period. The acceleration before and after the angular velocity changes sign have been neglected. Therefore, the cycle period is longer than the angular range divided by the nominal angular speed (about 18.6°/s). 13

2.6 The beam-substrate geometry is shown for positive (left-hand side) and negative (right-hand side) fixed incident angles ω. The red regions are the direct beam which propagates from right to left. The sample, supporting substrate, and sample holder are the green, dark gray, and light gray rectangles (not to scale), respectively. The ω shown is much larger than $\omega_{\max}$. 15

2.7 DOPC sample exposure at 30 °C using Fig. 2.5 protocol (left-hand side) and corresponding kLB ($\omega = 2.8°$; right-hand side) are shown, using the same linear grayscale. Both the DOPC exposure and the kLB were rotated to align the substrate normal and the p_z-axis. . . . 17

2.8 The difference of the sample exposure and the kLB is depicted. Red indicates negative values. 17

2.9 Exposures without (left-hand side) and with (right-hand side) a water film on the Si substrate are shown using the same grayscale. Red indicates negative values. The exposures were kLB subtracted and rotated such that the substrate normal and the p_z-axis are parallel. The vertical streak of intensity along $p_x \approx 490$ is the specular scattering from the Si wafer. 20

2.10 The water scattering intensity is plotted as a function of p_z, averaging over 200 pixels in p_x centered at $p_x = 850$. Δt is the approximate time after increasing the target temperature of the water circulator. The black line shows the intensity of the kLB subtracted DOPC exposure shown in Fig. 2.8 scaled to match the red line at $p_z = 800$. 21

2.11 The difference of the kLB subtracted DOPC exposure and kLB subtracted water exposure is shown. Red indicates negative values. . . . 22

2.12 The intensity between the blue and green rectangles in (a) is used to determine $A(p_z)$, $B(p_z)$, and $C(p_z)$, see $I'_{\mathrm{H_2O}}$ Eq. (2.5). The resulting $I'_{\mathrm{H_2O}}(p_x, p_z)$ is shown in (b). 22

2.13 The difference of the kLB subtracted DOPC exposure and $I'_{\mathrm{H_2O}}$ is shown. Red indicates negative values. 23

2.14 Comparing two different water background subtraction procedures, the remaining intensity is plotted as function of p_z, averaging over $710 \leq p_x \leq 730$ in Fig. 2.11 (blue squares) and in Fig. 2.13 (red circles). I_{m} and I_{kLB} are the total measured and kLB intensities, respectively. The intensity after subtracting $I'_{\mathrm{H_2O}}$ is more symmetrically distributed about 0. The black dashed line is a guide to the eye. 24

2.15 Intensity as a function of p_z ($700 \leq p_x \leq 740$), panel (a), and p_x ($395 \leq p_z \leq 435$), panel (b), are plotted at various stages in the background subtraction procedure. Note, the measured intensity I_{m} has been shifted down by 415 to facilitate visual comparison with the background subtracted curves. 24

3.1 A diagram of the bilayer stack is labeled to illustrate various fluctuation fields and definitions given in the text. The lighter colored region in the jth bilayer is shown expanded in the figure's right-hand side. D is the repeat distance in the z-direction. 27

3.2 A diagram of a single bilayer is labeled to describe the parameters in the tilt-independent electron density, Eq. (3.5). As α_{b} increases the membrane thickness $\mathcal{T}$ projected on the z-axis increases. 29

3.3 A diagram of a single bilayer is labeled to describe the additional parameters in the tilt-dependent electron density, Eq. (3.7). As the angle between $\mathbf{n}^{(\alpha)}$ and $\mathbf{N}^{(\alpha)}$ increases, the leaflet thickness $\mathcal{T}^{(\alpha)}$ projected on the z-axis decreases. Here $\mathbf{N}^{(\alpha)}$ and $\hat{\mathbf{z}}$ are parallel for convenience, but generally, $\mathbf{N}^{(\alpha)}$ and $\hat{\mathbf{z}}$ are not parallel. 30

3.4 Single membrane tilt-dependent (solid line) and tilt-independent (dashed line) height spectra are plotted. The vertical short dashed line indicates the crossover from Q_r^{-4} to Q_r^{-2} centered at $\sqrt{K_\theta/K_c}$. 42

4.1 $h_j(\rho, \ell, \tau)$ and $\tilde{h}_j(\rho, \ell, \tau)$ are plotted as functions of ρ for several j and $\ell = 0.1$. 48

4.2 The relative error of neglecting C^* as a function of ℓ. 51

4.3 The relative error of neglecting C^* as a function of j for $\ell = 2$ (black solid line) and $\ell = 0$ (red dashed line). The solid and dashed lines are upper and lower bounds, respectively, for the relative error. Even though it is a postive integer, j has been plotted as if it is a continuous variable. 52

4.4 $h_j(\rho, \ell, \tau)$ and its analytic approximation $\tilde{h}_j(\rho, \ell, \tau)$ are plotted as functions of ρ for several j and $\ell = 0.1$. $\tilde{h}_j(\rho, \ell, \tau)$ is a good approximation for $\rho \gg 1$. 60

4.5 $h_j(\rho, \ell, \tau)$ and its analytic approximation $\tilde{h}_j(\rho, \ell, \tau)$ are plotted as functions of ρ for several j and $\ell = 2$. $\tilde{h}_j(\rho, \ell, \tau)$ is a good approximation for $\rho \gg 1$. The small amplitude oscillations in $h_0(\rho, \ell, \tau)$ are caused by the interplay between ξ and ξ_θ. 61

4.6 The relative error of $h_j(\rho, \ell, \tau)$ and $\tilde{h}_j(\rho, \ell, \tau)$ is plotted as a function of ρ for several j and $\ell = 0.1$. The jagged features of the curves are likely numerical artifacts. 62

4.7 The relative error of $h_j(\rho, \ell, \tau)$ and $\tilde{h}_j(\rho, \ell, \tau)$ is plotted as a function of ρ for several j and $\ell = 2$. The jagged features of the curves are likely numerical artifacts. 62

5.1 The scattering geometry for a low angle scattering experiment is shown. The solid red lines indicate the path of an incident and scattered X-ray, and the dashed red line is the path of the direct beam after the sample (green rectangle). Sample and CCD are not to scale. The sample size is 5×30 mm, and the sensitive surface of the detector is about 73×73 mm. 74

5.2 Diagram defining transverse ξ_{T} and longitudinal ξ_{L} coherence lengths of the X-ray beam. The horizontal solid red line and arrow indicate the primary X-ray propagation direction. $\xi_{\mathrm{T}x}$, $\xi_{\mathrm{T}z}$, and ξ_{L} are not drawn to scale. 77

5.3 Scattering geometry for low angle scattering experiment. The unprimed and primed coordinates are the lab centered and sample centered coordinates, respectively. The sample is the green rectangle, and its supporting substrate has been omitted. 79

5.4 A xy-slice (constant z) of the coherence volume described by Eqs. (5.68)-(5.70). The colored dashed lines correspond to the colored inequalities. The yellow region satisfies all inequalities. Beyond a certain q_x-value, the yellow region transitions from a hexagon (left-hand side) to a parallelogram (right-hand side). 83

5.5 A yz-slice (constant x) of the coherence volume described by Eqs. (5.68)-(5.70). The colored dashed lines correspond to the colored inequalities. The yellow region satisfies both inequalities. Beyond a certain q_z-value, the yellow region transition from a octagon (left-hand side) to a parallelogram (right-hand side). 83

5.6 Scattering geometry for a low angle scattering experiment with details concerning the beam. The substrate is depicted by the dark gray rectangular cuboid, and the sample is the darker green rectangle. The beam and beam path are shown by the red rectangles and lines. The part of the beam that would pass under the substrate is blocked by the sample holder (not depicted). The intersection of the beam and the bare part of the substrate is red, and the intersection with the sample is bright green. The edges of the scattered beam are shown by the gray lines. The projection of the beam-sample footprint on the detector is also bright green. While the beam-sample footprint is a rectangle, see Fig. 5.7, its projection on the detector is a parallelogram, see Fig. 5.8. 87

5.7 Different perspectives of the scattering geometry depicted in Fig. 5.6. The left-hand side shows a side view of the substrate (gray rectangle) and multilamellar lipid bilayer sample (green rectangle). The thickness of the sample (10 μm) and substrate (2 mm) are not drawn to scale. The right-hand side shows a top view of the sample. The four white circles v_1 though v_4 label the vertices of the rectangular beam footprint on the sample. 87

5.8 The beam-sample footprint projected onto the detector is depicted by the green parallelogram. 89

5.9 $b'_x(p_x)$ Eq. (5.91) is plotted for $b_x = 3$ pixels, $L_\mathrm{s} = 5$ mm, and $s = (365$ mm$)$ /(0.07113 mm/pixel). b'_x increases by about a factor of 2 in the p_x range of interest. 90

5.10 $b'_z(p_z, \omega)$ Eq. (5.93) is plotted for $L_s = 5$ mm and $s \approx 5131$ pixels. The triangular (ω, p_z)-region patterned with red diagonal lines is not experimentally accessible because the substrate blocks the outgoing scattering, see Fig. 5.11. The cyan line indicates the p_z position of the specular scattering as a function of ω, $p_z = s \tan(2\omega)$. The boundary between grayscale and diagonally patterned lines is described by $p_z = s \tan \omega$. For fixed ω, b'_z significantly increases as a function of p_z. . . . 91

5.11 Scattering geometry describing the maximum substrate rotation angle ω before scattering from the sample (green rectangle) at pixel p_z is blocked by the substrate (gray rectangle). The red solid and dashed lines show the beam path without a sample. The thickness of the sample (10 μm) and substrate (1 mm) are not drawn to scale. 96

5.12 $q_z^{\ddagger}(0, p_z, \omega)$ Eq. (5.130) is plotted for $\lambda = 1.17$ Å, $p_s = 0.07113$ mm/pixel, and $\mathcal{S} = 365$ mm. The triangular (ω, p_z)-region patterned with red diagonal lines is not experimentally accessible because the substrate blocks the outgoing scattering. The cyan line indicates the p_z position of the specular scattering as a function of ω. 98

5.13 $q_z^{\ddagger}(300, p_z, \omega)$ Eq. (5.130) is plotted for $\lambda = 1.17$ Å, $p_s = 0.07113$ mm/pixel, and $\mathcal{S} = 365$ mm. 99

5.14 $q_x^{\ddagger}(p_x, p_z)$ Eq. (5.134) is plotted for $\lambda = 1.17$ Å, $p_s = 0.07113$ mm/pixel, and $\mathcal{S} = 365$ mm. $q_x(p_x, p_z)$ is better approximated by $q_x^*(p_x)$ for $p_x = 0$ as compared to $p_x = 300$. 100

5.15 The CCD integral q_y-limits as a function of q_x at various q_z values (as shown in the legend). The pairs of lines depict upper and lower limits. The red dashed line is a guide to the eye to emphasize the q_x-dependence. 103

6.1 The background subtracted scattering intensity from a stack of DOPC bilayers is shown. The beam stop covers the region defined by $q_z \lesssim 0.2$ Å^{-1} and $q_x \lesssim 0.08$ Å^{-1}. Intensity is indicated by the linear grayscale. The red pixels indicate intensity less than zero. The predicted theoretical intensity is fitted to measured data within the cyan rectangle ($0.01 \lesssim q_x \lesssim 0.22$ Å^{-1} and $0.3 \lesssim q_z \lesssim 0.6$ Å^{-1}). This chapter demonstrates why these are the data that are fitted to obtain mechanical moduli. 107

6.2 $S^{\mathrm{F}}_{\mathrm{CCD},1}$ is shown using a logarithmic grayscale for the parameter values in Table 6.1. The peaks along q_z centered at $q_x = 0$ correspond to the repeat out-of-plane distance. The peaks are decreasingly apparent for increasing q_z primarily because of bilayer midplane fluctuations. For constant q_z, $S^{\mathrm{F}}_{\mathrm{CCD},1}$ decays for increasing $|q_x|$. 109

6.3 $S^{\mathrm{F}}_{\mathrm{CCD},1}$ is plotted as a function of q_x for various K_c-values. The curves have been normalized at $q_x = 0.01$ Å^{-1}, and additionally, the solid lines are vertically offset by 10^{-1} to improve visibility. See Table 6.1 for parameter values. 110

6.4 $S^{\mathrm{F}}_{\mathrm{CCD},1}$ is plotted as a function of q_x for various B-values. The curves have been normalized at $q_x = 0.01$ Å^{-1}, and the solid lines are vertically offset by 10^{-1}. 111

6.5 $S^{\mathrm{F}}_{\mathrm{CCD},1}$ is plotted as a function of q_x for various K_θ-values. The curves have been normalized at $q_x = 0.01$ Å^{-1}. 112

6.6 $S^{\mathrm{F}}_{\mathrm{CCD},1}(q_x, q_z)$ is plotted as a function of q_x for $\mathscr{L}_r = 600$ Å and $\mathscr{L}_r = \xi_{\mathrm{T}x} \approx 6000$ Å. The curves have been normalized at $q_z = 1$ Å^{-1}. Beyond $q_z \approx 0.55$ Å^{-1} the curves continue to converge. 114

6.7 $S^{\mathrm{F}}_{\mathrm{CCD},1}(q_x, q_z)$ is plotted as a function of q_x for $\mathscr{L}_r = 600$ Åand 6000 Å. The curves have been normalized at $q_x = 0.2$ Å^{-1}. The vertical gray dashed-dotted line indicates the typical smallest analyzed q_x-value, see Fig. 6.1. Beyond $q_x \approx 0.1$ Å^{-1} the curves continue to converge. 115

6.8 $S^{\mathrm{F}}_{\mathrm{CCD},1}(q_x, q_z)$ is plotted as a function of q_z for $\mathscr{L}_z = 400$ Å and 800 Å. The curves have been normalized at $q_z = 1$ Å^{-1}. Beyond $q_z \approx 0.55$ Å^{-1} the curves continue to converge. 117

6.9 $S^{\mathrm{F}}_{\mathrm{CCD},1}(q_x, q_z)$ is plotted as a function of q_z for $\mathscr{L}_z = 400$ Å and 800 Å. The curves have been normalized at $q_z = 0.2$ Å^{-1}. Beyond $q_x \approx 0.1$ Å^{-1} the curves continue to converge. 118

6.10 $S^{\mathrm{F}}_{\mathrm{CCD},1}$ as a function of q_x is plotted for various a-values. The curves have been normalized at $q_x = 0.01$ Å^{-1}. 119

6.11 $S^{\mathrm{F}}_{\mathrm{CCD},1}(q_x, q_z)$ as a function of q_z for $q_x = 0.08$ Å^{-1} is plotted (solid lines) for various a-values, holding other parameters constant. The curves have been normalized at $q_z = 0.3$ Å^{-1}. Applying an approximate analytic relation for $S^{\mathrm{F}}_{\mathrm{CCD},1}$ as a function of a, the solid lines are nearly collapsed to a single dashed curve, vertically offset by 10^{-1} to improve visibility. The small peaks at $q_z \approx 0.1$ Å^{-1} ($h = 1$) are referred to as "spikes" in Section 5.3.2. 121

6.12 The ratio of the $a = 12$ Å and $a = 16$ Å q_z-curves to the $a = 8$ Å curve for $q_x = 0.08$ Å^{-1} is plotted. For $q_z \lesssim 0.25$ Å^{-1}, the ratios are nearly 1, but for larger q_z-values, the q_z-dependence of the different a-value curves is significant. In the figure legend, ★ is either 12 (darker gray solid line) or 16 (lighter gray solid line). 122

6.13 $S^{\mathrm{F}}_{\mathrm{CCD},1}(q_x, q_z)$ as a function of q_z is plotted for Gaussian and exponential subvolume distributions at $q_x = 0$ Å^{-1} and $q_x = 0.01$ Å^{-1}. The curves have been normalized at $q_z = 1$ Å^{-1}. Beyond $q_z \approx 0.55$ Å^{-1} the curves continue to converge. 124

6.14 $S^{\mathrm{F}}_{\mathrm{CCD},1}(q_x, q_z)$ as a function of q_x is plotted for Gaussian and exponential subvolume distributions at $q_z = 0.3$ Å^{-1} and $q_z = 0.35$ Å^{-1}. The curves have been normalized at $q_x = 0.2$ Å^{-1}. Beyond $q_x \approx 0.1$ Å^{-1} the curves continue to converge. The vertical dashed-dotted gray line shows the minimum q_x-value typically analyzed. 125

6.15 Relative difference Δh^{f}_j Eq. (6.5) is plotted as a function of ρ for several L_r/a with $j = 0$, $\ell = 0.06$, $\tau = 100$, and $J \to \infty$. Recall that $\rho = r/\xi$, and typically, $\xi \approx 50$ Å. The $j = 0$ case was chosen since it makes the dominant contribution to the predicted X-ray scattering intensity. . . 127

6.16 Relative difference Δh^{f}_j Eq. (6.5) is plotted as a function of ρ for several J with $j = 0$, $\ell = 0.06$, $\tau = 100$, and $L_r \to \infty$. 127

6.17 $S^{\mathrm{F}}_{\mathrm{CCD},1}$ (left-hand side) and $S^{\mathrm{F}}_{\mathrm{CCD},2}$ (right-hand side) are shown using the same logarithmic grayscale for the parameter values in Table 6.1. 129

6.18 $S^{\mathrm{F}}_{\mathrm{CCD},1}$ and $S^{\mathrm{F}}_{\mathrm{CCD},2}$ are plotted as functions of q_z for q_x-values of 0 Å^{-1} and 0.01 Å^{-1}. The curves are normalized at $q_z = 0.9$ Å^{-1}. 130

6.19 $S^{\mathrm{F}}_{\mathrm{CCD},1}$ and $S^{\mathrm{F}}_{\mathrm{CCD},2}$ are plotted as functions of q_x for q_z-values of 0.3 Å^{-1}, 0.35 Å^{-1}, and 0.7 Å^{-1}. The curves are normalized at $q_x = 0.2$ Å^{-1}. . 130

7.1 The background subtracted scattering intensity from a stack of DOPC bilayers is shown. Intensity is expressed by a linear grayscale except that red pixels indicate intensity less than zero and white indicates intensity greater than 200. The predicted theoretical intensity is compared to the measured data within either the two cyan dashed rectangles or within the solid magenta rectangle. σ^2_{back} is the mean square intensity within the yellow rectangle where the mean is essentially zero. The green circles show the positions of the Caillé peaks for $D = 63.8$ Å. 136

7.2 Measured data and tilt-dependent and -independent fits are plotted as functions of q_x for several q_z-values. Representative error bars for $q_z = 0.35$ Å^{-1} correspond to $\pm\sigma_{\text{e}}$. The curves have been vertically offset to improve visibility. Note, due to the logarithmic vertical axis, negative intensity values are not plotted. 138

7.3 After averaging over all fitted q_z-values, the measured data and tilt-dependent and -independent fits are plotted as functions of q_x. Also, the scaled residuals $\mathcal{R}$ for both fits are plotted as functions of q_x. The dashed-dotted gray line is a guide to the eye. 139

7.4 χ^2_{red}-values from tilt-dependent and -independent fits are plotted for 0.02 Å^{-1} wide q_x-ranges. 140

7.5 Scaled residuals $\mathcal{R}$ Eq. (7.6) of tilt-independent (left-hand side) and tilt-dependent (right-hand side) model fits. 140

7.6 Tilt-dependent and -independent (~~tilt~~) $\mathcal{R}$ distributions for (a) $0.01 \lesssim q_x \lesssim 0.06$ Å^{-1} and (b) $0.06 \lesssim q_x \lesssim 0.18$ Å^{-1}. The red and blue lines are Gaussian fits to the distributions, and Table 7.3 summarizes the fitted parameter values. The distributions have been normalized by the fitted Gaussian amplitudes. Representative error bars for the tilt-dependent distribution are the square root of the number of pixels whose $\mathcal{R}$-value is within a given $\mathcal{R}$-bin of size 0.1. The dashed-dotted gray lines are guides to the eye. 141

7.7 χ^2_{red}-values from suppressing $\mathscr{L}_i$ ($\not\mathscr{L}_i$) and fitting to determine $\mathscr{L}_i$-values are plotted for 0.02 Å^{-1} wide q_x-ranges. 144

7.8 $\mathcal{R}$ distributions corresponding to suppressed ($\mathscr{L}_i$) and fitted $\mathscr{L}_i$ for (a) $0.01 \lesssim q_x \lesssim 0.1$ Å^{-1} and (b) $0.1 \lesssim q_x \lesssim 0.22$ Å^{-1}. The lines are Gaussian fits to the distributions, and Table 7.5 summarizes the fitted parameter values. The distributions have been normalized by the fitted Gaussian amplitudes. Representative error bars for fitted $\mathscr{L}_i$ are the square root of the number of pixels whose $\mathcal{R}$-value is within a given $\mathcal{R}$-bin of size 0.1. The dashed-dotted gray lines are guides to the eye. 145

7.9 Scaled residuals $\mathcal{R}$ of tilt-dependent model fit for q_x, q_z-region within the magenta rectangle in Fig. 7.1. 147

7.10 Measured data and tilt-dependent and -independent model fits are plotted as functions of q_x, after averaging $0.41 \leq q_z \leq 0.47$ Å^{-1}. Representative error bars indicate 1 standard deviation. Also, the scaled residuals $\mathcal{R}$ for both fits are plotted as functions of q_x. The dashed-dotted gray line is a guide to the eye. 148

7.11 $\left\langle \left| F^{\mathrm{L}} \right|^2 \right\rangle$, $\left| \left\langle F^{\mathrm{L}} \right\rangle \right|^2$, and F_{Δ}^{L} are plotted for $K_A = 2.75 \times 10^{-21}$ J/Å^2, $A_o = 2000$ Å^2, and $D_c = 30$ Å. In the right-hand panel, the vertical axis is expanded as compared to the left-hand panel to highlight F_{Δ}^{L}. 154

7.12 The determined $|F(q_z)|^2$ and $F_{\Delta}(q_z)$ are plotted from both the parallel (top) and series (bottom) fitting methods on the same arbitrary scale. The dashed-dotted gray lines are guides to the eye. 156

7.13 $|F(q_z)|^2 + F_{\Delta}(q_z)$ is plotted from both the parallel and series fitting methods. 157

7.14 Measured data and the tilt-dependent, parallel, series, and tilt-independent fits are plotted as functions of q_x, averaging $0.41 \lesssim q_z \lesssim 0.47$ Å^{-1}. Representative error bars indicate 1 standard deviation. 158

7.15 The background subtracted intensity from a stack of DOPC bilayers is shown. Intensity is expressed by a linear grayscale except that red pixels indicate intensity less than zero and white indicates intensity greater than 200. $\Phi(q_z)$ is determined using the fitted $S_{\mathrm{CCD},1}^{\mathrm{F}}$ parameter values in Table 7.10 and the data within the yellow rectangle. The green circles indicate positions of Caillé peaks. 160

7.16 The determined $|F(q_z)|$ Eq. (7.16) are plotted for fitted $S^{\mathrm{F}}_{\mathrm{CCD},1}$ parameter values listed in Table 7.10. Commonly, a smooth baseline is subtracted from $\Phi(q_z)$ such that $|F(q_z)|$ is zero at apparent minima (for example $q_z \approx 0.28$ Å^{-1} and ≈ 0.42 Å^{-1}). The aforementioned subtraction was not performed. 161

7.17 $\Delta\chi^2$-values listed in Table 7.11 corresponding to K_c are plotted as a function of the % change in the best tilt-dependent K_c-value (8.5×10^{-13} ergs). The red dashed line is the best fit of Eq. (7.23). The right-hand plot emphasizes the small $\Delta\chi^2$-range, and the blue dotted-dashed line shows $\Delta\chi^2 = 1$. 164

8.1 The tilt-dependent values of K_c and K_θ listed in Table 8.2 are plotted as a function of year. In 2014, there were two exposures, both with fitted K_θ-value of 85 mN/m. 169

8.2 Tilt-dependent values of K_c and K_θ listed in Table 8.2 are plotted as functions of D. 170

8.3 Tilt-dependent and -independent height-height correlation functions $h_j(r/\xi, \ell, \tau)$ and $h_j(r/\xi, 0, \infty)$, see Eq. (8.7), are plotted as functions of r using the red parameter values in Table 8.2. 180

8.4 $\Delta\widetilde{\mathcal{F}}^{\cancel{\mathrm{tilt}}}_{\mathrm{fl}}$ and $\Delta\widetilde{\mathcal{F}}_{\mathrm{fl}}$ are plotted as functions of D'_{w}. The dashed lines are exponential fits to the correspondingly colored data. 183

B.1 Contour plots of $S_{\mathrm{MD}}\left(\sqrt{q_x^2+q_y^2}, 2\pi/D\right)$, left-hand side, and $S^{\mathrm{c}}_{\mathrm{MD}}(q_x, q_y, 2\pi/D)$, right-hand side, are shown. A logarithmic grayscale indicates the value, where white corresponds to most intense. Typical parameter value were used to calculate S_{MD} and $S^{\mathrm{c}}_{\mathrm{MD}}$. 197

B.2 A subregion of the q_x, q_y-region in the right-hand plot of Fig. B.1 is shown. Note, the q_x- and q_y-axes show different ranges. The yellow dashed lines and red solid lines indicate the range of integrated q_y-values for several q_x-values for the q_x-independent and q_x-dependent integration limits, respectively. 198

B.3 A subregion of the q_x, q_y-region in the right-hand plot of Fig. B.1 is shown. Note, the q_x- and q_y-axes show different ranges. The yellow solid and dashed lines indicate the q_x, q_y-trajectories probed by a row of CCD pixels during a fixed angle exposure. The $h = 1$ Bragg angle is $\omega_1^{\mathrm{B}} \approx 0.54°$. 199

B.4 The predicted intensity along the solid and dashed yellow lines involving $S_{\mathrm{MD}}^{\mathrm{c}}$ in Fig. B.3 is plotted as a function of q_x for $q_z = 2\pi/D$; the intensity is normalized at $q_x = 0.01$ Å^{-1}. For increasing ω beyond $\omega_1^{\mathrm{B}} \approx 0.54°$, a peak in intensity develops, and its center shifts to greater q_x. 200

C.1 The EDP from simulation $\rho_{\mathrm{sim}}^*(z)$ is plotted along with the corresponding EDP with fluctuations removed $\rho_{\mathrm{sim}}(z)$ as functions of the distance z from the bilayer midplane. 205

C.2 $\left\langle \left| F^{\mathrm{B}} \right|^2 \right\rangle$ Eq. (C.20), $\left| \left\langle F^{\mathrm{B}} \right\rangle \right|^2$ Eq. (C.21), and their difference F_Δ^{B} are plotted as functions of q_z. In the right panel, the vertical axis is expanded to highlight F_Δ^{B}. The arbitrary scale of the vertical axis is the same in the left and right panels. 206

C.3 The EDP from simulation $\rho_{\mathrm{sim}}^*(z)$ is plotted along with the corresponding EDP with fluctuations removed $\rho_{\mathrm{sim}}(z)$. The resulting EDP is nearly identical to the EDP plotted in Fig. C.1. 207

C.4 $\left\langle \left| F^{\mathrm{L}} \right|^2 \right\rangle$ Eq. (C.28), $\left| \left\langle F^{\mathrm{L}} \right\rangle \right|^2$ Eq. (C.29), and their difference F_Δ^{L} are plotted. In the right panel, the vertical axis is expanded as compared to the left panel to highlight F_Δ^{L}. The arbitrary scale of the vertical axis is the same in the left and right panels and the same as used in Fig. C.2. 208

C.5 $\left\langle \left| \boldsymbol{\nabla} z_0^+ \right| \right\rangle$, $\langle |\hat{\mathbf{m}}_0|^2 \rangle$, $\left\langle \left| \boldsymbol{\nabla} z_0^- \right| \right\rangle$, and $\langle |\bar{\mathbf{m}}_0|^2 \rangle$ – Eqs. (C.40), (C.66), (C.71), and (C.72), respectively – are plotted as functions of $\tilde{a}$. The relevant material parameter values are summarized in Table C.2. The curves are normalized at $\tilde{a} = 2$ nm. 220

D.1 The relative error of approximating the Bessel function with the first 2 terms in its Taylor series about 0 as a function of ρ for $\ell = 2$ (black solid line) and $\ell = 0$ (red dashed line). The solid and dashed lines are upper and lower bounds, respectively, for the relative error. A typical value of $\tau = 50$ was used. 224

E.1 The spherical and planar UC are plotted as functions of R/a for $\bar{\sigma} = 0$. The steplike features in $\Psi^{\mathrm{s}}_{\mathrm{UC}}$ are due to the discrete nature of L in Eq. (E.39). 236

E.2 The planar Eq. (E.33) and spherical Eq. (E.6) height spectra are plotted as functions of the wavenumber for $\sigma = 0$. The horizontal axis is log base 2. 237

E.3 $\Psi^{\mathrm{s}}_{\mathrm{UC}}$ is plotted as a function of $\bar{\sigma}$ for several values of R/a. 237

Chapter 1

Introduction

Preliminary Remarks

The current work combines theoretical results and experimental techniques to study the mechanical moduli and the structure of lipid bilayers. In part, this thesis is motivated by recently reported inconsistencies between height spectra determined from molecular dynamics (MD) simulations [1] and the prediction of the Helfrich-Canham model, see Section 1.1. These recent results instigated a series of theoretical extensions and reformulations of the lipid membrane free energy functional. A new single membrane free energy model is only one of several necessary elements in the present work since the studied experimental system is a stack of lipid bilayers. The stacked bilayers are described by a theory originally from smectic liquid crystal literature, see Section 1.2. Finally in Section 1.3, the thesis is briefly summarized, and aspects of particular Chapters are emphasized.

1.1 Fluid Phase Lipid Bilayers

The studied system is a stack of fluid phase lipid bilayers, where fluid describes the short range fluid-like in-plane correlations of the lipid molecules [2, 3]. A lipid is composed of a hydrophilic headgroup and typically two hydrophobic fatty acid chains. In water, lipids self-assemble into spatially ordered two- or three-dimensional structures, depending on the specific lipid molecule, temperature, and concentration [4]. This thesis is concerned with the class of lipids that spontaneously form bilayers in which the hydrophilic headgroups shield the hydrophobic acyl tails from the surrounding

water [5].

The fluid phase is often considered the most biologically relevant lipid bilayer phase since the majority of lipids in plasma and organelle membranes are in a fluid phase [6]. Single and many-component lipid bilayers are used as model biological membranes for various structural and chemical assays since they constitute the fundamental structure in which other biomolecules reside [7]. However, lipids comprise only a modest fraction of the molecular composition of typical biological membranes. The rest of the biological membrane is primarily composed of proteins and carbohydrates.

From a purely physical perspective, stacked lipid bilayers are an interesting model system to investigate various types of correlations. This is the perspective that most intimately connects with liquid crystal literature, see Section 1.2. The correlations in stacked bilayers are anisotropic. Perpendicular to the membrane planes, there is a characteristic repeat spacing, reminiscent of a one-dimensional crystal; however, as mentioned previously, the in-plane correlations are fluid-like. Additionally, the aspect ratio of a single membrane is very large; they are typically about 4.5 nm thick and can be larger than 100s of μm in lateral extent. Consequently, a single membrane is quasi-two-dimensional, having many in a confined volume leads to stacking order.

This thesis primarily focuses on the mechanical properties of lipid bilayers. Many biological processes involve changes to membrane topography [8, 9]. The energy required to deform a nominally flat membrane has traditionally been quantified by the Helfrich-Canham (HC) model [10, 11]. This is a continuum model which essentially treats the membrane as a deformable plate without internal structure [12]. For a tensionless, symmetric bilayer with fixed topology and no boundary, the only material descriptor in the model is the bending modulus K_c. Since this level of description is appropriate for many aspects of biomembrane mechanics [13], quantifying K_c has been the purpose of many experiments [14, 15, 16, 17].

Of lesser importance to the current work, but nonetheless integral, is the structure of lipid bilayers. The mechanical and structural attributes of the stacked bilayers are coupled. Therefore, lipid bilayer structure is also discussed, see in particular Sections 3.2.1 and 7.5.

1.1.1 Motivation to Extend Helfrich-Canham Model

For length scales shorter than several membrane thicknesses, many simulations [18, 19, 20, 21, 1, 22, 23, 24] have reported significant deviations from the HC model, most pertinently in the measured height-height fluctuation spectrum. At first, the differences were attributed to molecular protrusion modes [18, 19, 20]. By considering a free energy that includes molecular tilt with a corresponding material property, the tilt modulus K_θ, systematic deviations from HC model predictions have been derived [21, 1, 24], and estimates of K_θ have been reported from simulations [21, 22, 1, 23, 25, 24]. Using the so-called "direct Fourier method", the height spectrum from an MD simulation was originally reported to be inconsistent with the tilt-dependent spectrum [26]; however, the direct Fourier method was later shown to be flawed [27]. Additionally, the height spectrum has been derived from recent membrane models that explicitly include both tilt and protrusion contributions [1]. The derived height spectrum was compared to the height spectrum determined from MD simulations, and it was shown that the protrusion contribution is negligible [1]. [1]

Earlier, molecular tilt was invoked to discuss orientational order in vesicles [28] and to try to explain the origin of the ripple phase [29]. Additionally, a tilt contribution to the membrane free energy was investigated as an example of an internal degree of freedom [10] and later was invoked to explain inverted amphiphilic mesophases [30], as well as fluid membranes [31]. Interestingly in seminal work [10], Helfrich considered molecular tilt and an associated energetic penalty for nonzero tilt mediated by a modulus K_t. Helfrich predicted that $K_t \approx K_A$ [10], and therefore, he argued that "tilt should be minute and its elastic energy negligible in most practical cases [...], so i[t] appears pointless to develop a detailed molecular theory." For typical modern values of $K_A \approx 2.5\times10^{-19}$ J/nm^2 and $K_t = K_\theta \approx 1\times10^{-19}$ J/nm^2, $K_\theta \approx K_A/2.5$. Therefore, the tilt degree of freedom contributes somewhat more to membrane energetics than Helfrich posited.

The tilt $\mathbf{m}$ of a lipid molecule is quantified by the deviation of the director $\mathbf{n}$ of the molecule from the normal $\mathbf{N}$ to the monolayer surface,

[1] Interestingly, the reported tilt and protrusion dependent model is still inconsistent with the height spectrum determined from MD simulations for large wavevectors (short in-plane length scales) [1].

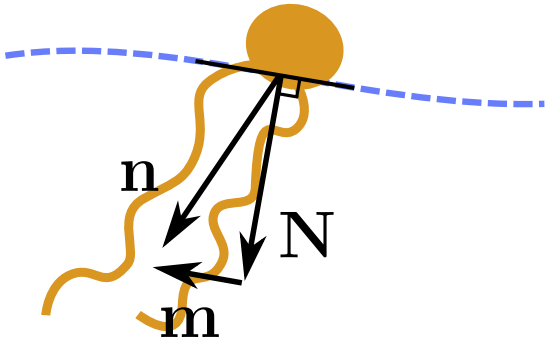


Figure 1.1: A cartoon of a lipid is shown with labeled vectors illustrating the definition of tilt $\mathbf{m}$ Eq. (1.1). The blue dashed line indicates the surface dividing the headgroup from the hydrocarbon tails.

$$\mathbf{m} = \frac{\mathbf{n}}{\mathbf{n} \cdot \mathbf{N}} - \mathbf{N}, \tag{1.1}$$

where $\mathbf{n}$ and $\mathbf{N}$ are unit vectors [28]. Eq. (1.1) is depicted in Fig. 1.1. By definition $\mathbf{m}$ always points tangent to the local membrane plane ($\mathbf{m} \cdot \mathbf{N} = 0$). More recently, other researchers have considered the ramifications of tilt on the spectra of simulated fluid lipid membranes [21, 22, 1, 24].

The inclusion of tilt-dependent terms in the single membrane free energy model is a fundamental modification to the HC model. As tilt is defined for each molecule, this modification asserts the importance of internal degrees of freedom on membrane mechanics. A tilt degree of freedom has previously been claimed to significantly influence inter-lipid, intermembrane, and membrane-protein interactions (see the introduction of [1] for a succinct review). For many decades, the HC model has been the touchstone for both theoretical and experimental membrane related research. Consequently, the relatively recent tilt-dependent models should motivate new and exciting future work. This thesis is one such tilt-dependent development. The first experimental support for the addition of tilt to the HC model to describe the fluid lamellar phase was recently reported [32]. This thesis is a further refinement of the previously published Letter and discusses many details regarding both the experimental procedure and analysis.

1.2 X-ray Scattering Methodologies and Analyses

The current X-ray scattering experimental methodology is an extension of a procedure designed to study smectic liquid crystals (LC). A smectic LC is a layered structure which is characterized by positional order perpendicular to the layer planes and fluid-like order within the planes. Structural studies of stacked lipid bilayers significantly predate the establishment of stacked bilayers as smectic LCs. Therefore, not until more recently (late 1980s) were smectic theoretical and experimental techniques leveraged in stacked bilayer studies to significant effect.

To study the structure of lipid bilayers, many researchers have used X-ray experimental procedures and associated analyses inspired by crystallographic techniques (at first not LC influenced) [33, 3]. In order to observe out-of-plane peaks, scattering from stacks of lipid bilayers is measured. Commonly, multilamellar vesicles are studied; less often, oriented bilayer stacks. The out-of-plane peak position and intensity are analyzed to determine out-of-plane membrane structure [34, 35]. Using the aforementioned experimental procedure, the structural characterization of bilayers in the most biologically relevant fluid phase is low resolution because very few out-of-plane peaks are observed; the peak intensity decreases rapidly as a function of increasing out-of-plane peak order. Eventually, it was appreciated that both short length scale intermembrane fluctuations [35] and longer length scale height fluctuations [36, 37, 38] reduce the number of observable scattering peaks [39].

In 1988-1989, stacked lipid bilayers were shown to be smectic LCs by measuring the power-law tails from their X-ray scattering peaks [36, 37]. Specifically, stacks of bilayers are classified as lyotropic smectic A (S_A) LCs. "Lyotropic" indicates that the bilayers form a LC only in a solvent (water). "A" indicates that the average molecular director $\mathbf{n}$ is parallel to the average normal to membrane plane $\mathbf{N}$. Since the lipids are chiral, the stacked bilayers may be further categorized as (S_A^*) [40]. The typical smectic free energy includes two terms. One term describes interlayer interactions, and the second term quantifies the energy required to bend a layer [40]. This second term is equivalent to the HC model for a tensionless, symmetric single lipid bilayer with fixed topology.

In previous foundational theoretical work [41], Caillé showed that the out-of-plane X-ray scattering peaks from smectic LCs have long power-law tails because of the quasi-long range order (QLRO) of the layers along the stacking direction [40]. Caillé's

prediction was experimentally supported in 1980 by measurements of the aforementioned power-law scattering peak tails [42]. Unlike classic crystallographic analyses in which the positions and intensities of the Bragg peaks are the primary measured quantities, the smectic LC analysis is concerned with the shape of the scattering peaks. Importantly, the analysis of the power-law tails yields information regarding the mechanical moduli of the studied smectic LC. [2] In the mid-1990s, a detailed theory for the peak shapes of X-ray scattering from multilamellar lipid vesicles was developed [38], following smectic LC theory [40], and utilized to show that correlations within multilamellar lipid vesicles (MLVs) are better described by the smectic LC theory than a paracrystalline theory [43].

With the advent of area detectors on X-ray scattering beamlines in the early 2000s, the experimental emphasis on peak shape began to diminish. Using an area detector, both the peak shape and surrounding diffuse scattering from stacked lipid bilayers are measured concurrently, and it was observed that the diffuse scattering covers much more of the area detector than the peak [44]. Several research groups took advantage of area detectors and applied smectic LC theory to analyze diffuse X-ray scattering from oriented stacked bilayers [44, 45, 46, 47]. The current experimental and analysis methodology closely follows Liu and Nagle [46].

1.3 Brief Summary of Thesis Content

The current work is a detailed analysis of the X-ray scattering from oriented stacks of lipid bilayers. In Chapter 2, the sample preparation and X-ray scattering methodology are described. For the most part, experimental methods follow previous work [48]; however, significant improvements have been made with regard to subtraction of background X-ray scattering, see Section 2.5. In Chapters 3 through 6, the detailed analysis of the measured X-ray scattering from stacked lipid bilayers is developed. While much of this parallels [44, 48], there are detailed differences in addition to the inclusion of tilt. In Chapter 7, a single X-ray scattering exposure is analyzed using several different fitting procedures. Finally in Chapter 8, many exposures from several different stacked lipid bilayer samples are analyzed to determine final mechanical moduli values and associated uncertainties.

[2] The value of the so-called Caillé η parameter is determined, where η is propotional to $(K_c B)^{-1/2}$, see Section 3.3.3.

Compared to Chapters 2, 7, and 8, Chapters 3 through 6 are more theoretically inclined. To appreciate the analysis of measured X-ray scattering described in Chapters 7 and 8, only the details discussed in Chapter 3 are absolutely necessary, specifically Sections 3.1 and 3.2. In Chapter 4, an analytic approximation to the height-height correlation function is derived, and several related topics are discussed. The theoretical scattering intensity derived in Section 3.2 is further developed in Chapter 5, where several sample and experimental issues are considered. The major result of Chapter 5 is a prediction for the measured X-ray scattering intensity from stacked lipid bilayers for the particular experimental methodology detailed in Section 2.4. Since the X-ray scattering prediction is quite complicated, several illuminating examples are given in Chapter 6, and it is established that the values of the unknown model parameters (mostly mechanical moduli) can be plausibly determined by fitting the measured X-ray scattering.

This thesis includes several Appendices. Appendix A provides details regarding derivations in Chapter 3. In Appendix B, so-called Cartesian and cylindrical structure factors, see Section 5.1, are compared, an important theoretical issue but not absolutely necessary to understand the rest of the thesis. Since out-of-plane membrane structure in this thesis is of secondary importance compared to membrane mechanics, Appendix C provides details regarding the form factor, see Sections 3.2.2 and 7.5. The effects of peristaltic modes on out-of-plane bilayer electron density are modeled, see Section C.1, and the so-called undulation correction is defined and discussed, see Section C.2. In Appendix D, several miscellaneous issues are discussed. Importantly, an approximate analytic relation for the effect of the long wavevector cutoff on the predicted scattering intensity, see Section D.1, and the fluctuation free energy per unit area of a single bilayer, see Section D.4, are derived.

Appendices E and F discuss issues tangentially related to the primary focus of this thesis. In Appendix E, an undulation correction is derived for the scattering from unilamellar vesicles, a necessary result to quantitatively compare the determined vesicle form factor and form factors measured by using other samples or techniques (for example form factors from multilamellar samples or determined from molecular dynamics simulations). In Appendix F, several results are derived using a tilt-dependent free energy in order to relate the tilt modulus to the order parameter describing lipid acyl tail-tail correlations that is obtained by other techniques.

Chapter 2

Experimental Methods

The experimental methodology used in the present work mostly follows previously described procedures [48, 49, 50]. Below, only the most significant aspects of the X-ray scattering experiment and sample preparation are reviewed as well as recent amendments and improvements. Most notably, a new background subtraction process is discussed in Section 2.5. This is important for extracting the relatively weak scattering intensity associated with the new tilt-dependent model that is the focus of this thesis.

2.1 Oriented Samples

Oriented stacks of lipid bilayers were deposited using previously described techniques [51]. Briefly, the lipids of interest were dissolved in a mixture of two organic solvents and plated onto clean Silicon wafers. Importantly, the substrate was manually moved to coax the lipid solution to evenly coat the entire wafer during primary evaporation of the solvent. Deposited samples were left in a fume hood for about 1 day and then in a vacuum oven for several hours to complete solvent evaporation. For DOPC [3], 4 mg of lyophilized lipid is adequate to deposit about 2000 bilayers, about 10 μm thick, given the 1.5×3 cm Si substrate surface. Finally, stacked bilayer samples were trimmed to final dimensions 0.5×3 cm.

[3] 1,2-dioleoyl-*sn*-glycero-3-phosphatidylcholine

2.2 Flightpath Components

2.2.1 X-ray optics

The synchrotron X-ray experiments were performed at the G1 station at the Cornell High Energy Synchrotron Source (CHESS). A simplified schematic of the flightpath setup is shown in Fig. 2.1. The G1 station is equipped with a W/B_4C multilayer monochromator producing a beam with an energy dispersion of about 1%. Before 2015, the multilayers were adjusted to reflect a beam with a mean energy of ~10.5 keV (1.18 Å). At the end of 2014, the wiggler feeding the G-line was replaced by a compact undulator, and as a result a ~11.2 keV (1.108 Å) beam was used in 2015, motivated by the change in the white beam's spectrum. Pairs of vertical and horizontal slits were used to define an incident X-ray beam about 0.2 mm wide and 1 mm tall. [4] The size of the beam was measured at several distances downstream of the final pair of slits using an area detector and an attenuated beam. Typical divergence values were 0.5×10^{-4} rad in the x-direction and 1×10^{-4} rad in the z-direction.

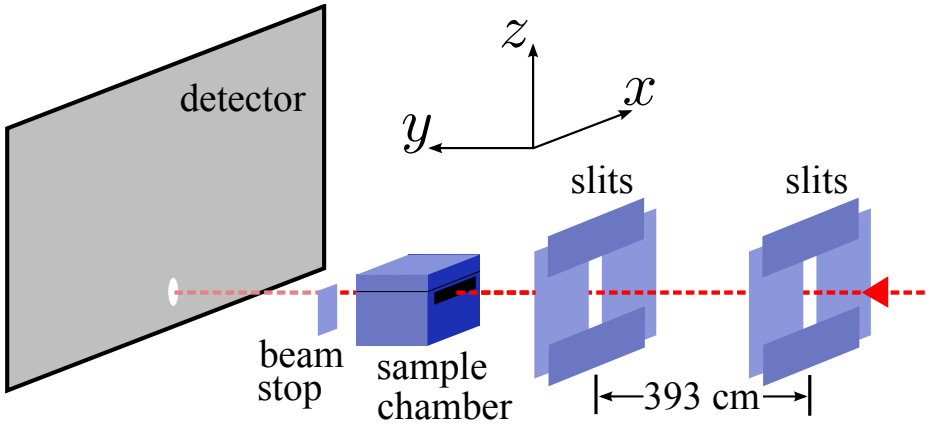


Figure 2.1: A simplified schematic of the flightpath is shown. Two pairs of horizontal and vertical slits define the beam's cross section. The Molybdenum beam stop attenuates the direct beam and is placed close to the sample chamber (about 1 mm) to block the detector from background scattering. The sizes and distances between flightpath elements are not to scale.

[4] The tall beam ensures that the entire sample is always within the beam's footprint for any angle of incidence ω used.

2.2.2 Beam Stop

The X-ray scattering of interest spans many orders of magnitude in intensity, but the dynamic range of the detector is only from 1 to 65436. A Molybdenum semi-transparent beam stop attenuates the scattering that would otherwise saturate the detector. In particular, the beam stop is often positioned to attenuate both the direct beam and intense low order out-of-plane peaks from a stacked bilayer sample, see the left-hand side of Fig. 2.2 for a typical sample exposure. The semi-transparent beam stop allows simultaneous assessment of sample scattering and the direct beam. The measured intensities and nominal unattenuated intensities are summarized for several common scattering features in Table 2.1. h is a whole number which indexes the out-of-plane lamellar repeat peaks. Fig. 2.2 shows a view of the beam through the beam stop, and typical beam profiles in the p_x- and p_z-directions are plotted in Fig 2.3.

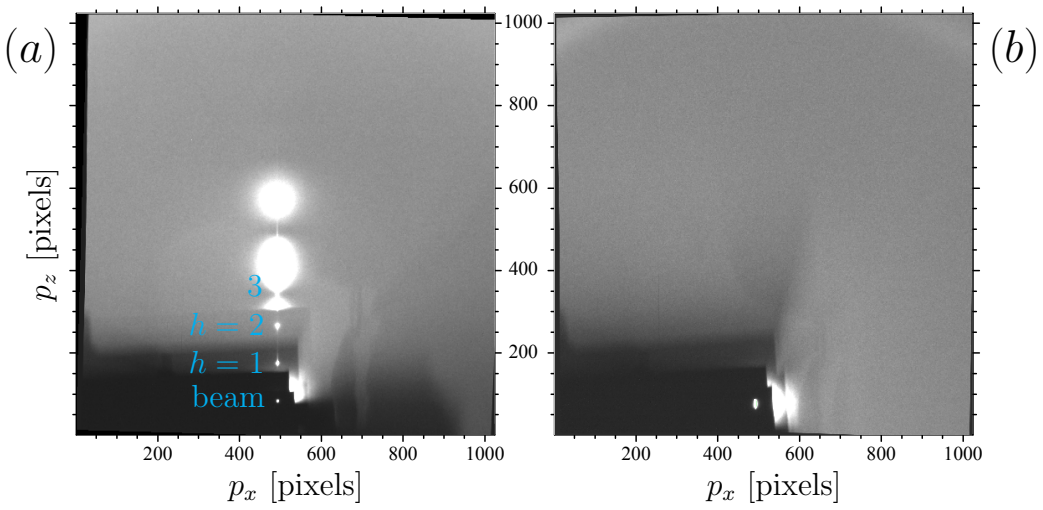


Figure 2.2: DOPC sample and direct beam exposures are shown in (a) and (b), respectively. The attenuated direct beam is visible through the beam stop centered at about $(490, 75)$. Intensity is indicated by the linear grayscale where white corresponds to most intense. The dark rectangular feature in the lower left corner is the shadow of the beam stop. The bright feature to the right of the beam stop shadow is the beam's splash. The beam and several out-of-plane orders are identified by the cyan text.

2.2.3 CCD Detector

A charged-coupled device (CCD) detector "Flicam" (Finger Lakes Instrumentation, Lima, NY) with 1024×1024 pixels and 0.07113 mm/pixel size was used at the G1-

Table 2.1: Intensity of several common scattering features in panel (a) of Fig. 2.2

Feature	Measured Intensity [$\times 10^3$]	Attenuation Factor	Nominal Intensity
beam	11	$6^9 \approx 10^7$	1×10^{11}
$h = 1$	17	$6^4 \approx 1.3 \times 10^3$	2×10^7
$h = 2$	4	1.3×10^3	5×10^6
between $h = 3$ and $h = 4$	2	1	2×10^3

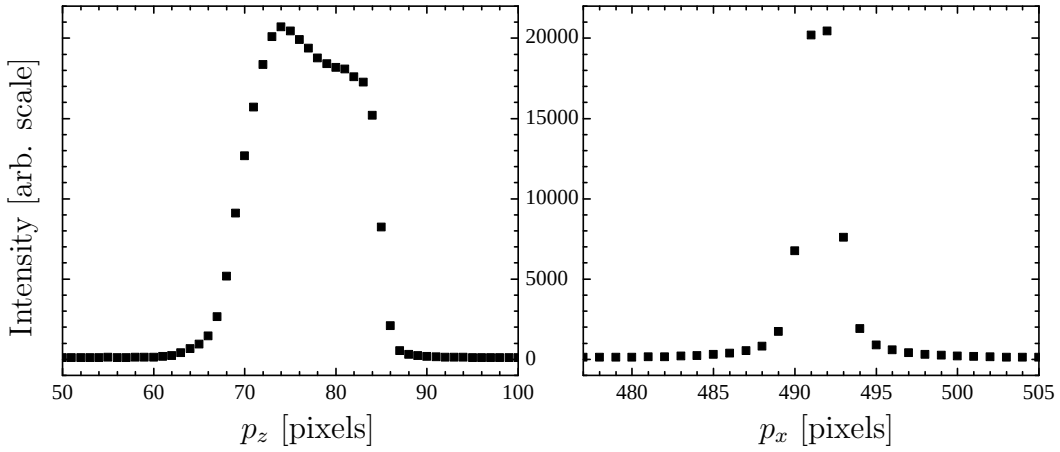


Figure 2.3: The intensity of the beam through the beam stop, see panel (b) in Fig. 2.2, is plotted as a function of p_z (left-hand side) and p_x (right-hand side). Ideal beam profiles are a boxcar and a Gaussian in the p_z- and p_x-directions, respectively.

station. Typically, the detector was located such that the direct beam was incident in the middle of the detector horizontally and about 100 pixels from the bottom, see panel (b) in Fig. 2.2. Before analyzing the measured X-ray scattering, the CCD exposure must be corrected for several known effects; zingers, CCD dark background, and distortion and intensity corrections [52]. The aforementioned corrections were performed by CHESS software at the G1-station.

2.3 Sample Chamber

During an X-ray scattering experiment, a stacked bilayer sample is housed within a temperature controlled chamber [48], see Fig. 2.4. To moderate the sample temper-

ature, a thermostatted bath circulates water through channels in the one inch thick aluminum chamber walls. The chamber contains a reservoir of water, and typical relative humidity after closing the chamber reaches 99.9%. Even so, 100% relative humidity is often desirable to attain maximum repeat-spacing, and therefore, the sample is placed on top of a Peltier element which is fixed to a sample holder. Commonly, the Peltier cools the sample relative to the water reservoir to increase the relative humidity at the sample. The sample holder is mounted on the shaft of a rotation motor which allows continuous rotation of the sample during typical data collection. The incident and scattered X-rays enter and exit the sample chamber through pairs of mylar windows. Typically, air in the hydration chamber and entrance and exit windows is replaced with Helium to reduce X-ray scattering from gas.

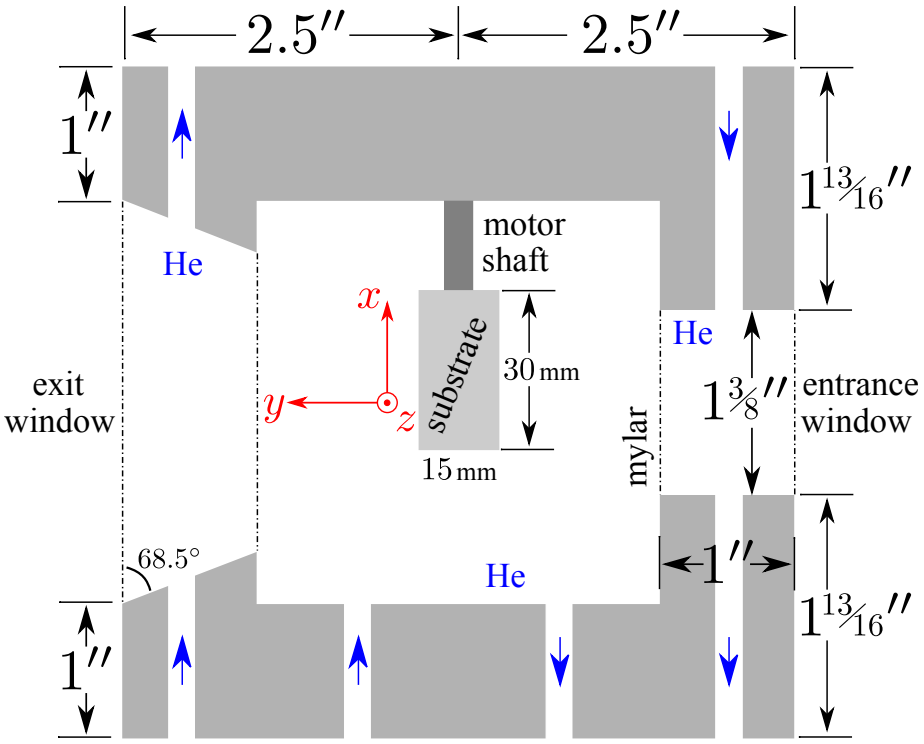


Figure 2.4: A top view of the sample chamber is shown. Substrate and chamber dimensions are drawn to scale. The dash-dot lines are the 1.5-6 μm thick mylar windows. The blue arrows indicate entrance and exit holes for He. The X-rays propagate from right to left.

2.4 Low Angle X-ray Scattering

The current procedure for Low Angle X-ray Scattering (LAXS) experiments closely follows the original methodology [48]. During a LAXS exposure, the angle between the sample and direct beam ω, is continuously varied by rotating the sample, $-\omega_{\min} \leq \omega \leq \omega_{\max}$. When rotating, the magnitude of the sample's angular velocity $|\boldsymbol{\alpha}|$ is assumed to be constant, and Fig. 2.5 shows a simplified ω as a function of the oscillation period $\omega(t)$. $\omega_{\min}$ and $\omega_{\max}$ are chosen to ensure that the sample is moving at a constant angular speed while the sample scattering intensity incident on the detector is nonzero. Typical values are $\omega_{\min} = 1.6°$ and $\omega_{\max} = 7°$ or $11°$. The sample is rotated to a negative angle to block the beam from the sample while it accelerates. The sample rotation speed and exposure time are chosen such that a large whole number of oscillations are completed during a tens of seconds exposure. The sample to detector distance is determined by the scattering of interest. For common lipids and $10.5 - 11.2$ keV X-rays, the detector is positioned about 370 mm from the sample position, allowing an out-of-plane momentum transfer range of $0 \lesssim q_z \lesssim 1$ Å^{-1} to be probed. Typical first order lamellar repeat scattering is centered at $q_z \approx 0.1$ Å^{-1}, so as many as 10 orders could be detected.

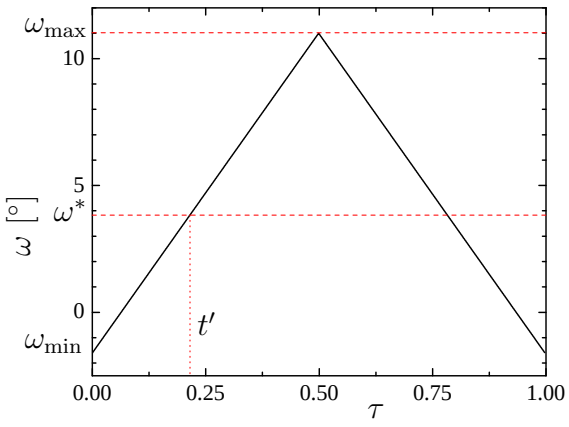


Figure 2.5: The simplified sample rotation as a function of time is plotted, where τ is the cycle period. The acceleration before and after the angular velocity changes sign have been neglected. Therefore, the cycle period is longer than the angular range divided by the nominal angular speed (about 18.6°/s).

2.5 Background Subtraction

The intensity I_{m} measured by the detector includes contributions from several sources including the bilayers I_{b}, various vapors I_{vap} (helium, water, and air), the sample chamber windows I_{win}, and water between the bilayers $I_{\mathrm{H_2O}}$,

$$I_{\mathrm{m}}(p_x, p_z) \equiv I_{\mathrm{b}}(p_x, p_z) + I_{\mathrm{vap}}(p_x, p_z) + I_{\mathrm{win}}(p_x, p_z) + I_{\mathrm{H_2O}}(p_x, p_z). \tag{2.1}$$

Background scattering refers to the intensity from all sources besides the bilayers, and only scattering from the direct beam will be quantitatively modeled. In Section 2.5.1, a methodology for assessing and removing I_{vap} and I_{win} is discussed. Section 2.5.2 describes the $I_{\mathrm{H_2O}}$ subtraction procedure.

2.5.1 Light Background

The combination of the scattering from vapor within the sample chamber I_{vap} and the scattering from the sample chamber windows I_{win} is referred to as the Light Background (LB). The LB measurement procedure is described for two types of X-ray scattering experiments. During an exposure, the sample's orientation with respect to the beam is either fixed, a so-called fixed angle exposure, or more often continuously rotated. First, the LB measurement procedure is described for a fixed angle experiment. Since a continuously rotated sample experiment can be viewed as a series of fixed angle experiments, the rotated angle LB measurement procedure follows conceptually from its fixed angle analog.

The beam-substrate geometry for a fixed angle exposure is shown in Fig. 2.6, where ω is the angle between the substrate and the incident beam. I_{vap} and I_{win} are each the sum of scattering sources upstream and downstream of the sample. To approximately measure $I_{\mathrm{vap}} + I_{\mathrm{win}}$ of a fixed angle exposure, an exposure in which ω is set to $-\omega$ is recorded [53]. Importantly, the substrate is sufficiently thick such that for the $-\omega$ condition no X-rays penetrate the substrate to scatter from the sample. Comparing the ω and $-\omega$ setups, see Fig. 2.6, the amount of vapor along the beam path is nearly the same except for the small volume above the sample, and the fraction of beam passing through the sample chamber exit windows only depends on $|\omega|$. Since the beam path above the sample is small (~ 15 mm) compared to the total beam path

inside the sample chamber (128 mm), the $-\omega$ setup adequately approximates the LB of an ω exposure. The volume of beam above the sample is always less than 12% of the total beam volume in the sample chamber. The difference of ω and $-\omega$ exposures is approximately $I_{\mathrm{b}} + I_{\mathrm{H_2O}}$.

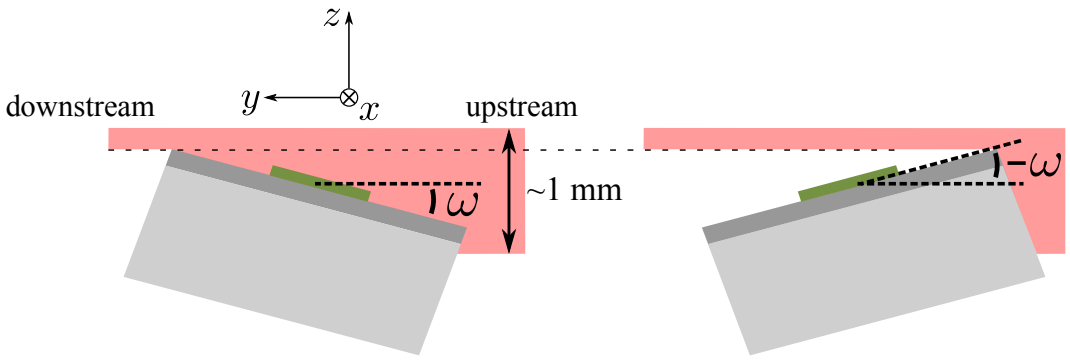


Figure 2.6: The beam-substrate geometry is shown for positive (left-hand side) and negative (right-hand side) fixed incident angles ω. The red regions are the direct beam which propagates from right to left. The sample, supporting substrate, and sample holder are the green, dark gray, and light gray rectangles (not to scale), respectively. The ω shown is much larger than ω_{max}.

During most LAXS exposures, the sample is rotated between fixed positive and negative angles, $-\omega_{\mathrm{min}} \leq \omega \leq \omega_{\mathrm{max}}$. In analogy to the fixed angle LB measurement procedure, one might consider the rotation scheme, $\omega_{\mathrm{min}} \leq \omega \leq -\omega_{\mathrm{max}}$, but then for $\omega > 0$, X-rays scatter from the sample. Therefore, the aforementioned scheme does not isolate $I_{\mathrm{vap}} + I_{\mathrm{win}}$. Instead, the LAXS LB is approximated by a fixed angle LB where the fixed angle was chosen to mimic the LB originating downstream of the sample. A fixed angle LB measurement intended to approximate the LAXS LB will be referred to as a kludged Light Background (kLB). [5] Since the typical beam is about 1 mm tall, the substrate will completely block the direct beam for an incident angle ω^*, see the right-hand side of Fig. 2.6,

$$\omega^* = \sin^{-1}\left(\frac{b_z}{L_{\mathrm{s}}}\right), \tag{2.2}$$

where b_z is the height of the beam and L_{s} is the width of the substrate. For $\omega > \omega^*$, there will be no downstream direct beam to yield additional background scattering.

[5] Professor Nagle conceived the idea of a kLB.

Considering the LB from scattering downstream (ds) of the sample, the average of the incident angle $\overline{\omega}_{\rm ds}$ is calculated with the condition that $\omega > \omega^*$ are equivalent to ω^*,

$$\overline{\omega}_{\rm ds} = \frac{2}{\tau}\left[\int_0^{t'} {\rm d}t\ |\omega(t)| + \int_{t'}^{\tau/2} {\rm d}t\ \omega^*\right] \tag{2.3}$$

$$= \frac{2}{\tau}\left[\frac{\omega_{\rm min}^2}{\alpha} + \frac{\alpha t'^2}{2} - \omega_{\rm min}t' + \omega^*\left(\frac{\tau}{2} - t'\right)\right], \tag{2.4}$$

where $t' \equiv (\omega_{\rm min} + \omega^*)/\alpha$ and τ is the time of one complete cycle, see Fig. 2.5. For typical values of $\omega_{\rm min} = 1.6°$, $\omega^* = 3.8°$, $\alpha = 18.6°/\text{sec}$, and $\tau = 1.5$ sec, $\overline{\omega}_{\rm ds} \approx 2.9°$. Experiments suggest that the kLB is not strongly dependent on the fixed angle chosen, but it is dependent on the position of the sample chamber. A kLB is often measured soon before or after its corresponding LAXS exposure because the LB is known to be a function of many time dependent experimental conditions (beam intensity, vapors in the sample chamber, motor positions, etc.)

Fig. 2.7 shows a typical 2015 sample exposure and the corresponding kLB with $\omega = 2.8°$.[6] In Fig. 2.7a part of the direct beam passes over the substrate, is attenuated by the Mo beam stop, and is incident on the detector at approximately $(490, 75)$. Directly above the beam in Fig. 2.7a are the Mo attenuated (by 1300) first two out-of-plane peaks, indicating a repeat distance of 63.8 Å. The beam stop shadow ends at $p_z \approx 300$. In principal, the sample scattering should be left-right symmetric with respect to the meridian at $p_x \approx 490$. Fig. 2.7 emphasizes that much of the left-right asymmetry of the sample exposure is due to LB scattering. The kLB subtracted sample exposure is shown in Fig. 2.8 and is much more symmetric with respect to $p_x \approx 490$.

In the next section, the intensity visible in the upper corners of the detector in Fig. 2.8 will be shown to be water scattering $I_{\rm H_2O}$. Two methods to approximate $I_{\rm H_2O}$ are summarized. First in Subsection 2.5.2, scattering from a water film on a Si substrate is measured and compared to the residual scattering after kLB subtraction shown in Fig. 2.8. The water film scattering and the residual intensity are shown to differ systematically, see Fig. 2.11, and therefore in Subsection 2.5.2, the so-called

[6]The LB in 2015 was particularly strong because of gas scattering from the G1 flightpath (upstream of the sample). During experiments prior to 2015, great care was taken to minimize gas scattering in the G1 flightpath. The kLB makes such efforts less necessary.

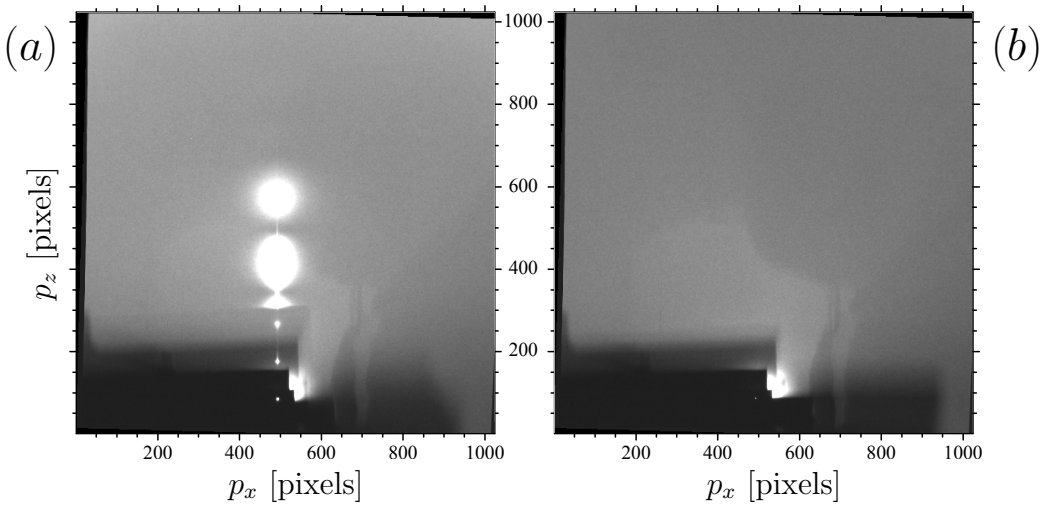


Figure 2.7: DOPC sample exposure at 30 °C using Fig. 2.5 protocol (left-hand side) and corresponding kLB ($\omega = 2.8°$; right-hand side) are shown, using the same linear grayscale. Both the DOPC exposure and the kLB were rotated to align the substrate normal and the p_z-axis.

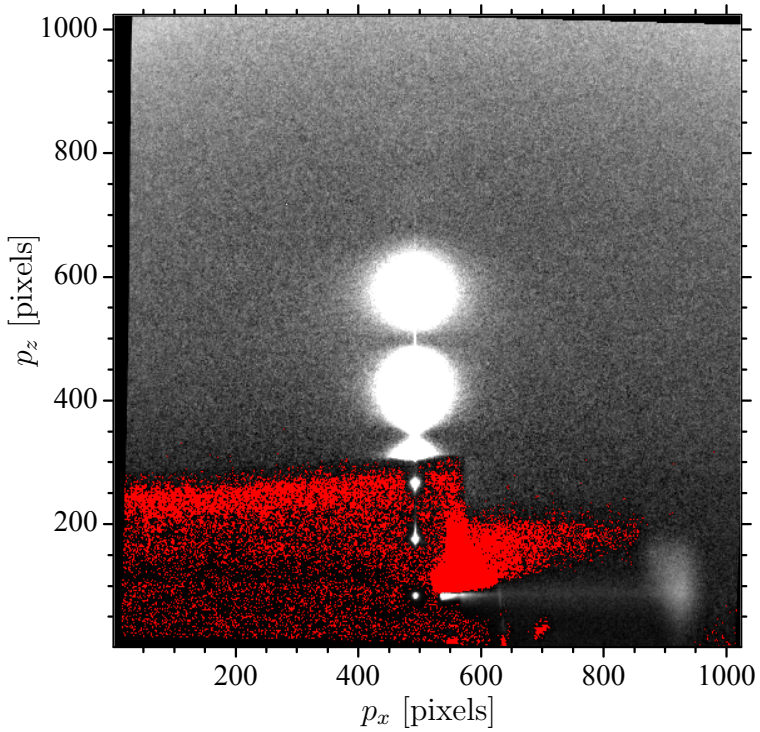


Figure 2.8: The difference of the sample exposure and the kLB is depicted. Red indicates negative values.

two box method is used to approximate $I_{\mathrm{H_2O}}$. Finally, the background subtracted

exposure using the two box method is shown in Fig. 2.13.

2.5.2 Water Background

Scattering from Water Film

The scattering from the water between the bilayers I_{H_2O} can be approximated by a water film on a Si wafer. [7] A clean Si wafer is placed on the sample holder. Then, the sample chamber is closed and filled with He. Next, the target temperature of the thermostatted water circulator is increased, commonly from 30 °C to 37 °C. A heating element in the water circulator rapidly raises the temperature of the circulating water and via conduction the water reservoir in the chamber. The substrate temperature also increases but lags behind the temperature of the chamber water reservoir. Within about 20 min, the substrate and water reservoir re-equilibrate to the same temperature. In the meantime, the substrate is colder than the water vapor so water condenses on the substrate. Fig. 2.9 shows typical detector exposures without and with water, after subtracting a kLB. The sample was rotated continuously between -1.6° and 11° during the exposures. Fig. 2.10 shows the kLB subtracted water scattering as a function of time. The water scattering increases as the water film thickness increases.

The water scattering visible in the right-hand side of Fig. 2.9 is qualitatively similar to the residual scattering in the kLB subtracted DOPC exposure, see Fig. 2.8. The amount of water between the bilayers and in the bulk water film are unlikely to be the same. Therefore, the water scattering intensity is scaled by a multiplicative factor to best mimic the residual scattering in a kLB subtracted bilayer stack exposure. The difference of the scaled water scattering and a kLB subtracted DOPC exposure is shown in Fig. 2.11. Even after the subtraction, there remains p_z-dependent scattering in regions of the detector where the intensity is expected to be distributed about 0.

Absorption of the scattered X-rays by the sample could yield a p_z-dependent difference between the measured water scattering and the scattering from water between the bilayers. The scattering at smaller p_z are more strongly attenuated by the sample as compared to scattering at higher p_z. The aforementioned effect can be quantitatively determined if the thickness of the water sample is known, see Section 5.3.4. Since the water film thickness is unknown, a different methodology is used to approximate I_{H_2O}.

[7] Dr. Tristram-Nagle first suggested that I_{H_2O} be subtracted from LAXS expsoures after a kLB subtraction.

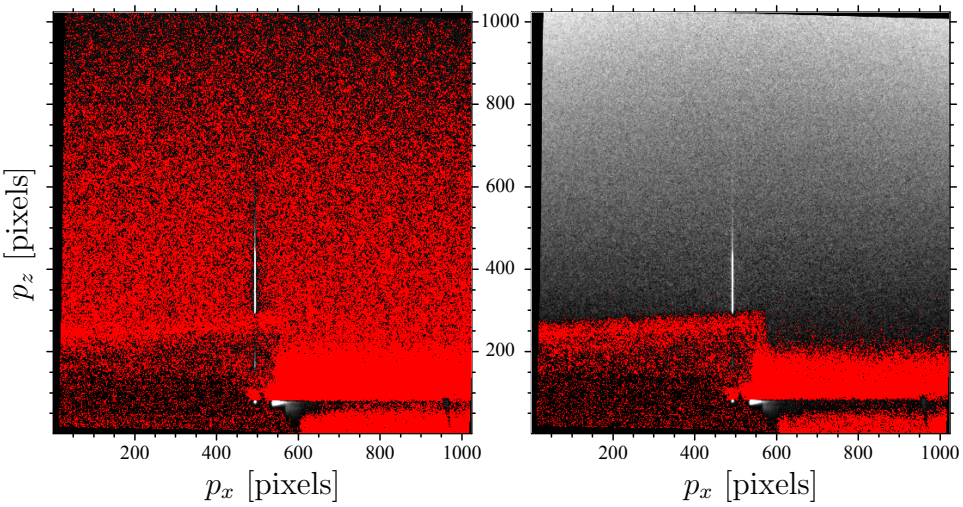


Figure 2.9: Exposures without (left-hand side) and with (right-hand side) a water film on the Si substrate are shown using the same grayscale. Red indicates negative values. The exposures were kLB subtracted and rotated such that the substrate normal and the p_z-axis are parallel. The vertical streak of intensity along $p_x \approx 490$ is the specular scattering from the Si wafer.

Two Box Method

The scattering from the water between the bilayers and any other residual scattering is assumed to be of the form

$$I'_{\mathrm{H_2O}}(p_x, p_z) \equiv A(p_z) + B(p_z)p_x + C(p_z)p_x^2. \tag{2.5}$$

$A(p_z)$, $B(p_z)$, and $C(p_z)$ are determined by a linear least squares fit using data symmetrically chosen with respect to the p_x beam center, see the green and blue boxes in the left-hand side of Fig. 2.12. [8] The resulting $I'_{\mathrm{H_2O}}(p_x, p_z)$ is plotted on the right-hand side of Fig. 2.12. The difference of $I'_{\mathrm{H_2O}}(p_x, p_z)$ and the kLB subtracted DOPC exposure is shown in Fig. 2.13. Fig. 2.14 compares the two discussed water background subtraction procedures; the remaining intensity after water background subtraction is plotted as functions of p_z, averaging over $710 \leq p_x \leq 730$. Far from the bilayer scattering, the intensity after $I'_{\mathrm{H_2O}}$ subtraction is distributed about 0.

The background subtraction results are summarized in Fig. 2.15. Intensity as a

[8] The so-called two box method was implemented by Dr. Yufeng Liu as part of his graduate work in the Nagle lab [48].

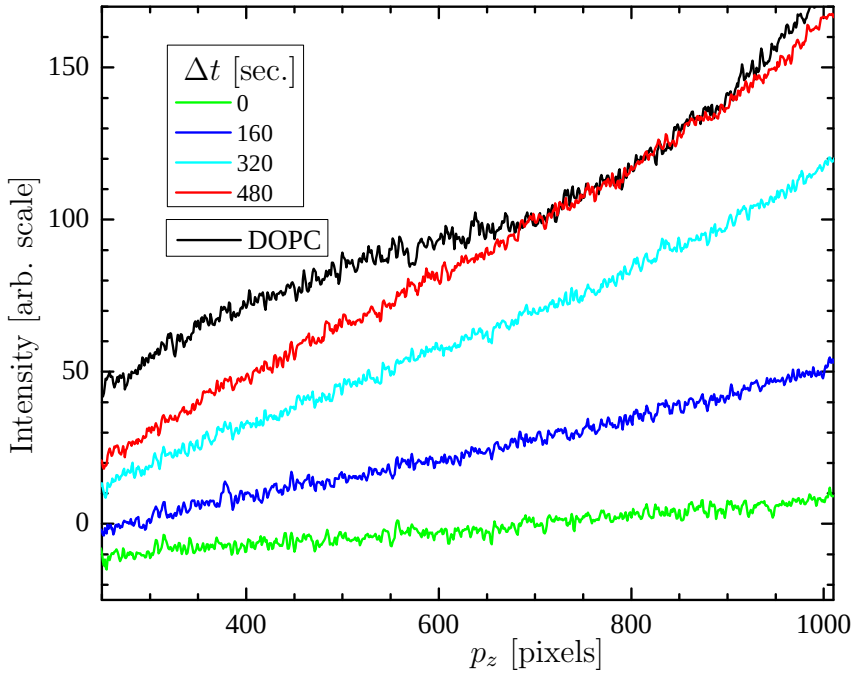


Figure 2.10: The water scattering intensity is plotted as a function of p_z, averaging over 200 pixels in p_x centered at $p_x = 850$. Δt is the approximate time after increasing the target temperature of the water circulator. The black line shows the intensity of the kLB subtracted DOPC exposure shown in Fig. 2.8 scaled to match the red line at $p_z = 800$.

function of p_z and p_x highlight the effects of the kLB and $I'_{\mathrm{H_2O}}$ subtractions. Before background subtraction I_{m} is asymmetric with respect to the meridian, $p_x \approx 490$, see panel (b) Fig. 2.15. $I_{\mathrm{m}} - I_{\mathrm{kLB}}$ is considerably more symmetric, but far from the meridian in the p_x-direction, the remaining intensity is nonzero. Additionally, $I_{\mathrm{m}} - I_{\mathrm{kLB}}$ increases as a function of p_z due to $I_{\mathrm{H_2O}}$, see panel (a) Fig. 2.15. Using the two box method, $I'_{\mathrm{H_2O}}$ is determined, and far from bilayer scattering, $I_{\mathrm{m}} - I_{\mathrm{kLB}} - I'_{\mathrm{H_2O}}$ is distributed about 0.

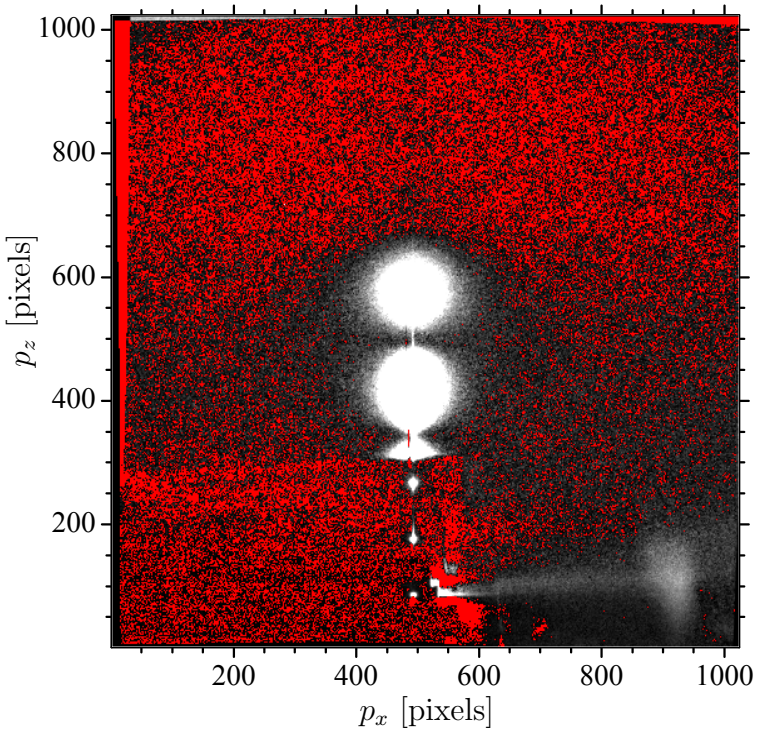


Figure 2.11: The difference of the kLB subtracted DOPC exposure and kLB subtracted water exposure is shown. Red indicates negative values.

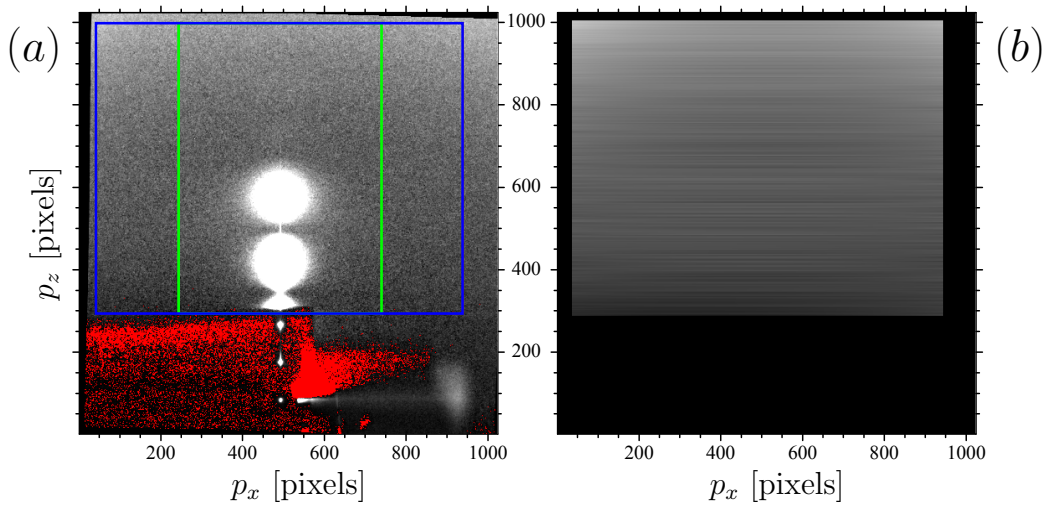


Figure 2.12: The intensity between the blue and green rectangles in (a) is used to determine $A(p_z)$, $B(p_z)$, and $C(p_z)$, see $I'_{\mathrm{H_2O}}$ Eq. (2.5). The resulting $I'_{\mathrm{H_2O}}(p_x, p_z)$ is shown in (b).

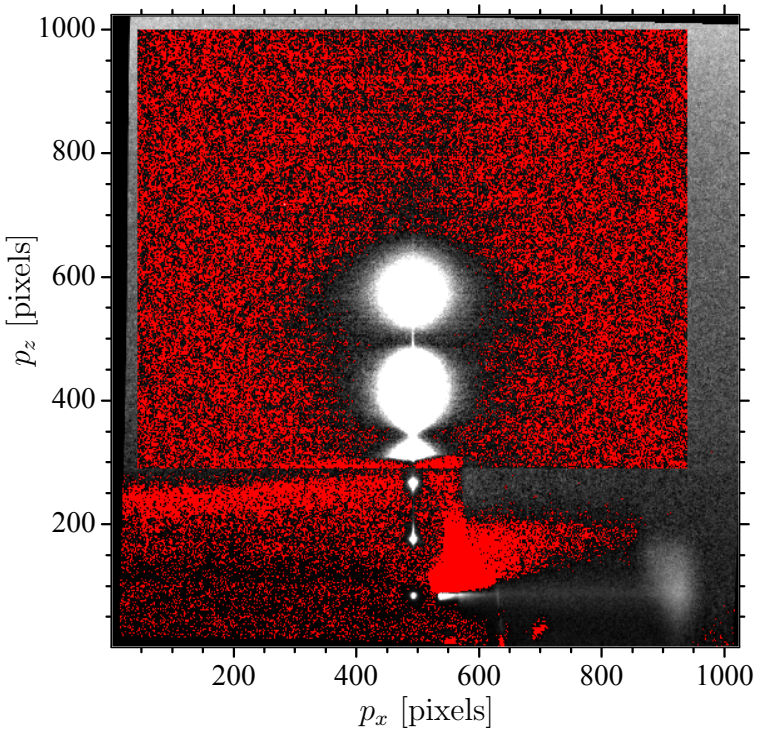


Figure 2.13: The difference of the kLB subtracted DOPC exposure and I'_{H_2O} is shown. Red indicates negative values.

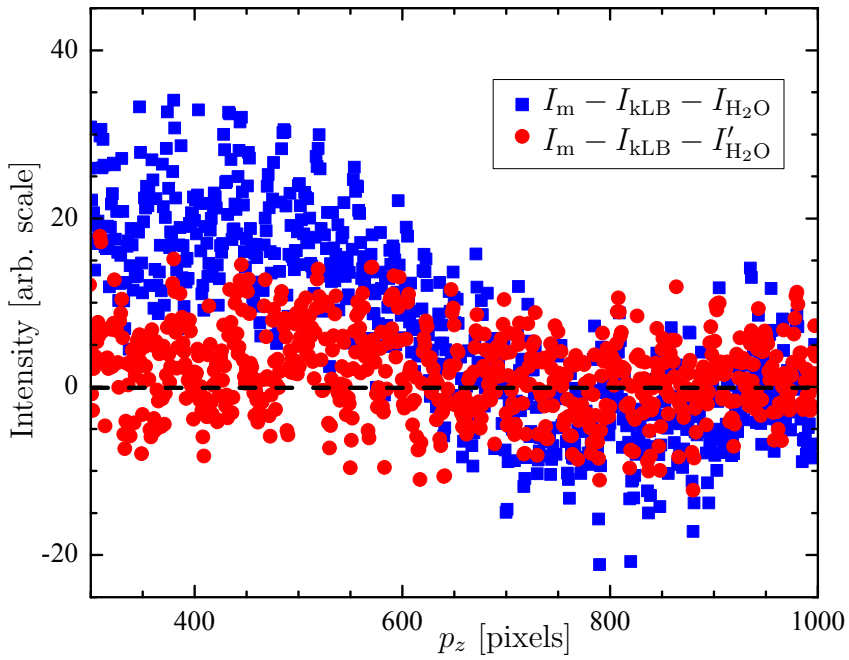


Figure 2.14: Comparing two different water background subtraction procedures, the remaining intensity is plotted as function of p_z, averaging over $710 \leq p_x \leq 730$ in Fig. 2.11 (blue squares) and in Fig. 2.13 (red circles). I_m and I_kLB are the total measured and kLB intensities, respectively. The intensity after subtracting $I'_{\mathrm{H_2O}}$ is more symmetrically distributed about 0. The black dashed line is a guide to the eye.

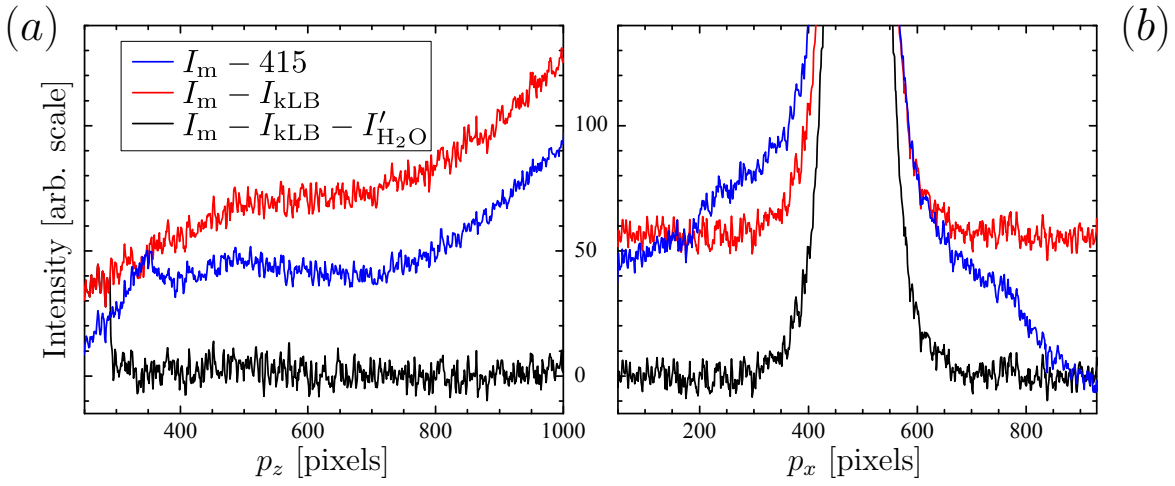


Figure 2.15: Intensity as a function of p_z ($700 \leq p_x \leq 740$), panel (a), and p_x ($395 \leq p_z \leq 435$), panel (b), are plotted at various stages in the background subtraction procedure. Note, the measured intensity I_m has been shifted down by 415 to facilitate visual comparison with the background subtracted curves.

Chapter 3

Tilt-Dependent Membrane Model

Several researchers have postulated tilt-dependent membrane free energy functionals [31, 1, 22, 28, 54]. The current work follows the model hypothesized by Watson *et al.* [1]. Since the most significant thrust of the presented work is to appreciate the effects of a tilt-dependent model on a previously established X-ray scattering experimental methodology [44, 46], Section 3.1 presents the simplest tilt-dependent membrane model which can be supported experimentally. For various other secondary theoretical and experimental issues, the complete Watson *et al.* model [1] is invoked.

Using the tilt-dependent model forwarded in Section 3.1, we begin to derive the theoretical X-ray scattering intensity from a bilayer stack. First in Section 3.2.1, a tilt-dependent electron density profile is posited. Then, the theoretical scattering intensity is decomposed into the sum of two terms in Section 3.2.2. Importantly, the height-height correlation function is shown to be the most significant statistical quantity in describing the predicted scattering. Finally, the height fluctuation spectrum is determined and then used to evaluate the height-height correlation function, see Sections 3.3.2 and 3.3.3, respectively.

3.1 Membrane Model Relevant to X-ray Scattering

Previously, measured low angle X-ray scattering (LAXS) from lipid bilayers [44, 46] was compared to predictions derived using the discrete Smectic A model [55, 56, 57]. Neglecting the interlayer interaction term, the Smectic A model is equivalent to

the Helfrich-Canham model [10, 11] for a tensionless, symmetric bilayer with fixed topology. In the HC model, membrane shape is a function of only the height field. The current work follows the model hypothesized by Watson *et al.* [1] in which the bilayer free energy is a sum of so-called undulation modes (4 fields; 1 of which is the height field) and peristaltic modes (3 fields). The undulation modes describe the overall membrane shape, and the peristaltic modes characterize fluctuations in bilayer thickness. Theoretically, fluctuations of all seven fields influence the LAXS from lipid bilayers, yet prior analyses based on the HC model compared favorably with X-ray measurements [44, 46], suggesting that there exists a hierarchy of the seven fields with regard to their influence on scattering from bilayers. Therefore, instead of extending the single field (HC) model to include all six new fields, the present work seeks to establish the next most important field (after the height field) for the analysis of LAXS from membranes.

In the Watson model [1], the height field is only coupled to other fields in the description of the undulation modes. Therefore, the undulation modes are inferred to be more significant for the analysis of membrane scattering than the peristaltic modes. Still, the peristaltic modes are not entirely neglected; *en masse*, their influence on the bilayer electron density is semi-quantitatively considered, see Sections 3.2.1 and 3.2.2.[9] Further, the protrusion-dependent fields are neglected since they have been shown to be unnecessary to explain simulation data [1]. Retaining only the undulation free energy terms reduces the complete Watson model to the free energy functional $\mathcal{F}_{\mathrm{W}}$ presented by Watson *et al.* in [22]. $\mathcal{F}_{\mathrm{W}}$ could be extended to describe a bilayer stack $\mathcal{F}_{\mathrm{W}}^{\mathrm{s}}$, but anticipating later results, $\mathcal{F}_{\mathrm{W}}$ is first even further simplified.

$\mathcal{F}_{\mathrm{W}}^{\mathrm{s}}$ is a complicated model which is limitedly probed by LAXS experiments. Importantly, the predicted X-ray scattering from stacked lipid bilayers primarily depends on the height spectrum, see Section 3.3.2. Therefore, $\mathcal{F}_{\mathrm{W}}^{\mathrm{s}}$ is simplified to the minimal model $\mathcal{F}_{\mathrm{u}}$ that predicts an equivalent height spectrum. Besides reducing mathematical overhead, $\mathcal{F}_{\mathrm{u}}$ makes clear the extent to which the presented experimental results support a tilt-dependent theory. Additionally, the simplification eases comparison with prior experimental work [44, 46, 55, 45].

For much of the current work, membrane fluctuations are described by only two fields $z^{+}(\mathbf{r})$ and $\hat{\mathbf{m}}(\mathbf{r})$ following the notation in [1], where $\mathbf{r} = (x, y)$ is the indepedent

[9] Specifically, the consideration of peristaltic fluctuations yields the second term (I_{bf}) in the intensity decomposition $I(\mathbf{q}) \equiv I_{\mathrm{c}}(\mathbf{q}) + I_{\mathrm{bf}}(\mathbf{q})$, see Eq. (3.32).

in-plane variable. Fig. 3.1 shows a diagram of these fields. z^+ is the average of the surfaces $z^{(\alpha)}$ dividing the headgroups and hydrocarbon tails of each monolayer, $z^+(\mathbf{r}) \equiv \frac{1}{2}\left[z^{(1)} + z^{(2)}\right]$, where the superscripts in parentheses indicate the upper (1) or lower (2) leaflet, respectively. z^+ is analogous to the mid-plane height field used by Helfrich and Canham [10, 11] to describe membrane shape.

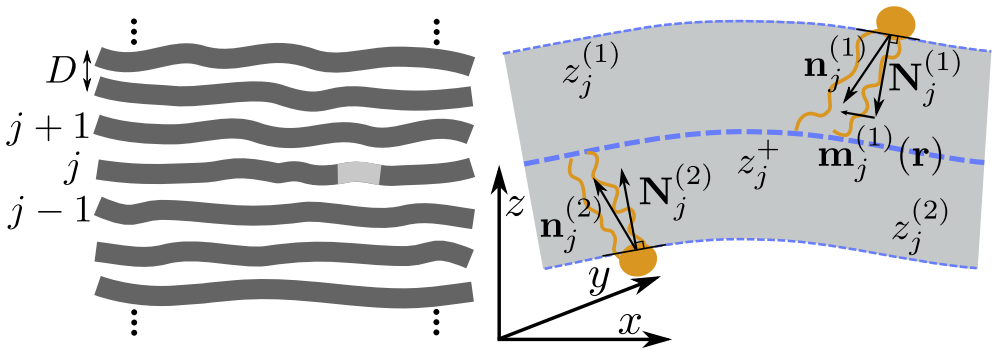


Figure 3.1: A diagram of the bilayer stack is labeled to illustrate various fluctuation fields and definitions given in the text. The lighter colored region in the jth bilayer is shown expanded in the figure's right-hand side. D is the repeat distance in the z-direction.

The second field $\hat{\mathbf{m}}$ describes the tilt of the membrane. Tilt is defined by

$$\mathbf{m}^{(\alpha)} \equiv \frac{\mathbf{n}^{(\alpha)}}{\mathbf{n}^{(\alpha)} \cdot \mathbf{N}^{(\alpha)}} - \mathbf{N}^{(\alpha)}, \tag{3.1}$$

where $\mathbf{n}^{(\alpha)}$ is the unit vector pointing from the headgroups towards the hydrocarbon tails and $\mathbf{N}^{(\alpha)}$ is the unit vector normal to the headgroup/hydrocarbon interface, pointing towards the interior of the membrane. Assuming that the angle between $\mathbf{n}^{(\alpha)}$ and $\mathbf{N}^{(\alpha)}$ is sufficiently small, the xy-components of $\mathbf{m}$ is approximated as

$$\mathbf{m}_{xy}^{(\alpha)} = \mathbf{n}_{xy}^{(\alpha)} - \mathbf{N}_{xy}^{(\alpha)}. \tag{3.2}$$

Finally, a membrane tilt field is expressed in terms of the individual leaflet tilt fields, $\hat{\mathbf{m}}(\mathbf{r}) \equiv \frac{1}{2}\left[\mathbf{m}_{xy}^{(1)} - \mathbf{m}_{xy}^{(2)}\right]$.

The simplified single membrane free energy functional is

$$\mathcal{F}_\mathrm{s} = \frac{1}{2}\int_{A_\mathrm{p}} \mathrm{d}^2\mathbf{r}\ \left[K_c\left(\nabla^2 z^+ + \boldsymbol{\nabla}\cdot\hat{\mathbf{m}}\right)^2 + K_\theta|\hat{\mathbf{m}}|^2\right], \tag{3.3}$$

where A_p is the area of the membrane projected onto the xy-plane. $\mathcal{F}_\mathrm{s}$ Eq. (3.3)

is a function of two membrane moduli; bending modulus K_c and tilt modulus K_θ, and two fluctuation fields; $z^+(\mathbf{r})$ and $\hat{\mathbf{m}}(\mathbf{r})$. The first and second terms account for the bending and tilt energy of the membrane, respectively. To describe a membrane stack, the fluctuation fields are written as functions of the stacked bilayer index j. $z_j^+(\mathbf{r})$ describes the height fluctuations of the jth bilayer about $z = jD$, see Fig. 3.1. Additionally, a term to describe interactions between adjacent membranes must be included,

$$\mathcal{F}_\mathrm{u} = \frac{1}{2}\sum_j \int_{A_\mathrm{p}} \mathrm{d}^2\mathbf{r} \left[K_c \left(\nabla^2 z_j^+ + \boldsymbol{\nabla}\cdot\hat{\mathbf{m}}_j\right)^2 + K_\theta |\hat{\mathbf{m}}_j|^2 + B\left(z_{j+1}^+ - z_j^+\right)^2 \right], \tag{3.4}$$

where B is the bulk modulus. The intermembrane interaction term is expressed in a discrete fashion to respect that the system is composed of well separated distinct layers [56, 55, 57]. $\mathcal{F}_\mathrm{u}$ Eq. (3.4) can be viewed as a tilt-dependent extension of a discrete free energy functional previously utilized to describe X-ray scattering from membrane stacks [58, 55, 57, 44, 46, 59, 60, 47], originally from liquid crystal literature [40]. The intermembrane interaction term in $\mathcal{F}_\mathrm{u}$ Eq. (3.4) is conceptually equivalent to the analogous term in the tilt-independent model.

3.2 Theoretical Scattering Intensity

The theoretical X-ray scattering intensity for a bilayer stack is derived. First, a tilt-dependent electron density is posited, see $\rho_j(\mathbf{r}, z)$ Eq. (3.7). Using $\rho_j(\mathbf{r}, z)$ the theoretical scattering intensity is decomposed into the sum of two terms, see Eq. (3.28) for the final result.

3.2.1 Membrane Electron Density

In general, the X-ray scattering intensity from a sample is related to the sample's electron density $\rho(\mathbf{R})$, where $\mathbf{R} = (x, y, z)$. Fig. 3.2 shows a tilt-independent representation of a single bilayer. Previous work quantitatively considered membrane electron density as a function of the bilayer midplane field z_j^+ [44, 46],

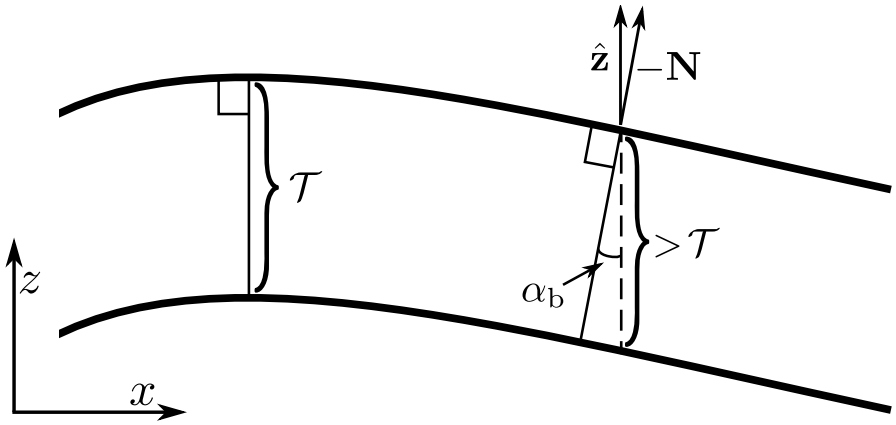


Figure 3.2: A diagram of a single bilayer is labeled to describe the parameters in the tilt-independent electron density, Eq. (3.5). As α_b increases the membrane thickness $\mathcal{T}$ projected on the z-axis increases.

$$\rho_j^{\cancel{\text{tilt}}}(\mathbf{r}, z) = \rho_\mathrm{s}\left([z - jD - z_j^+(\mathbf{r})]\,(-\mathbf{N}\cdot\hat{\mathbf{z}})\right) + \rho_\mathrm{w}(\mathbf{R}) \tag{3.5}$$

$$= \rho_\mathrm{s}\left([z - jD - z_j^+(\mathbf{r})]\cos\alpha_b\right) + \rho_\mathrm{w}(\mathbf{R}), \tag{3.6}$$

where $\rho_\mathrm{s}(\mathbf{r}, z)$ is the electron density profile of a single bilayer centered at $z = 0$ with normal in the z-direction and $\rho_\mathrm{w}(\mathbf{R})$ is the electron density of the water between the bilayers. D is the bilayer stack repeat distance in the z-direction. Assuming that $\rho_\mathrm{w}(\mathbf{R})$ is approximately a constant, it is neglected in later equations since it only contributes to scattering at $\mathbf{q} = 0$; this is known as the "minus fluid" convention [61]. $-\mathbf{N}\cdot\hat{\mathbf{z}} = \cos\alpha_\mathrm{b}$ is a geometric factor that accounts for deviations of the local membrane normal $\mathbf{N}$ from the z-axis. For increasing α_b the projection of the membrane thickness along the z-axis increases [39, 48]. It was recognized that other membrane fluctuations, such as thickness fluctuations, also influence $\rho_j^{\cancel{\text{tilt}}}(\mathbf{r}, z)$ [38] (see Appendix). It has been argued that so-called local fluctuations in lipid molecules are included on average in $\rho_j^{\cancel{\text{tilt}}}(\mathbf{r}, z)$, assuming that these local fluctuations are uncorrelated with z_j^+ [48].

Given the tilt-dependent free energy functional $\mathcal{F}_\mathrm{u}$ Eq. (3.4), a tilt-dependent electron density is considered. Based on both the complete Watson *et al.* model [1] and molecular dynamics simulations, Kopelevich and Nagle have shown that the length of

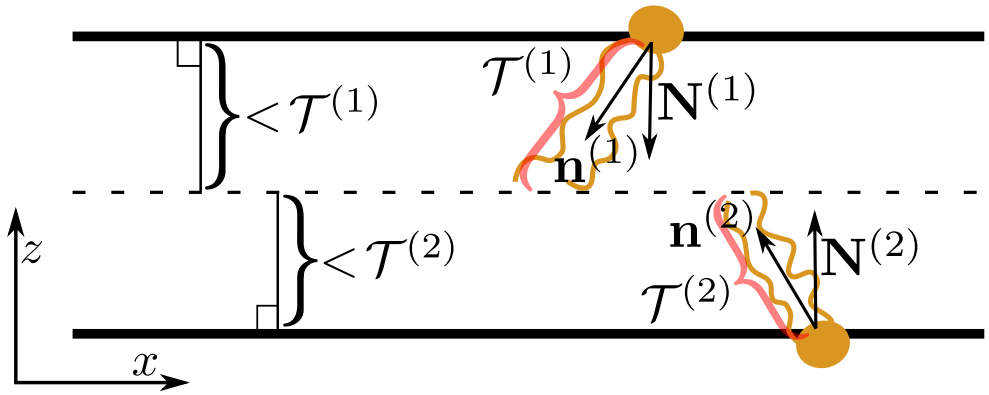


Figure 3.3: A diagram of a single bilayer is labeled to describe the additional parameters in the tilt-dependent electron density, Eq. (3.7). As the angle between $\mathbf{n}^{(\alpha)}$ and $\mathbf{N}^{(\alpha)}$ increases, the leaflet thickness $\mathcal{T}^{(\alpha)}$ projected on the z-axis decreases. Here $\mathbf{N}^{(\alpha)}$ and $\hat{\mathbf{z}}$ are parallel for convenience, but generally, $\mathbf{N}^{(\alpha)}$ and $\hat{\mathbf{z}}$ are not parallel.

lipid chains are nearly uncorrelated with tilt which implies that the membrane thickness along $\hat{\mathbf{z}}$ diminishes when $\mathbf{n}^{(\alpha)}$ and $\mathbf{N}^{(\alpha)}$ are not parallel [submitted manuscript]. The effect of tilt fluctuations on apparent membrane thickness is opposite to the effect of fluctuations in the local membrane normal. Fig. 3.3 depicts the tilt-dependent characterization of a single bilayer which is quantified by

$$\rho_j(\mathbf{r}, z) = \rho_{\mathrm{s}}\left(\left[z - jD - z_j^+(\mathbf{r})\right] \frac{-\mathbf{N}_j^{(1)} \cdot \hat{\mathbf{z}} - \mathbf{N}_j^{(2)} \cdot \hat{\mathbf{z}}}{\mathbf{N}_j^{(1)} \cdot \mathbf{n}_j^{(1)} + \mathbf{N}_j^{(2)} \cdot \mathbf{n}_j^{(2)}}, P_j(\mathbf{r}) \right) \tag{3.7}$$

$$\equiv \rho_{\mathrm{s}}\Big(\left[z - jD - z_j^+(\mathbf{r})\right] \Psi_j(\mathbf{r}), P_j(\mathbf{r}) \Big), \tag{3.8}$$

where $\mathbf{N}_j^{(\alpha)}$ and $\mathbf{n}_j^{(\alpha)}$ are the local leaflet normal and director, respectively. ρ_{s} is explicitly written as a function of a single effective peristaltic mode $P_j(\mathbf{r})$; P_j does not include protrusions. In [1], it is shown that protrusion modes have no spatial correlations, and additionally, they are uncorrelated with undulation modes and peristaltic modes. Therefore, ρ_{s} is interpreted to be inherently broadened in the z-direction by protrusions modes. The so-defined $\Psi_j(\mathbf{r})$ is a geometric factor due to fluctuations that quantifies systematic deviations of the bilayer electron density along $\hat{\mathbf{z}}$ from $\rho_{\mathrm{s}}(\mathbf{r}, z)$. The numerator of Ψ_j is the extension of the single bilayer geometric factor when the local normal of each monolayer is considered, and the denominator of Ψ_j accounts for apparent thinning of each monolayer due to deviations of $\mathbf{N}^{(\alpha)}$ from $\mathbf{n}^{(\alpha)}$. The

electron density of a bilayer stack is then

$$\rho(\mathbf{R}) = \sum_j \rho_j(\mathbf{r}, z). \tag{3.9}$$

3.2.2 Separation of the Structure and Form Factors

The predicted X-ray scattering intensity is derived for a stack of fluid phase lipid bilayers described by $\rho(\mathbf{R})$ Eq. (3.9). Since the system is described within a continuum approximation, it is unreasonable to expect that the stacked membrane free energy functional $\mathcal{F}_\mathrm{u}$ Eq. (3.4) accurately predicts scattering features known to be due to short length scale phenomena (for instance the wide angle scattering peak centered near $q \sim$1.4 Å^{-1} attributed to correlations between lipid acyl tails). Therefore, many assumptions are made concerning the extent to which various fluctuation fields are correlated over length scales consistent with the continuum approximation and probed by the low angle X-ray scattering measurements ($q \lesssim 1$ Å^{-1}).

In the Born approximation [62], the X-ray scattering intensity I and the sample's electron density ρ are related by

$$I(\mathbf{q}) = \left\langle \left| \int_V \mathrm{d}^3\mathbf{R}\ \rho(\mathbf{R}) e^{i\mathbf{q}\cdot\mathbf{R}} \right|^2 \right\rangle, \tag{3.10}$$

where V is the sample volume illuminated by the X-ray beam. The angle brackets correspond to a time-average over the measurement period. Assuming ergodicity, later angle brackets denote ensemble averages unless otherwise noted.

Combining $\rho(\mathbf{R})$ Eq. (3.9) and $I(\mathbf{q})$ Eq. (3.10), the relation for the scattering intensity is rewritten,

$$I(\mathbf{q}) = \left\langle \int\int \mathrm{d}^3\mathbf{R}\ \mathrm{d}^3\mathbf{R}'\ e^{i\mathbf{q}\cdot(\mathbf{R}-\mathbf{R}')} \sum_{j,j'} \rho_j(\mathbf{r}, z)\rho_{j'}(\mathbf{r}', z') \right\rangle. \tag{3.11}$$

Following the common procedure for molecular liquids, see for example pp. 127 [62], the double sum in Eq. (3.11) is decomposed into a sum over $j = j'$ and a sum over $j \neq j'$,

$$I(\mathbf{q}) = \left\langle \int\int \mathrm{d}^3\mathbf{R}\ \mathrm{d}^3\mathbf{R}'\ e^{i\mathbf{q}\cdot(\mathbf{R}-\mathbf{R}')} \sum_j \rho_j(\mathbf{r},z)\rho_j(\mathbf{r}',z') \right\rangle +$$
$$\left\langle \int\int \mathrm{d}^3\mathbf{R}\ \mathrm{d}^3\mathbf{R}'\ e^{i\mathbf{q}\cdot(\mathbf{R}-\mathbf{R}')} \sum_{j\neq j'} \rho_j(\mathbf{r},z)\rho_{j'}(\mathbf{r}',z') \right\rangle \tag{3.12}$$
$$= I_j(\mathbf{q}) + I_{j,j'}(\mathbf{q}). \tag{3.13}$$

The sum is decomposed into $j = j'$ (intramembrane correlations) and $j \neq j'$ (intermembrane correlations) in anticipation of treating these two types of correlations differently. Rewriting I_j using $\rho_j(\mathbf{r}, j)$ Eq. (3.7) and making the substitution

$$\tilde{z} = \left[z - jD - z_j^+(\mathbf{r})\right] \Psi_j(\mathbf{r}), \tag{3.14}$$

$$I_j(\mathbf{q})$$
$$= \sum_j \int\int \mathrm{d}^2\mathbf{r}\ \mathrm{d}^2\mathbf{r}'\ e^{i\mathbf{q}_\mathbf{r}\cdot(\mathbf{r}-\mathbf{r}')}.$$
$$\left\langle \int_{-\frac{D}{2}+jD+z_j^+(\mathbf{r})}^{\frac{D}{2}+jD+z_j^+(\mathbf{r})} \int_{-\frac{D}{2}+jD+z_j^+(\mathbf{r}')}^{\frac{D}{2}+jD+z_j^+(\mathbf{r}')} \mathrm{d}z\ \mathrm{d}z'\ e^{iq_z\left[z_j^+(\mathbf{r})-z_j^+(\mathbf{r}')\right]} \rho_j(\mathbf{r},z)\rho_j(\mathbf{r}',z') \right\rangle \tag{3.15}$$
$$= \sum_j \int\int \mathrm{d}^2\mathbf{r}\ \mathrm{d}^2\mathbf{r}'\ e^{i\mathbf{q}_\mathbf{r}\cdot(\mathbf{r}-\mathbf{r}')}.$$
$$\left\langle \int_{-\frac{D}{2}\Psi_j(\mathbf{r})}^{\frac{D}{2}\Psi_j(\mathbf{r})} \int_{-\frac{D}{2}\Psi_j(\mathbf{r}')}^{\frac{D}{2}\Psi_j(\mathbf{r}')} \mathrm{d}\tilde{z}\ \mathrm{d}\tilde{z}'\ e^{iq_z\left[z_j^+(\mathbf{r})-z_j^+(\mathbf{r}')\right]} \frac{\rho_\mathrm{s}[\tilde{z},P_j(\mathbf{r})]\rho_\mathrm{s}[\tilde{z}',P_j(\mathbf{r}')]}{\Psi_j(\mathbf{r})\Psi_j(\mathbf{r}')} e^{iq_z\left(\frac{\tilde{z}}{\Psi_j(\mathbf{r})}-\frac{\tilde{z}'}{\Psi_j(\mathbf{r}')}\right)} \right\rangle. \tag{3.16}$$

Within the "minus fluid" convention, the electron density between the bilayers is zero. Assuming that Ψ_j does not modify the integration limits too much, $\frac{D}{2}\Psi_j(\mathbf{r}) \approx \frac{D}{2}$, and Eq. (3.16) is expressed as

$$I_j(\mathbf{q}) \approx I_j^{\mathrm{a}}(\mathbf{q}) \equiv \sum_j \int\int \mathrm{d}^2\mathbf{r}\ \mathrm{d}^2\mathbf{r}'\ e^{i\mathbf{q}_\mathbf{r}\cdot(\mathbf{r}-\mathbf{r}')} \left\langle e^{iq_z\left[z_j^+(\mathbf{r})-z_j^+(\mathbf{r}')\right]} F_j(\mathbf{r},q_z)F_j(\mathbf{r}',q_z)\right\rangle, \tag{3.17}$$

where F is called the form factor,

$$F_j(\mathbf{r},q_z) \equiv \int_{-D/2}^{D/2} \mathrm{d}\tilde{z}\ \frac{\rho_\mathrm{s}[\tilde{z},P_j(\mathbf{r})]}{\Psi_j(\mathbf{r})} \exp\left\{iq_z\tilde{z}/\Psi_j(\mathbf{r})\right\}. \tag{3.18}$$

The stacked bilayers are assumed to be translationally invariant along the stacking direction $\left[z_j^+(\mathbf{r})-z_j^+(\mathbf{r}')\right] \rightarrow \left[z_0^+(\mathbf{r})-z_0^+(\mathbf{r}')\right]$, $F_j(\mathbf{r},q_z) \rightarrow F_0(\mathbf{r},q_z)$, and $P_j(\mathbf{r}) \rightarrow P_0(\mathbf{r})$. The variance of $\Psi_0(\mathbf{r})$ is shown to be small in Appendix A.2.2. Therefore $\psi_0(\mathbf{r}) \rightarrow \langle\psi_0\rangle$ and

$$F_0(\mathbf{r},q_z) \approx \int_{-D/2}^{D/2} \mathrm{d}\tilde{z}\ \frac{\rho_\mathrm{s}[\tilde{z},P_0(\mathbf{r})]}{\langle\Psi_0\rangle} \exp\left\{iq_z\tilde{z}/\langle\Psi_0\rangle\right\}. \tag{3.19}$$

Then, I_j^{a} Eq. (3.17) is further simplified assuming that the peristaltic fluctuations $P_0(\mathbf{r})$ of ρ_s are uncorrelated with z_0^+ over long length scales,

$$I_j^{\mathrm{a}}(\mathbf{q}) \approx I_j^{\mathrm{b}}(\mathbf{q}) \equiv \sum_j \int\int \mathrm{d}^2\mathbf{r}\ \mathrm{d}^2\mathbf{r}'\ e^{i\mathbf{q}_\mathbf{r}\cdot(\mathbf{r}-\mathbf{r}')} \left\langle e^{iq_z\left[z_0^+(\mathbf{r})-z_0^+(\mathbf{r}')\right]}\right\rangle \left\langle |F_0(\mathbf{r},q_z)|^2\right\rangle. \tag{3.20}$$

Moving on to rewrite $I_{j,j'}$, see Eq. (3.13), and making the substitution $\tilde{z} = \left[z - jD - z_j^+(\mathbf{r})\right]\langle\Psi_j(\mathbf{r})\rangle$,

$$I_{j,j'}(\mathbf{q}) = \int\int \mathrm{d}^3\mathbf{R}\ \mathrm{d}^3\mathbf{R}'\ \cdot \left\langle e^{i\mathbf{q}_\mathbf{r}\cdot(\mathbf{r}-\mathbf{r}')} \sum_{j\neq j'} e^{iq_z\left[\frac{\tilde{z}}{\left\langle\Psi_j(\mathbf{r})\right\rangle}-\frac{\tilde{z}'}{\left\langle\Psi_{j'}(\mathbf{r}')\right\rangle}+(j-j')D+z_j^+(\mathbf{r})-z_{j'}^+(\mathbf{r}')\right]} \frac{\rho_\mathrm{s}[\tilde{z},P_j(\mathbf{r})]\rho_\mathrm{s}[\tilde{z}',P_{j'}(\mathbf{r}')]}{\langle\Psi_j(\mathbf{r})\rangle\langle\Psi_{j'}(\mathbf{r}')\rangle}\right\rangle. \tag{3.21}$$

Electron density fluctuations due to peristaltic modes $P_j(\mathbf{r})$ are assumed to be sufficiently uncorrelated between different bilayers,

$$\left\langle \rho_{\rm s}[\tilde{z}, P_j(\mathbf{r})]\rho_{\rm s}[\tilde{z}', P_{j'}(\mathbf{r}')]\right\rangle \rightarrow \left\langle \rho_{\rm s}[\tilde{z}, P_j(\mathbf{r})]\right\rangle\left\langle \rho_{\rm s}[\tilde{z}', P_{j'}(\mathbf{r}')]\right\rangle. \tag{3.22}$$

Invoking translational invariance in the z-direction and using $F_0(\mathbf{r}, q_z)$ Eq. (3.19),

$$I_{j,j'}(\mathbf{q}) \approx I^{\rm a}_{j,j'}(\mathbf{q}) \tag{3.23}$$

$$\equiv \sum_{j\neq j'} \int\int {\rm d}^2\mathbf{r}\ {\rm d}^2\mathbf{r}'\ e^{i\mathbf{q}_\mathbf{r}\cdot(\mathbf{r}-\mathbf{r}')+iq_zD(j-j')} \left\langle e^{iq_z\left[z_j^+(\mathbf{r})-z_{j'}^+(\mathbf{r}')\right]}\right\rangle \left|\langle F_0(\mathbf{r}, q_z)\rangle\right|^2, \tag{3.24}$$

again using the assumption that P_j is uncorrelated with z_j^+ over long length scales.

Substituting $I_j^{\rm b}$ Eq. (3.20) and $I^{\rm a}_{j,j'}$ Eq. (3.24) into $I(\mathbf{q})$ Eq. (3.13),

$$I(\mathbf{q}) \approx \sum_j \int\int {\rm d}^2\mathbf{r}\ {\rm d}^2\mathbf{r}'\ e^{i\mathbf{q}_\mathbf{r}\cdot(\mathbf{r}-\mathbf{r}')} \left\langle e^{iq_z\left[z_0^+(\mathbf{r})-z_0^+(\mathbf{r}')\right]}\right\rangle \left\langle |F_0(\mathbf{r}, q_z)|^2\right\rangle + \sum_{j\neq j'} \int\int {\rm d}^2\mathbf{r}\ {\rm d}^2\mathbf{r}'\ e^{i\mathbf{q}_\mathbf{r}\cdot(\mathbf{r}-\mathbf{r}')+iq_zD(j-j')} \left\langle e^{iq_z\left[z_j^+(\mathbf{r})-z_{j'}^+(\mathbf{r}')\right]}\right\rangle \left|\langle F_0(\mathbf{r}, q_z)\rangle\right|^2. \tag{3.25}$$

Adding and subtracting the term,

$$\sum_j \int\int {\rm d}^2\mathbf{r}\ {\rm d}^2\mathbf{r}'\ e^{i\mathbf{q}_\mathbf{r}\cdot(\mathbf{r}-\mathbf{r}')} \left\langle e^{iq_z\left[z_0^+(\mathbf{r})-z_0^+(\mathbf{r}')\right]}\right\rangle \left|\langle F_0(\mathbf{r}, q_z)\rangle\right|^2, \tag{3.26}$$

from $I(\mathbf{q})$ Eq. (3.25) and grouping like terms,

$$I(\mathbf{q}) \approx \sum_j \int\int {\rm d}^2\mathbf{r}\ {\rm d}^2\mathbf{r}'\ e^{i\mathbf{q}_\mathbf{r}\cdot(\mathbf{r}-\mathbf{r}')} \left\langle e^{iq_z\left[z_0^+(\mathbf{r})-z_0^+(\mathbf{r}')\right]}\right\rangle \left[\left\langle |F_0(\mathbf{r}, q_z)|^2\right\rangle - \left|\langle F_0(\mathbf{r}, q_z)\rangle\right|^2\right] + \sum_{j,j'} \int\int {\rm d}^2\mathbf{r}\ {\rm d}^2\mathbf{r}'\ e^{i\mathbf{q}_\mathbf{r}\cdot(\mathbf{r}-\mathbf{r}')+iq_zD(j-j')} \left\langle e^{iq_z\left[z_j^+(\mathbf{r})-z_{j'}^+(\mathbf{r}')\right]}\right\rangle \left|\langle F_0(\mathbf{r}, q_z)\rangle\right|^2. \tag{3.27}$$

For sufficiently small length scales, fluctuations in $F_0(\mathbf{r}, q_z)$ are known to be significantly correlated; a scattering peak due to correlations between acyl tails is observed at $q_r \sim$1.4 Å^{-1} [3, 2, 53]. The current analysis focuses on $q_r < 0.3$ Å^{-1}. Enforcing liquid-like short range order by assuming that the fluctuations in $F_0(\mathbf{r}, q_z)$ are

uncorrelated over long length scales, $I(\mathbf{q})$ Eq. (3.27) is further simplified to

$$I(\mathbf{q}) \approx \left[\overline{\left\langle |F_0(\mathbf{r},q_z)|^2 \right\rangle} - \left|\overline{\langle F_0(\mathbf{r},q_z)\rangle}\right|^2\right] S_0(\mathbf{q}) + \left|\overline{\langle F_0(\mathbf{r},q_z)\rangle}\right|^2 S(\mathbf{q}) \tag{3.28}$$

where $\overline{\ }$ indicates an in-plane spatial average,

$$\overline{f(\mathbf{r},q_z)} = \frac{1}{A}\int_A \mathrm{d}^2\mathbf{r}\ f(\mathbf{r},q_z). \tag{3.29}$$

We call

$$S(\mathbf{q}) \equiv \sum_{j,j'} \int\int \mathrm{d}^2\mathbf{r}\ \mathrm{d}^2\mathbf{r}'\ e^{iq_z(j-j')D + i\mathbf{q}_\mathbf{r}\cdot(\mathbf{r}-\mathbf{r}')} \left\langle e^{iq_z\left[z_j^+(\mathbf{r}) - z_{j'}^+(\mathbf{r}')\right]} \right\rangle \tag{3.30}$$

the structure factor of the stack, and

$$S_0(\mathbf{q}) \equiv \sum_{j} \int\int \mathrm{d}^2\mathbf{r}\ \mathrm{d}^2\mathbf{r}'\ e^{i\mathbf{q}_\mathbf{r}\cdot(\mathbf{r}-\mathbf{r}')} \left\langle e^{iq_z\left[z_0^+(\mathbf{r}) - z_0^+(\mathbf{r}')\right]} \right\rangle. \tag{3.31}$$

is the structure factor describing the fluctuations of single bilayers within the stack. For later notational convenience, $I(\mathbf{q})$ Eq. (3.28) is defined as

$$I(\mathbf{q}) \equiv I_\mathrm{c}(\mathbf{q}) + I_\mathrm{bf}(\mathbf{q}), \tag{3.32}$$

where the "common" (c) intensity is

$$I_\mathrm{c} \equiv |F(q_z)|^2\, S(\mathbf{q}) \tag{3.33}$$

and

$$F(q_z) \equiv \overline{\langle F_0(\mathbf{r},q_z)\rangle}. \tag{3.34}$$

$F(q_z)$ is referred to as the form factor following many previous researchers [44, 46, 38]. The intensity due to single "bilayer fluctuations" (bf) is

$$I_{\rm bf}(\mathbf{q}) \equiv F_{\Delta}(q_z) S_0(\mathbf{q}), \tag{3.35}$$

where

$$F_{\Delta}(q_z) \equiv \left[\overline{\left\langle \left| F_0(\mathbf{r}, q_z) \right|^2 \right\rangle} - \left| \overline{\left\langle F_0(\mathbf{r}, q_z) \right\rangle} \right|^2 \right]. \tag{3.36}$$

Commonly, only $I_{\rm c}$ has been used to quantitatively describe the measured scattering from stacked lipid bilayers [44, 46, 38, 47, 55, 45]. The term describing internal bilayer fluctuations $I_{\rm bf}(\mathbf{q}) \equiv F_{\Delta}(q_z) S_0(\mathbf{q})$ is unique to the present work. Expressing the scattering intensity as a sum of two terms is routine for liquid-like samples [62, 63, 64]. Previously, a relation similar to Eq. (3.28) was suggested in the Appendix of [38] to describe the scattering from stacked lipid bilayers. Closely following Guinier [65] (see pp. 52-53), it was argued that the term $I'_{\rm bf} = J F_{\Delta}(q_z)$, where J is the number of layers, predicts broad diffuse scattering that could be nonnegligible far from the lamellar peaks.

$S(\mathbf{q})$ in Eq. (3.30) and $S_0(\mathbf{q})$ in Eq. (3.31) can be further simplified if $\left[z_j^+(\mathbf{r}) - z_{j'}^+(\mathbf{r}') \right]$ is assumed to be normally distributed [66]. Deviations from normality have been studied by Monte Carlo simulations [67]. Assuming normality,

$$S(\mathbf{q}) = \sum_{j,j'} \int \int \mathrm{d}^2\mathbf{r} \; \mathrm{d}^2\mathbf{r}' \; e^{i q_z (j-j') D + i \mathbf{q}_{\mathbf{r}} \cdot (\mathbf{r} - \mathbf{r}')} e^{-\frac{q_z^2}{2} \left\langle \left[z_j^+(\mathbf{r}) - z_{j'}^+(\mathbf{r}') \right]^2 \right\rangle} \tag{3.37}$$

and

$$S_0(\mathbf{q}) = \sum_{j} \int \int \mathrm{d}^2\mathbf{r} \; \mathrm{d}^2\mathbf{r}' \; e^{i \mathbf{q}_{\mathbf{r}} \cdot (\mathbf{r} - \mathbf{r}')} e^{-\frac{q_z^2}{2} \left\langle \left[z_0^+(\mathbf{r}) - z_0^+(\mathbf{r}') \right]^2 \right\rangle}, \tag{3.38}$$

where $\left\langle \left[z_j^+(\mathbf{r}) - z_{j'}^+(\mathbf{r}') \right]^2 \right\rangle$ is the height-height correlation function, the critical statistical quantity in the predicted X-ray scattering intensity. The structure factors $S(\mathbf{q})$ and $S_0(\mathbf{q})$ are the principal focus of this thesis. Since $S(\mathbf{q})$ and $S_0(\mathbf{q})$ are functions of an ensemble average involving z_j^+, the necessary statistical predictions of the

previously presented free energy functional $\mathcal{F}_\mathrm{u}$ Eq. (3.4) are derived.

3.3 Determining Statistical Quantities

Within Section 3.3, the previously introduced membrane free energy functional $\mathcal{F}_\mathrm{u}$ Eq. (3.4) is reexpressed in Fourier space. Then, the tilt-dependent height fluctuation spectrum (Section 3.3.2) and height-height correlation function (Section 3.3.3) are derived.

3.3.1 Free energy in Fourier Space

For completeness, the membrane free energy $\mathcal{F}_\mathrm{u}$ Eq. (3.4) is reproduced,

$$\mathcal{F}_\mathrm{u} = \frac{1}{2}\sum_j \int_{A_\mathrm{p}} \mathrm{d}^2\mathbf{r}\, \Big[K_c \left(\nabla^2 z_j^+ + \boldsymbol{\nabla}\cdot\hat{\mathbf{m}}_j\right)^2 + K_\theta |\hat{\mathbf{m}}_j|^2 + B\left(z_{j+1}^+ - z_j^+\right)^2\Big]. \tag{3.39}$$

Since $\mathcal{F}_\mathrm{u}$ Eq. (3.39) is classical and harmonic, the fluctuations are Fourier analyzed into normal modes. Assuming periodic boundary conditions both in- and out-of-plane, the fluctuation variables are written in terms of Fourier sums. Fourier transforms of the bilayer fluctuation fields are defined by

$$g_\mathbf{Q} \equiv \frac{1}{\sqrt{A_\mathrm{p} J}} \int \mathrm{d}^2\mathbf{r}\, \sum_j g_j(\mathbf{r}) e^{i\mathbf{Q}_\mathbf{r}\cdot\mathbf{r} + iQ_z jD} \tag{3.40}$$

$$g_j(\mathbf{r}) \equiv \frac{1}{\sqrt{A_\mathrm{p} J}} \sum_\mathbf{Q} g_\mathbf{Q} e^{i\mathbf{Q}_\mathbf{r}\cdot\mathbf{r} + iQ_z jD}, \tag{3.41}$$

where g stands for any one of the fluctuation fields, A_p is the area of the membrane projection onto the xy-plane, and J is the total number of bilayers in the stack. Throughout the thesis $\mathbf{Q}$ is reserved for the Fourier space of the fluctuations while $\mathbf{q}$ describes the scattering Fourier space. [10]

Boundary conditions besides periodic ones have been explored [59, 57, 68, 69, 70].

[10] $\mathbf{q}$ is also known as the wavevector transfer or the scattering vector.

For sufficiently large samples, different boundary conditions only primarily influence fluctuations on long length scales similar to the sample size. The current X-ray scattering experiments only probe fluctuations on length scales much shorter than the sample size.[11] Therefore, the boundary conditions most amenable to analytic calculations are used.

Following [1], the tilt field $\hat{\mathbf{m}}(\mathbf{r})$ is decomposed into longitudinal $\hat{m}_j^{\parallel}(\mathbf{r})$ and transverse $\hat{m}_j^{\perp}(\mathbf{r})$ components. In Fourier space, the longitudinal and transverse components are

$$\hat{m}_{\mathbf{Q}}^{\parallel} = \frac{\mathbf{Q_r} \cdot \hat{\mathbf{m}}_{\mathbf{Q}}}{Q_r} \tag{3.42}$$

$$\hat{m}_{\mathbf{Q}}^{\perp} = \frac{(\mathbf{Q_r} \times \hat{\mathbf{m}}_{\mathbf{Q}}) \cdot \hat{\mathbf{z}}}{Q_r}, \tag{3.43}$$

respectively, where $\mathbf{Q_r} \equiv (Q_x, Q_y)$. Given Eq. (3.42), $\boldsymbol{\nabla} \cdot \hat{\mathbf{m}}_j$ in $\mathcal{F}_{\rm u}$ Eq. (3.39) is particularly simple in Fourier space,

$$\boldsymbol{\nabla} \cdot \hat{\mathbf{m}}_j \rightarrow i Q_r \hat{m}_{\mathbf{Q}}^{\parallel}. \tag{3.44}$$

Using the definition of the Fourier transform Eq. (3.41) and Eq. (3.44), $\mathcal{F}_{\rm u}$ Eq. (3.39) is expressed in Fourier space,

$$\begin{aligned}
\mathcal{F}_{\rm u} = \frac{1}{2A_{\rm p}J} \int {\rm d}^2\mathbf{r} \sum_{j=0}^{J-1} \sum_{\mathbf{Q},\mathbf{Q}'} \Bigg\{ \Big[& \\
& K_c \left(-Q_r^2 z_{\mathbf{Q}}^{+} + i Q_r \hat{m}_{\mathbf{Q}}^{\parallel} \right) \left(-{Q'_r}^2 z_{\mathbf{Q}'}^{+} + i Q'_r \hat{m}_{\mathbf{Q}'}^{\parallel} \right) \\
& + K_\theta \left(\hat{m}_{\mathbf{Q}}^{\parallel} \hat{m}_{\mathbf{Q}'}^{\parallel} + \hat{m}_{\mathbf{Q}}^{\perp} \hat{m}_{\mathbf{Q}'}^{\perp} \right) \Big] e^{i(Q_z + Q'_z) jD} \\
& + B z_{\mathbf{Q}}^{+} z_{\mathbf{Q}'}^{+} \left(e^{iQ_z(j+1)D} - e^{iQ_z jD} \right) \left(e^{iQ'_z(j+1)D} - e^{iQ'_z jD} \right) \Bigg\} e^{i(\mathbf{Q_r} + \mathbf{Q'_r}) \cdot \mathbf{r}}.
\end{aligned} \tag{3.45}$$

The integral in $\mathcal{F}_{\rm u}$ Eq. (3.45) is evaluated using,

[11] The sample coherence volume determines the longest length scale correlations that can be directly probed by an X-ray scattering experiment, see Section 5.3.2.

$$\int_{A_\mathrm{p}} \mathrm{d}^2\mathbf{r}\; e^{i(\mathbf{Q_r}+\mathbf{Q'_r})\cdot\mathbf{r}} = A_\mathrm{p}\,\delta\left(\mathbf{Q_r}+\mathbf{Q'_r}\right)\,, \tag{3.46}$$

where δ is the Dirac delta. Because Q_z and Q'_z only take on discrete values with periodic boundary conditions,

$$\sum_{j=0}^{J-1} e^{i(Q_z+Q'_z)jD} = \frac{1-e^{i(Q_z+Q'_z)JD}}{1-e^{i(Q_z+Q'_z)D}} = \begin{cases} 0, & Q_z+Q'_z \neq 0 \\ J, & Q_z+Q'_z = 0 \end{cases} \tag{3.47}$$

and

$$\sum_{j=0}^{J-1}\left(e^{iQ_z(j+1)D}-e^{iQ_zjD}\right)\left(e^{iQ'_z(j+1)D}-e^{iQ'_zjD}\right) = 4J\sin^2(Q_zD/2)\;\delta_{Q_z+Q'_z,0}, \tag{3.48}$$

where the above δ is the Kronecker delta. Utilizing Eqs. (3.46), (3.47), and (3.48), $\mathcal{F}_\mathrm{u}$ expressed in Fourier space Eq. (3.45) is simplified,

$$\begin{aligned}\mathcal{F}_\mathrm{u} = \frac{1}{2}\sum_{\mathbf{Q}}\Big[&K_c\left(-Q_r^2 z^+_{\mathbf{Q}} + iQ_r\hat{m}^{\parallel}_{\mathbf{Q}}\right)\left(-Q_r^2 z^+_{-\mathbf{Q}} - iQ_r\hat{m}^{\parallel}_{-\mathbf{Q}}\right) \\ &+ K_\theta\left(\hat{m}^{\parallel}_{\mathbf{Q}}\hat{m}^{\parallel}_{-\mathbf{Q}} + \hat{m}^{\perp}_{\mathbf{Q}}\hat{m}^{\perp}_{-\mathbf{Q}}\right) + 4Bz^+_{\mathbf{Q}}z^+_{-\mathbf{Q}}\sin^2(Q_zD/2)\Big].\end{aligned} \tag{3.49}$$

Following Watson *et al.* [1], it is convenient to express $\mathcal{F}_\mathrm{u}$ Eq. (3.49) in terms of matrices in order to calculate thermal averages. Defining the vector,

$$\mathbf{f}_\mathrm{u}(\mathbf{Q}) = \left(z^+_{\mathbf{Q}},\, \hat{m}^{\parallel}_{\mathbf{Q}},\, \hat{m}^{\perp}_{\mathbf{Q}}\right), \tag{3.50}$$

$\mathcal{F}_\mathrm{u}$ Eq. (3.49) is expressed as an inner product involving a Hermitian matrix $\mathbb{U}$,

$$\mathcal{F}_\mathrm{u} = \frac{1}{2}\sum_{\mathbf{Q}} \mathbf{f}_\mathrm{u}(-\mathbf{Q})\,\mathbb{U}\,\mathbf{f}_\mathrm{u}^T(\mathbf{Q}), \tag{3.51}$$

where

$$\mathbb{U} = \begin{pmatrix} K_c Q_r^4 + 4B\sin^2(Q_z D/2) & -iK_c Q_r^3 & 0 \\ iK_c Q_r^3 & K_c Q_r^2 + K_\theta & 0 \\ 0 & 0 & K_\theta \end{pmatrix}. \tag{3.52}$$

To determine thermal averages, the equipartition theorem is applied to the eigenmodes of $\mathbb{U}$. As is well known [21], various thermal averages are related to $\mathbb{U}^{-1}$ (see Appendix A.1),

$$\left\langle \mathbf{f}_{\mathrm{u}}^T(\mathbf{Q}) \mathbf{f}_{\mathrm{u}}(\mathbf{Q}') \right\rangle = k_{\mathrm{B}} T \, \mathbb{U}^{-1} \, \delta_{\mathbf{Q},-\mathbf{Q}'}, \tag{3.53}$$

where

$$\mathbb{U}^{-1} = \frac{1}{C} \begin{pmatrix} 1 + \xi_\theta^2 Q_r^2 & i\xi_\theta^2 Q_r^3 & 0 \\ -i\xi_\theta^2 Q_r^3 & \frac{K_c Q_r^4 + 4B\sin^2(Q_z D/2)}{K_\theta} & 0 \\ 0 & 0 & \frac{C}{K_\theta} \end{pmatrix}, \tag{3.54}$$

$$C \equiv K_c Q_r^4 + 4B\left(1 + \xi_\theta^2 Q_r^2\right)\sin^2\left(Q_z D/2\right), \tag{3.55}$$

$$\xi_\theta^2 \equiv K_c / K_\theta, \tag{3.56}$$

k_{B} is the Boltzmann constant, and T is the temperature.

3.3.2 Height Fluctuation Spectrum

The height fluctuation spectrum $\left\langle |z_{\mathbf{Q}}^+|^2 \right\rangle$ is required to calculate the structure factors $S(\mathbf{q})$ Eq. (3.37) and $S_0(\mathbf{q})$ Eq. (3.38) and consequently, the X-ray scattering intensity from a stack of membranes. Using Eq. (3.53) and $\mathbb{U}^{-1}$ Eq. (3.54),

$$\begin{aligned} \left\langle |z_{\mathbf{Q}}^+|^2 \right\rangle &= k_{\mathrm{B}} T \, \mathbb{U}_{1,1}^{-1} \delta_{\mathbf{Q},-\mathbf{Q}'} \\ &= k_{\mathrm{B}} T \frac{1 + \xi_\theta^2 Q_r^2}{K_c Q_r^4 + 4B(1 + \xi_\theta^2 Q_r^2)\sin^2(Q_z D/2)} \, \delta_{\mathbf{Q},-\mathbf{Q}'} \\ &= \frac{k_{\mathrm{B}} T}{4B} \frac{1}{\aleph^2 + \sin^2(Q_z D/2)} \, \delta_{\mathbf{Q},-\mathbf{Q}'} \end{aligned} \tag{3.57}$$

where

$$\aleph^2 = \frac{\xi^4 Q_r^4}{4(1+\xi_\theta^2 Q_r^2)} \tag{3.58}$$

and

$$\xi^4 \equiv K_c/B. \tag{3.59}$$

Several membrane free energy functionals make equivalent predictions for the height spectrum. In order to compare to the derived bilayer stack height spectrum in Eq. (3.57), literature single membrane free energy functionals are extended to describe bilayer stacks by adding the intermembrane interaction term

$$\propto B\left(z_{j+1}^+ - z_j^+\right)^2. \tag{3.60}$$

The augmented model advanced by Watson *et al.* [22] predicts Eq. (3.57), where $K_c = K_c^b - \widetilde{\Omega}^2/(4K_A)$ was used. The extension of the Hamm and Kozlov free energy [31] to describe a stack of bilayers leads to a free energy functional similar to $\mathcal{F}_{\rm u}$ Eq. (3.4), but Hamm and Kozlov were describing a monolayer.

Tilt-dependent and -independent Height Fluctuation Spectra

The most pertinent difference between tilt-dependent and tilt-independent models is their predictions for the height fluctuation spectrum. The tilt-independent height spectrum is the limiting case of the tilt-dependent spectrum $\left\langle |z_{\mathbf{Q}}^+|^2 \right\rangle$ Eq. (3.57) when $K_\theta \to \infty$ (or equivalently $\xi_\theta = 0$),

$$\left\langle |z_{\mathbf{Q}}^+|^2 \right\rangle^{\cancel{\rm tilt}} = \lim_{K_\theta \to \infty} \left\langle |z_{\mathbf{Q}}^+|^2 \right\rangle \tag{3.61}$$

$$= k_{\rm B}T \frac{1}{K_c Q_r^4 + 4B\sin^2(Q_z D/2)}\, \delta_{\mathbf{Q},-\mathbf{Q}'}. \tag{3.62}$$

In various specific cases, the tilt-dependent height fluctuation spectrum is consistent with expected results. The single membrane height fluctuation spectra ($Q_z = 2\pi/D$)

are $\left\langle |z^+_{\mathbf{Q}}|^2 \right\rangle \propto \left(\frac{1}{K_c Q_r^4} + \frac{1}{K_\theta Q_r^2} \right)$ [22, 21, 1] and $\left\langle |z^+_{\mathbf{Q}}|^2 \right\rangle^{\cancel{\text{tilt}}} \propto \frac{1}{K_c Q_r^4}$. The K_θ-dependent term in $\left\langle |z^+_{\mathbf{Q}}|^2 \right\rangle$ results in more power in the height spectrum for large wavevectors, short real-space length scales, as compared to $\left\langle |z^+_{\mathbf{Q}}|^2 \right\rangle^{\cancel{\text{tilt}}}$. Fig. 3.4 shows the single membrane versions of $\left\langle |z^+_{\mathbf{Q}}|^2 \right\rangle$ and $\left\langle |z^+_{\mathbf{Q}}|^2 \right\rangle^{\cancel{\text{tilt}}}$. Note, that $1/\xi_\theta = \sqrt{K_\theta / K_c}$ separates the bending dominated regime at lesser Q_r and the tilt mode dominated regime at greater Q_r.

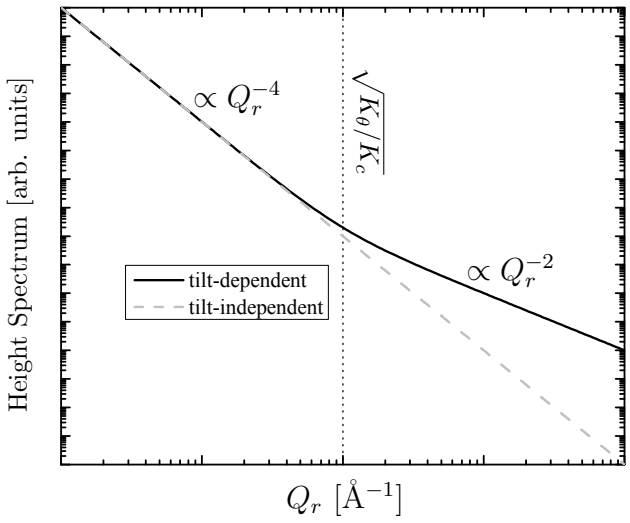


Figure 3.4: Single membrane tilt-dependent (solid line) and tilt-independent (dashed line) height spectra are plotted. The vertical short dashed line indicates the crossover from Q_r^{-4} to Q_r^{-2} centered at $\sqrt{K_\theta/K_c}$.

3.3.3 Height-height Correlation Function

The theoretical structure factors $S(\mathbf{q})$ Eq. (3.37) and $S_0(\mathbf{q})$ Eq. (3.38) are functions of the height-height correlation function

$$\left\langle \left[z_j^+(\mathbf{r}) - z_{j'}^+(\mathbf{r}') \right]^2 \right\rangle$$

$$= \left\langle \left| \frac{1}{\sqrt{A_\mathrm{p} J}} \sum_{\mathbf{Q}} z^+_{\mathbf{Q}} \left(e^{i\mathbf{Q}_\mathbf{r}\cdot\mathbf{r} + iQ_z z} - e^{i\mathbf{Q}_\mathbf{r}\cdot\mathbf{r}' + iQ_z z'} \right) \right|^2 \right\rangle \tag{3.63}$$

$$= \frac{1}{A_\mathrm{p} J} \sum_{\mathbf{Q},\mathbf{Q}'} \left\langle z^+_{\mathbf{Q}} z^+_{\mathbf{Q}'} \right\rangle \left(e^{i\mathbf{Q}_\mathbf{r}\cdot\mathbf{r} + iQ_z z} - e^{i\mathbf{Q}_\mathbf{r}\cdot\mathbf{r}' + iQ_z z'} \right) \left(e^{i\mathbf{Q}'_\mathbf{r}\cdot\mathbf{r} + iQ'_z z} - e^{i\mathbf{Q}'_\mathbf{r}\cdot\mathbf{r}' + iQ'_z z'} \right). \tag{3.64}$$

Substituting $\left\langle |z^+_{\mathbf{Q}}|^2 \right\rangle$ Eq. (3.57) into Eq. (3.64),

$$\begin{aligned}
&\left\langle \left[z_j^+(\mathbf{r}) - z_{j'}^+(\mathbf{r}') \right]^2 \right\rangle \\
&= \frac{k_\mathrm{B}T}{4BA_\mathrm{p}J} \sum_{\mathbf{Q}} \frac{\left(e^{i\mathbf{Q_r}\cdot\mathbf{r}+iQ_z z} - e^{i\mathbf{Q_r}\cdot\mathbf{r}'+iQ_z z'} \right)\left(e^{-i\mathbf{Q_r}\cdot\mathbf{r}-iQ_z z} - e^{-i\mathbf{Q_r}\cdot\mathbf{r}'-iQ_z z'} \right)}{\aleph^2 + \sin^2(Q_z D/2)} \qquad (3.65) \\
&= \frac{k_\mathrm{B}T}{2BA_\mathrm{p}J} \sum_{\mathbf{Q}} \frac{1 - \cos[\mathbf{Q_r}\cdot(\mathbf{r}-\mathbf{r}') + Q_z(z-z')]}{\aleph^2 + \sin^2(Q_z D/2)}. \qquad (3.66)
\end{aligned}$$

Assuming the step size in Q_r is sufficiently small, $\sum_{\mathbf{Q}}$ in Eq. (3.66) is replaced by $\frac{A_\mathrm{p}}{(2\pi)^2} \int \mathrm{d}\mathbf{Q_r} \sum_{Q_z}$,

$$\begin{aligned}
&\left\langle \left[z_j^+(\mathbf{r}) - z_{j'}^+(\mathbf{r}') \right]^2 \right\rangle \\
&= \frac{k_\mathrm{B}T}{8\pi^2 JB} \int \mathrm{d}\mathbf{Q_r} \sum_{Q_z} \frac{1 - \cos[\mathbf{Q_r}\cdot(\mathbf{r}-\mathbf{r}') + Q_z(z-z')]}{\aleph^2 + \sin^2(Q_z D/2)} \qquad (3.67) \\
&= \frac{k_\mathrm{B}T}{8\pi^2 JB} \int_0^{\pi/a} \mathrm{d}Q_r \; Q_r \int_{-\pi}^{\pi} \mathrm{d}\theta \sum_{Q_z} \frac{1 - \cos[\mathbf{Q_r}\cdot(\mathbf{r}-\mathbf{r}') + Q_z(z-z')]}{\aleph^2 + \sin^2(Q_z D/2)} \qquad (3.68) \\
&= \frac{k_\mathrm{B}T}{4\pi JB} \int_0^{\pi/a} \mathrm{d}Q_r \; Q_r \sum_{Q_z} \frac{1 - J_0(Q_r|r-r'|)\cos[Q_z(z-z')]}{\aleph^2 + \sin^2(Q_z D/2)} \qquad (3.69) \\
&= \frac{k_\mathrm{B}T}{4\pi JB} \int_0^{\pi/a} \mathrm{d}Q_r \; Q_r \sum_{Q_z} \frac{1 - J_0(Q_r|r-r'|)\cos[Q_z(j-j')D]}{\aleph^2 + \sin^2(Q_z D/2)}, \qquad (3.70)
\end{aligned}$$

where π/a is the longest Q_r mode beyond which the continuum aproximation of the system is no longer valid. Note, the lower integration limit is 0 since the system size is assumed to be infinite, see Section 6.3 for further discussion.

The sum over Q_z in Eq. (3.70) runs from $Q_z = \frac{2\pi j}{JD}$ ($j = -J/2{+}1, ..., -1, 0, 1, ..., J/2$). J is assumed to be sufficiently large that the sum in Eq. (3.70) is approximated by an integral, $\sum_{Q_z} \to \frac{JD}{2\pi} \int_{-\pi/D}^{\pi/D} \mathrm{d}Q_z$,

$$\left\langle \left[z_j^+(r) - z_{j'}^+(r')\right]^2 \right\rangle = \frac{k_{\mathrm{B}}TD}{8\pi^2 B}\int_0^{\pi/a} \mathrm{d}Q_r\; Q_r \int_{-\pi/D}^{\pi/D} \mathrm{d}Q_z \frac{1 - J_0(Q_r|r-r'|)\cos[Q_z(j-j')D]}{\aleph^2 + \sin^2(Q_z D/2)}. \quad (3.71)$$

As Q_r and Q_z simultaneously approach zero, the integrand of Eq. (3.71) diverges. The aforementioned divergence issue exists for the tilt-independent free energy and was solved by Ning Lei [56] by analytically evaluating the Q_z-dependent integral. Lei's work was followed by later researchers [44, 46]. The resulting Q_r-dependent integrand no longer diverges as Q_r approaches zero, and therefore, the Q_r-dependent integral can be numerically computed without the aforementioned concern. Using Lei's results [56, 55],

$$\int_{-\pi}^{\pi} \mathrm{d}\omega\; \frac{1}{\aleph^2 + \sin^2(\frac{\omega}{2})} = \frac{2\pi}{\sqrt{\aleph^2 + \aleph^4}} \quad (3.72)$$

and

$$\int_{-\pi}^{\pi} \mathrm{d}\omega\; \frac{e^{im\omega}}{\aleph^2 + \sin^2(\frac{\omega}{2})} = \frac{2\pi\Delta^{|m|}}{\sqrt{\aleph^2 + \aleph^4}}, \quad (3.73)$$

where $\Delta = \left(\sqrt{1+\aleph^2} - \aleph\right)^2$, the Q_z-dependent integral in Eq. (3.71) is evaluated analytically after the substitution $\omega = Q_z D$,

$$\left\langle \left[z_j^+(r) - z_{j'}^+(r')\right]^2 \right\rangle = \frac{k_{\mathrm{B}}T}{4\pi B}\int_0^{\pi/a} \mathrm{d}Q_r\; Q_r \frac{1 - J_0(Q_r|r-r'|)\Delta^{|j-j'|}}{\sqrt{\aleph^2 + \aleph^4}} \quad (3.74)$$

$$= \frac{k_{\mathrm{B}}T}{2\pi B\xi^2}\int_0^{\pi/a} \mathrm{d}Q_r\; \frac{1 - J_0(Q_r|r-r'|)\left(\sqrt{1 + \frac{\xi^4 Q_r^4}{4(1+\xi_\theta^2 Q_r^2)}} - \frac{\xi^2 Q_r^2}{2\sqrt{1+\xi_\theta^2 Q_r^2}}\right)^{2|j-j'|}}{\frac{Q_r}{\sqrt{1+\xi_\theta^2 Q_r^2}}\sqrt{1 + \frac{\xi^4 Q_r^4}{4(1+\xi_\theta^2 Q_r^2)}}}. \quad (3.75)$$

Defining $v = \frac{\xi^2 Q_r^2}{2}$ and substituting into Eq. (3.75),

$$\left\langle \left[z_j^+(r) - z_{j'}^+(r') \right]^2 \right\rangle$$
$$= \frac{k_\mathrm{B}T}{4\pi B\xi^2} \int_0^{\frac{1}{2}\left(\frac{\pi\xi}{a}\right)^2} \mathrm{d}v \; \frac{1 - J_0\left(\sqrt{2v}\frac{|r-r'|}{\xi}\right) \left(\sqrt{1 + \frac{v^2}{1+2v\frac{\xi_\theta^2}{\xi^2}}} - \frac{v}{\sqrt{1+2v\frac{\xi_\theta^2}{\xi^2}}} \right)^{2|j-j'|}}{\frac{v}{\sqrt{1+2v\frac{\xi_\theta^2}{\xi^2}}} \sqrt{1 + \frac{v^2}{1+2v\frac{\xi_\theta^2}{\xi^2}}}}. \quad (3.76)$$

The right hand side of Eq. (3.76) only depends on the magnitude of the separation between two points, $|r - r'| \to r$ and $|j - j'| \to j$. Defining dimensionless parameters

$$\rho \equiv r/\xi, \quad (3.77)$$
$$\ell \equiv 2\xi_\theta^2/\xi^2, \quad (3.78)$$
$$\eta \equiv \frac{\pi k_\mathrm{B}T}{2D^2B\xi^2}, \quad (3.79)$$

and

$$\tau \equiv \frac{1}{2}\left(\frac{\pi\xi}{a}\right)^2, \quad (3.80)$$

$\left\langle \left[z_j^+(r) - z_{j'}^+(r') \right]^2 \right\rangle$ Eq. (3.76) is compactly expressed,

$$\left\langle \left[z_j^+(r) - z_0^+(0) \right]^2 \right\rangle = \frac{D^2\eta}{2\pi^2} \int_0^\tau \mathrm{d}v \; \frac{1 - J_0\left(\sqrt{2v}\rho\right) \left(\sqrt{1 + \frac{v^2}{1+v\ell}} - \frac{v}{\sqrt{1+v\ell}} \right)^{2j}}{\frac{v}{\sqrt{1+v\ell}} \sqrt{1 + \frac{v^2}{1+v\ell}}} \quad (3.81)$$
$$\equiv h_j(\rho, \ell, \tau). \quad (3.82)$$

The natural parameters of the theory are the three dimensionless variables the Caillé η, in-plane length ρ, and tilt strength ℓ from which K_c, K_θ, and B are determined. τ is the dimensionless long wavevector cutoff.

Tilt-dependent vs -independent Height-Height Correlation Functions

A critical difference between the tilt-dependent and -independent height-height functions is the decay of their respective integrands. In the limit $K_\theta \to \infty$ ($\ell \to 0$), $h_j(\rho, \ell, \tau)$ Eq. (3.81) reduces to the tilt-independent theory [55],

$$\lim_{\ell \to 0} h_j(\rho, \ell, \tau) = h_j^{\not{\text{tilt}}}(\rho, \tau) \equiv \frac{D^2\eta}{2\pi^2} \int_0^\tau \mathrm{d}v \, \frac{1 - J_0\left(\sqrt{2v}\rho\right)\left(\sqrt{1+v^2} - v\right)^{2j}}{v\sqrt{1+v^2}}. \tag{3.83}$$

For large v the integrand of $h_j(\rho, \ell, \tau)$ Eq. (3.81) decays like v^{-1} as opposed to v^{-2} for $h_j^{\not{\text{tilt}}}(\rho, \tau)$ Eq. (3.83). Because of the rapid decay of the tilt-independent integrand, the upper integration limit often has been replaced by ∞, assuming that the upper limit was sufficiently large [48, 56],

$$h_j^{\not{\text{tilt}}}(\rho) \approx \frac{D^2\eta}{2\pi^2} \int_0^\infty \mathrm{d}v \, \frac{1 - J_0\left(\sqrt{2v}\rho\right)\left(\sqrt{1+v^2} - v\right)^{2j}}{v\sqrt{1+v^2}}. \tag{3.84}$$

Since the tilt-dependent integrand decays like v^{-1}, its upper integration limit can not be replaced by ∞. The ξ- and a-dependent upper integration limit complicates computation of $h_j(\rho, \ell, \tau)$ Eq. (3.81), a topic further explored in Section 4.1.

Chapter 4

Calculating the Height-Height Correlation Function

Numerically calculating the theoretical height-height correlation function $h_j(\rho, \ell, \tau)$ is an essential step for analyzing the experimental scattering data. $h_j(\rho, \ell, \tau)$ Eq. (3.81) derived in Section 3.3.3 is reproduced for convenience,

$$h_j(\rho, \ell, \tau) = \frac{D^2\eta}{2\pi^2} \int_0^\tau \mathrm{d}v \; \frac{1 - J_0\left(\sqrt{2v}\rho\right)\left(\sqrt{1 + \frac{v^2}{1+v\ell}} - \frac{v}{\sqrt{1+v\ell}}\right)^{2j}}{\frac{v}{\sqrt{1+v\ell}}\sqrt{1 + \frac{v^2}{1+v\ell}}}, \tag{4.1}$$

where the dimensionless variables ρ, ℓ, τ, and η are defined prior to Eq. (3.81); ρ (the scaled in-plane distance), τ (the long wavevector cutoff), and the Caillé η parameter are familiar from the tilt-independent theory; ℓ is a new tilt-dependent parameter. Since $h_j(\rho, \ell, \tau)$ is related to an integral with an oscillatory integrand care must be paid to its computation. Additionally, $h_j(\rho, \ell, \tau)$ is nested within other integrals in the definitions of the structure factors, $S(\mathbf{q})$ in Eq. (3.37) and $S_0(\mathbf{q})$ in Eq. (3.38), and therefore, its computation should be as fast as possible to minimize analysis time.

Various approximations are made to expedite the calculation of $h_j(\rho, \ell, \tau)$. Section 4.1 describes the general procedure to compute $h_j(\rho, \ell, \tau)$. Following a similar methodology as previous researchers [48, 46, 38], values of $h_j(\rho, \ell, \tau)$ as a function of ρ, ℓ, and j are computed and stored in a table. When analyzing data, the table is queried, and its entries are used to interpolate values of $h_j(\rho, \ell, \tau)$. In Section 4.2 an analytic approximation $\tilde{h}_j(\rho, \ell, \tau)$ is derived, taking inspiration from the deriva-

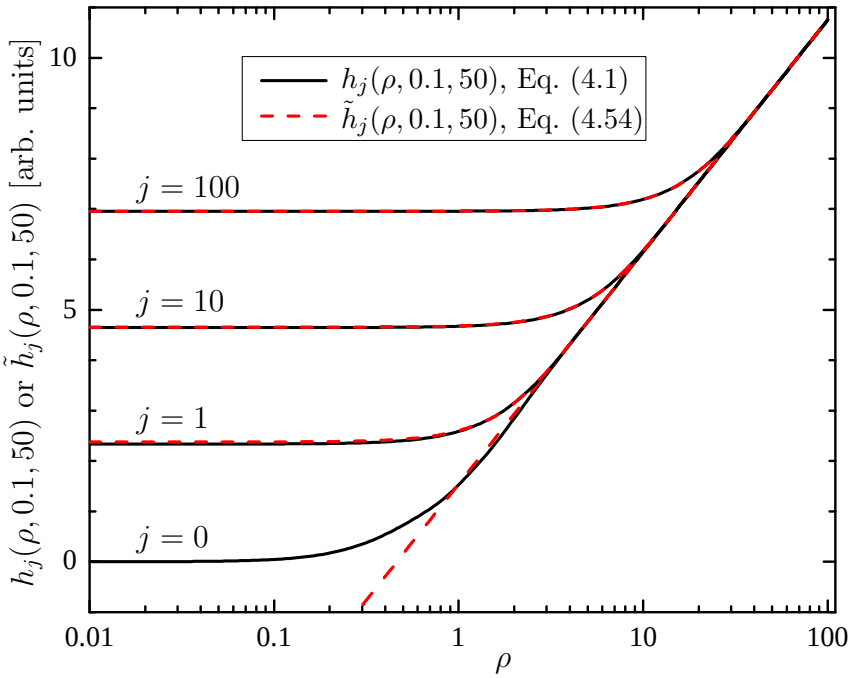


Figure 4.1: $h_j(\rho, \ell, \tau)$ and $\tilde{h}_j(\rho, \ell, \tau)$ are plotted as functions of ρ for several j and $\ell = 0.1$.

tion of the tilt-independent analog [56].[12] For $\rho \gg 1$, $\tilde{h}_j(\rho, \ell, \tau)$ is used to determine $h_j(\rho, \ell, \tau)$, diminishing the necessary maximum ρ-value of the $h_j(\rho, \ell, \tau)$ table. Additionally, $\tilde{h}_j(\rho, \ell, \tau)$ is derived to compare it to its tilt-independent analog $\tilde{h}_j(\rho, 0, \infty)$. $\tilde{h}_j(\rho, 0, \infty)$ is important since it was used to predict the power law decay of the scattering peaks from smectic A liquid crystals [41] (of which stacked bilayers are an example). Finally, in Section 4.3, it is argued that from a scattering perspective the most significant differences of tilt-dependent and -independent height-height correlation functions are for $j \sim 1$ and $\rho \ll 1$.

Since the behavior of $h_j(\rho, \ell, \tau)$ is not readily apparent from Eq. (4.1) and to preview the main conclusion of Section 4.2, $h_j(\rho, \ell, \tau)$ Eq. (4.1) and $\tilde{h}_j(\rho, \ell, \tau)$ Eq. (4.54) are plotted in Fig. 4.1 for $\ell = 0.1$ and $\tau = 50$ (typical values). $\tilde{h}_j(\rho, \ell, \tau)$ well approximates $h_j(\rho, \ell, \tau)$ for $\rho \gg 1$.

[12] In [56], an analytic approximation of the tilt-independent height-height correlation function for $\rho \ll 1$ is also derived. The corresponding analytic result for the tilt-dependent theory is outstanding. Given such a result, the size of the $h_j(\rho, \ell, \tau)$ table could be further diminished. Additionally, using the $\rho \ll 1$ analytic approximation, it may be possible to determine a K_θ-value from the decay of the measured scattering intensity $I(q_x, q_z)$ for large q_x in a similar methodology to the early power-law analyses that determined η [42].

4.1 Tabling $h_j(\rho, \ell, \tau)$

To determine the elastic moduli values that lead to the best agreement between theory and data, $h_j(\rho, \ell, \tau)$ Eq. (4.1) is evaluated many times in a nonlinear least squares fitting procedure (see Chapter 7). To reduce the computational overhead for fitting the data, values of $h_j(\rho, \ell, \tau)$ as a function of ρ, ℓ, and τ for each value of j can be stored in a table. At run-time, the 4-dimensional table could be queried and a 3-dimensional interpolation would yield a value of $h_j(\rho, \ell, \tau)$ for a given j value. The aforementioned scheme reduces the time required to fit data since a single evaluation of an interpolation to approximate an integral is traded for many evaluations of the integrand. Assuming that 1000 floating point values (4 bytes each) are sampled for each dimensionless parameter, the size of such a $h_j(\rho, \ell, \tau)$ table would be 4 TB, much too large to easily store and retrieve using a standard desktop computer. A lower dimensional tabling scheme is presented in Section 4.1.1.

4.1.1 Considering the Finite Upper Limit τ

$h_j(\rho, \ell, \tau)$ Eq. (4.1) is approximately expressed in a simpler form which is stored as a 3-dimensional table. Given a chosen constant for the upper limit of integration τ, $h_j(\rho, \ell, \tau)$ is tabled as a function of ρ and ℓ for each j value, a 3-dimensional table. $h_j(\rho, \ell, \tau)$ is calculated using the tabled values and a two-dimensional interpolation scheme for each value of j. The aforementioned method over- or underestimates $h_j(\rho, \ell, \tau)$ because of the difference between the true ξ- and a-dependent upper limit, τ', and the chosen τ value.

$$h_j(\rho, \ell, \tau') = h_j(\rho, \ell, \tau) + \frac{D^2\eta}{2\pi^2} C(\tau, \tau', \ell, \rho, j) \tag{4.2}$$

where $C(\tau, \tau', \ell, \rho, j)$ is the over- or underestimation of the integral in $h_j(\rho, \ell, \tau)$ Eq. (4.1).

An approximate relation for $C(\tau, \tau', \ell, \rho, j)$ is derived. The smallest reasonable value of τ is $\pi^2/2$ because the in-plane correlation length ξ must be larger than the short length scale cutoff a. Beginning with $h_j(\rho, \ell, \tau)$ Eq. (4.1) and assuming $\tau' > \tau > \pi^2/2$,

$$C(\tau,\tau',\ell,\rho,j) \equiv \int_\tau^{\tau'} \mathrm{d}v\ \frac{1-J_0\left(\sqrt{2v}\rho\right)\left(\sqrt{1+\frac{v^2}{1+v\ell}}-\frac{v}{\sqrt{1+v\ell}}\right)^{2j}}{\frac{v}{\sqrt{1+v\ell}}\sqrt{1+\frac{v^2}{1+v\ell}}} \tag{4.3}$$

$$= \int_\tau^{\tau'} \mathrm{d}v\ \frac{1+v\ell}{v\sqrt{1+v\ell+v^2}} - \int_\tau^{\tau'} \mathrm{d}x\ \frac{J_0\left(\sqrt{2v}\rho\right)\left(\sqrt{1+\frac{v^2}{1+v\ell}}-\frac{v}{\sqrt{1+v\ell}}\right)^{2j}}{\frac{v}{\sqrt{1+v\ell}}\sqrt{1+\frac{x^2}{1+v\ell}}}$$

$$= C^\dagger(\tau,\tau',\ell) - C^*(\tau,\tau',\ell,\rho,j), \tag{4.4}$$

where in the final line the correction was split into ρ- and j-dependent and -independent parts. $C^\dagger$ is evaluated analytically,

$$C^\dagger(\tau,\tau',\ell) \equiv \int_\tau^{\tau'} \mathrm{d}v\ \frac{1+v\ell}{v\sqrt{1+v\ell+v^2}} \tag{4.5}$$

$$= \ln\left(\frac{\tau'}{\tau}\right) + \ell\ln\left(\frac{\ell+2\tau'+2f_c(\tau')}{\ell+2\tau+2f_c(\tau)}\right) - \ln\left(\frac{2+\ell\tau'+2f_c(\tau')}{2+\ell\tau+2f_c(\tau)}\right), \tag{4.6}$$

where $f_c(x) \equiv \sqrt{1+x\ell+x^2}$. Moving on to C^*,

$$C^*(\tau,\tau',\ell,\rho,j) \equiv \int_\tau^{\tau'} \mathrm{d}v\ \frac{J_0\left(\sqrt{2v}\rho\right)\left(\sqrt{1+\frac{v^2}{1+v\ell}}-\frac{v}{\sqrt{1+v\ell}}\right)^{2j}}{\frac{v}{\sqrt{1+v\ell}}\sqrt{1+\frac{v^2}{1+v\ell}}}. \tag{4.7}$$

In general, $C^* \ll C^\dagger$ because its integrand oscillates about zero and

$$\left(\sqrt{1+\frac{v^2}{1+v\ell}}-\frac{v}{\sqrt{1+v\ell}}\right)^{2j}$$

decays rapidly as a function of j. For $j>1$, C^* is negligible, and therefore,

$$C(\tau,\tau',\ell,\rho,j>1) \approx C^\dagger(\tau,\tau',\ell) \tag{4.8}$$

$$\Rightarrow h_{j>1}(\rho,\ell,\tau') \approx h_{j>1}(\rho,\ell,\tau) + \frac{D^2\eta}{2\pi^2}C^\dagger(\tau,\tau',\ell). \tag{4.9}$$

$h_{j>1}(\rho,\ell,\tau)$ in Eq. (4.9) is determined using a 3-dimensional (ρ, ℓ, j) table. $C^\dagger$ is efficiently calculated at run-time using Eq. (4.6). For $j=\{0,1\}$, $h_j(\rho,\ell,\tau)$ Eq. (4.1) is evaluated at run-time. Still, the prodedure discussed above significantly reduces the amount of run-time computation. $h_j(\rho,\ell,\tau)$ is tabled for $2 \le j \le j_{\max}$, where typically $j_{\max} \approx 2000$ (approximately the number of bilayers in the sample).

In Figs. 4.2 and 4.3, Eqs. (4.2) and (4.9) are quantitatively compared, where

$$\Delta h_j(\rho,\ell,\tau') \equiv \left| 1 - \frac{h_j(\rho,\ell,\tau=\pi^2/2) + \frac{D^2\eta}{2\pi^2} C^\dagger(\tau=\pi^2/2,\tau',\ell)}{h_j(\rho,\ell,\tau')} \right| \tag{4.10}$$

is the relative error of neglecting C^*. For all comparisons, $\rho = 0$ is chosen because that maximizes C^* and therefore provides an upper bound on $\rho > 0$ as well as $j > 2$. Values of $\tau = \pi^2/2$ and $\tau' = 50$ were chosen. In Fig. 4.2, $\Delta h_j(\rho,\ell,\tau')$ Eq. (4.10) is plotted as a function of ℓ. Clearly C^* is most significant for $\ell = 2$, an upper bound on ℓ assuming $\xi_\theta \le \xi$. Typically, $\xi_\theta < \xi$ and $\ell \approx 0.1$. Next, $\Delta h_j(\rho,\ell,\tau')$ Eq. (4.10) is plotted in Fig. 4.3 as a function of j for $\ell = 2$ or 0 . For $j > 1$, C^* is neglected with errors $< 10^{-3}$.

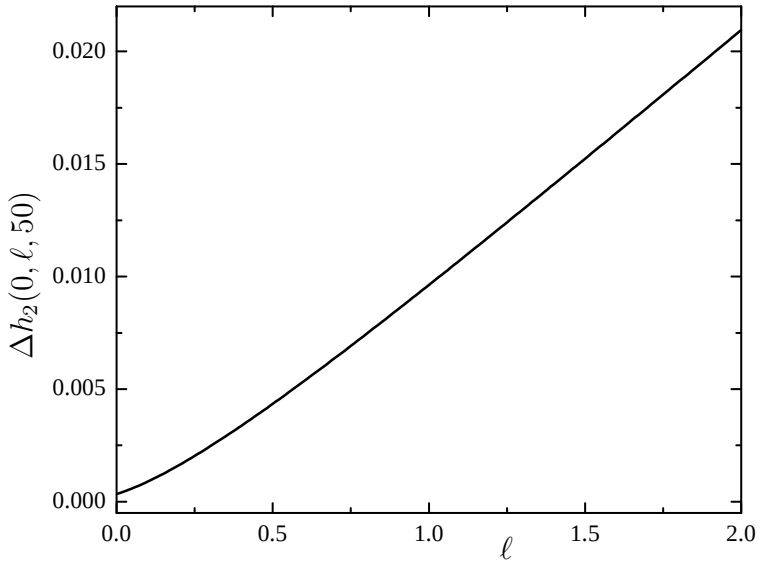


Figure 4.2: The relative error of neglecting C^* as a function of ℓ.

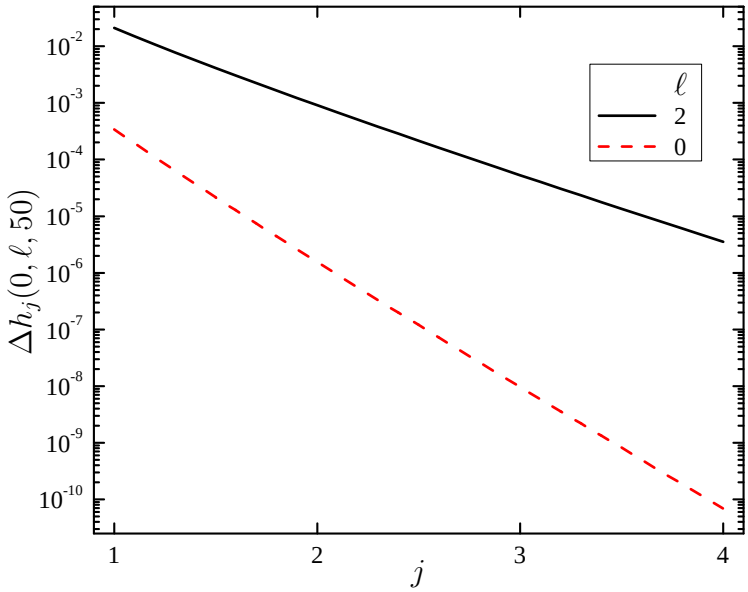


Figure 4.3: The relative error of neglecting C^* as a function of j for $\ell = 2$ (black solid line) and $\ell = 0$ (red dashed line). The solid and dashed lines are upper and lower bounds, respectively, for the relative error. Even though it is a postive integer, j has been plotted as if it is a continuous variable.

4.2 Analytic Approximation of $h_j(\rho, \ell, \tau)$

An analytic approximation for $h_j(\rho, \ell, \tau)$ for $\rho \gg 1$ is derived to reduce the dimensions of the (ρ, ℓ, j) table and to compare to the tilt-independent analytic approximation, see Eq. (4.54) for the final result. Starting from $h_j(\rho, \ell, \tau)$ Eq. (4.1),

$$\tilde{h}_j(\rho, \ell, \tau) \equiv h_j(\rho \gg 1, \ell, \tau) \tag{4.11}$$

$$= \frac{D^2\eta}{2\pi^2} \lim_{\epsilon \to 0} (I_1 - I_2), \tag{4.12}$$

where

$$I_1(\ell, \tau; \epsilon) \equiv \int_\epsilon^\tau \mathrm{d}v \, \frac{1}{\sqrt{\frac{v^2}{1+v\ell} + \left(\frac{v^2}{1+v\ell}\right)^2}} \tag{4.13}$$

and

$$I_2(\rho, \ell, \tau, j; \epsilon) \equiv \int_\epsilon^\tau \mathrm{d}v \, \frac{J_0\left(\sqrt{2v}\rho\right)\left(\sqrt{1 + \frac{v^2}{1+v\ell}} - \frac{v}{\sqrt{1+v\ell}}\right)^{2j}}{\sqrt{\frac{v^2}{1+v\ell} + \left(\frac{v^2}{1+v\ell}\right)^2}}. \tag{4.14}$$

I_1 Eq. (4.13) is evaluated analytically,

$$I_1(\ell, \tau; \epsilon) = \ln\left(\frac{\tau[\ell + 2\tau + 2f_c(\tau)]^\ell}{2 + \ell\tau + 2f_c(\tau)}\right) - \ln\left(\frac{\epsilon[\ell + 2\epsilon + 2f_c(\epsilon)]^\ell}{2 + \ell\epsilon + 2f_c(\epsilon)}\right), \tag{4.15}$$

where $f_c(x) = \sqrt{1 + \ell x + x^2}$. Moving on to I_2 Eq. (4.14) for $\rho \gg 1$, the contribution to I_2 is mainly for $v \ll 1$ because of the increasingly oscillatory nature of the Bessel function. For $v \ll 1$,

$$\sqrt{\frac{v^2}{1+v\ell} + \left(\frac{v^2}{1+v\ell}\right)^2} \approx v. \tag{4.16}$$

For $jv \ll 1$,

$$\left(\sqrt{1+\frac{v^2}{1+v\ell}}-\frac{v}{\sqrt{1+v\ell}}\right)^{2j}\approx\exp\left\{-\frac{2jv}{\sqrt{1+v\ell}}\right\}. \tag{4.17}$$

For $v\ell \ll 1$,

$$\exp\left\{-\frac{2jv}{\sqrt{1+v\ell}}\right\}\approx e^{j\ell v^2}e^{-2jv} \tag{4.18}$$

$$\approx \left(1+j\ell v^2\right)e^{-2jv}. \tag{4.19}$$

Substituting Eqs. (4.16), (4.17), and (4.19) into I_2 Eq. (4.14),

$$I_2 \approx I_{2\mathrm{a}} \equiv \int_\epsilon^\tau \mathrm{d}v\ \frac{(1+j\ell v^2)e^{-2jv}J_0\left(\sqrt{2v}\rho\right)}{v}. \tag{4.20}$$

For $v \gg 1$, the integrand of Eq. (4.20) rapidly decays,

$$\propto \begin{cases} v^{-5/4}, & j=0 \\ v^{3/4}e^{-2jv}, & j>0 \end{cases}, \tag{4.21}$$

and therefore, the upper limit of integration is extended to ∞.

$$I_{2\mathrm{a}}(\rho,\ell,\tau,j;\epsilon) \approx I_{2\mathrm{b}}(\rho,\ell,j;\epsilon) \equiv \int_\epsilon^\infty \mathrm{d}v\ \frac{(1+j\ell v^2)e^{-2jv}J_0\left(\sqrt{2v}\rho\right)}{v}. \tag{4.22}$$

Note, Eq. (4.22) is reasonable for $j > 0$. After completing the derivation of the $j > 0$ analytic approximation, the special case of $j = 0$ is discussed, see Eq. (4.48). Replacing $J_0\left(\sqrt{2v}\rho\right)$ in Eq. (4.22) with its Taylor series about $v = 0$,

$$I_{2\mathrm{b}} = \int_\epsilon^\infty \mathrm{d}v\ \frac{(1+j\ell v^2)\, e^{-2jv}}{v} \sum_{k=0}^{\infty} \frac{(-1)^k}{(k!)^2} \left(\frac{\sqrt{2v}\rho}{2}\right)^{2k} \tag{4.23}$$

$$= \sum_{k=0}^{\infty} (-1)^k \left(\frac{\rho}{\sqrt{2}}\right)^{2k} \left(\int_\epsilon^\infty \mathrm{d}v\ \frac{v^{k-1}e^{-2jv}}{(k!)^2} + j\ell \int_\epsilon^\infty \mathrm{d}v\ \frac{v^{k+1}e^{-2jv}}{(k!)^2} \right). \tag{4.24}$$

Substituting $y = 2jv$,

$$I_{2\mathrm{b}}(\rho, \ell, j > 0; \epsilon)$$
$$= \sum_{k=0}^{\infty} (-1)^k \left(\frac{\rho}{\sqrt{2}}\right)^{2k} \frac{1}{(2j)^k} \left(\int_{2j\epsilon}^\infty \mathrm{d}y\ \frac{y^{k-1}e^{-y}}{(k!)^2} + \frac{\ell}{4j} \int_{2j\epsilon}^\infty \mathrm{d}y\ \frac{y^{k+1}e^{-y}}{(k!)^2} \right). \tag{4.25}$$

First, the $k = 0$ term $I_{2\mathrm{b}.1}$ in $I_{2\mathrm{b}}$ Eq. (4.25) is evaluated,

$$I_{2\mathrm{b}.1} \equiv \int_{2j\epsilon}^\infty \mathrm{d}y\ e^{-y} \left(\frac{1}{y} + \frac{\ell y}{4j}\right) = E_1(2j\epsilon) + \frac{\ell}{4j}(1+2j\epsilon)e^{-2j\epsilon}, \tag{4.26}$$

where $E_1(x)$ is the exponential integral. Moving on to the $k \neq 0$ terms in $I_{2\mathrm{b}.2}$ Eq. (4.25) and allowing $\epsilon \to 0$,

$$I_{2\mathrm{b}.2} \equiv \sum_{k=1}^{\infty} \frac{(-1)^k}{(k!)^2} \left(\frac{\rho^2}{4j}\right)^k \left(\int_0^\infty \mathrm{d}y\ y^{k-1}e^{-y} + \frac{\ell}{4j} \int_0^\infty \mathrm{d}y\ y^{k+1}e^{-y} \right) \tag{4.27}$$

$$= \sum_{k=1}^{\infty} \frac{(-1)^k}{(k!)^2} \left(\frac{\rho^2}{4j}\right)^k \left(\Gamma(k) + \frac{\ell}{4j}\Gamma(k+2) \right). \tag{4.28}$$

Using $\Gamma(t+1) = t\Gamma(t)$ and $\Gamma(t) = (t-1)!$ if t is a positive integer, Eq. (4.28) is further rewritten,

$$I_{2\text{b}.2} = \sum_{k=1}^{\infty} \frac{(-1)^k}{(k!)^2} \left(\frac{\rho^2}{4j}\right)^k \left(\Gamma(k) + \frac{\ell}{4j} k(k+1)\Gamma(k)\right) \tag{4.29}$$

$$= \sum_{k=1}^{\infty} \frac{(-1)^k}{(k!)^2} (k-1)! \left(\frac{\rho^2}{4j}\right)^k \left(1 + \frac{\ell}{4j} k(k+1)\right) \tag{4.30}$$

$$= \sum_{k=1}^{\infty} \frac{(-1)^k}{k(k!)} \left(\frac{\rho^2}{4j}\right)^k \left(1 + \frac{\ell}{4j} k(k+1)\right). \tag{4.31}$$

Using,

$$\sum_{k=1}^{\infty} \frac{(-1)^k}{k(k!)} x^k = -\gamma - \ln x - E_1(x), \tag{4.32}$$

$$\sum_{k=1}^{\infty} \frac{(-x)^k}{k!} = e^{-x} - 1, \tag{4.33}$$

and

$$\sum_{k=1}^{\infty} k \frac{(-x)^k}{k!} = -xe^{-x} \tag{4.34}$$

where γ is the Euler-Mascheroni constant, $I_{2\text{b}.2}$ Eq. (4.31) is expressed as

$$I_{2\text{b}.2} = \sum_{k=1}^{\infty} \frac{(-1)^k}{k(k!)} \left(\frac{\rho^2}{4j}\right)^k \left(1 + \frac{\ell}{4j} k(k+1)\right) \tag{4.35}$$

$$= -\gamma - \ln\left(\frac{\rho^2}{4j}\right) - E_1\left(\frac{\rho^2}{4j}\right) + \frac{\ell}{4j}(-xe^{-x} + e^{-x} - 1), \tag{4.36}$$

where $x = \rho^2/4j$. Adding $I_{2\text{b}.1}$ Eq. (4.26) and $I_{2\text{b}.2}$ Eq. (4.36), I_{2b} Eq. (4.25) is written

$$I_{2\text{b}} = E_1(2j\epsilon) + \frac{\ell}{4j}(1 + 2j\epsilon)e^{-2j\epsilon} - \gamma - \ln\left(\frac{\rho^2}{4j}\right) - E_1\left(\frac{\rho^2}{4j}\right) + \frac{\ell}{4j}(-xe^{-x} + e^{-x} - 1). \tag{4.37}$$

Returning to $\tilde{h}_j(\rho, \ell, \tau)$ Eq. (4.12) and using I_1 Eq. (4.15) and $I_{2\text{b}}$ Eq. (4.37),

$$\left(\frac{2\pi^2}{D^2\eta}\right)\tilde{h}_{j>0}(\rho,\ell,\tau) = \lim_{\epsilon\to 0}\Big[I_1(\ell,\tau;\epsilon) - I_{2b}(\rho,\ell,j>0;\epsilon)\Big] \tag{4.38}$$

$$\begin{aligned}
&\approx \ln\left(\frac{\tau[\ell+2\tau+2f_c(\tau)]^\ell}{2+\ell\tau+2f_c(\tau)}\right) \\
&\quad - \lim_{\epsilon\to 0}\left[\ln\left(\frac{\epsilon[\ell+2\epsilon+2f_c(\epsilon)]^\ell}{2+\ell\epsilon+2f_c(\epsilon)}\right) + E_1(2j\epsilon) + \frac{\ell}{4j}(1+2j\epsilon)e^{-2j\epsilon}\right] \\
&\quad + \gamma + \ln\left(\frac{\rho^2}{4j}\right) + E_1\left(\frac{\rho^2}{4j}\right) + \frac{\ell}{4j}(xe^{-x} - e^{-x} + 1).
\end{aligned} \tag{4.39}$$

Focusing on the ϵ-dependent terms in Eq. (4.39),

$$\begin{aligned}
&\lim_{\epsilon\to 0}\left[\ln\left(\frac{\epsilon[\ell+2\epsilon+2f_c(\epsilon)]^\ell}{2+\ell\epsilon+2f_c(\epsilon)}\right) + E_1(2j\epsilon) + \frac{\ell}{4j}(1+2j\epsilon)e^{-2j\epsilon}\right] \\
&= \lim_{\epsilon\to 0}\left[\ln\left(\frac{\epsilon[\ell+2\epsilon+2f_c(\epsilon)]^\ell}{2+\ell\epsilon+2f_c(\epsilon)}\right) - \ln(2j\epsilon) - \sum_{k=1}^{\infty}\frac{(-2j\epsilon)^k}{k(k!)}\right] - \gamma + \frac{\ell}{4j} \qquad (4.40) \\
&= \lim_{\epsilon\to 0}\left[\ln\left(\frac{[\ell+2\epsilon+2f_c(\epsilon)]^\ell}{2j[2+\ell\epsilon+2f_c(\epsilon)]}\right)\right] - \gamma + \frac{\ell}{4j} \qquad (4.41) \\
&= \ln\left(\frac{(\ell+2)^\ell}{8j}\right) - \gamma + \frac{\ell}{4j}, \qquad (4.42)
\end{aligned}$$

where

$$E_1(x) = -\gamma - \ln x - \sum_{k=1}^{\infty}\frac{(-1)^k}{k(k!)}x^k \tag{4.43}$$

was used to obtain the second line, see Eq. (4.32). Substituting Eq. (4.42) into Eq. (4.39),

$$\left(\frac{2\pi^2}{D^2\eta}\right)\tilde{h}_{j>0}(\rho,\ell,\tau)$$
$$\approx \ln\left(\frac{\tau[\ell+2\tau+2f_c(\tau)]^\ell}{2+\ell\tau+2f_c(\tau)}\right)-\ln\left(\frac{(\ell+2)^\ell}{8j}\right)+2\gamma-\frac{\ell}{4j}+\ln\left(\frac{\rho^2}{4j}\right)+E_1\left(\frac{\rho^2}{4j}\right)$$
$$+\frac{\ell}{4j}(xe^{-x}-e^{-x}+1) \tag{4.44}$$
$$=\ln\left(\frac{\tau[\ell+2\tau+2f_c(\tau)]^\ell}{2+\ell\tau+2f_c(\tau)}\right)-\ln\left(\frac{(\ell+2)^\ell}{2}\right)+2\gamma+\ln(\rho^2)+E_1\left(\frac{\rho^2}{4j}\right)$$
$$+\frac{\ell}{4j}\left(\frac{\rho^2}{4j}-1\right)\exp\left\{-\frac{\rho^2}{4j}\right\}. \tag{4.45}$$

The final ρ-dependent term in Eq. (4.45),

$$\frac{\ell}{4j}\left(\frac{\rho^2}{4j}-1\right)\exp\left\{-\frac{\rho^2}{4j}\right\}, \tag{4.46}$$

is always a small contribution. Neglecting it, Eq. (4.45) is simplified

$$\tilde{h}_{j>0}(\rho,\ell,\tau)$$
$$\approx \frac{D^2\eta}{2\pi^2}\left[E_1\left(\frac{\rho^2}{4j}\right)+\ln\left(\rho^2\right)+2\gamma+\ln\left(\frac{\tau[\ell+2\tau+2f_c(\tau)]^\ell}{2+\ell\tau+2f_c(\tau)}\right)-\ln\left(\frac{(\ell+2)^\ell}{2}\right)\right]. \tag{4.47}$$

To complete the derivation of the $\rho \gg 1$ analytic approximation of $h_j(\rho,\ell,\tau)$, the special case of $j=0$ is considered. Returning to I_{2b} Eq. (4.22) for $j=0$,

$$I_{2\mathrm{b}}(\rho,\ell,j=0;\epsilon)=\int_\epsilon^\infty \mathrm{d}v\ \frac{J_0\left(\sqrt{2v}\rho\right)}{v}, \tag{4.48}$$

Substituting $y=\sqrt{2v}\rho$,

$$I_{2\mathrm{b}}(\rho,\ell,0;\epsilon) = 2\int_{\sqrt{2\epsilon}\rho}^{\infty} \mathrm{d}y\ \frac{J_0(y)}{y} \tag{4.49}$$

$$= -2\gamma - \ln(\rho^2) - \ln\left(\frac{\epsilon}{2}\right) + 2\int_0^{\sqrt{2\epsilon}\rho} \mathrm{d}y\ \frac{1-J_0(y)}{y}, \tag{4.50}$$

where Eq. (4.50) follows from a formula found in Abramowitz and Stegun [71], (11.1.20). Finally, substituting I_1 Eq. (4.15) and $I_{2\mathrm{b}}$ Eq. (4.50) into Eq. (4.12)

$$\left(\frac{2\pi^2}{D^2\eta}\right)\tilde{h}_0(\rho,\ell,\tau)$$

$$= \lim_{\epsilon\to 0}\Big[I_1(\ell,\tau;\epsilon) - I_{2b}(\rho\gg 1,\ell,0;\epsilon)\Big] \tag{4.51}$$

$$\approx \ln\left(\frac{\tau[\ell+2\tau+2f_c(\tau)]^\ell}{2+\ell\tau+2f_c(\tau)}\right) + 2\gamma + \ln\left(\rho^2\right)$$

$$- \lim_{\epsilon\to 0}\left[\ln\left(\frac{\epsilon[\ell+2\epsilon+2f_c(\epsilon)]^\ell}{2+\ell\epsilon+2f_c(\epsilon)}\right) - \ln\left(\frac{\epsilon}{2}\right) + 2\int_0^{\sqrt{2\epsilon}\rho}\mathrm{d}y\frac{1-J_0(y)}{y}\right] \tag{4.52}$$

$$= \ln\left(\rho^2\right) + 2\gamma + \ln\left(\frac{\tau[\ell+2\tau+2f_c(\tau)]^\ell}{2+\ell\tau+2f_c(\tau)}\right) - \ln\left(\frac{(\ell+2)^\ell}{2}\right). \tag{4.53}$$

$\tilde{h}_{j>0}(\rho,\ell,\tau)$ and $\tilde{h}_0(\rho,\ell,\tau)$ are combined since for $j=0$, $E_1(\rho^2/4j)=0$. Therefore, using Eqs. (4.47) and (4.53), the analytic approximation is compactly expressed as

$$\tilde{h}_j(\rho,\ell,\tau) = \tilde{h}_j^{\cancel{\mathrm{tilt}}}(\rho) + \frac{D^2\eta}{2\pi^2}\Lambda(\ell,\tau), \tag{4.54}$$

where

$$\Lambda(\ell,\tau) \equiv \ln\left(\frac{\tau[\ell+2\tau+2f_c(\tau)]^\ell}{2+\ell\tau+2f_c(\tau)}\right) - \ln\left(\frac{(\ell+2)^\ell}{2}\right) \tag{4.55}$$

and $\tilde{h}_j^{\cancel{\mathrm{tilt}}}(\rho)$ is the tilt-independent analytic approximation,

$$\tilde{h}_j^{\cancel{\mathrm{tilt}}}(\rho) \equiv \frac{D^2\eta}{2\pi^2}\left[E_1\left(\frac{\rho^2}{4j}\right) + \ln\left(\rho^2\right) + 2\gamma\right]. \tag{4.56}$$

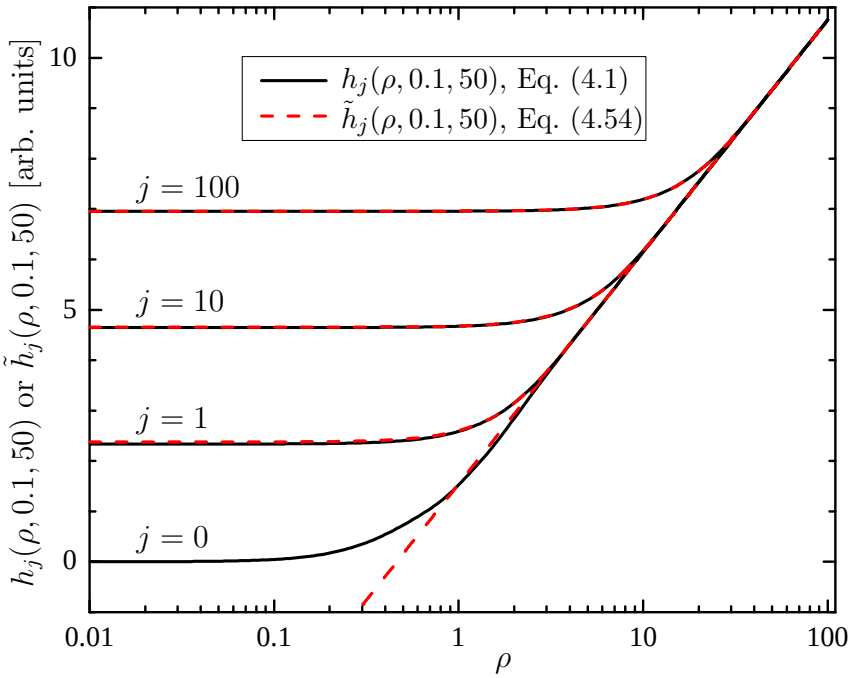


Figure 4.4: $h_j(\rho, \ell, \tau)$ and its analytic approximation $\tilde{h}_j(\rho, \ell, \tau)$ are plotted as functions of ρ for several j and $\ell = 0.1$. $\tilde{h}_j(\rho, \ell, \tau)$ is a good approximation for $\rho \gg 1$.

In the limit $\ell \to 0$ and $\tau \to \infty$, $\Lambda(\ell, \tau) \to 0$, and $\tilde{h}_j(\rho, \ell, \tau) \to \tilde{h}_j(\rho)^{\cancel{\text{tilt}}}$. The ρ-dependence of the tilt-dependent and -independent theories is approximately the same. The lowest order ρ-dependent correction to $\tilde{h}_j(\rho, \ell, \tau)$ was neglected, see Eq. (4.46). The primary effect of including tilt is to contribute the additive factor

$$\frac{D^2\eta}{2\pi^2}\Lambda(\ell, \tau). \tag{4.57}$$

Fig. 4.4 (plotted again for convenience from the beginning of the chapter) and Fig. 4.5 show $h_j(\rho, \ell, \tau)$ Eq. (4.1) and $\tilde{h}_j(\rho, \ell, \tau)$ Eq. (4.54) for various j-values and $\ell = 0.1$ and $\ell = 2$, respectively. $\ell \approx 0.1$ and $\tau \approx 50$ are typical values, and $\ell = 2$ is the largest reasonable ℓ-value. Figs. 4.6 and 4.7 show the relative error of $h_j(\rho, \ell, \tau)$ and $\tilde{h}_j(\rho, \ell, \tau)$. $\tilde{h}_j(\rho, \ell, \tau)$ is used to approximate $h_j(\rho, \ell, \tau)$ for $\rho > 10$, where the relative error is less than 10^{-3} for $\ell \leq 2$.

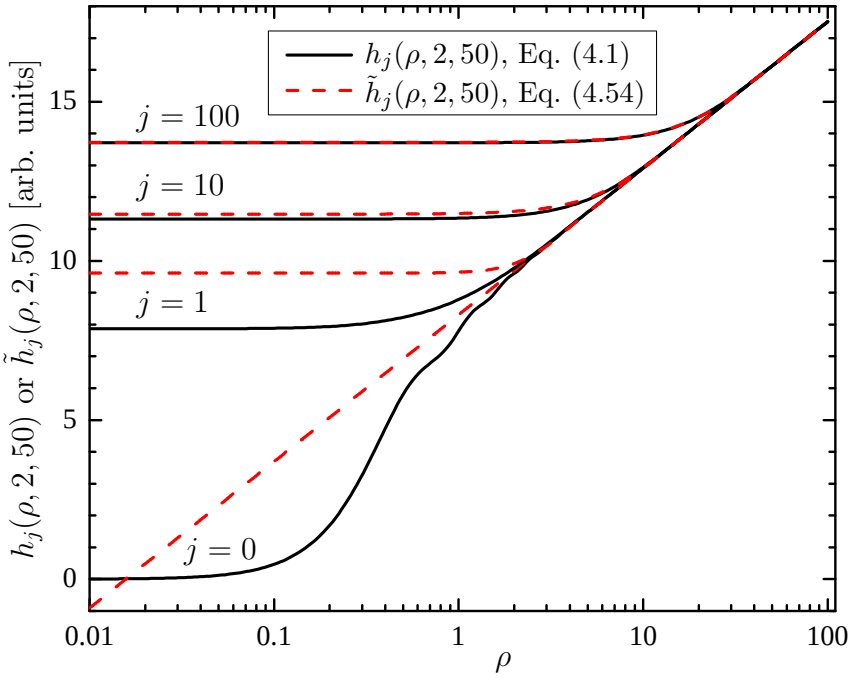


Figure 4.5: $h_j(\rho,\ell,\tau)$ and its analytic approximation $\tilde{h}_j(\rho,\ell,\tau)$ are plotted as functions of ρ for several j and $\ell = 2$. $\tilde{h}_j(\rho,\ell,\tau)$ is a good approximation for $\rho \gg 1$. The small amplitude oscillations in $h_0(\rho,\ell,\tau)$ are caused by the interplay between ξ and ξ_θ.

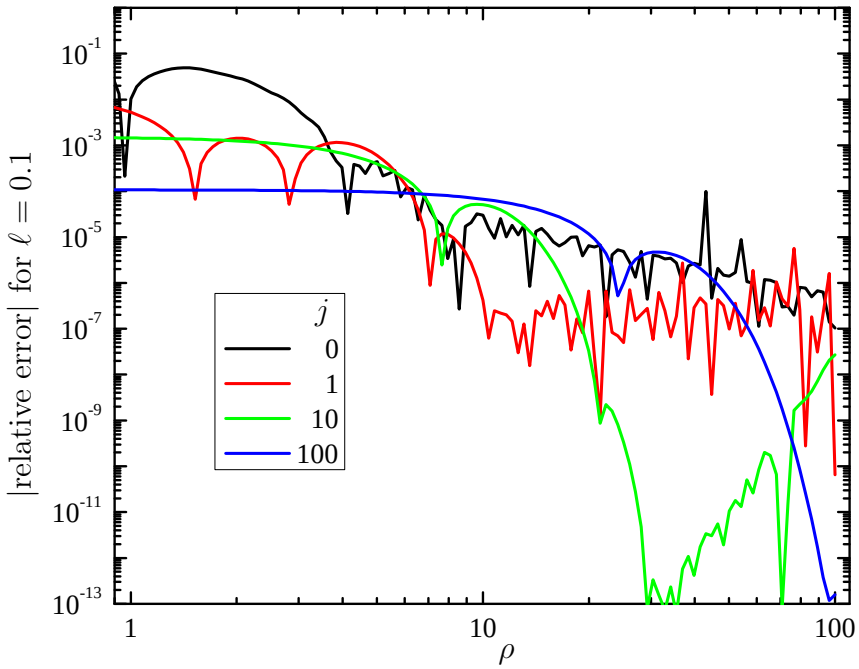


Figure 4.6: The relative error of $h_j(\rho, \ell, \tau)$ and $\tilde{h}_j(\rho, \ell, \tau)$ is plotted as a function of ρ for several j and $\ell = 0.1$. The jagged features of the curves are likely numerical artifacts.

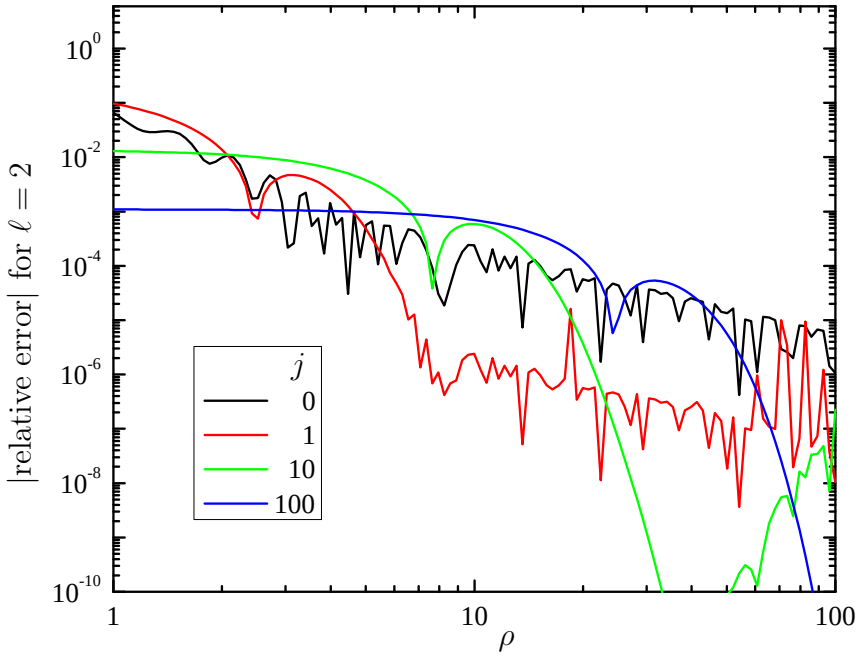


Figure 4.7: The relative error of $h_j(\rho, \ell, \tau)$ and $\tilde{h}_j(\rho, \ell, \tau)$ is plotted as a function of ρ for several j and $\ell = 2$. The jagged features of the curves are likely numerical artifacts.

4.3 Difference of Tilt-dependent and -independent Height-Height Correlations

In Section 4.2 it was shown that in the limit $\rho \gg 1$ the difference between tilt-dependent and -independent height-height correlation functions is approximately, $\frac{D^2\eta}{2\pi^2}\Lambda(\ell,\tau)$, see Eq. (4.54). Below, it is shown that in the limit $j \gg 1$, the difference between tilt-dependent and -independent correlation functions is also $\frac{D^2\eta}{2\pi^2}\Lambda(\ell,\tau)$. Using $h_j(\rho,\ell,\tau)$ Eq. (4.1),

$$\frac{D^2\eta}{2\pi^2}\Lambda'(\ell,\tau) \equiv \lim_{j\gg 1}\left[h_j(\rho,\ell,\tau) - h_j^{\cancel{\text{tilt}}}(\rho)\right] \tag{4.58}$$

$$= \lim_{j\gg 1}\left[h_j(\rho,\ell,\tau) - h_j(\rho,0,\tau)\right] \tag{4.59}$$

$$\Rightarrow \Lambda'(\ell,\tau) = \lim_{j\gg 1}\left[\int_0^\tau \mathrm{d}v\ \frac{1-J_0\left(\sqrt{2v}\rho\right)\left(\sqrt{1+\frac{v^2}{1+v\ell}}-\frac{v}{\sqrt{1+v\ell}}\right)^{2|j|}}{\frac{v}{\sqrt{1+v\ell}}\sqrt{1+\frac{v^2}{1+v\ell}}}\right. \tag{4.60}$$

$$\left. - \int_0^\tau \mathrm{d}v\ \frac{1-J_0\left(\sqrt{2v}\rho\right)\left(\sqrt{1+v^2}-v\right)^{2|j|}}{v\sqrt{1+v^2}}\right]. \tag{4.61}$$

The terms raised to the $2|j|$ decay very rapidly as functions of v, and decay increasingly rapidly for increasing j. Therefore the aforementioned terms are neglected in the limit $j \gg 1$. Simplifying Λ' Eq. (4.61),

$$\Lambda'(\ell,\tau) = \int_0^\tau \mathrm{d}v\ \left(\frac{1}{\frac{v}{\sqrt{1+v\ell}}\sqrt{1+\frac{v^2}{1+v\ell}}} - \frac{1}{v\sqrt{1+v^2}}\right) \tag{4.62}$$

$$= \left[\ln\left(\frac{[\ell+2v+2f_c(v)]^\ell}{2+\ell x+2f_c(v)}\right)+\ln\left(1+\sqrt{1+v^2}\right)\right]\Bigg|_0^\tau \tag{4.63}$$

$$= \ln\left(\frac{[\ell+2\tau+2f_c(\tau)]^\ell}{2+\ell\tau+2f_c(\tau)}\right)+\ln\left(1+\sqrt{1+\tau^2}\right)-\ln\left(\frac{(\ell+2)^\ell}{8}\right) \tag{4.64}$$

$$\approx \ln\left(\frac{\tau[\ell+2\tau+2f_c(\tau)]^\ell}{2+\ell\tau+2f_c(\tau)}\right)-\ln\left(\frac{(\ell+2)^\ell}{8}\right) \tag{4.65}$$

$$= \Lambda(\ell,\tau). \tag{4.66}$$

Λ' Eq. (4.65) is the same as Λ Eq. (4.55). For $j \gg 1$ or $\rho \gg 1$, the difference of tilt-dependent and -independent height-height correlation functions is approximately a constant.

It can be shown that adding a constant (such as Λ) to the height-height correlation function has a predictable influence on the predicted scattering intensity, see Appendix D.1 for an analogous argument regarding a different issue, and that this influence can not be used to differentiate tilt-dependent and -independent models. Therefore as expected, the most significant difference between tilt-dependent and -independent height-height correlation functions occur for $j \sim 1$ and $\rho \ll 1$.

4.4 Corresponding Caillé Exponents

Previous researchers have used the $\rho \gg 1$ tilt-independent approximation of the height-height correlation function $\tilde{h}_j^{\cancel{\text{tilt}}}(\rho)$ Eq. (4.56) to interpret scattering from smectic liquid crystals [42, 37]. Consequently, the corresponding analytic approximation of the tilt-dependent height-height correlation function $\tilde{h}_j(\rho, \ell, \tau)$ Eq. (4.54) is important in order to allow comparison with previous work. Quasi-long range order in smectic A liquid crystals was first established by analyzing X-ray scattering. Considering a continuous infinite smectic liquid crystal, Caillé predicted that the out-of-plane X-ray peaks have power-law tails, a consequence of the logarithmic divergence for increasing ρ of $\tilde{h}_j^{\cancel{\text{tilt}}}(\rho)$ Eq. (4.56). The predicted power law tails are

$$S\left(q_r, 2\pi h/D\right) \propto q_r^{-(4-2\eta_h)} \tag{4.67}$$

$$S\left(0, \Delta q_{z,h}\right) \propto \Delta q_{z,h}^{-(2-\eta_h)}, \tag{4.68}$$

where

$$\eta_h \equiv h^2 \eta, \tag{4.69}$$

$$\Delta q_{z,h} \equiv q_z - q_{z,h}, \tag{4.70}$$

and $q_{z,h}$ is the q_z-position of the hth out-of-plane Caillé peak. h is a positive integer that indexes the out-of-plane peaks. Later, Als Nielsen *et al.* experimentally observed

the aforementioned power-law tails, verifying Caillé's predictions [42]. In 1988-89, it was shown that the scattering from a stack of lipid bilayers is also well described by smectic liquid crystal theory [36, 37]. Finally, Ning Lei derived that the power-law exponents for a smectic free energy, discrete in the z-direction, are the same as predicted by Caillé [56, 55].

In Section 4.2, it was shown that $\tilde{h}_j(\rho, \ell, \tau)$ and $\tilde{h}_j^{\cancel{\text{tilt}}}(\rho)$ have approximately the same ρ-dependence. Therefore, the scattering power law exponents derived by Lei and Caillé are negligibly modified by considering tilt. Consequently, previous measurements focused on the scattering intensity in the tails of the Caillé peaks can not be meaningfully reanalyzed to obtain tilt-associated information. The effect of considering tilt is to modify the height-height spectrum for large Q_r, short real-space length scales (see Section 3.3.2). Therefore as expected, the $r \gg \xi$ analytic approximation of $h_j(\rho, \ell, \tau)$ and related predicted scattering peak power-law exponents are insignificantly influenced by including tilt.

Chapter 5

Predicted Experimental Scattering Intensity

The theoretical scattering intensity from stacked lipid bilayers was introduced in Section 3.2.2. The measured intensity differs from the theoretical scattering intensity because of several sample-dependent and experimental issues. The sample-dependent effects are discussed first, followed by the experimental ones. First in Section 5.1, the theoretical structure factor $S(\mathbf{q})$ is rewritten in cylindrical coordinates, assuming that the scattering intensity from the sample is the incoherent sum of scattering from sample subvolumes of cylindrical shape. Next in Section 5.2, the effects of domain mosaicity are briefly reviewed, finishing the derivation of the predicted scattering from multidomain stacked bilayers.

The effects of experimental issues on the predicted scattering intensity are discussed in Section 5.3. First the scattering geometry is described in Subsection 5.3.1. In Subsection 5.3.2 the X-ray beam's coherence is defined, and the sample coherence volume is derived. Then in Subsection 5.3.3, the beam shape on the detector is modeled. In Subsection 5.3.4 absorption effects are discussed, completing the derivation of the predicted scattering intensity for a fixed incident angle X-ray exposure. For most low angle X-ray scattering data, the incident angle is continuously varied during an exposure. Therefore, the fixed angle exposure prediction is integrated over all relevant incident angles in Subsection 5.3.5.

Since the current work can be viewed as an extension of previous research and fitting software (NFIT) [48, 46], many issues in this chapter are compared to the prior work.

5.1 Structure Factor for Cylindrical Subvolumes

In Lyatskaya *et al.* [44], the structure factor $S(\mathbf{q})$ Eq. (3.37) was presented in cylindrical coordinates. Later, $S(\mathbf{q})$ was expressed in Cartesian coordinates, motivated by the consideration of X-ray coherence issues [48, 46] (see Section 5.3.2) and assuming rectangular cuboid domains. Appendix B further discusses $S(\mathbf{q})$ in Cartesian coordinates and shows that the predicted scattering from rectangular cuboid domains includes features that are not experimentally observed. Therefore, $S(\mathbf{q})$ is expressed in cylindrical coordinates.

In Section 3.2.2, the scattering intensity was decomposed into the sum of two terms, see Eq. (3.28),

$$I(\mathbf{q}) \approx F_{\Delta}(q_z) S_0(\mathbf{q}) + |F(q_z)|^2 S(\mathbf{q}), \tag{5.1}$$

where

$$S(\mathbf{q}) = \sum_{j,j'} \int\int \mathrm{d}^2\mathbf{r}\ \mathrm{d}^2\mathbf{r}'\ e^{iq_z(j-j')D + i\mathbf{q}_\mathbf{r}\cdot(\mathbf{r}-\mathbf{r}')} e^{-\frac{q_z^2}{2}\left\langle\left[z_j^+(\mathbf{r}) - z_{j'}(\mathbf{r}')\right]^2\right\rangle} \tag{5.2}$$

$$= \sum_{j,j'} \int\int \mathrm{d}^2\mathbf{r}\ \mathrm{d}^2\mathbf{r}'\ e^{iq_z(j-j')D + i\mathbf{q}_\mathbf{r}\cdot(\mathbf{r}-\mathbf{r}')} G(\mathbf{r}, \mathbf{r}', j, j', q_z) \tag{5.3}$$

$$S_0(\mathbf{q}) = \sum_{j} \int\int \mathrm{d}^2\mathbf{r}\ \mathrm{d}^2\mathbf{r}'\ e^{i\mathbf{q}_\mathbf{r}\cdot(\mathbf{r}-\mathbf{r}')} G(\mathbf{r}, \mathbf{r}', 0, 0, q_z) \tag{5.4}$$

$$= \sum_{j,j'} \delta_{j,j'} \int\int \mathrm{d}^2\mathbf{r}\ \mathrm{d}^2\mathbf{r}'\ e^{i\mathbf{q}_\mathbf{r}\cdot(\mathbf{r}-\mathbf{r}')} G(\mathbf{r}, \mathbf{r}', j, j', q_z). \tag{5.5}$$

$G(\mathbf{r}, \mathbf{r}', j, j', q_z)$ is the pair scattering correlation function, and $\delta_{j,j'}$ is the Kronecker delta function. Since $S_0(\mathbf{q})$ Eq. (5.5) is a special case of $S(\mathbf{q})$ Eq. (5.3), the following derivations only involve $S(\mathbf{q})$. Using Eq. (5.3) and following similar previous work [44], $S(\mathbf{q})$ of a cylindrically symmetric single domain (SD) composed of J layers with diameter L_r is expressed as

$$S_{\mathrm{SD}}(q_r, q_z; L_r, J) \equiv \sum_{j,j'=0}^{J-1} e^{iq_z(j-j')D} \int_{|r|,|r'|\leq L_r/2} \mathrm{d}^2\mathbf{r}\ \mathrm{d}^2\mathbf{r}'\ e^{i\mathbf{q}_\mathbf{r}\cdot(\mathbf{r}-\mathbf{r}')} G(\mathbf{r}, \mathbf{r}', j, j', q_z). \tag{5.6}$$

Since the height-height correlations only depend on the in-plane magnitude r and the out-of-plane distance $|j - j'|D$ (translational invariance), the pair scattering correlation function G in Eq. (5.6) is more simply expressed,

$$G(\mathbf{r}, \mathbf{r}', j, j', q_z) \to G(|\mathbf{r} - \mathbf{r}'|, |j - j'|, q_z) \tag{5.7}$$

$$= G(r, j, q_z). \tag{5.8}$$

Using G Eq. (5.8), S_{SD} Eq. (5.6) is written

$$S_{\mathrm{SD}}(q_r, q_z; L_r, J) = \pi L_r^2 \sum_{j=0}^{J-1}{}' (J - j) \cos(q_z j D) \int_0^{L_r} \mathrm{d}r\ r F_r\left(\frac{r}{L_r}\right) J_0(q_r r)\ G(r, j, q_z), \tag{5.9}$$

where

$$\sum (2 - \delta_{j,0}) = \sum{}' \equiv \begin{cases} \text{multiply element by } 1, & j = 0 \\ \text{multiply element by } 2, & j \neq 0 \end{cases} \tag{5.10}$$

and

$$F_r(x) \equiv \begin{cases} \cos^{-1}(x) - x\sqrt{1 - x^2}\,, & x \leq 1 \\ 0\,, & x > 1, \end{cases} \tag{5.11}$$

accounting for the area overlap of two equal radius circles with centers separated by a fraction of their radius x [72].

Further modeling of the stacked bilayers is affected by both sample attributes and experimental details. The stacked bilayer sample is unlikely to be a single crystal. Due to defects, inhomogeineity, and various other nonidealities, positional correlations generally do not exist between all points in a macroscopic sample. Consequently, the stacked bilayers are assumed to be composed of many cylindrical domains with

characteristic sizes $\mathscr{L}_r$ and $\mathscr{L}_z$. By definition fluctuations in different domains are uncorrelated, and therefore, $\mathscr{L}_r$ and $\mathscr{L}_z$ limit long length scale correlations in the sample. Importantly, the perception of long length scale correlations is influenced by details of the scattering experiment. Only the scattering from points within a sample coherence volume (diameter of $\mathcal{L}_r$ and height $\mathcal{L}_z$) are added coherently, see Section 5.3.2. Therefore, only correlations shorter than $\mathcal{L}_r$ and $\mathcal{L}_z$ are probed during an X-ray scattering experiment. Finally, the scattering from the sample is assumed to be the incoherent sum of scattering from many cylindrical subvolumes. The sizes of the subvolumes are determined by the smaller of the characteristic sample domain sizes ($\mathscr{L}_r$ and $\mathscr{L}_z$) and the sample coherence volume ($\mathcal{L}_r$ and $\mathcal{L}_z$).[13]

Further, the diameter and height of the subvolumes are described by distributions P_r and P_z, respectively. P_r and P_z are assumed to be independent and are unknown. Previously, either Gaussians [38, 44] or exponentials [46, 73] have been used. For upcoming theoretical derivations, only the characteristic length of the distribution is important, the mean or the $1/e$ length for a Gaussian or an exponential, respectively; the particular functional form of P_r and P_z is unimportant. Therefore, the decision to use Gaussian or exponential distributions is postponed (see Section 6.2). Derivations specific to Gaussian and exponential distributions are presented in Sections 5.1.1 and 5.1.2, respectively. From a data fitting perspective, the most significant difference between Gaussian and exponential distributions is the number of required parameters: two for a Gaussian (mean and standard deviation) and one for an exponential ($1/e$ length).

The structure factor of the many domain (MD) sample S_{MD} is expressed as the sum over the single domain S_{SD} Eq. (5.9),

[13] As an illuminating example, the case of an infinite single crystal ($\mathscr{L}_r = \mathscr{L}_z = \infty$) is discussed. By construction, positional correlations persist over the entire crystal. However, an X-ray scattering measurement only probes correlations over length scales less than $\mathcal{L}_r$ and $\mathcal{L}_z$. Therefore, the effective sizes of the cylindrical subvolumes are $\mathcal{L}_r$ and $\mathcal{L}_z$.

$$S_{\mathrm{MD}}(q_r, q_z) \equiv \int_0^\infty \mathrm{d}L_z \; P_z(L_z) \int_0^\infty \mathrm{d}L_r \; P_r(L_r) S_{\mathrm{SD}}(q_r, q_z) \tag{5.12}$$

$$= \int_0^\infty \mathrm{d}L_z \; P_z(L_z) \sum_{j=0}^{J-1}{}' (J-j)\cos(q_z j D) \cdot \int_0^\infty \mathrm{d}L_r \; P_r(L_r) \int_0^{L_r} \mathrm{d}r \; r\pi L_r^2 F_r(r/L_r) J_0(q_r r) G(r, j, q_z). \tag{5.13}$$

The second line of Eq. (5.13) is an example of an iterated integral. The upper limit of the inner r-dependent integral is a function of the integration variable of the outer L_r-dependent integral. The integration order of the two integrals can be reversed if the integration limits are suitably modified. Similarly, the order of the j-dependent sum and L_z-dependent integral can be changed. Exchanging the integrals and modifying their limits, S_{MD} Eq. (5.13) is succinctly written as

$$S_{\mathrm{MD}}(q_r, q_z) = \sum_{j=0}^{\infty}{}' H_z(jD)\cos(q_z j D) \int_0^\infty \mathrm{d}r \; r H_r(r) J_0(q_r r) G(r, j, q_z), \tag{5.14}$$

where

$$H_r(r) = \pi \int_r^\infty \mathrm{d}L_r \; P_r(L_r) L_r^2 F_r(r/L_r) \tag{5.15}$$

and

$$H_z(z) \equiv \int_z^\infty \mathrm{d}L_z \; P_z(L_z)(L_z - z)/D \tag{5.16}$$

are effective in- and out-of-plane finite-size factors, respectively. For completeness, the S_0 analog to S_{MD} Eq. (5.14) is

$$S_{0,\mathrm{MD}}(q_r, q_z) \equiv \sum_{j=0}^{\infty}{}' \delta_{j,0} \, H_z(jD)\cos(q_z j D) \int_0^\infty \mathrm{d}r \; r H_r(r) J_0(q_r r) G(r, j, q_z). \tag{5.17}$$

5.1.1 Gaussian Subvolume Distributions

The mean diameter $\mathfrak{L}_r$ and height $\mathfrak{L}_z$ are determined by the smaller of the domain size ($\mathscr{L}_r$ and $\mathscr{L}_z$) and the sample coherence length ($\mathcal{L}_r$ and $\mathcal{L}_z$), see Eqs. (5.79) and (5.81). Assuming that the X-ray wavepackets are Gaussian, both the in- and out-of-plane coherence length distributions would be Gaussian [74], and Gaussian domain size distributions are reasonable [38],

$$P_r(L_r) \equiv \frac{1}{\sigma_r} \exp\left\{-\left(L_r - \mathfrak{L}_r\right)^2 / 2\sigma_r^2\right\} \tag{5.18}$$

and

$$P_z(L_z) \equiv \frac{1}{\sigma_z \mathfrak{L}_z} \exp\left\{-\left(L_z - \mathfrak{L}_z\right)^2 / 2\sigma_z^2\right\}, \tag{5.19}$$

where σ_r and σ_z are assumed to be constants.

The factor of $\mathfrak{L}_z$ in the denominator of P_z accounts for the fixed number of layers in the sample; $\mathfrak{L}_z^{-1}$ is proportional to the number of subvolumes with height $\mathfrak{L}_z$ in the X-ray illuminated sample volume. Earlier work in this lab also assumed Gaussian distributions [44, 38]. H_z Eq. (5.16) is expressed in terms of tabled functions

$$H_z(z) = \frac{\sqrt{2}}{2D\mathfrak{L}_z}\left[\sqrt{2}\sigma_z \exp\left\{-\left(\frac{z-\mathfrak{L}_z}{\sqrt{2}\sigma_z}\right)^2\right\} + \sqrt{\pi}\left(\mathfrak{L}_z - z\right)\operatorname{erfc}\left(\frac{z-\mathfrak{L}_z}{\sqrt{2}\sigma_z}\right)\right], \tag{5.20}$$

where erfc is the complementary error function

$$\operatorname{erfc}(x) = \frac{2}{\sqrt{\pi}} \int_x^\infty \mathrm{d}u \; e^{-u^2}. \tag{5.21}$$

5.1.2 Exponential Subvolume Distributions

Originally, Gaussian domain size distribution functions were proposed in the modified Caillé theory [38]. Soon afterwards, exponential distribution functions were shown to fit X-ray scattering data from multilamellar vesicles as well as if not better than

Gaussian distributions [73] (see pp. 18-22). Subsequently, exponential distributions were used to describe both the domain size and sample coherence distributions [48, 46].

The exponential analogs to Eqs. (5.18) and (5.19) are

$$P'_r(L_r) \equiv \frac{1}{\mathfrak{L}_r}\exp\left\{-L_r/\mathfrak{L}_r\right\} \tag{5.22}$$

and

$$P'_z(L_z) \equiv \frac{1}{\mathfrak{L}_z^2}\exp\left\{-L_z/\mathfrak{L}_z\right\}. \tag{5.23}$$

The second factor of $\mathfrak{L}_z$ in the denominator of P'_z accounts for the fixed number of layers in the sample. Since the exponential distributions are peaked at 0, a significant fraction of the domains are too small for the correlation functions to be reasonably approximated by an infinite domain, see Section 6.3. For an exponential distribution, H_z Eq. (5.16) is evaluated analytically

$$H_z(z) = \frac{1}{D}\exp\left\{-z/\mathfrak{L}_z\right\}. \tag{5.24}$$

5.2 Mosaicity

In Section 5.1 the sample was assumed to be composed of many domains with different sizes. Ideally, all of the domains would be oriented such that their out-of-plane repeat direction is parallel to the substrate normal. Similarly to the description of orientational disorder of crystallites within a polycrystalline solid, the bilayer domain normals are described by a peaked orientational distribution function, often called the mosaic spread distribution. Typically for lipid bilayer stacks, the distribution function has a single maximum along the substrate normal and has no azimuthal dependence. A previous tilt-independent LAXS analysis considered a Gaussian mosaic spread distribution [48]. Motivated by recent experimental results (Nagle lab in preparation), the current methodology replaces the Gaussian distribution function with a Lorentzian

$$P_{\mathrm{m}}(\theta) \equiv \frac{2\gamma_{\mathrm{m}}}{\pi} \frac{1}{4\theta^2 + \gamma_{\mathrm{m}}^2}, \tag{5.25}$$

where γ_{m} is the full width at half maximum (FWHM) of the Lorentzian. For the best oriented samples, the mosaicity is sufficiently small ($\sim 0.1^\circ$) that the effect of mosaic spread is modeled as a convolution along planes of constant q_z [48], as opposed to a double integral over polar and azimuthal angles along surfaces of constant q [50]. Using $I(\mathbf{q})$ Eq. (5.1), the theoretically predicted scattering intensity from a sample composed of many misoriented domains is

$$I^{\mathrm{m}}(\mathbf{q}) \equiv I(q_r, q_z) * P_{\mathrm{m}}(q_r), \tag{5.26}$$

where $*$ indicates a convolution. Substituting S_{MD} Eq. (5.13) and $S_{0,\mathrm{MD}}$ Eq. (5.17) into I^{m} Eq. (5.26),

$$I^{\mathrm{m}}(\mathbf{q}) = |F(q_z)|^2 \Big[S_{\mathrm{MD}}(q_r, q_z) * P_{\mathrm{m}}(q_r) \Big] + F_\Delta(q_z) \Big[S_{0,\mathrm{MD}}(q_r, q_z) * P_{\mathrm{m}}(q_r) \Big] \tag{5.27}$$

$$= |F(q_z)|^2 \, S^{\mathrm{m}}_{\mathrm{MD}}(\mathbf{q}) + F_\Delta(q_z) S^{\mathrm{m}}_{0,\mathrm{MD}}(\mathbf{q}). \tag{5.28}$$

The effect of larger mosaic spread is not dealt with in this thesis.

5.3 Experimental Details

Various experimental details influence the measured X-ray scattering intensity. First in Section 5.3.1, the scattering geometry for a fixed low angle X-ray scattering experiment is described, and the well-known relationship between detector space (p_x, p_z, ω) and $\mathbf{q}$-space is derived. Next in Section 5.3.2, the beam's coherence is defined, and the sample coherence volume is evaluated. Then in Section 5.3.3, a general formalism to determine the beam shape on the detector is presented, and the effect of the beam size on the predicted scattering intensity is modeled. Absorption of the incident and scattered X-rays by the sample is considered in Section 5.3.4, concluding the description of the predicted scattering from a fixed angle exposure. Finally, since the incident

angle is continuously varied during most LAXS exposures, the fixed angle prediction is summed over all relevant incident angles in Section 5.3.5.

5.3.1 Scattering Geometry

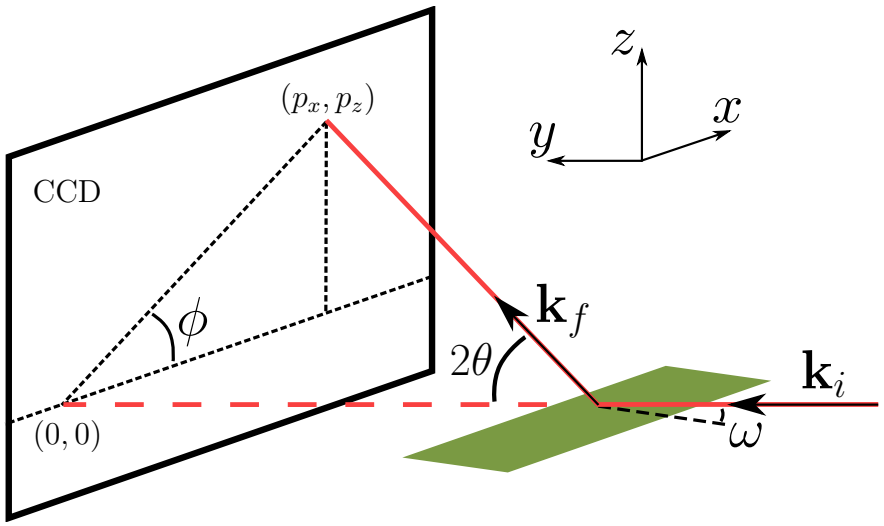


Figure 5.1: The scattering geometry for a low angle scattering experiment is shown. The solid red lines indicate the path of an incident and scattered X-ray, and the dashed red line is the path of the direct beam after the sample (green rectangle). Sample and CCD are not to scale. The sample size is 5×30 mm, and the sensitive surface of the detector is about 73×73 mm.

The scattering geometry for a fixed angle experiment is shown in Fig. 5.1. ω is the angle of incidence, 2θ is the angle between the direct and scattered beams, and ϕ is the angle between the line $p_x = 0$ and the scattered beam measured on the detector. (p_x, p_z) is a position on the flat detector surface, and for notational convenience the direct beam is incident upon the detector at $(0, 0)$. The incident and outgoing wavevectors are

$$\mathbf{k}_i = \frac{2\pi}{\lambda}\hat{\mathbf{y}} \tag{5.29}$$

and

$$\mathbf{k}_f = \frac{2\pi}{\lambda}\Big(\hat{\mathbf{x}}\sin(2\theta)\cos\phi + \hat{\mathbf{y}}\cos(2\theta) + \hat{\mathbf{z}}\sin(2\theta)\sin\phi\Big), \tag{5.30}$$

respectively, where λ is the X-ray wavelength.

The momentum transfer vector, or scattering vector, is

$$\mathbf{q} \equiv \mathbf{k}_f - \mathbf{k}_i. \tag{5.31}$$

As the sample is rotated about the x-axis by an angle ω, the projection of $\mathbf{q}$ along the sample centered coordinates changes. The sample coordinates (primed) are expressed as functions of the unrotated coordinates and ω,

$$\hat{\mathbf{x}}' = \hat{\mathbf{x}} \tag{5.32}$$
$$\hat{\mathbf{y}}' = \hat{\mathbf{y}}\cos\omega + \hat{\mathbf{z}}\sin\omega \tag{5.33}$$
$$\hat{\mathbf{z}}' = -\hat{\mathbf{y}}\sin\omega + \hat{\mathbf{z}}\cos\omega. \tag{5.34}$$

Finally, the components of $\mathbf{q}$ in sample coordinates are

$$q_x = \mathbf{q}\cdot\hat{\mathbf{x}}' = q\cos\theta\cos\phi, \tag{5.35}$$
$$q_y = \mathbf{q}\cdot\hat{\mathbf{y}}' = q(-\sin\theta\cos\omega + \cos\theta\sin\phi\sin\omega), \tag{5.36}$$
$$q_z = \mathbf{q}\cdot\hat{\mathbf{z}}' = q(\sin\theta\sin\omega + \cos\theta\sin\phi\cos\omega), \tag{5.37}$$

and $q = 4\pi\sin\theta/\lambda$.

In following sections, the relation between CCD space (p_x, p_z, ω) and $\mathbf{q}$-space is required. Rewriting Eqs. (5.35), (5.36), and (5.37) in terms of p_x, p_z, and ω,

$$q_x(p_x, p_z) = \frac{2\pi p_x}{\lambda s} \frac{1}{\sqrt{\delta(p_x, p_z)}} \tag{5.38}$$

$$q_y(p_x, p_z, \omega) = \frac{2\pi}{\lambda} \left[\left(\frac{1}{\sqrt{\delta(p_x, p_z)}} - 1 \right) \cos\omega + \frac{p_z \sin\omega}{s} \frac{1}{\sqrt{\delta(p_x, p_z)}} \right] \tag{5.39}$$

$$q_z(p_x, p_z, \omega) = \frac{2\pi}{\lambda} \left[\left(1 - \frac{1}{\sqrt{\delta(p_x, p_z)}} \right) \sin\omega + \frac{p_z \cos\omega}{s} \frac{1}{\sqrt{\delta(p_x, p_z)}} \right], \tag{5.40}$$

where

$$\delta(p_x, p_z) \equiv 1 + \frac{p_x^2 + p_z^2}{s^2} \tag{5.41}$$

and s is the sample to detector distance in units of pixels.

For small 2θ (or equivalently $p_x^2 + p_z^2 \ll s^2$) and ω, Eqs. (5.38), (5.39), and (5.40) are approximately written

$$q_x(p_x, p_z) \approx \frac{2\pi}{\lambda s} p_x, \tag{5.42}$$

$$q_y(p_x, p_z, \omega) \approx \frac{2\pi}{\lambda} \left[-\frac{p_x^2 + p_z^2}{2s^2} + \frac{p_z \omega}{s} \right], \tag{5.43}$$

$$q_z(p_x, p_z, \omega) \approx \frac{2\pi}{\lambda s} p_z. \tag{5.44}$$

q_x (q_z) is approximately linear in p_x (p_z).

5.3.2 Coherence Effects

An X-ray beam is not perfectly collimated or monochromatic. Due to angular divergence and energy dispersion, an X-ray beam has a finite volume over which it is coherent; the phases of X-rays within a coherent volume are not too dissimilar so the X-rays interfere with each other [62]. Making the simplifying assumption of a sharp coherence cutoff, one may conveniently define a coherence volume. If the coherent volume is smaller than the total illuminated sample volume, then the scattering from the sample is an incoherent sum of the scattering from coherent subvolumes. The beam coherence volume projected onto the sample is referred as the sample coherence volume. The sample coherence volume is derived and shown to be smaller than

the total illuminated sample volume.

The coherence of the X-ray beam is described by three coherence lengths, two transverse and one longitudinal [62], see Fig. 5.2. The transverse coherence lengths are related to the angular divergence of the beam

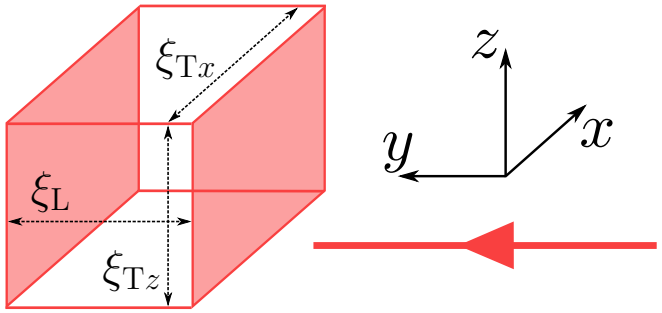


Figure 5.2: Diagram defining transverse ξ_{T} and longitudinal ξ_{L} coherence lengths of the X-ray beam. The horizontal solid red line and arrow indicate the primary X-ray propagation direction. $\xi_{\mathrm{T}x}$, $\xi_{\mathrm{T}z}$, and ξ_{L} are not drawn to scale.

$$\xi_{\mathrm{T}x} \equiv \frac{\lambda}{2\Delta\gamma_x} \tag{5.45}$$

$$\xi_{\mathrm{T}z} \equiv \frac{\lambda}{2\Delta\gamma_z}, \tag{5.46}$$

where $\Delta\gamma_x$ and $\Delta\gamma_z$ are the angular divergence of the beam in the x- and z-directions, respectively, and λ is the X-ray wavelength. The longitudinal coherence length is related to the energy spread of the beam $\Delta\lambda$,

$$\xi_{\mathrm{L}} \equiv \frac{\lambda^2}{2\Delta\lambda}. \tag{5.47}$$

For our experimental setup, $\lambda \simeq 1.2$ Å, $\Delta\gamma_x \simeq \Delta\gamma_z = 10^{-4}$ rad, and $\Delta\lambda/\lambda \approx 0.01$ for low resolution W/B_4C multilayers and $\Delta\lambda/\lambda \approx 10^{-4}$ for high resolution double bounce Si channel cut. Therefore, $\xi_{\mathrm{T}x} \approx \xi_{\mathrm{T}z} \approx 6000$ Å and $\xi_{\mathrm{L}} \approx 60$ Å or $\xi_{\mathrm{L}} \approx 6000$ Å. Note, the coherent volume of the beam is not equivalent to the coherent sample volume.

Sidenote

Often, the incident X-ray beam's energy dispersion and angular divergence are considered when assessing the **q**-resolution of the experiment. A **q**-resolution function $W(\mathbf{q})$ is

commonly convoluted with the theoretical scattering intensity,

$$I^{\mathrm{R}}(\mathbf{q}) = \int \mathrm{d}^3\mathbf{q}'\ I(\mathbf{q}')W(\mathbf{q}-\mathbf{q}'), \tag{5.48}$$

where $W(\mathbf{q})$ is assumed to be a peaked function with rapidly decaying tails [75]. Substituting $I^{\mathrm{m}}(\mathbf{q})$ Eq. (5.28) into Eq. (5.48),

$$I^{\mathrm{R}}(\mathbf{q}) = \int \mathrm{d}^3\mathbf{q}'\ \left[|F(q_z)|^2\, S^{\mathrm{m}}_{\mathrm{MD}}(\mathbf{q}) + F_\Delta(q_z) S^{\mathrm{m}}_{0,\mathrm{MD}}(\mathbf{q})\right] W(\mathbf{q}-\mathbf{q}'). \tag{5.49}$$

Finite resolution mixes $|F(q_z)|^2$ and $F_\Delta(q_z)$ with $S^{\mathrm{m}}_{\mathrm{MD}}(\mathbf{q})$ and $S^{\mathrm{m}}_{0,\mathrm{MD}}(\mathbf{q})$, respectively. Since $|F(q_z)|^2$ and $F_\Delta(q_z)$ are approximately constant for Δq_z similar to the width of $W(\mathbf{q})$, the effect of $\mathbf{q}$-resolution is well approximated by

$$I^{\mathrm{R}}(\mathbf{q}) \approx |F(q_z)|^2 \int \mathrm{d}^3\mathbf{q}'\ S^{\mathrm{m}}_{\mathrm{MD}}(\mathbf{q})W(\mathbf{q}-\mathbf{q}') + F_\Delta(q_z) \int \mathrm{d}^3\mathbf{q}'\ S^{\mathrm{m}}_{0,\mathrm{MD}}(\mathbf{q})W(\mathbf{q}-\mathbf{q}'). \tag{5.50}$$

$|F(q_z)|^2$ is well-known to be a slowly varying function of q_z [76], and based on a model, Appendix C.1 predicts that $F_\Delta(q_z)$ is also a slowly varying function of q_z.

Following the ideas of previous researchers [74, 75], the integrals in Eq. (5.50) are expressed in real space by invoking the convolution theorem. Using the $S^{\mathrm{m}}_{\mathrm{MD}}$-dependent integral as a sufficient example,

$$\int \mathrm{d}^3\mathbf{q}'\ S^{\mathrm{m}}_{\mathrm{MD}}(\mathbf{q})W(\mathbf{q}-\mathbf{q}') = \int \mathrm{d}^3\mathbf{R}\ \tilde{S}^{\mathrm{m}}_{\mathrm{MD}}(\mathbf{R})\widetilde{W}(\mathbf{R})e^{i\mathbf{q}\cdot\mathbf{R}} \tag{5.51}$$

where the convolution theorem was used and $\tilde{S}^{\mathrm{m}}_{\mathrm{MD}}$ and $\widetilde{W}(\mathbf{R})$ are the Fourier transforms of $S^{\mathrm{m}}_{\mathrm{MD}}$ and $W(\mathbf{q})$, respectively. $\widetilde{W}(\mathbf{R})$ is a peaked function and limits the longest length scale correlations included in the calculation of $I^{\mathrm{R}}(\mathbf{q})$. From this perspective, $\widetilde{W}(\mathbf{R})$ has been identified as defining a sample coherence volume [74, 75]. The rest of this Section is devoted to a quantitative discussion of the sample coherence volume in real space.

The scattering from the sample is assumed to be the incoherent sum of scattering from coherent subvolumes. On pp. 2746 of Ref. [74], the authors address the size of a coherent sample volume:

> "The coherence lengths can also be used to estimate the range of separation between two points in the sample from which scattering can interfere. If these points are separated by a distance ΔR, then the condition is that ΔR

must be less than ~~either~~ both $\xi_s/\sin\alpha$ (where α is the angle between $\mathbf{\Delta R}$ and the incident beam direction) ~~or~~ and $k_0\xi_L/q_0$, where q_0 is the component of $\mathbf{q}$ along $\mathbf{\Delta R}$."

The blue text indicates a different notation, and the red amendment to the original text is motivated by an email correspondence in which Professor Sinha agreed that

$$\Delta R \leq \text{Min}\left[\frac{\xi_s}{\sin\alpha}, \frac{k_0\xi_L}{q_0}\right], \tag{5.52}$$

similar to the conclusion stated in [48]. Min[...] returns the minimum value of its arguments. Additionally, the same conclusion is declared in a recent publication on which Professor Sinha is the first author [77]. ξ_s is not exactly the transverse coherence length of the X-ray beam in the z-direction ξ_{Tz} (see Fig. 5.2), but given the typical experimental setup, the difference is negligible [74]. ξ_L is the longitudinal coherence length of the beam. ΔR Eq. (5.52) is utilized to derive the size of a coherent sample volume as a function of $\mathbf{q}$, the incident angle of the incoming X-rays, and the coherence lengths of the X-ray beam.

Transverse Sample Coherence Lengths

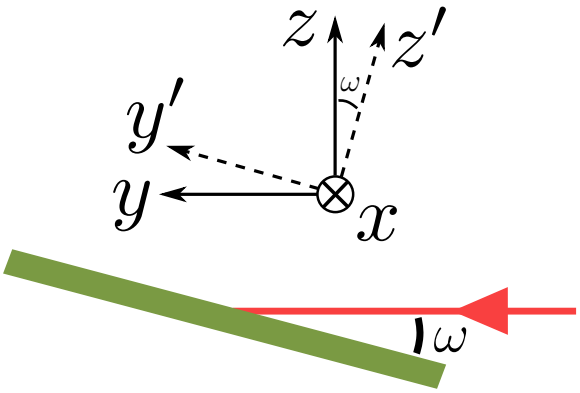


Figure 5.3: Scattering geometry for low angle scattering experiment. The unprimed and primed coordinates are the lab centered and sample centered coordinates, respectively. The sample is the green rectangle, and its supporting substrate has been omitted.

The scattering geometry is depicted in Fig. 5.3. In the following derivation, the primed coordinates are the sample centered coordinates, and the unprimed coordinates represent the lab reference frame. During an experiment, the beam propagates

in the $\hat{\mathbf{y}}$-direction, and the sample is rotated about the x-axis. The incident wavevector is $\mathbf{k}_i = k_0\,\hat{\mathbf{y}}$. The transverse sample coherence regions are determined by the relations,

$$\Delta R_{yz} \leq \frac{\xi_{\mathrm{T}z}}{\sin\alpha} \tag{5.53}$$

and

$$\Delta R_x \leq \xi_{\mathrm{T}x}, \tag{5.54}$$

where $\Delta R_{yz} \equiv |\mathcal{L}_y\hat{\mathbf{y}}' + \mathcal{L}_z\hat{\mathbf{z}}'|$ is a distance in the $y'z'$ plane, $\Delta R_x \equiv |\mathcal{L}_x\hat{\mathbf{x}}'|$, and α is the angle between $\Delta\mathbf{R}$ and the incident beam direction $\hat{\mathbf{y}}$. Working towards a relation for $\sin\alpha$,

$$\Delta\mathbf{R}_{yz}\cdot\hat{\mathbf{y}} = \Delta R_{yz}\cos\alpha, \tag{5.55}$$

and also

$$\Delta\mathbf{R}_{yz}\cdot\hat{\mathbf{y}} = \mathcal{L}_y\hat{\mathbf{y}}'\cdot\hat{\mathbf{y}} + \mathcal{L}_z\hat{\mathbf{z}}'\cdot\hat{\mathbf{y}} \tag{5.56}$$

$$\Rightarrow \Delta R_{yz}\cos\alpha = \mathcal{L}_y\cos\omega - \mathcal{L}_z\sin\omega, \tag{5.57}$$

where ω is the angle of incidence. Solving Eq. (5.57) for $\sin\alpha$,

$$\sin\alpha = \sqrt{1 - \left(\frac{\mathcal{L}_y\cos\omega - \mathcal{L}_z\sin\omega}{\Delta R_{yz}}\right)^2}. \tag{5.58}$$

Using $\sin\alpha$ Eq. (5.58) to rewrite ΔR_{yz} Eq. (5.53),

$$\Delta R_{yz} \leq \frac{\xi_{\mathrm{T}z}}{\sin\alpha} \rightarrow \sqrt{\left(\Delta R_{yz}\right)^2 - \left(\mathcal{L}_y \cos\omega - \mathcal{L}_z \sin\omega\right)^2} \leq \xi_{Tz} \tag{5.59}$$

$$\Rightarrow\ \mathcal{L}_y \sin\omega + \mathcal{L}_z \cos\omega \leq \xi_{\mathrm{T}z}. \tag{5.60}$$

For ω sufficiently small to use the small angle approximations of sine and cosine,

$$\mathcal{L}_y\omega + \mathcal{L}_z \lesssim \xi_{\mathrm{T}z}. \tag{5.61}$$

$\mathcal{L}_z$ is approximately ω-independent, and $\mathcal{L}_y$ is significantly extended for small ω.

Longitudinal Sample Coherence Lengths

The longitudinal sample coherence lengths are determined by the relation,

$$\Delta R \leq \frac{k_0 \xi_\ell}{q_0}. \tag{5.62}$$

Let $\mathbf{q} = q_x\hat{\mathbf{x}}' + q_y\hat{\mathbf{y}}' + q_z\hat{\mathbf{z}}'$. By definition q_0 is the component of $\mathbf{q}$ parallel to $\Delta\mathbf{R}$,

$$q_0 \equiv \mathbf{q} \cdot \frac{\Delta\mathbf{R}}{\Delta R} \tag{5.63}$$

$$= \frac{|q_x\mathcal{L}_x| + |q_y\mathcal{L}_y| + |q_z\mathcal{L}_z|}{\Delta R}. \tag{5.64}$$

Using q_0 Eq. (5.64) to rewrite ΔR Eq. (5.62) in sample Cartesian coordinates,

$$\Delta R \leq \frac{k_0 \xi_{\mathrm{L}}}{q_0} \tag{5.65}$$

$$\leq \frac{2\pi\xi_{\mathrm{L}}}{\frac{\lambda}{\Delta R}\left(|q_x\mathcal{L}_x| + |q_y\mathcal{L}_y| + |q_z\mathcal{L}_z|\right)} \tag{5.66}$$

$$\Rightarrow \left(|q_x\mathcal{L}_x| + |q_y\mathcal{L}_y| + |q_z\mathcal{L}_z|\right) \leq \frac{2\pi\xi_{\mathrm{L}}}{\lambda}. \tag{5.67}$$

The ξ_{L}-related cut-off lengths depend on the specific part of $\mathbf{q}$-space probed.

Size of Coherent Sample Volume

The extent of a coherent sample volume is defined by,

$$\mathcal{L}_x \leq \xi_{\mathrm{T}x} \tag{5.68}$$

$$\mathcal{L}_y\omega + \mathcal{L}_z \lesssim \xi_{\mathrm{T}z} \tag{5.69}$$

$$(|q_x\mathcal{L}_x| + |q_y\mathcal{L}_y| + |q_z\mathcal{L}_z|) \leq \frac{2\pi\xi_{\mathrm{L}}}{\lambda}, \tag{5.70}$$

summarizing previous conclusions. Eqs. (5.68)–(5.70) describe a volume with boundaries which are not perpendicular to the Cartesian axes. Additionally, the size of the sample coherent volume in one direction is related to its size in the other two directions.[14]

A xy-slice (constant z) of the sample coherence volume is shown in Fig. 5.4. Typically, the extent of the coherence region in the y-direction is significantly greater than in the x-direction since $|q_y| \ll |q_x|$. For

$$|q_x| > \frac{2}{\xi_{\mathrm{T}x}}\left(\frac{\pi\xi_{\mathrm{L}}}{\lambda} - |q_z z|\right), \tag{5.71}$$

the xy coherence slice transitions from a hexagon to a parallelogram. A yz-slice (constant x) of the sample coherence volume is shown in Fig. 5.5. Typically, the extent of the coherence region in the y-direction is significantly greater than in the z-direction since $|q_y| \ll |q_z|$. For

$$|q_z| > \frac{2}{\xi_{\mathrm{T}z}}\left(\frac{\pi\xi_{\mathrm{L}}}{\lambda} - |q_x x|\right), \tag{5.72}$$

the yz coherence slice transitions from a octagon to a parallelogram.

[14] Eq. (5.70) provides a new insight regarding the "spikes" predicted by the currently implemented X-ray scattering theory. The "spikes" are peaked features centered at $2\pi h/D$ that extend in the q_x-direction from the centers of the Caillé peaks, especially visible for $h = 1, 2$ (see [48] Figure 4.6, [44], and Fig. 6.11 in this thesis). These "spikes" are not observed experimentally. The prediction of the "spikes" is unusual because otherwise the scattering theory predicts increasingly broad features for increasing q_r or q_z. Eq. (5.70) describes a systematic reduction of $\mathcal{L}_z$ as a function of increasing $\mathcal{L}_x$ for finite q_x and q_z. In other words, for correlations between two points to be assessable, the points can not be separated by both a large in-plane distance and many bilayers. The "spikes" may be the result of simultaneously allowing both $\mathcal{L}_x$ and $\mathcal{L}_z$ to be large. Certainly, a narrow feature along q_z is impossible if correlations between only a few bilayers are considered. The "spikes" are sufficiently weak in the typically analyzed q_z-range ($h > 2$) that the aforementioned issue is not further addressed.

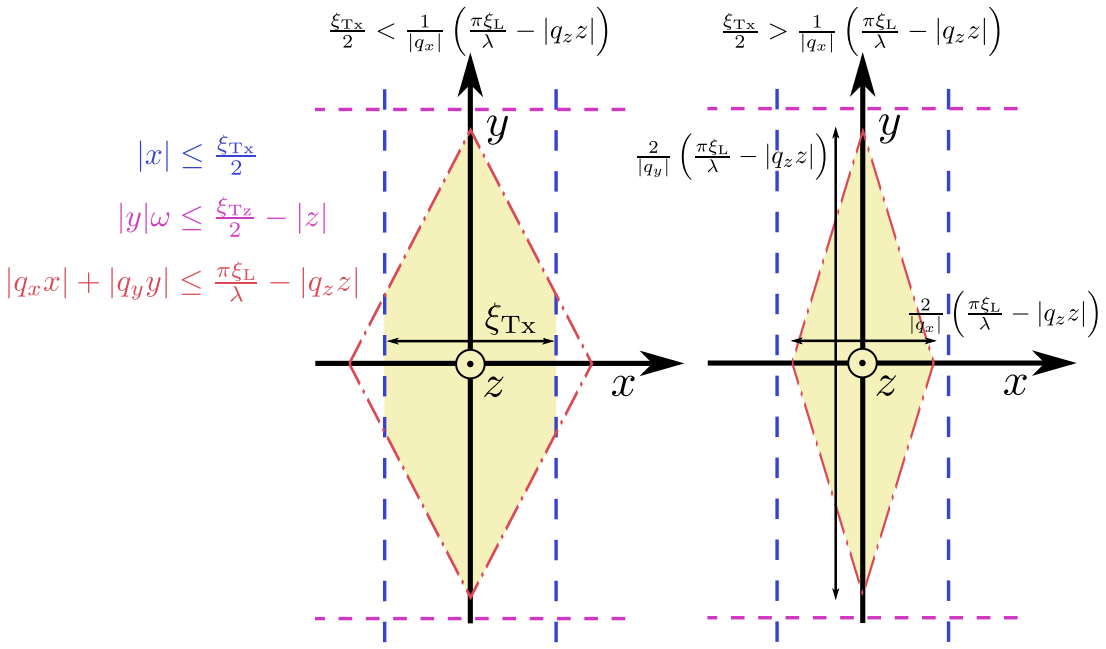


Figure 5.4: A xy-slice (constant z) of the coherence volume described by Eqs. (5.68)-(5.70). The colored dashed lines correspond to the colored inequalities. The yellow region satisfies all inequalities. Beyond a certain q_x-value, the yellow region transitions from a hexagon (left-hand side) to a parallelogram (right-hand side).

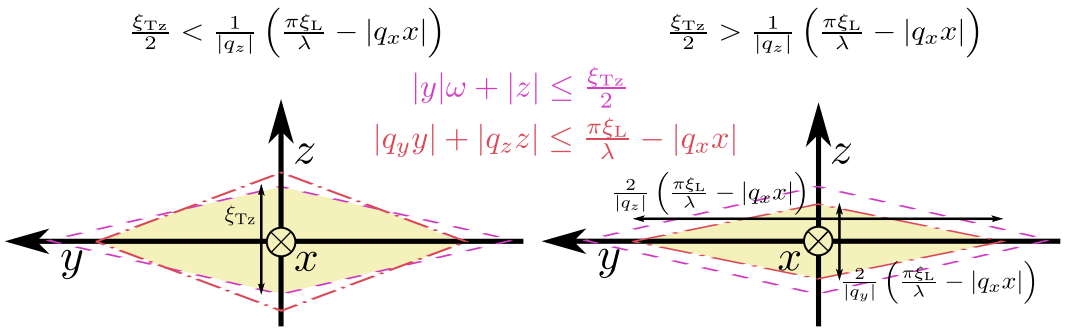


Figure 5.5: A yz-slice (constant x) of the coherence volume described by Eqs. (5.68)-(5.70). The colored dashed lines correspond to the colored inequalities. The yellow region satisfies both inequalities. Beyond a certain q_z-value, the yellow region transition from a octagon (left-hand side) to a parallelogram (right-hand side).

Making several assumptions, the boundaries of the sample coherence volume are approximated. The X-ray scattering intensity is dominated by short length scale correlations because the pair scattering correlation function decays as a power law for increasing correlation distances, see Eq. (5.3). Therefore, as long as the coherent volume is sufficiently large, the X-ray scattering intensity is fairly insensitive to exactly where the boundaries are placed. More formally, the conditions for boundary insensitivity are

$$\begin{aligned} \mathcal{L}_x &\gg \xi = \sqrt[4]{K_c/B} \\ \mathcal{L}_y &\gg \xi \\ \mathcal{L}_z &\gg D. \end{aligned} \tag{5.73}$$

Typical values of ξ (the in-plane correlation length) and D are about 50 Å and 60 Å, respectively.[15] Since the relations in Eq. (5.73) are true for the experiments in question, interdependence of various coherent volume sizes is neglected, and Eqs. (5.68) - (5.70) are approximated by

$$\begin{aligned} \mathcal{L}_x(q_x) &\approx \text{Min}\left[\xi_{\text{T}x}, \frac{2\pi\xi_{\text{L}}}{|q_x|\lambda}\right] \\ \mathcal{L}_y(q_y,\omega) &\approx \text{Min}\left[\frac{\xi_{\text{T}z}}{\omega}, \frac{2\pi\xi_{\text{L}}}{|q_y|\lambda}\right] \\ \mathcal{L}_z(q_z) &\approx \text{Min}\left[\xi_{\text{T}z}, \frac{2\pi\xi_{\text{L}}}{|q_z|\lambda}\right]. \end{aligned} \tag{5.74}$$

The relations in (5.74) overestimate the size of the sample coherence volume. For common experimental and data analysis parameter values summarized in Table 5.1, the equations in (5.74) are simplified,

$$\mathcal{L}_x \approx \xi_{\text{T}x} \tag{5.75}$$

$$\mathcal{L}_y \gtrsim \xi_{\text{T}z} \tag{5.76}$$

$$\mathcal{L}_z(q_z) \approx \text{Min}\left[\xi_{\text{T}z}, \frac{2\pi\xi_{\text{L}}}{q_z\lambda}\right]. \tag{5.77}$$

[15] Following simply from the relation between real- and reciprocal-spaces, the scattering at small q is dependent on the longest length scale correlations in a sample. Consequently for sufficiently small q, the measured scattering intensity is sensitive to the detailed shape of the sample coherence volume. Therefore, the present analysis is restricted to $q_x \gtrsim 2\pi/\mathcal{L}_x$.

Table 5.1: Typical experimental parameter values and ranges of q for analysis.

parameter	[units]	value
λ	[Å]	1.2
$\xi_{\mathrm{T}x}$	[Å]	6000
$\xi_{\mathrm{T}z}$	[Å]	6000
ξ_{L}	[Å]	60
ω	[°]	$0 \leftrightarrow 11$
ξ	[Å]	60
$\lvert q_x \rvert$	[Å^{-1}]	$0.01 \leftrightarrow 0.3$
$\lvert q_y \rvert$	[Å^{-1}]	$0 \leftrightarrow 0.1$
q_z	[Å^{-1}]	$0.2 \leftrightarrow 1.0$

For $q_x > (2\pi\xi_{\mathrm{L}}) \,/\, (\xi_{\mathrm{T}z}\lambda)$, Eq. (5.75) overestimates $\mathcal{L}_x$. In Eq. (5.76) the q_y-dependence of $\mathcal{L}_y$ was neglected since q_y is always small, see Section 5.3.5 for a discussion of experimentally assessed q_y-values. Since $\mathcal{L}_x \gg \xi$ and $\mathcal{L}_y \gg \xi$, the details of the coherence volume boundary are not too important, and therefore, the coherence volume is approximated as a cylinder with diameter $\mathcal{L}_r \equiv \mathrm{Min}\,[\mathcal{L}_x, \mathcal{L}_y]$ and height $\mathcal{L}_z(q_z)$.

Having completed the sample coherence volume derivation, the characteristic in- and out-of-plane subvolume sizes can be quantitatively determined, see Sections 5.1.1 and 5.1.2. Using the derived sample coherence lengths, Eqs. (5.75), (5.76), and (5.77),

$$\begin{aligned} \mathfrak{L}_r &= \mathrm{Min}\,[\mathscr{L}_r, \mathcal{L}_r] && (5.78) \\ &= \mathrm{Min}\,[\mathscr{L}_r, \mathcal{L}_x, \mathcal{L}_y] \\ &\approx \mathrm{Min}\,[\mathscr{L}_r, \xi_{\mathrm{T}x}, \xi_{\mathrm{T}z}] && (5.79) \end{aligned}$$

and

$$\begin{aligned} \mathfrak{L}_z(q_z) &= \mathrm{Min}\,[\mathscr{L}_z, \mathcal{L}_z(q_z)] && (5.80) \\ &= \mathrm{Min}\left[\mathscr{L}_z, \mathrm{Min}\left[\xi_{\mathrm{T}z}, \frac{2\pi\xi_{\mathrm{L}}}{q_z\lambda}\right]\right] \\ &= \mathrm{Min}\left[\mathscr{L}_z, \xi_{\mathrm{T}z}, \frac{2\pi\xi_{\mathrm{L}}}{q_z\lambda}\right], && (5.81) \end{aligned}$$

where $\mathscr{L}_r$ and $\mathscr{L}_z$ are characteristic sample domain sizes, independent of the sample coherence volume. Given the dependencies of Eqs. (5.79) and (5.81), the sample subvolume distributions are more specifically written $P_r(L_r)$ and $P_z(L_z, q_z)$. Note, the functional forms of the distribution functions are assumed to be independent of the domain size and the beam's coherence lengths.

5.3.3 Beam Size Effects

X-rays scattered from different parts of the beam's footprint on the sample strike the detector at different places and can have the same value of $\mathbf{q}$, see Fig. 5.6. Therefore, a particular point on the CCD samples a range of $\mathbf{q}$-values. First, the beam's shape on the detector is derived as a function of the experimental geometry. Then, the effect of the beam's shape on the measured intensity is discussed.

Projection of Beam-sample Footprint on Detector

Fig. 5.6 shows the scattering geometry with details concerning the beam and its footprint on the sample. The center of the sample is the origin of the lab Cartesian coordinate system, and the detector is described by a plane a distance s (in pixels) away along the $\hat{\mathbf{y}}$-direction, $y = s$. The beam height b_z is chosen such that $b_z > L_\mathrm{s} \sin\omega_\mathrm{max}$, where ω_max is the maximum incident angle and L_s is the width of the sample. For typical values of $L_\mathrm{s} = 5$ mm and $\omega_\mathrm{max} \approx 11°$, $L_\mathrm{s} \sin\omega_\mathrm{max} \approx 0.95$ mm and $b_z \approx 1$ mm. Therefore, for all ω, only part of the beam is incident on the sample; some of the beam is above or below the sample.

Fig. 5.7 shows two different perspectives of Fig. 5.6. Importantly, the vertices of the beam-sample footprint are defined $\mathbf{v}_1$ through $\mathbf{v}_4$,

$$\begin{aligned}
\mathbf{v}_1 &= \Big(-\frac{b_x}{2}, -\frac{L_\mathrm{s}}{2}\cos\omega, -\frac{L_\mathrm{s}}{2}\sin\omega\Big) \\
\mathbf{v}_2 &= \Big(-\frac{b_x}{2}, \quad \frac{L_\mathrm{s}}{2}\cos\omega, \quad \frac{L_\mathrm{s}}{2}\sin\omega,\Big) \\
\mathbf{v}_3 &= \Big(\quad \frac{b_x}{2}, \quad \frac{L_\mathrm{s}}{2}\cos\omega, \quad \frac{L_\mathrm{s}}{2}\sin\omega,\Big) \\
\mathbf{v}_4 &= \Big(\quad \frac{b_x}{2}, -\frac{L_\mathrm{s}}{2}\cos\omega, -\frac{L_\mathrm{s}}{2}\sin\omega,\Big),
\end{aligned} \tag{5.82}$$

where b_x is the width of the beam. The beam shape on the detector is a parallel projection of the beam-sample footprint which maps $\mathbf{v}_i$ to $\mathbf{V}_i$ that end on the detector

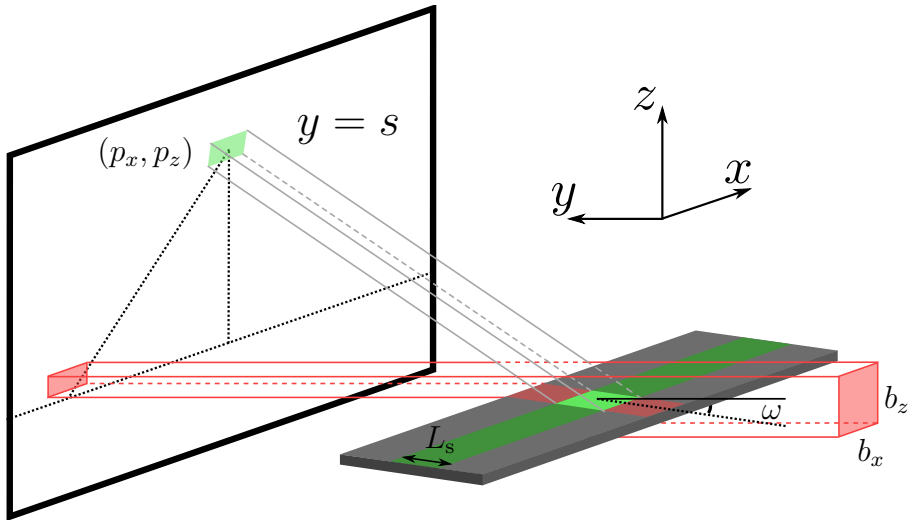


Figure 5.6: Scattering geometry for a low angle scattering experiment with details concerning the beam. The substrate is depicted by the dark gray rectangular cuboid, and the sample is the darker green rectangle. The beam and beam path are shown by the red rectangles and lines. The part of the beam that would pass under the substrate is blocked by the sample holder (not depicted). The intersection of the beam and the bare part of the substrate is red, and the intersection with the sample is bright green. The edges of the scattered beam are shown by the gray lines. The projection of the beam-sample footprint on the detector is also bright green. While the beam-sample footprint is a rectangle, see Fig. 5.7, its projection on the detector is a parallelogram, see Fig. 5.8.

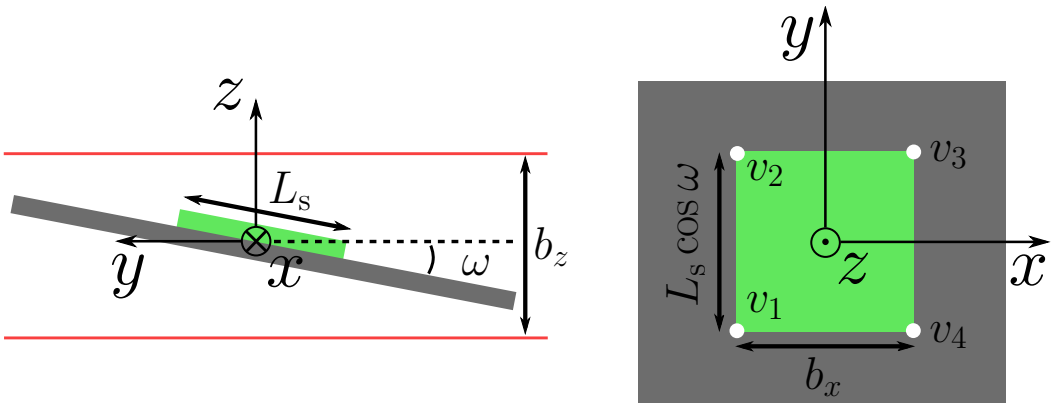


Figure 5.7: Different perspectives of the scattering geometry depicted in Fig. 5.6. The left-hand side shows a side view of the substrate (gray rectangle) and multilamellar lipid bilayer sample (green rectangle). The thickness of the sample (10 μm) and substrate (2 mm) are not drawn to scale. The right-hand side shows a top view of the sample. The four white circles v_1 though v_4 label the vertices of the rectangular beam footprint on the sample.

$y = s$ plane. Given a central pixel for the scattered beam on the detector (p_x, p_z), the direction of the parallel projection is along $\mathbf{d} = (p_\mathrm{s} p_x, \mathcal{S}, p_\mathrm{s} p_z)$, where p_s is the size in millimeters of 1 pixel, 0.07113 mm/pixel for the FLIcam, and $\mathcal{S} \equiv p_\mathrm{s} s$. $\mathbf{V}_i$ is expressed by

$$\begin{aligned} \mathbf{V}_i &= \mathbf{v}_i + t\mathbf{d} && (5.83) \\ &= (v_{ix} + t p_\mathrm{s} p_x, v_{iy} + t\mathcal{S}, v_{iz} + t p_\mathrm{s} p_z)\,, && (5.84) \end{aligned}$$

where t is a scalar determined by requiring that $\mathbf{V}_i$ ends on the detector,

$$\begin{aligned} V_{iy} &= v_{iy} + t\mathcal{S} = \mathcal{S} && (5.85) \\ \Rightarrow t &= 1 - \frac{v_{iy}}{\mathcal{S}}. && (5.86) \end{aligned}$$

The parallel projection is compactly expressed as a matrix equation,

$$\mathbb{P}_\mathrm{p} \tilde{\mathbf{v}}_i^\mathrm{T} = \widetilde{\mathbf{V}}^\mathrm{T}, \tag{5.87}$$

where $\tilde{\mathbf{v}}$ indicates $\mathbf{v}$ expressed in homogeneous coordinates, $\mathbf{v} = (v_x, v_y, v_z) \rightarrow \tilde{\mathbf{v}} = (v_x, v_y, v_z, 1)$ and

$$\mathbb{P}_\mathrm{p} \equiv \begin{pmatrix} 1 & -p_x/s & 0 & p_x \\ 0 & 0 & 0 & s \\ 0 & -p_z/s & 1 & p_z \\ 0 & 0 & 0 & 1 \end{pmatrix}. \tag{5.88}$$

Using Eqs. (5.82) and (5.87) and converting back to standard Cartesian coordinates from homogeneous coordinates

$$
\begin{aligned}
\mathbf{V}_1 &= \Big(-\frac{b_x}{2} + p_{\rm s}p_x + \frac{p_x L_{\rm s}}{2s}\cos\omega,\ \mathcal{S},\ -\frac{L_{\rm s}}{2}\sin\omega + p_{\rm s}p_z + \frac{p_z L_{\rm s}}{2s}\cos\omega\Big) \\
\mathbf{V}_2 &= \Big(-\frac{b_x}{2} + p_{\rm s}p_x - \frac{p_x L_{\rm s}}{2s}\cos\omega,\ \mathcal{S},\ \ \frac{L_{\rm s}}{2}\sin\omega + p_{\rm s}p_z - \frac{p_z L_{\rm s}}{2s}\cos\omega\Big) \\
\mathbf{V}_3 &= \Big(\ \frac{b_x}{2} + p_{\rm s}p_x - \frac{p_x L_{\rm s}}{2s}\cos\omega,\ \mathcal{S},\ \ \frac{L_{\rm s}}{2}\sin\omega + p_{\rm s}p_z - \frac{p_z L_{\rm s}}{2s}\cos\omega\Big) \\
\mathbf{V}_4 &= \Big(\ \frac{b_x}{2} + p_{\rm s}p_x + \frac{p_x L_{\rm s}}{2s}\cos\omega,\ \mathcal{S},\ -\frac{L_{\rm s}}{2}\sin\omega + p_{\rm s}p_z + \frac{p_z L_{\rm s}}{2s}\cos\omega\Big).
\end{aligned}
\tag{5.89}
$$

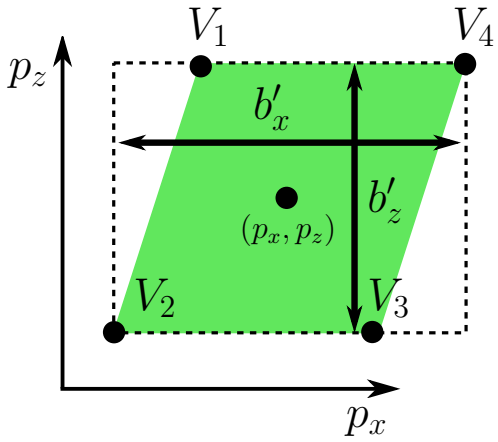


Figure 5.8: The beam-sample footprint projected onto the detector is depicted by the green parallelogram.

All $\mathbf{V}_i$ in Eq. (5.89) end on the detector since $V_{i,y} = \mathcal{S}$, and the ends of $\mathbf{V}_i$ describe a parallelogram, see Fig. 5.8. Approximating the parallelogram as a rectangle, the width and height of the projected beam on the detector are

$$
\begin{aligned}
b'_x(p_x) &\equiv V_{4x} - V_{2x} && (5.90)\\
&= b_x + \frac{p_x L_{\rm s}}{s}\cos\omega \\
&\approx b_x + \frac{p_x L_{\rm s}}{s} && (5.91)
\end{aligned}
$$

and for $p_z > s\tan\omega$

$$b'_z(p_z,\omega) \equiv V_{4z} - V_{3z} \tag{5.92}$$

$$= \frac{p_z L_\mathrm{s}}{s}\cos\omega - L_\mathrm{s}\sin\omega$$

$$\approx \frac{p_z L_\mathrm{s}}{s} - L_\mathrm{s}\omega \tag{5.93}$$

respectively, using $\omega \geq 0°$. For given p_z, the maximum value of ω before the substrate blocks the scattering from the sample is

$$\omega_\mathrm{C}(p_z) \equiv \tan^{-1}(p_z/s) \tag{5.94}$$

(see Fig. 5.11), and therefore $b'_z \geq 0$. $b'_x(p_x)$ Eq. (5.91) and $b'_z(p_z,\omega)$ Eq. (5.93) are plotted in Figs. 5.9 and 5.10, respectively. Previously, the geometric broadening in the p_x-direction was assumed to be constant (independent of p_x), and only the p_z dependence of the vertical geometric broadening was considered (not the ω-dependence) [48]. Now, the geometric broadening is dependent on p_x, p_z, and ω.

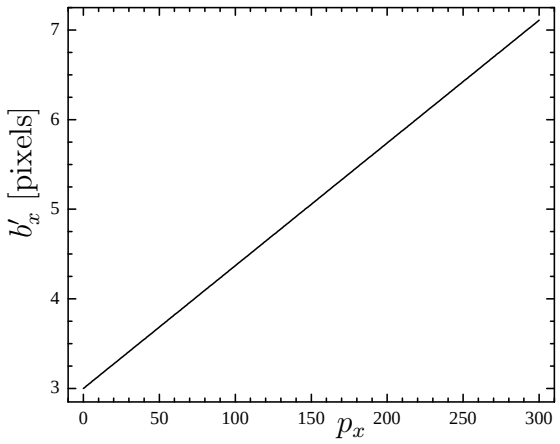


Figure 5.9: $b'_x(p_x)$ Eq. (5.91) is plotted for $b_x = 3$ pixels, $L_\mathrm{s} = 5$ mm, and $s = (365$ mm) /(0.07113 mm/pixel). b'_x increases by about a factor of 2 in the p_x range of interest.

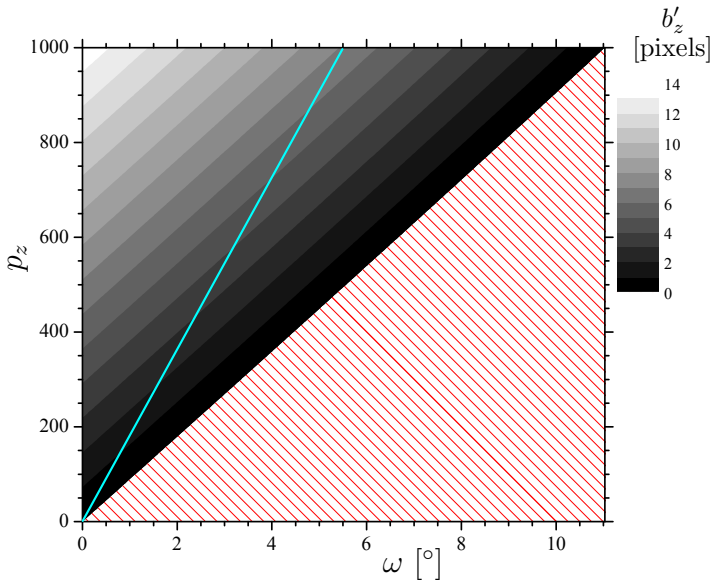


Figure 5.10: $b'_z(p_z, \omega)$ Eq. (5.93) is plotted for $L_\mathrm{s} = 5$ mm and $s \approx 5131$ pixels. The triangular (ω, p_z)-region patterned with red diagonal lines is not experimentally accessible because the substrate blocks the outgoing scattering, see Fig. 5.11. The cyan line indicates the p_z position of the specular scattering as a function of ω, $p_z = s \tan(2\omega)$. The boundary between grayscale and diagonally patterned lines is described by $p_z = s \tan \omega$. For fixed ω, b'_z significantly increases as a function of p_z.

Measured Intensity Considering Beam Size: $I^{\mathrm{B}}_{\mathbf{CCD}}$

Using $b'_x(p_x)$ Eq. (5.91) and $b'_z(p_z,\omega)$ Eq. (5.93), the beam projected onto the detector with central pixel (p_x, p_z) is modeled as a product of two Gaussians,

$$B\left(\tilde{p}_x, p_x, \tilde{p}_z, p_z, \omega\right) \equiv B_x\left(\tilde{p}_x, p_x\right) B_z\left(\tilde{p}_z, p_z, \omega\right), \tag{5.95}$$

where

$$B_x\left(\tilde{p}_x, p_x\right) \equiv \frac{1}{\sqrt{2\pi\sigma_x^2(p_x)}} \exp\left\{-\frac{\left(p_x - \tilde{p}_x\right)^2}{2\sigma_x^2(p_x)}\right\} \tag{5.96}$$

$$B_z\left(\tilde{p}_z, p_z, \omega\right) \equiv \frac{1}{\sqrt{2\pi\sigma_z^2(p_z,\omega)}} \exp\left\{-\frac{\left(p_z - \tilde{p}_z\right)^2}{2\sigma_z^2(p_z,\omega)}\right\} \tag{5.97}$$

$$\sigma_x(p_x) \equiv \frac{b'_x(p_x)}{\Upsilon p_{\mathrm{s}}} \tag{5.98}$$

$$\sigma_z(p_z,\omega) \equiv \frac{b'_z(p_z,\omega)}{\Upsilon p_{\mathrm{s}}}, \tag{5.99}$$

where

$$\Upsilon \equiv 2\sqrt{2\ln 2} \approx 2.3548 \tag{5.100}$$

converts from the full-width half maximum (FWHM) of a Gaussian to one standard deviation. Using B Eq. (5.95) the theoretical scattering intensity on the detector $I^{\mathrm{B}}_{\mathrm{CCD}}$ is

$$I^{\mathrm{B}}_{\mathrm{CCD}}(p_x, p_z, \omega) \equiv \int \mathrm{d}\tilde{p}_x \; B_x(\tilde{p}_x, p_x) \int \mathrm{d}\tilde{p}_z \; B_z(\tilde{p}_z, p_z, \omega) I^{\mathrm{m}}(\tilde{p}_x, \tilde{p}_z, \omega). \tag{5.101}$$

I^{m} is the predicted scattering intensity considering mosaicity, see Section 5.2.

Since the scattering theory is more conveniently expressed in terms of $\mathbf{q}$, $I^{\mathrm{B}}_{\mathrm{CCD}}$ Eq. (5.101) is rewritten. For small 2θ and ω, q_z (q_x) is approximately linear in p_z (p_x), see Eqs. (5.42) and (5.44), and therefore, Eq. (5.101) is approximately expressed as

$$I^{\mathrm{B}}_{\mathrm{CCD}}(p_x, p_z, \omega) \approx I^{\mathrm{B}}_{\mathrm{CCD}}(q_x, q_z, \omega) \tag{5.102}$$

$$= \left(\frac{\lambda s}{2\pi}\right)^2 \int \mathrm{d}\tilde{q}_x \; B_x(\tilde{q}_x, q_x) \int \mathrm{d}\tilde{q}_z \; B_z(\tilde{q}_z, q_z, \omega) I^{\mathrm{m}}\left[\tilde{q}_x, q_y(\tilde{q}_x, \tilde{q}_z, \omega), \tilde{q}_z\right], \tag{5.103}$$

where

$$B_x\left(\tilde{q}_x, q_x\right) \equiv \frac{1}{\sqrt{2\pi\tilde{\sigma}_x^2(q_x)}} \exp\left\{-\frac{\left(q_x - \tilde{q}_x\right)^2}{2\tilde{\sigma}_x^2(q_x)}\right\} \tag{5.104}$$

$$B_z\left(\tilde{q}_z, q_z, \omega\right) \equiv \frac{1}{\sqrt{2\pi\tilde{\sigma}_z^2(q_z, \omega)}} \exp\left\{-\frac{\left(q_z - \tilde{q}_z\right)^2}{2\tilde{\sigma}_z^2(q_z, \omega)}\right\} \tag{5.105}$$

$$\tilde{\sigma}_x(q_x) \equiv \frac{1}{\Upsilon\mathcal{S}}\left(\frac{2\pi}{\lambda} b_x + L_{\mathrm{s}} q_x\right) \tag{5.106}$$

$$\tilde{\sigma}_z(q_z, \omega) \equiv \frac{L_{\mathrm{s}}}{\Upsilon\mathcal{S}}\left(q_z - \frac{2\pi}{\lambda}\omega\right) \tag{5.107}$$

$$q_y(q_x, q_z, \omega) \approx -\frac{\lambda}{4\pi}\left(q_x^2 + q_z^2\right) + q_z\omega. \tag{5.108}$$

Eq. (5.108) is the result of substituting Eqs. (5.42) and (5.44) into Eq. (5.43). Since the intensity is not measured on an absolute scale, the prefactor in Eq. (5.103) is neglected.

Following the numerical analysis of the tilt-independent theory [48], the $\tilde{q}_z$-dependent integral is completed analytically assuming that $|F(q_z)|^2$ is locally constant on the scale of the beam height. The effect of beam shape on the scattering intensity is evaluated using $S^{\mathrm{m}}_{\mathrm{MD}}$ Eq. (5.28). By analogy, the result for $F_\Delta(q_z) S^{\mathrm{m}}_{0,\mathrm{MD}}(\mathbf{q})$ Eq. (5.28) is deduced at the end, see Eq. (5.118).

Substituting $S^{\mathrm{m}}_{\mathrm{MD}}(\mathbf{q})$, see Eqs. (5.28) and (5.14), into $I^{\mathrm{B}}_{\mathrm{CCD}}$ Eq. (5.103),

$$
\begin{aligned}
&I^{\mathrm{B}}_{\mathrm{CCD},1}(q_x, q_z, \omega) \\
&\approx \int \mathrm{d}\tilde{q}_x \; B_x(\tilde{q}_x, q_x) \int \mathrm{d}\tilde{q}_z \; B_z(\tilde{q}_z, q_z, \omega) \left|F(\tilde{q}_z)\right|^2 S^{\mathrm{m}}_{\mathrm{MD}}(\tilde{\mathbf{q}}) \qquad (5.109) \\
&= \sum_{j=0}^{\infty}{}' \int \mathrm{d}r \int_{-\infty}^{\infty} \mathrm{d}\tilde{q}_x \; B_x(\tilde{q}_x, q_x) r H_r(r) \cdot \\
&\quad \int_{-\infty}^{\infty} \mathrm{d}\tilde{q}_z \; B_z(\tilde{q}_z, q_z, \omega) \left|F(\tilde{q}_z)\right|^2 J_{\mathrm{m}}(\tilde{q}_r r) H_z(jD, \tilde{q}_z) \cos\left(jD\tilde{q}_z\right) e^{-\frac{\tilde{q}_z^2}{2} h_j(\rho,\ell,\tau)}, \qquad (5.110)
\end{aligned}
$$

where

$$
\tilde{q}_r(\tilde{q}_x, \tilde{q}_z, \omega) = \sqrt{\tilde{q}_x^2 + q_y^2\left(\tilde{q}_x, \tilde{q}_z, \omega\right)} \qquad (5.111)
$$

and

$$
J_{\mathrm{m}}(\tilde{q}_r r) \equiv \Big[J_0(q_r r) * P_{\mathrm{m}}(q_r) \Big](\tilde{q}_r). \qquad (5.112)
$$

Since B_z is narrow in $\tilde{q}_z$ compared to $H_z(jD, \tilde{q}_z)$, $\left|F(\tilde{q}_z)\right|^2$, and $q_y(\tilde{q}_x, \tilde{q}_z, \omega)$, the $\tilde{q}$-dependence of the aforementioned functions is replaced by q_z,

$$
\begin{aligned}
I^{\mathrm{B}}_{\mathrm{CCD},1}(q_x, q_z, \omega) \approx \left|F(q_z)\right|^2 \sum_{j=0}^{\infty}{}' \int \mathrm{d}r \; T_1\left(r, j, \omega, q_x, q_z\right) \cdot \\
\mathrm{Re}\left[\int_{-\infty}^{\infty} \mathrm{d}\tilde{q}_z \; B_z(\tilde{q}_z, q_z, \omega) e^{ijD\tilde{q}_z} e^{-\frac{\tilde{q}_z^2}{2} h_j(\rho,\ell,\tau)} \right], \qquad (5.113)
\end{aligned}
$$

where Re[...] returns the real part of its argument and

$$
T_1(r, j, \omega, q_x, q_z) \equiv \int_{-\infty}^{\infty} \mathrm{d}\tilde{q}_x \; B_x(\tilde{q}_x, q_x) r H_r(r) J_{\mathrm{m}}\left(\sqrt{\tilde{q}_x^2 + q_y^2(\tilde{q}_x, q_z, \omega)}\; r\right) H_z(jD, q_z). \qquad (5.114)
$$

Completing the $\tilde{q}_z$-dependent integral in Eq. (5.113) analytically,

$$T_2(\rho,\ell,\tau,j,\omega,q_z) \equiv \mathrm{Re}\left[\frac{1}{\sqrt{2\pi\tilde{\sigma}_z^2(q_z,\omega)}}\int_{-\infty}^{\infty}\mathrm{d}\tilde{q}_z\; e^{ijD\tilde{q}_z}e^{-\frac{\tilde{q}_z^2}{2}h_j(\rho,\ell,\tau)}e^{-\frac{(q_z-\tilde{q}_z)^2}{2\tilde{\sigma}_z^2(q_z,\omega)}}\right] \quad (5.115)$$

$$= \frac{1}{\sqrt{1+h_j\tilde{\sigma}_z^2}}\exp\left\{\frac{-q_z^2h_j - j^2D^2\tilde{\sigma}_z^2}{2\left(1+h_j\tilde{\sigma}_z^2\right)}\right\}\cos\left(\frac{q_zjD}{1+h_j\tilde{\sigma}_z^2}\right). \quad (5.116)$$

Substituting T_2 Eq. (5.116) into $I^{\mathrm{B}}_{\mathrm{CCD},1}$ Eq. (5.113)

$$I^{\mathrm{B}}_{\mathrm{CCD},1}(q_x,q_z,\omega) \approx |F(q_z)|^2\sum_{j=0}^{\infty}{}'\int \mathrm{d}r\; T_1(r,j,\omega,q_x,q_z)\,T_2(\rho,\ell,\tau,j,\omega,q_z). \quad (5.117)$$

The analogous result to $I^{\mathrm{B}}_{\mathrm{CCD},1}$ Eq. (5.117) involving $F_\Delta(q_z)S^{\mathrm{m}}_{0,\mathrm{MD}}(\mathbf{q})$ is

$$I^{\mathrm{B}}_{\mathrm{CCD},2}(q_x,q_z,\omega) \approx F_\Delta(q_z)\sum_{j}^{\infty}\delta_{j,0}\int \mathrm{d}r\; T_1(r,j,\omega,q_x,q_z)\,T_2(\rho,\ell,\tau,j,\omega,q_z). \quad (5.118)$$

5.3.4 Absorption Correction

Incident and scattered X-rays are attenuated by the sample. Also, scattering to different parts of the detector travel different path lengths within the sample. An absorption correction for low angle scattering as a function of p_z and ω has been previously derived [50]. The p_x-dependence is neglected since the X-ray path within the sample is nearly in the yz-plane for low angle scattering.

The absorption factor is, see Eq. (28) in [50],

$$A(\omega,p_z) \equiv \frac{\mu}{t_{\mathrm{s}}}\frac{1-\exp\left\{-\frac{t_{\mathrm{s}}}{\mu}g(\omega,p_z)\right\}}{g(\omega,p_z)}, \quad (5.119)$$

where

$$g(\omega,p_z) \equiv \frac{1}{\sin\omega} + \frac{1}{\sin\left[\tan^{-1}(p_z/s)-\omega\right]}, \quad (5.120)$$

μ is the X-ray absorption length in the sample, and t_{s} is the sample thickness. Using $I^{\mathrm{B}}_{\mathrm{CCD},1}$ Eq. (5.117) and $I^{\mathrm{B}}_{\mathrm{CCD},2}$ Eq. (5.118), the prediction for a fixed angle exposure is

$$I^{\mathrm{A}}_{\mathrm{CCD}}(q_x, q_z, \omega) \equiv A[\omega, p_z(q_x, q_z, \omega)] \left[I^{\mathrm{B}}_{\mathrm{CCD},1}(q_x, q_z, \omega) + I^{\mathrm{B}}_{\mathrm{CCD},2}(q_x, q_z, \omega) \right]. \quad (5.121)$$

5.3.5 CCD Integral

During an X-ray exposure, the incident angle ω was continuously varied by rotating the sample. The aforementioned effect is quantified by integrating the predicted fixed angle intensity $I^{\mathrm{A}}_{\mathrm{CCD}}$ Eq. (5.121) over the appropriate ω-values to give the final (F) theoretical intensity on the CCD,

$$I^{\mathrm{F}}_{\mathrm{CCD}}(p_x, p_z) \equiv \int_0^{\omega_{\mathrm{C}}(p_z)} \mathrm{d}\omega \; I^{\mathrm{A}}_{\mathrm{CCD}}(p_x, p_z, \omega), \quad (5.122)$$

where 0 and $\omega_{\mathrm{C}}(p_z)$ are the minimum and maximum incident angle, respectively, for which scattering from the sample to a given p_z-height on the detector is not blocked by the substrate, see Fig. 5.11,

$$\omega_{\mathrm{C}}(p_z) \equiv \tan^{-1}\left(\frac{p_z}{s}\right). \quad (5.123)$$

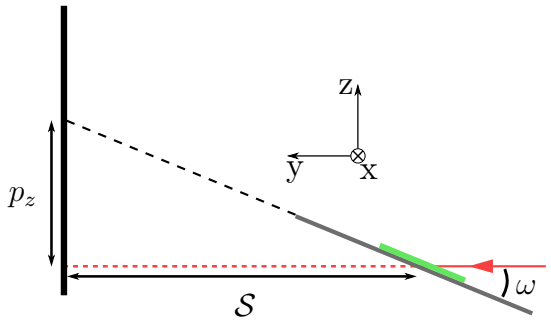


Figure 5.11: Scattering geometry describing the maximum substrate rotation angle ω before scattering from the sample (green rectangle) at pixel p_z is blocked by the substrate (gray rectangle). The red solid and dashed lines show the beam path without a sample. The thickness of the sample (10 μm) and substrate (1 mm) are not drawn to scale.

As written, $I^{\mathrm{F}}_{\mathrm{CCD}}$ Eq. (5.122) is awkward to calculate since the scattering intensity is more conveniently expressed in terms of $\mathbf{q}$. In the following derivation, the right-hand side of Eq. (5.122) is written and evaluated as a function of $\mathbf{q}$. In order to

proceed, several approximations regarding the transformation between (p_x, p_z, ω) and (q_x, q_y, q_z) are discussed.

Eqs. (5.38), (5.39), and (5.40) describe the relationship between (p_x, p_z, ω) and (q_x, q_y, q_z) and are reproduced below for convenience:

$$q_x(p_x, p_z) = \frac{2\pi p_x}{\lambda s} \frac{1}{\sqrt{\delta(p_x, p_z)}} \tag{5.124}$$

$$q_y(p_x, p_z, \omega) = \frac{2\pi}{\lambda} \left[\left(\frac{1}{\sqrt{\delta(p_x, p_z)}} - 1 \right) \cos\omega + \frac{p_z \sin\omega}{s} \frac{1}{\sqrt{\delta(p_x, p_z)}} \right] \tag{5.125}$$

$$q_z(p_x, p_z, \omega) = \frac{2\pi}{\lambda} \left[\left(1 - \frac{1}{\sqrt{\delta(p_x, p_z)}} \right) \sin\omega + \frac{p_z \cos\omega}{s} \frac{1}{\sqrt{\delta(p_x, p_z)}} \right]. \tag{5.126}$$

For a given pixel coordinate (p_x, p_z), varying ω describes a **q**-space trajectory which is a function of q_y and q_z in a plane of constant q_x. $I^{\mathrm{F}}_{\mathrm{CCD}}$ in Eq. (5.122) is expressed as

$$I^{\mathrm{F}}_{\mathrm{CCD}}(p_x, p_z) = \int_0^{\omega_{\mathrm{C}}(p_z)} \mathrm{d}\omega \; I^{\mathrm{A}}_{\mathrm{CCD}} \left[q_x(p_x, p_z), q_z(p_x, p_z, \omega), \omega \right]. \tag{5.127}$$

The p_x- and ω-dependences of q_z complicate the evaluation of Eq. (5.127). Therefore, $q_z(p_x, p_z, \omega)$ is approximated,[16]

$$q_z(p_x, p_z, \omega) \approx q^*_z(p_z) \equiv \frac{4\pi}{\lambda} \sin\left[\frac{1}{2} \tan^{-1}\left(\frac{p_z}{s} \right) \right] \tag{5.128}$$

$$= q_z[0, p_z, \omega_{\mathrm{C}}(p_z)/2]. \tag{5.129}$$

To establish the approximation in Eq. (5.128),

$$q^{\ddagger}_z(p_x, p_z, \omega) \equiv q_z(p_x, p_z, \omega) - q^*_z(p_z) \tag{5.130}$$

is plotted in Figs. 5.12 and 5.13 for $p_x = 0$ and $p_x = 300$, respectively. The narrowest

[16] Eq. (5.128) is further modified to correct for the difference in index of refraction between air and lipids following an Appendix in [48], but this makes negligible difference for the range $q_z > 0.2$ Å^{-1} typically analyzed.

q_z features are the Caillé peaks on the meridian ($p_x = 0$) whose FWHM increase with increasing peak index [41, 42, 43]. The first peak width can be less than 5×10^{-3} Å^{-1}, depending on the sample properties and the coherence of the incident beam, but higher index peaks are considerably broader. For reference, the height of 1 pixel is about $2\pi/(\lambda s) \approx 10^{-3}$ Å^{-1}, given the typical experimental geometry. q_z^* is a worse approximation for increasing p_x (see Fig. 5.13), but no narrow q_z features for large p_x and p_z are predicted. Therefore, $q_z^*(p_z)$ is an adequate approximation for $q_z(p_x, p_z, \omega)$ since $|q_z^\ddagger| \lesssim 1 \times 10^{-3}$ Å^{-1} for $p_x = 0$ and $p_z \lesssim 600$ which limits the p_z-range for the structure factor analysis.[17]

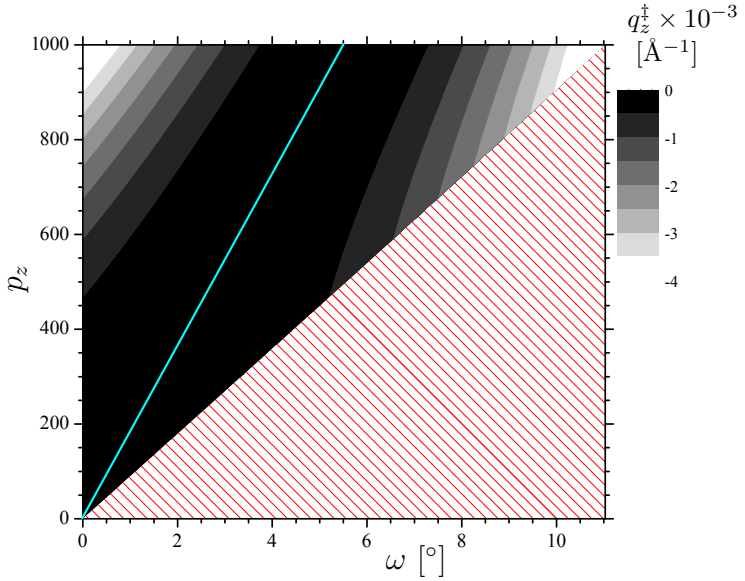


Figure 5.12: $q_z^\ddagger(0, p_z, \omega)$ Eq. (5.130) is plotted for $\lambda = 1.17$ Å, $p_s = 0.07113$ mm/pixel, and $\mathcal{S} = 365$ mm. The triangular (ω, p_z)-region patterned with red diagonal lines is not experimentally accessible because the substrate blocks the outgoing scattering. The cyan line indicates the p_z position of the specular scattering as a function of ω.

Substituting q_z^* Eq. (5.128) into $I_{\text{CCD}}^{\text{F}}$ Eq. (5.127),

$$I_{\text{CCD}}^{\text{F}}(p_x, p_z) \approx \int_0^{\omega_{\text{C}}(p_z)} \mathrm{d}\omega \; I_{\text{CCD}}^{\text{A}}\Big[q_x(p_x, p_z), q_z^*(p_z), \omega\Big]. \tag{5.131}$$

Eq. (5.131) is further approximated by neglecting the p_z-dependence of $q_x(p_x, p_z)$,

[17] For $p_z \gtrsim 600$, the measured $|F(q_z)|^2$ is an average over nearby $|F(p_z)|^2$-values.

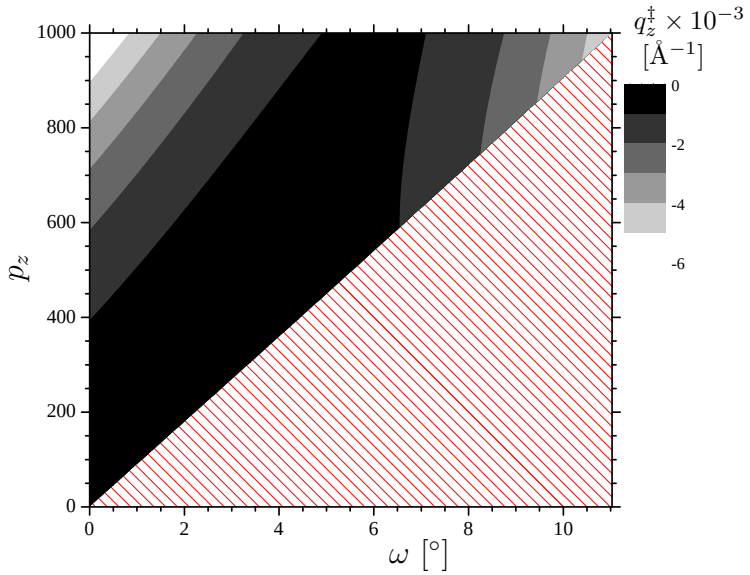


Figure 5.13: $q_z^{\ddagger}(300, p_z, \omega)$ Eq. (5.130) is plotted for $\lambda = 1.17$ Å, $p_s = 0.07113$ mm/pixel, and $\mathcal{S} = 365$ mm.

$$I^{\mathrm{F}}_{\mathrm{CCD}}(p_x, p_z) \approx \int_0^{\omega_{\mathrm{C}}(q_z)} \mathrm{d}\omega \; I^{\mathrm{A}}_{\mathrm{CCD}}\left[q_x^*(p_x), q_z^*(p_z), \omega\right], \tag{5.132}$$

where

$$q_x^*(p_x) \equiv \frac{2\pi}{\lambda} \sin\left[\tan^{-1}\left(\frac{p_x}{s}\right)\right]. \tag{5.133}$$

In Fig. 5.14,

$$q_x^{\ddagger}(p_x, p_z) \equiv q_x(p_x, p_z) - q_x^*(p_x) \tag{5.134}$$

is plotted. $\left|q_x^{\ddagger}(p_x, p_z)\right|$ varies by less than 6×10^{-3} Å^{-1}. Note that a difference of 1 pixel corresponds to a change in q_x of about 10^{-3} Å^{-1}. Since no narrow q_x features away from $p_x = 0$ are predicted, q_x^* is a reasonable approximation.

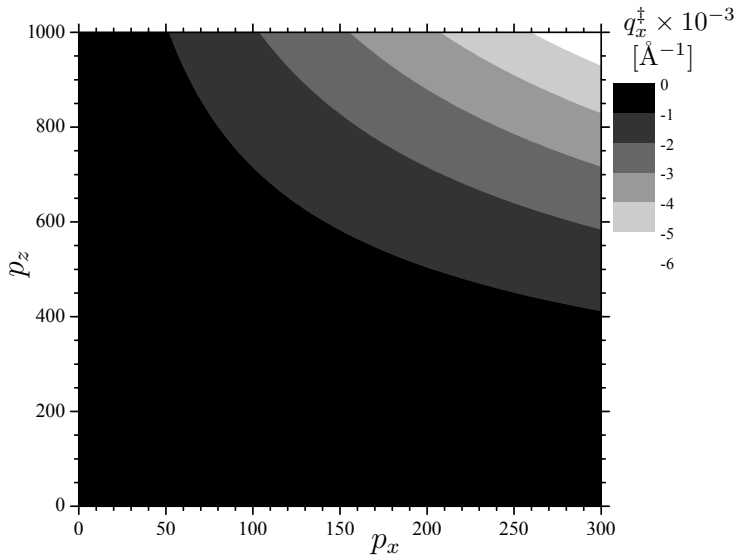


Figure 5.14: $q_x^{\ddagger}(p_x, p_z)$ Eq. (5.134) is plotted for $\lambda = 1.17$ Å, $p_s = 0.07113$ mm/pixel, and $\mathcal{S} = 365$ mm. $q_x(p_x, p_z)$ is better approximated by $q_x^*(p_x)$ for $p_x = 0$ as compared to $p_x = 300$.

5.4 Calculating the Final Structure Factor

Substituting $I^{\mathrm{A}}_{\mathrm{CCD}}$ Eq. (5.121) into $I^{\mathrm{F}}_{\mathrm{CCD}}$ Eq. (5.132) yields a final relation for the scattering intensity,

$$I^{\mathrm{F}}_{\mathrm{CCD}}(p_x, p_z) \approx I^{\mathrm{F}}_{\mathrm{CCD},1}[q^*_x(p_x), q^*_z(p_z)] + I^{\mathrm{F}}_{\mathrm{CCD},2}[q^*_x(p_x), q^*_z(p_z)] \tag{5.135}$$

where

$$\begin{aligned} I^{\mathrm{F}}_{\mathrm{CCD},1}(q_x, q_z) = |F(q_z)|^2 \int_0^{\omega_{\mathrm{C}}} \mathrm{d}\omega \; A(\omega, q_z) \int_{-\infty}^{\infty} \mathrm{d}\tilde{q}_x \, \frac{\exp\left\{-\frac{(\tilde{q}_x - q_x)^2}{2\tilde{\sigma}^2_x(q_x)}\right\}}{\sqrt{2\pi\tilde{\sigma}^2_x(q_x)}} \cdot \\ \int_0^{\infty} \mathrm{d}r \; r H_r(r) J_{\mathrm{m}}\left(\sqrt{\tilde{q}_x^2 + q_y^2(\tilde{q}_x, q_z, \omega)}\; r\right) \cdot \\ \sum_{j=0}^{\infty}{}' \, \frac{H_z(jD, q_z)}{\sqrt{1 + h_j\tilde{\sigma}_z^2}} \exp\left\{\frac{-q_z^2 h_j - j^2 D^2 \tilde{\sigma}_z^2}{2\,(1 + h_j\tilde{\sigma}_z^2)}\right\} \cos\left(\frac{q_z j D}{1 + h_j\tilde{\sigma}_z^2}\right) \end{aligned} \tag{5.136}$$

and $I^{\mathrm{F}}_{\mathrm{CCD},2}(q_x, q_z)$ follows by analogy from Eq. (5.136), replacing $|F(q_z)|^2$ by $F_\Delta(q_z)$ and introducing $\delta_{j\,0}$ after $\sum'$. Note, the dependences of several functions were not written explicitly in Eq. (5.136): $h_j(\rho, \ell, \tau)$, $\tilde{\sigma}_z(q_z, \omega)$, and $\omega_{\mathrm{C}}(p_z)$.

To further simplify the calculation of $I^{\mathrm{F}}_{\mathrm{CCD}}$, $\tilde{\sigma}_z(q_z, \omega)$ is approximated,

$$\tilde{\sigma}_z(q_z, \omega) \approx \tilde{\sigma}^*_z\left[q_z, \omega_{\mathrm{C}}(q_z)/2\right]. \tag{5.137}$$

$\tilde{\sigma}^*_z = \tilde{\sigma}_z$ for scattering along the meridian ($q_r = 0$) so the q_z heights of the Caillé peaks are correctly broadened within the aforementioned approximation. For pixels off the meridian, the correct geometrically broadened beam height is a function of ω. Because a particular (q_x, q_z) pair is accessible for an increasingly large range of ω-values for increasing q_x, $\tilde{\sigma}^*_z$ is an increasingly poor approximation for increasing q_x. Nevertheless, $\tilde{\sigma}^*_z$ is reasonable since no narrow q_z features far from the meridian are predicted.

Additionally, the ω-dependent integral is rewritten in terms of q_y to more easily interface with previous work [48]. Differentiating $q_y(q_x, q_y, \omega)$ Eq. (5.108) with respect

to ω,

$$\frac{\partial q_y}{\partial \omega} = q_z \tag{5.138}$$

$$\Rightarrow \partial\omega = \frac{\partial q_y}{q_z}. \tag{5.139}$$

The factor of q_z in the denominator of Eq. (5.139) is the standard Lorentz factor for oriented samples. Substituting Eq. (5.139) into $I^{\mathrm{F}}_{\mathrm{CCD},1}$ Eq. (5.136),

$$\begin{aligned} I^{\mathrm{F}}_{\mathrm{CCD},1}(q_x, q_z) = \frac{|F(q_z)|^2}{q_z} \int_{q_{y,\mathrm{lb}}}^{q_{y,\mathrm{ub}}} \mathrm{d}q_y \; A[\omega(q_x, q_y, q_z), q_z] \int_{-\infty}^{\infty} \mathrm{d}\tilde{q}_x \, \frac{\exp\left\{-\frac{(\tilde{q}_x - q_x)^2}{2\tilde{\sigma}_x^2(q_x)}\right\}}{\sqrt{2\pi\tilde{\sigma}_x^2(q_x)}} \cdot \\ \int_0^{\infty} \mathrm{d}r \; r H_r(r) J_{\mathrm{m}}\left(\sqrt{\tilde{q}_x^2 + q_y^2}\; r\right) \cdot \\ \sum_{j=0}^{\infty}{}' \, \frac{H_z(jD, q_z)}{\sqrt{1 + h_j\tilde{\sigma}_z^2}} \exp\left\{\frac{-q_z^2 h_j - j^2 D^2 \tilde{\sigma}_z^2}{2\left(1 + h_j\tilde{\sigma}_z^2\right)}\right\} \cos\left(\frac{q_z j D}{1 + h_j\tilde{\sigma}_z^2}\right) \end{aligned} \tag{5.140}$$

where

$$\omega(q_x, q_y, q_z) \approx \frac{1}{q_z}\left[q_y + \frac{\lambda}{4\pi}\left(q_x^2 + q_z^2\right)\right], \tag{5.141}$$

$$q_{y,\mathrm{lb}}(q_x, q_z) \equiv -\frac{\lambda}{4\pi}\left(q_x^2 + q_z^2\right), \tag{5.142}$$

$$q_{y,\mathrm{ub}}(q_x, q_z) \equiv -\frac{\lambda}{4\pi}\left(q_x^2 + q_z^2\right) + q_z\omega_{\mathrm{C}}(q_z), \tag{5.143}$$

$$\omega_{\mathrm{C}}(q_z) \approx \tan^{-1}\left(\frac{\lambda q_z}{2\pi}\right), \tag{5.144}$$

and again, $I^{\mathrm{F}}_{\mathrm{CCD},2}(q_x, q_z)$ follows by analogy.

Previous work [48] neglected the q_x-dependence of the q_y-integration limits, assuming $q_z \gg q_x$. Fig. 5.15 shows the derived q_y integration limits. For comparison, the previous q_x-independent integration limits would be horizontal lines in Fig. 5.15, overlapping the depicted limits at $q_x = 0$. The q_y integration range increases for increasing q_z. Most importantly, the q_y integration range does not include $q_y = 0$ at sufficiently large q_x. For instance, see the pair of solid black lines in Fig. 5.15.

The q_x-dependence of the CCD integral's limits is emphasized when comparing the predictions of structure factors expressed in Cartesian vs. cylindrical coordinates, see Appendix B.

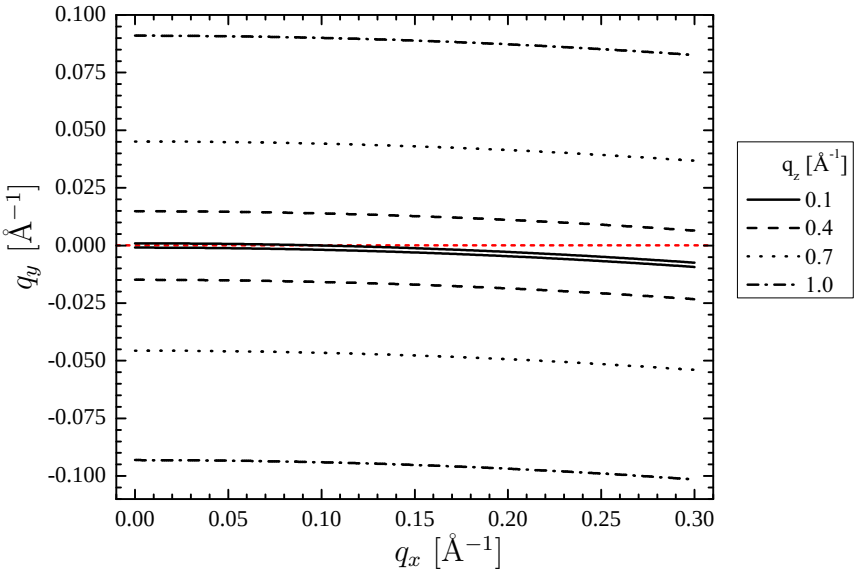


Figure 5.15: The CCD integral q_y-limits as a function of q_x at various q_z values (as shown in the legend). The pairs of lines depict upper and lower limits. The red dashed line is a guide to the eye to emphasize the q_x-dependence.

$I^{\mathrm{F}}_{\mathrm{CCD},i}$ are nontrivial to numerically evaluate because of the several nested integrals. Following previous work [48], $I^{\mathrm{F}}_{\mathrm{CCD},1}$ is expressed in a more computationally convenient form,

$$f_1(\rho, q_z) \equiv \sum_{j=0}^{\infty}{}' \frac{H_z(jD, q_z)}{\sqrt{1 + h_j \tilde{\sigma}_z^{*2}}} \exp\left\{ -\frac{q_z^2 h_j + j^2 D^2 \tilde{\sigma}_z^{*2}}{2\left(1 + h_j \tilde{\sigma}_z^{*2}\right)} \right\} \cos\left(\frac{q_z j D}{1 + h_j \tilde{\sigma}_z^{*2}} \right) \tag{5.145}$$

$$f_2(q_r, q_z) \equiv \int_0^{\infty} \mathrm{d}r \; r H_r(r) J_{\mathrm{m}}(q_r r) f_1(\rho, q_z) \tag{5.146}$$

$$f_3(q_x, q_z) \equiv \int_{q_{y,\mathrm{lb}}}^{q_{y,\mathrm{ub}}} \mathrm{d}q_y \; A[\omega(q_x, q_y, q_z), q_z] \, f_2\left(\sqrt{q_x^2 + q_y^2}, q_z \right) \tag{5.147}$$

$$I^{\mathrm{F}}_{\mathrm{CCD},1}(q_x, q_z) \approx \frac{|F(q_z)|^2}{q_z} \int_{-\infty}^{\infty} \mathrm{d}\tilde{q}_x \; \frac{\exp\left\{ -\frac{(\tilde{q}_x - q_x)^2}{2\tilde{\sigma}_x^2(q_x)} \right\}}{\sqrt{2\pi \tilde{\sigma}_x^2(q_x)}} f_3\left(\tilde{q}_x, q_z\right) \tag{5.148}$$

$$\equiv \frac{|F(q_z|^2}{q_z} S^{\mathrm{F}}_{\mathrm{CCD},1}(q_x, q_z). \tag{5.149}$$

In turn, each f_i is evaluated and the results tabled to be later interpolated when evaluating f_{i+1}. The aforementioned methodology significantly reduces the number of times f_1, f_2, and f_3 are evaluated as compared to a naive evaluation of $I^{\mathrm{F}}_{\mathrm{CCD},1}$ Eq. (5.136). For similar equations derived and used in previous work, see the Section "Cache the curves" pp. 65-66 in Dr. Liu's thesis [48]. Note, if $|F(q_z)|^2$ is replaced by $F_\Delta(q_z)$ and $\delta_{j\,0}$ is introduced after $\sum'$, the resulting modified f_i efficiently calculate $I^{\mathrm{F}}_{\mathrm{CCD},2}$,

$$f_1'(\rho, q_z) \equiv \sum_{j=0}^{\infty}{}' \delta_{j\,0} \frac{H_z(jD, q_z)}{\sqrt{1+h_j\tilde{\sigma}_z^{*2}}} \exp\left\{-\frac{q_z^2 h_j + j^2 D^2 \tilde{\sigma}_z^{*2}}{2\left(1+h_j\tilde{\sigma}_z^{*2}\right)}\right\} \cos\left(\frac{q_z j D}{1+h_j\tilde{\sigma}_z^{*2}}\right) \tag{5.150}$$

$$I^{\mathrm{F}}_{\mathrm{CCD},2}(q_x, q_z) \equiv \frac{F_\Delta(q_z)}{q_z} S^{\mathrm{F}}_{\mathrm{CCD},2}(q_x, q_z). \tag{5.151}$$

The theoretical prediction for the measured scattering intensity is

$$I^{\mathrm{F}}_{\mathrm{CCD}}\left[q_x(p_x), q_z(p_z)\right] = \frac{|F(q_z)|^2}{q_z} S^{\mathrm{F}}_{\mathrm{CCD},1}(q_x, q_z) + \frac{F_\Delta(q_z)}{q_z} S^{\mathrm{F}}_{\mathrm{CCD},2}(q_x, q_z) \tag{5.152}$$

$$= I_{\mathrm{m}}\left(p_x, p_z\right) - c(p_z), \tag{5.153}$$

where $I_{\mathrm{m}}(p_x, p_z)$ is the measured scattering intensity and $c(p_z)$ models remaining background scattering. The approximate relations between **q**-space and CCD-space were presented earlier, see Eq. (5.128) and Eq. (5.133). While predictions for $S^{\mathrm{F}}_{\mathrm{CCD},1}$ and $S^{\mathrm{F}}_{\mathrm{CCD},2}$ have been derived, both $F(q_z)$ and $F_\Delta(q_z)$ are unknown functions, if possible determined by analyzing data.

Chapter 6

Survey of Predicted Structure Factors

Before fitting measured scattering intensity, many attributes of the experimental structure factors, $S^{\mathrm{F}}_{\mathrm{CCD},1}$ Eq. (5.149) and $S^{\mathrm{F}}_{\mathrm{CCD},2}$ Eq. (5.151), are highlighted in an effort to reduce the number of model parameters and constrain parameter values. $S^{\mathrm{F}}_{\mathrm{CCD},1}$ and $S^{\mathrm{F}}_{\mathrm{CCD},2}$ are functions of many parameters, see Table 6.1 for typical values. Except for $\{K_c,\, B,\, K_\theta,\, \mathscr{L}_r,\, \mathscr{L}_z,\, a\}$, all other parameter values are either known *a priori* or evaluated prior to the structure factor analysis. $\{K_c,\, B,\, \mathscr{L}_r,\, \mathscr{L}_z\}$ are familiar from the tilt-independent model [48]; $\{K_\theta,\, a\}$ are new parameters.

First, the sensitivity of $S^{\mathrm{F}}_{\mathrm{CCD},1}$ to the six primary structure factor parameters $\{K_c,\, B,\, K_\theta,\, \mathscr{L}_r,\, \mathscr{L}_z,\, a\}$ is established in Section 6.1. Anticipating later results, $S^{\mathrm{F}}_{\mathrm{CCD},2}$ is ignored and only exponential subvolume distribution functions are considered. The moduli K_c, K_θ, and B are the primary material descriptors of the model stacked membrane system. In Section 6.1.1, it is shown that each modulus affects $S^{\mathrm{F}}_{\mathrm{CCD},1}$ significantly and differently, and therefore, it is plausible that all three moduli can be determined by fitting experimental data. $\mathscr{L}_r$ and $\mathscr{L}_z$ are characteristic domain dimensions, and in Sections 6.1.2 and 6.1.3, $S^{\mathrm{F}}_{\mathrm{CCD},1}$ is shown to be fairly insensitive to values of both $\mathscr{L}_r$ and $\mathscr{L}_z$ in the chosen fitting region. The a parameter limits short in-plane correlations, and $S^{\mathrm{F}}_{\mathrm{CCD},1}$ as a function of a is discussed in Section 6.1.4.

Gaussian and exponential subvolume distributions are compared in Section 6.2. It is established that the two functions predict similar $S^{\mathrm{F}}_{\mathrm{CCD},1}$, and therefore, to minimize the number of model parameters, exponential distributions are employed. Then in Section 6.3, the extent to which finite sized domains are quantitatively described by

the derived infinite sized domain height-height correlation function is investigated, and minimum reasonable values of $\mathscr{L}_r$ and $\mathscr{L}_z$ are forwarded. Finally, $S^{\mathrm{F}}_{\mathrm{CCD},1}$ and $S^{\mathrm{F}}_{\mathrm{CCD},2}$ are compared in Section 6.4.

The relevant regions of $S^{\mathrm{F}}_{\mathrm{CCD},1}(q_x, q_z)$ and $S^{\mathrm{F}}_{\mathrm{CCD},2}(q_x, q_z)$ are determined by the the measured and analyzed q_x, q_z-regions. Fig. 6.1 shows a typical detector exposure and corresponding commonly analyzed q_x, q_z-region ($0.01 \lesssim q_x \lesssim 0.22$ Å^{-1} and $0.3 \lesssim q_z \lesssim 0.6$ Å^{-1}). The analyzed q_x, q_z-region is primarily dictated by where the measured intensity is significant.[18] The lower bound of the q_x-range is greater than zero for several reasons. First, the predicted scattering intensity neglects the specular scattering from the substrate, known to be significant near $q_x = 0$ along q_z. Second, the predicted scattering intensity is increasingly dependent on long length scale phenomena for decreasing $|q_x|$. The measured and predicted intensity are compared over a q_x-range which will be shown to be sensitive to the most important parameters $\{K_c$, B, $K_\theta\}$ and nearly insensitive to the less important long length scale parameters $\{\mathscr{L}_r$, $\mathscr{L}_z\}$.

Unless otherwise stated, the parameter values used to plot $S^{\mathrm{F}}_{\mathrm{CCD},1}$ and $S^{\mathrm{F}}_{\mathrm{CCD},2}$ in this chapter are listed in Table 6.1. Since $|F(q_z)|^2$ and $F_\Delta(q_z)$ are unknown, $S^{\mathrm{F}}_{\mathrm{CCD},1}(q_x, q_z)$ parameter values are primarily determined by the q_x-dependence of $S^{\mathrm{F}}_{\mathrm{CCD},1}$. Therefore, $S^{\mathrm{F}}_{\mathrm{CCD},1}$ is often plotted as a function of q_x for several representative q_z-values, and these curves are normalized at $q_x = 0.01$ Å^{-1} to emphasize the q_x-dependence for larger q_x. Fig. 6.2 shows $S^{\mathrm{F}}_{\mathrm{CCD},1}$ for the parameter values listed in Table 6.1. Because of the out-of-plane periodicity of the stacked bilayer sample, $S^{\mathrm{F}}_{\mathrm{CCD},1}$ for $q_x = 0$ is a local maximum at $q_z = 2\pi h/D$ and a local minimum near $q_z = 2\pi\left(h + \frac{1}{2}\right)/D$, where the whole number h indexes the peaks. $S^{\mathrm{F}}_{\mathrm{CCD},1}$ as a function of q_x is often plotted at q_z-values that correspond to the $h = 3$ peak and halfway between the $h = 3$ and $h = 4$ peaks (0.3 Å^{-1} and 0.35 Å^{-1}, respectively, for $D = 20\pi$ Å). These q_z-values are representative in the sense that they are the center ($2\pi h/D$) and boundary ($2\pi\left(h + \frac{1}{2}\right)/D$) of a Brillouin Zone. Additionally, $q_z = 0.3$ Å^{-1} and 0.35 Å^{-1} correspond to the most intense data within the commonly analyzed region.

[18] The bilayer scattering for $q_z \lesssim 0.2$ Å^{-1} is known to be strong but is not commonly analyzed because of outstanding issues [48].

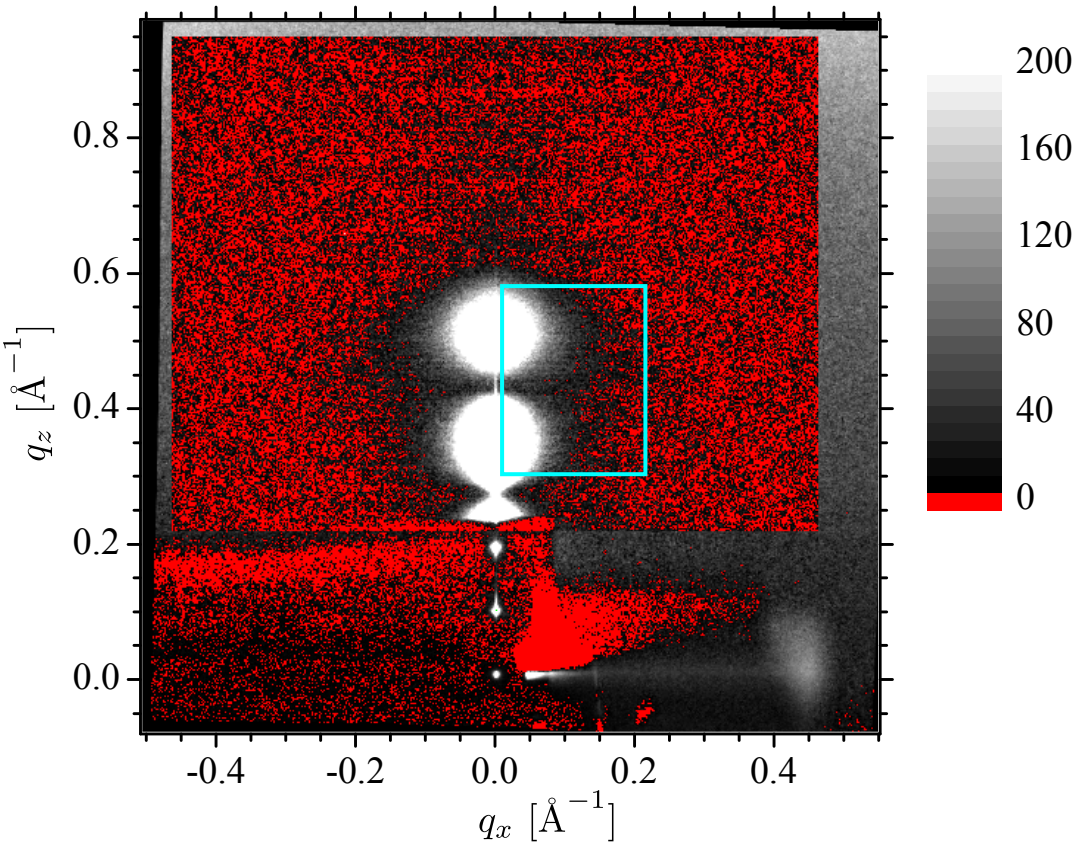


Figure 6.1: The background subtracted scattering intensity from a stack of DOPC bilayers is shown. The beam stop covers the region defined by $q_z \lesssim 0.2$ Å^{-1} and $q_x \lesssim 0.08$ Å^{-1}. Intensity is indicated by the linear grayscale. The red pixels indicate intensity less than zero. The predicted theoretical intensity is fitted to measured data within the cyan rectangle ($0.01 \lesssim q_x \lesssim 0.22$ Å^{-1} and $0.3 \lesssim q_z \lesssim 0.6$ Å^{-1}). This chapter demonstrates why these are the data that are fitted to obtain mechanical moduli.

Table 6.1: Default parameter values used to calculate examples of $S^{\mathrm{F}}_{\mathrm{CCD},1}$ and $S^{\mathrm{F}}_{\mathrm{CCD},2}$

	parameter	[units]	value	description
primary model	K_c	[ergs]	8×10^{-13}	bending modulus
	B	[ergs/cm^4]	1×10^{13}	bulk modulus
	K_θ	[mN/m]	95	tilt modulus
	$\mathscr{L}_r$	[Å]	5000	characteristic domain diameter
	$\mathscr{L}_z$	[Å]	$10D$	characteristic domain height
	a	[Å]	12	shortest in-plane length
sample	D	[Å]	62.8	out-of-plane repeat distance
	T	[°C]	30	temperature
	L_{s}	[mm]	5	sample length along beam
	t_{s}	[μm]	10	sample thickness
	γ_{m}	[°]	0	FWHM of mosaicity distribution
	μ	[mm]	2.6	$1/e$ X-ray absorption length in sample
	ϵ		0.999998	index of refraction
experimental	λ	[Å]	1.175	X-ray wavelength
	$\mathcal{S}$	[mm]	360	sample to detector distance
	p_{s}	[mm/pixel]	0.07113	pixel size
	b_x	[pixels]	2.3	beam width on CCD in x-direction
	$\Delta\lambda/\lambda$		0.0134	energy dispersion
	$\Delta\gamma_x$		1×10^{-4}	beam angular divergence in x-direction
	$\Delta\gamma_z$		1×10^{-4}	beam angular divergence in z-direction
coherence	$\xi_{\mathrm{T}x}$	[Å]	6000	transverse beam coherence along $\hat{\mathbf{x}}$
	$\xi_{\mathrm{T}z}$	[Å]	6000	transverse beam coherence along $\hat{\mathbf{z}}$
	ξ_{L}	[Å]	44	longitudinal beam coherence

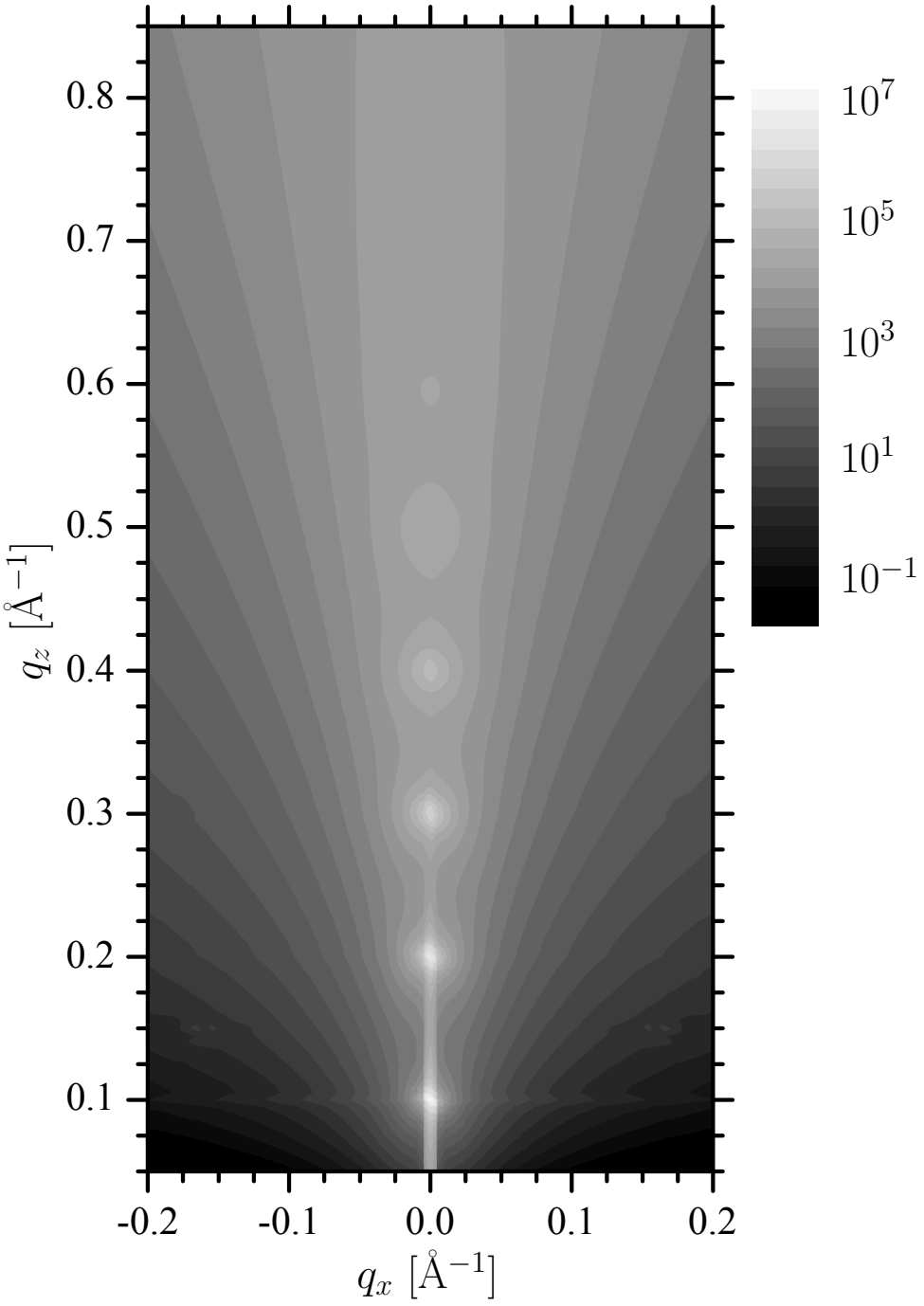


Figure 6.2: $S^{\mathrm{F}}_{\mathrm{CCD},1}$ is shown using a logarithmic grayscale for the parameter values in Table 6.1. The peaks along q_z centered at $q_x = 0$ correspond to the repeat out-of-plane distance. The peaks are decreasingly apparent for increasing q_z primarily because of bilayer midplane fluctuations. For constant q_z, $S^{\mathrm{F}}_{\mathrm{CCD},1}$ decays for increasing $|q_x|$.

6.1 Primary Structure Factor Parameters

First in Section 6.1.1, $S^{\mathrm{F}}_{\mathrm{CCD},1}(q_x, q_z)$ is investigated as a function of varying the values of K_c, B, and K_θ. Then in Sections 6.1.2 and 6.1.3, the sensitivity of $S^{\mathrm{F}}_{\mathrm{CCD},1}$ on the values of the characteristic sample domain lengths $\mathscr{L}_r$ and $\mathscr{L}_z$ is demonstrated.

6.1.1 K_c, B, and K_θ

Fig. 6.3 shows $S^{\mathrm{F}}_{\mathrm{CCD},1}(q_x, q_z)$ as a function of q_x for various values of K_c. As K_c increases, $S^{\mathrm{F}}_{\mathrm{CCD},1}$ monotonically decreases for all nonzero q_x-values. For $q_z = 2\pi\left(h + \frac{1}{2}\right)/D$, $S^{\mathrm{F}}_{\mathrm{CCD},1}$ decays less rapidly than when $q_z = 2\pi h/D$ or $q_z = 2\pi(h+1)/D$ [44].

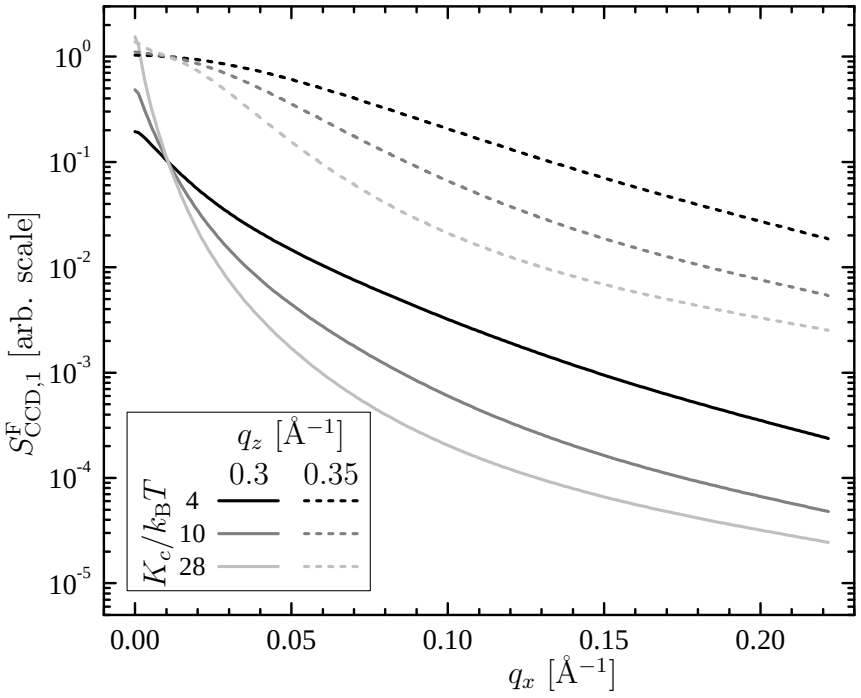


Figure 6.3: $S^{\mathrm{F}}_{\mathrm{CCD},1}$ is plotted as a function of q_x for various K_c-values. The curves have been normalized at $q_x = 0.01$ Å^{-1}, and additionally, the solid lines are vertically offset by 10^{-1} to improve visibility. See Table 6.1 for parameter values.

Fig. 6.4 shows $S^{\mathrm{F}}_{\mathrm{CCD},1}$ as a function of q_x for various values of B. For $q_z = 0.3$ Å^{-1}, increasing B affects $S^{\mathrm{F}}_{\mathrm{CCD},1}$ similarly to increasing K_c in Fig. 6.3. However, increasing B increases $S^{\mathrm{F}}_{\mathrm{CCD},1}$ for $q_z = 0.35$ Å^{-1} (see Fig. 6.4), opposite to the effect of increasing K_c. Therefore, values of both K_c and B are determined by fitting the experimental data as a function of both q_x and q_z, as was emphasized in earlier work [44].

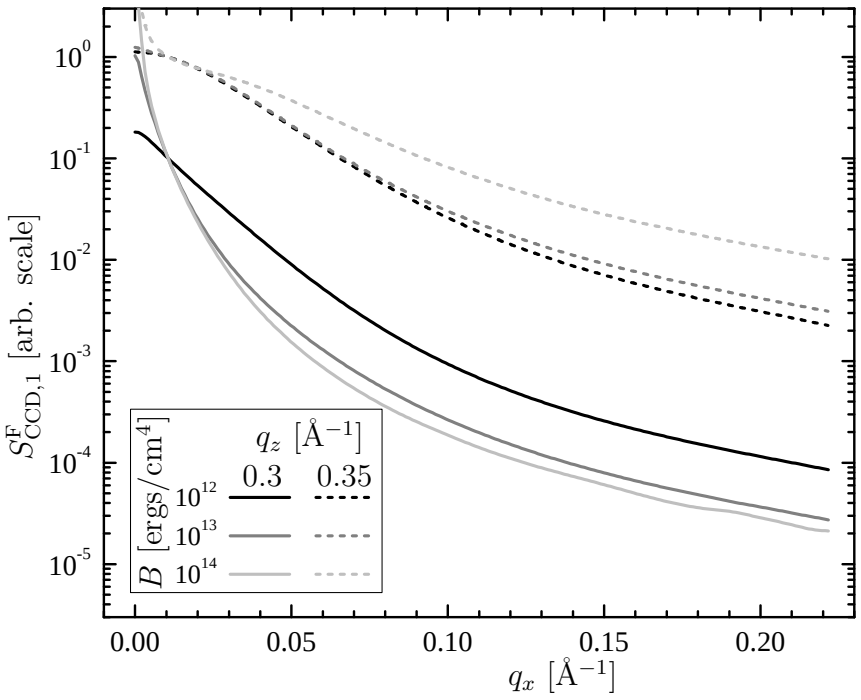


Figure 6.4: $S^{\mathrm{F}}_{\mathrm{CCD},1}$ is plotted as a function of q_x for various B-values. The curves have been normalized at $q_x = 0.01$ Å^{-1}, and the solid lines are vertically offset by 10^{-1}.

Fig. 6.5 shows $S^{\mathrm{F}}_{\mathrm{CCD},1}$ as a function of q_x for various values of K_θ. The $K_\theta = \infty$ curve is the tilt-independent prediction. As K_θ increases, $S^{\mathrm{F}}_{\mathrm{CCD},1}$ more rapidly decays, qualitatively similar to increasing K_c. Importantly, modifying K_θ primarily affects $S^{\mathrm{F}}_{\mathrm{CCD},1}$ for $q_x > 0.05$ Å^{-1} as expected since tilt is related to shorter length scales than undulations. A tilt-dependent model is required to increase the predicted $S^{\mathrm{F}}_{\mathrm{CCD},1}$ at larger q_x without significantly altering $S^{\mathrm{F}}_{\mathrm{CCD},1}$ at smaller q_x. Finally, since K_c, B, and K_θ uniquely influence the experimental structure factor within the typically analyzed q_x, q_z-region, the values of all three moduli should be quantifiable.

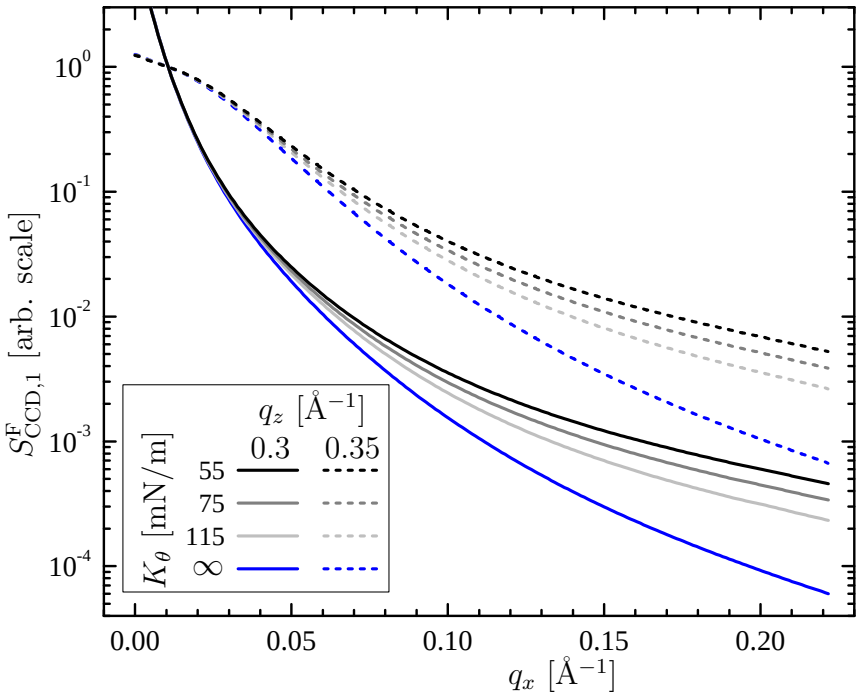


Figure 6.5: $S^{\mathrm{F}}_{\mathrm{CCD},1}$ is plotted as a function of q_x for various K_θ-values. The curves have been normalized at $q_x = 0.01$ Å^{-1}.

6.1.2 $\mathscr{L}_r$

$\mathscr{L}_r$ was first introduced in Section 5.1 and describes the characteristic in-plane domain size. The value of $\mathscr{L}_r$ is compared to the appropriate beam coherence lengths projected onto the sample $\{\mathcal{L}_x, \mathcal{L}_y\}$ to determine the characteristic in-plane size $\mathfrak{L}_r$ of the subvolume distribution function, see Section 5.3.2,

$$\begin{aligned} \mathfrak{L}_r &= \mathrm{Min}\left[\mathcal{L}_x, \mathcal{L}_y, \mathscr{L}_r\right] \\ &\approx \mathrm{Min}\left[\xi_{\mathrm{T}x}, \xi_{\mathrm{T}z}, \mathscr{L}_r\right]. \end{aligned} \tag{6.1}$$

The values of $\xi_{\mathrm{T}x}$ and $\xi_{\mathrm{T}z}$ are known and related to the experimentally determined beam angular divergence. In contrast, the value of $\mathscr{L}_r$ is unknown. Importantly given Eq. (6.1), $S^{\mathrm{F}}_{\mathrm{CCD},1}$ is independent of $\mathscr{L}_r$ for all values of $\mathscr{L}_r$ greater than both $\xi_{\mathrm{T}x}$ and $\xi_{\mathrm{T}z}$; for the values listed in Table 6.1, the effective maximum of $\mathscr{L}_r$ is nearly the same as $\xi_{\mathrm{T}x} = \xi_{\mathrm{T}z} \approx 6000$ Å. Fig. 6.6 shows $S^{\mathrm{F}}_{\mathrm{CCD},1}$ as a function of q_z for $\mathscr{L}_r = 600$ Å and $\mathscr{L}_r = \xi_{\mathrm{T}x}$. The curves become increasingly similar for increasing q_x, comparing solid ($q_x = 0$ Å^{-1}) and dashed ($q_x = 0.01$ Å^{-1}) lines. Fig. 6.7 shows $S^{\mathrm{F}}_{\mathrm{CCD},1}$ as a function of q_x at two q_z-values. $\mathscr{L}_r$ is most influential at small q_x and q_z. For increasing $\mathscr{L}_r$, intensity is shifted towards $q_x = 0$, making the peaks narrower in q_x. In the typically analyzed q_x, q_z-region, the precise value of $\mathscr{L}_r$ does not significantly affect $S^{\mathrm{F}}_{\mathrm{CCD},1}$. Fitting results presented in Section 7.2 further address the extent to which $\mathscr{L}_r$ is a necessary model parameter.

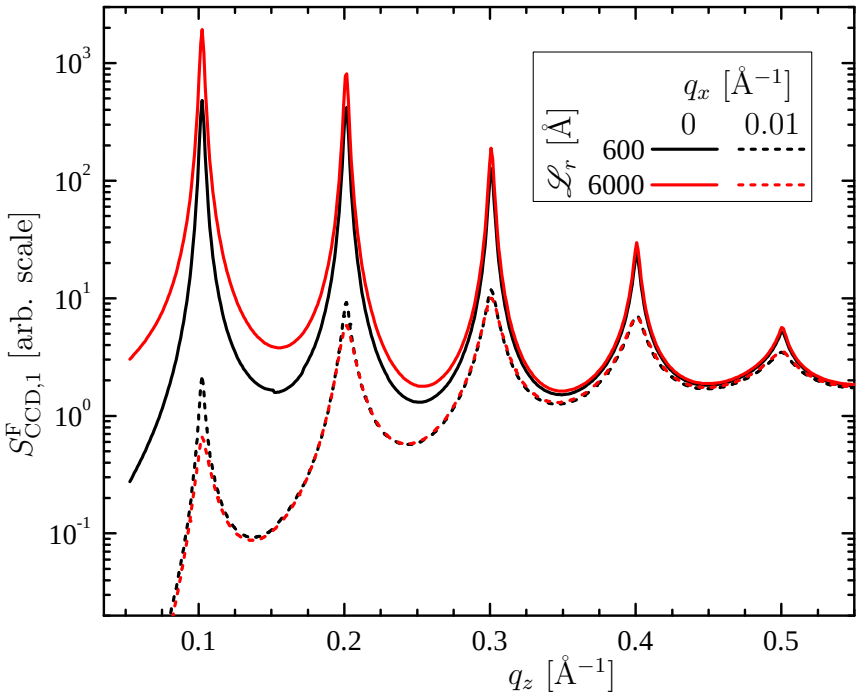


Figure 6.6: $S^{\mathrm{F}}_{\mathrm{CCD},1}(q_x, q_z)$ is plotted as a function of q_x for $\mathscr{L}_r = 600$ Å and $\mathscr{L}_r = \xi_{\mathrm{T}x} \approx 6000$ Å. The curves have been normalized at $q_z = 1$ Å^{-1}. Beyond $q_z \approx 0.55$ Å^{-1} the curves continue to converge.

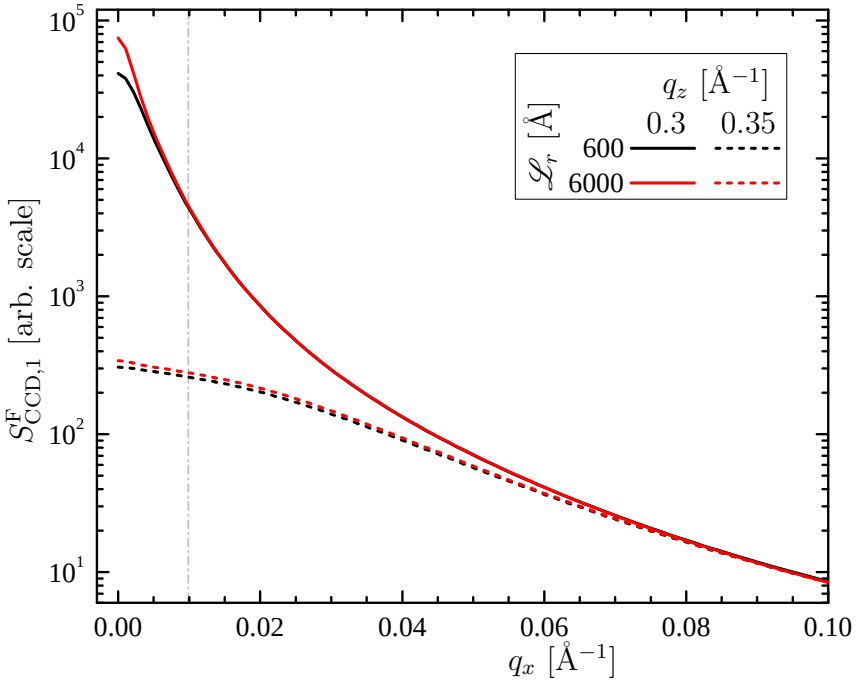


Figure 6.7: $S^{\mathrm{F}}_{\mathrm{CCD},1}(q_x, q_z)$ is plotted as a function of q_x for $\mathscr{L}_r = 600$ Åand 6000 Å. The curves have been normalized at $q_x = 0.2$ Å^{-1}. The vertical gray dashed-dotted line indicates the typical smallest analyzed q_x-value, see Fig. 6.1. Beyond $q_x \approx 0.1$ Å^{-1} the curves continue to converge.

6.1.3 $\mathscr{L}_z$

$\mathscr{L}_z$ was first introduced in Section 5.1 and describes the characteristic out-of-plane domain size. The value of $\mathscr{L}_z$ is compared to the appropriate beam coherence lengths projected onto the sample to determine the characteristic out-of-plane size $\mathfrak{L}_z$ of the subvolume distribution function, see Section 5.3.2,

$$\mathfrak{L}_z = \text{Min}\left[\xi_{\text{T}z}, \frac{2\pi\xi_{\text{L}}}{q_z\lambda}, \mathscr{L}_z\right]. \tag{6.2}$$

The values of $\xi_{\text{T}z}$ and ξ_{L} are experimentally determined and are fixed input values to the fitting program. However, the value of $\mathscr{L}_z$ is unknown. Importantly, given Eq. (6.2) and the parameter values in Table 6.1, all $\mathscr{L}_z$-values greater than about 800 Å are effectively equivalent, given the typical q_z-range for structure factor analysis (see Fig. 6.1).

Fig. 6.8 shows $S^{\text{F}}_{\text{CCD},1}$ as a function of q_z for $\mathscr{L}_z = 400$ Å and 800 Å. The curves become increasingly similar for increasing q_x, comparing solid ($q_x = 0$ Å^{-1}) and dashed ($q_x = 0.01$ Å^{-1}) lines. Fig. 6.9 shows $S^{\text{F}}_{\text{CCD},1}$ as a function of q_x for two q_z-values. $\mathscr{L}_z$ is most influential at small q_x and q_z; increasing $\mathscr{L}_z$ primarily narrows the peaks in q_z.

$S^{\text{F}}_{\text{CCD},1}$ as a function of q_x is fairly insensitive to $\mathscr{L}_z$ in the commonly analyzed q_x, q_z-region. To reduce the number of model parameters, the appropriate coherence lengths, $\xi_{\text{T}z}$ and ξ_{L}, can be assumed to determine the limiting out-of-plane correlation lengths if $\mathscr{L}_z$ is fixed such that $\mathscr{L}_z > \xi_{\text{T}z}$ and $\mathscr{L}_z > (2\pi\xi_{\text{L}})/(q_z\lambda)$. Within the aforementioned procedure, $\mathfrak{L}_z$ will be q_z-dependent, varying monotonically from about 800 Å to 400 Å for 0.3 Å$^{-1} \lesssim q_z \lesssim 0.6$ Å^{-1}. In the commonly analyzed q_x, q_z-region, the precise value of $\mathscr{L}_z$ does not significantly influence $S^{\text{F}}_{\text{CCD},1}$. The extent to which $\mathscr{L}_z$ is a necessary model parameter is further evaluated by fitting the experimental data, see Section 7.2.

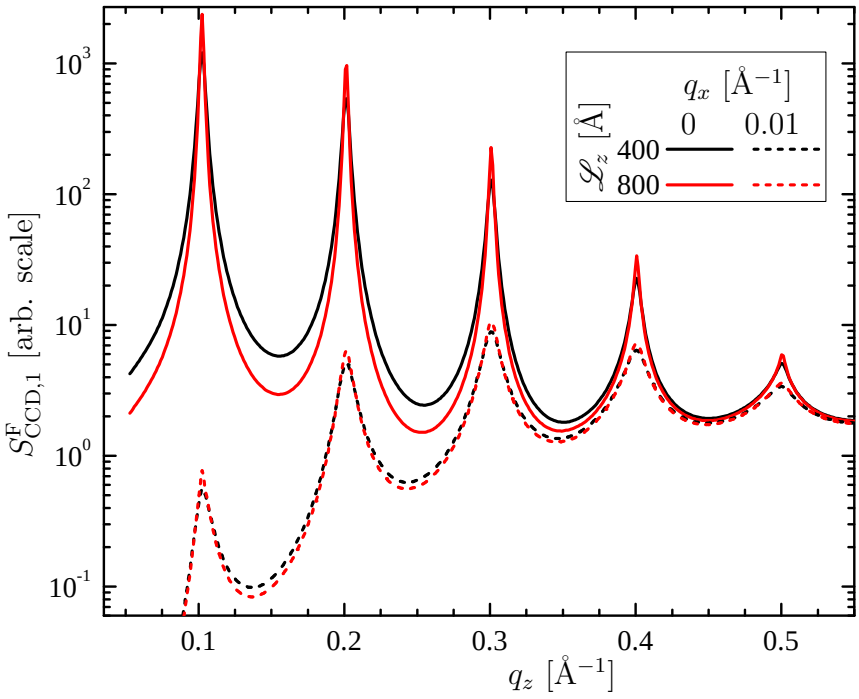


Figure 6.8: $S^{\mathrm{F}}_{\mathrm{CCD},1}(q_x, q_z)$ is plotted as a function of q_z for $\mathscr{L}_z = 400$ Å and 800 Å. The curves have been normalized at $q_z = 1$ Å^{-1}. Beyond $q_z \approx 0.55$ Å^{-1} the curves continue to converge.

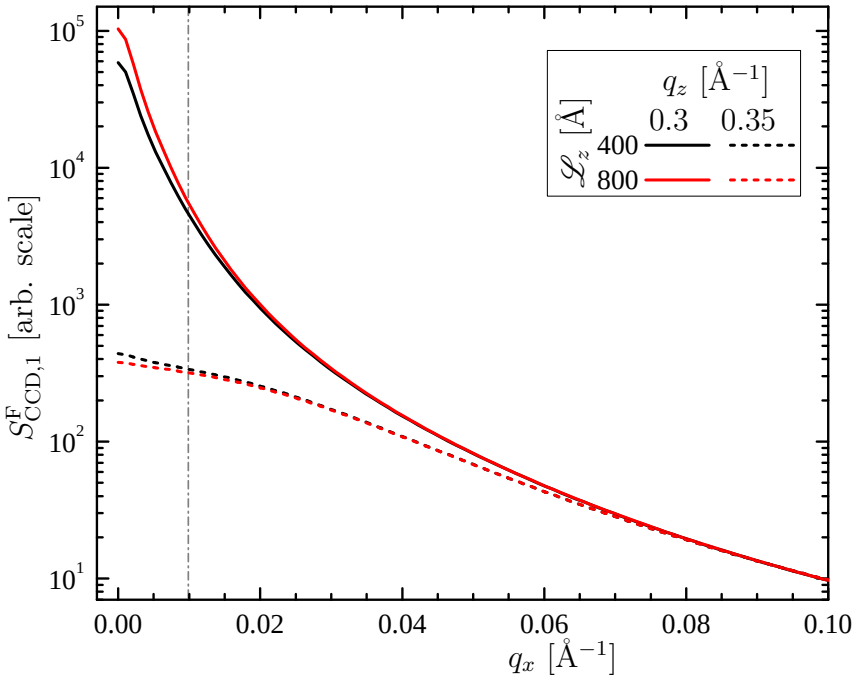


Figure 6.9: $S^{\mathrm{F}}_{\mathrm{CCD},1}(q_x, q_z)$ is plotted as a function of q_z for $\mathscr{L}_z = 400$ Å and 800 Å. The curves have been normalized at $q_z = 0.2$ Å^{-1}. Beyond $q_x \approx 0.1$ Å^{-1} the curves continue to converge.

6.1.4 Minimum In-plane Length: a

π/a is the longest considered in-plane mode, see Eq. (3.70). Fig. 6.10 shows $S^{\mathrm{F}}_{\mathrm{CCD},1}$ as a function of q_x for various values of a. For $q_x \gtrsim \pi/a$, $S^{\mathrm{F}}_{\mathrm{CCD},1}$ decays precipitously. Since a finite q_x-range is probed experimentally, only an upper bound on a can be determined if $a < \pi/q_{x,\mathrm{max}}$, where $q_{x,\mathrm{max}}$ is the maximum q_x-value with analyzable intensity. Typically, $q_{x,\mathrm{max}} \approx 0.2$ Å^{-1}, and therefore the smallest determinable value of a is about 16 Å. For $a \lesssim 16$ Å, the precise value of a is of little concern for the quantification of $\{K_c, B, K_\theta, \mathscr{L}_r, \mathscr{L}_z\}$ because in the q_x-direction a only significantly affects $S^{\mathrm{F}}_{\mathrm{CCD},1}$ for the largest typically analyzed q_x-values.

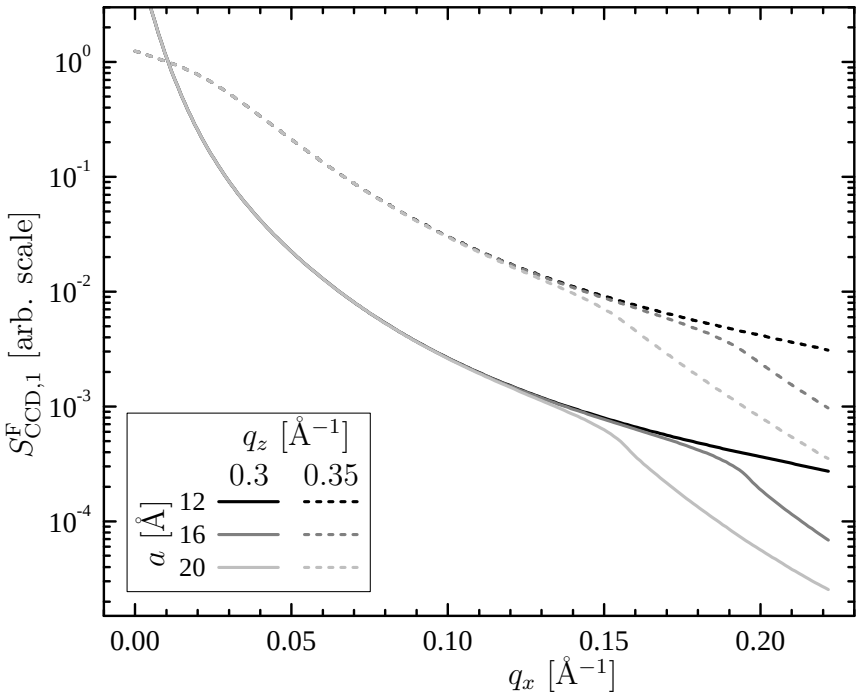


Figure 6.10: $S^{\mathrm{F}}_{\mathrm{CCD},1}$ as a function of q_x is plotted for various a-values. The curves have been normalized at $q_x = 0.01$ Å^{-1}.

The more significant concern regarding the uncertainty in the value of a (Δa) is its influence on $|F(q_z)|^2$, and consequently, the q_z-dependence of $S^{\mathrm{F}}_{\mathrm{CCD},1}$ is explored as a function of a. Commonly, $|F(q_z)|^2$ is determined using data between $q_x \approx 0.03$ Å^{-1} and $q_x \approx 0.13$ Å^{-1} [48]. Therefore, $S^{\mathrm{F}}_{\mathrm{CCD},1}$ is plotted as a function of q_z for $q_x = 0.08$ Å^{-1} (about 80 pixels from the meridian) in Fig. 6.11. For increasing a, $S^{\mathrm{F}}_{\mathrm{CCD},1}$ increases more rapidly as a function of q_z but only significantly so for larger

q_z. Δa is of little concern for determining $\{K_c,\ B,\ K_\theta,\ \mathscr{L}_r,\ \mathscr{L}_z\}$ because a hardly affects $S^{\mathrm{F}}_{\mathrm{CCD},1}$ for $q_z \lesssim 0.6$ Å^{-1}. However, since the product $|F(q_z)|^2\, S^{\mathrm{F}}_{\mathrm{CCD},1}(q_x, q_z)$ is fixed by the measured scattering intensity, the uncertainty of $S^{\mathrm{F}}_{\mathrm{CCD},1}$ at higher q_z due to Δa leads to uncertainty in $|F|^2$.

The uncertainty in $S^{\mathrm{F}}_{\mathrm{CCD},1}$ (or equivalently $|F|^2$) can be semi-quantitatively assessed using an approximate theoretical relation, see Appendix D.1. Using the approximate relation, the $a = 12$ Å and $a = 16$ Å curves in Fig. 6.11 have been scaled to match $a = 8$ Å, collapsing the curves for most of the presented q_z-range (see dashed lines in Fig. 6.11). Therefore, even if the value of a is unknown, the approximate theoretical relation can be used to estimate the uncertainty in $S^{\mathrm{F}}_{\mathrm{CCD},1}$, or more importantly $|F|^2$. To emphasize the a-dependence of the curves, the $a = 12$ Å and $a = 16$ Å curves are divided by the $a = 8$ Å curve and plotted in Fig. 6.12. If only an upper bound on a can be established using the intensity decay in the q_x-direction, the magnitude of $|F(q_z)|^2$ is considerably uncertain for $q_z \gtrsim 0.5$ Å^{-1}. The uncertainty in $|F(q_z)|^2$ due to Δa can be estimated using the approximate theoretical scaling relation.

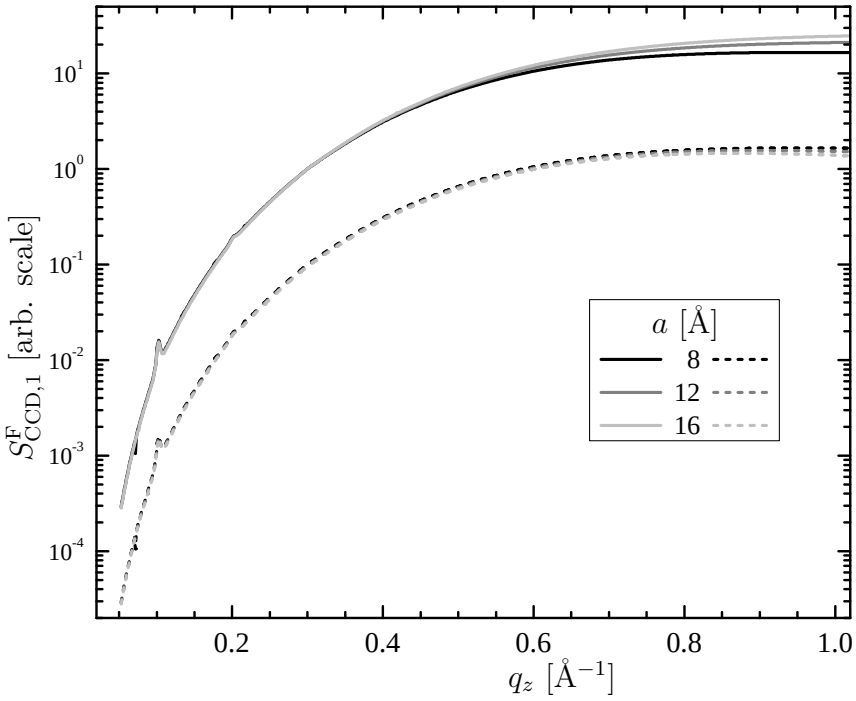


Figure 6.11: $S^{\mathrm{F}}_{\mathrm{CCD},1}(q_x, q_z)$ as a function of q_z for $q_x = 0.08$ Å^{-1} is plotted (solid lines) for various a-values, holding other parameters constant. The curves have been normalized at $q_z = 0.3$ Å^{-1}. Applying an approximate analytic relation for $S^{\mathrm{F}}_{\mathrm{CCD},1}$ as a function of a, the solid lines are nearly collapsed to a single dashed curve, vertically offset by 10^{-1} to improve visibility. The small peaks at $q_z \approx 0.1$ Å^{-1} ($h = 1$) are referred to as "spikes" in Section 5.3.2.

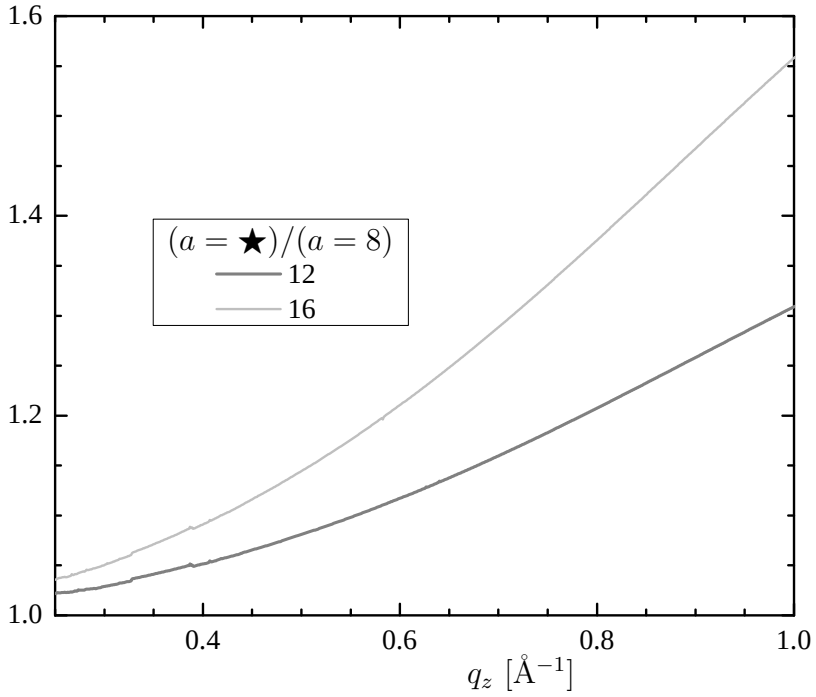


Figure 6.12: The ratio of the $a = 12$ Å and $a = 16$ Å q_z-curves to the $a = 8$ Å curve for $q_x = 0.08$ Å^{-1} is plotted. For $q_z \lesssim 0.25$ Å^{-1}, the ratios are nearly 1, but for larger q_z-values, the q_z-dependence of the different a-value curves is significant. In the figure legend, $\bigstar$ is either 12 (darker gray solid line) or 16 (lighter gray solid line).

6.2 Gaussian vs Exponential Distributions

In Section 5.1, the scattering from the sample was assumed to be the incoherent sum of the scattering from cylindrical subvolumes. The subvolumes' dimensions are determined by a competition between the sample domain size and the sample coherence lengths, see Section 5.3.2. Both Gaussian and exponential subvolume distribution functions were considered plausible, see Sections 5.1.1 and 5.1.2. $S^{\mathrm{F}}_{\mathrm{CCD},1}(q_x, q_z)$ is now calculated using Gaussian and exponential distribution functions and the results are compared.

In Fig. 6.13, $S^{\mathrm{F}}_{\mathrm{CCD},1}(q_x, q_z)$ is plotted as a function of q_z for $q_x = 0$ Å^{-1} and $q_x = 0.01$ Å^{-1}. The standard deviations of the Gaussians are $\mathscr{L}_r/3$ and $\mathscr{L}_z/3$. While the Gaussian and exponential curves differ for $q_x = 0$ Å^{-1}, their predictions are similar for $q_x = 0.01$ Å^{-1}, the minimum q_x-value typically analyzed. In Fig. 6.14, $S^{\mathrm{F}}_{\mathrm{CCD},1}(q_x, q_z)$ is plotted as a function of q_x for $q_z = 0.3$ Å^{-1} and $q_z = 0.35$ Å^{-1}. The Gaussian and exponential predictions are similar for $q_x > 0.01$ Å^{-1}. Since $S^{\mathrm{F}}_{\mathrm{CCD},1}$ calculated using Gaussian and exponential subvolume distributions are similar in the commonly analyzed q_x, q_z-region, exponential distribution functions will be used because they are described by a single parameter, as opposed to 2 parameters for a Gaussian. All later experimental structure factor calculations use exponential domain distributions.

6.3 Finite-sized Domains

Due to defects, inhomogeneity, and various other nonidealities, positional correlations only persist over subvolumes of the sample, commonly referred to as domains. It is assumed that there are no correlations between domains, and the X-ray scattering from defects and domain boundaries is neglected. In principle, the correlations within a domain are sensitive to the domain's boundaries which may in turn be affected by the domain's position in the sample. For samples deposited on a solid substrate, both the flat solid and upper free interfaces may influence bilayer fluctuations [78, 47, 69, 57, 68, 70]. Although, it has been argued that the bulk of a lipid bilayer stack becomes effectively detached from the surfaces [79]. Following previous work [44, 46, 48, 55, 56, 45], height-height correlations within finite-sized domains are modeled using the height-height correlation function of an infinite domain assuming periodic

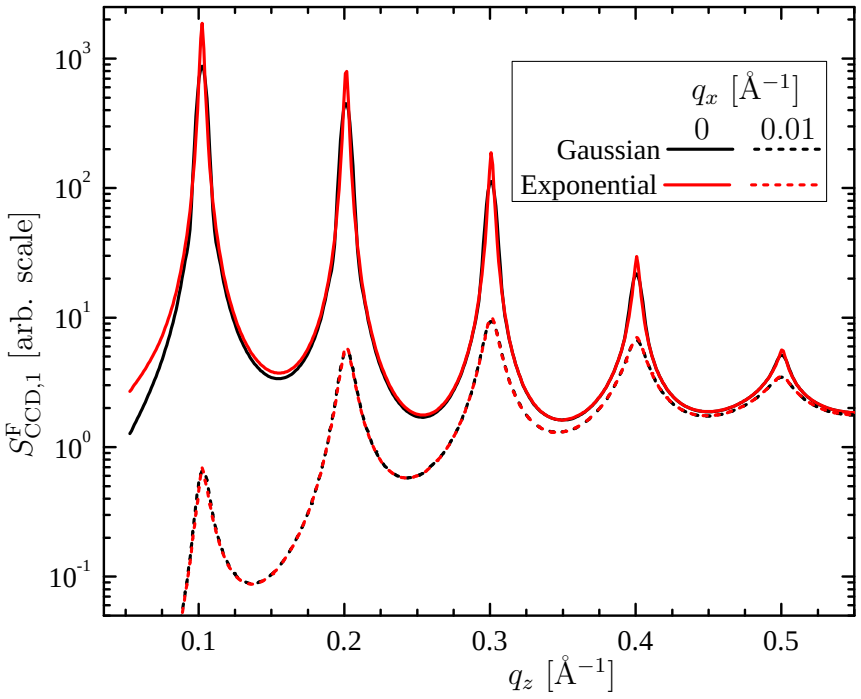


Figure 6.13: $S^{\mathrm{F}}_{\mathrm{CCD},1}(q_x, q_z)$ as a function of q_z is plotted for Gaussian and exponential subvolume distributions at $q_x = 0$ Å^{-1} and $q_x = 0.01$ Å^{-1}. The curves have been normalized at $q_z = 1$ Å^{-1}. Beyond $q_z \approx 0.55$ Å^{-1} the curves continue to converge.

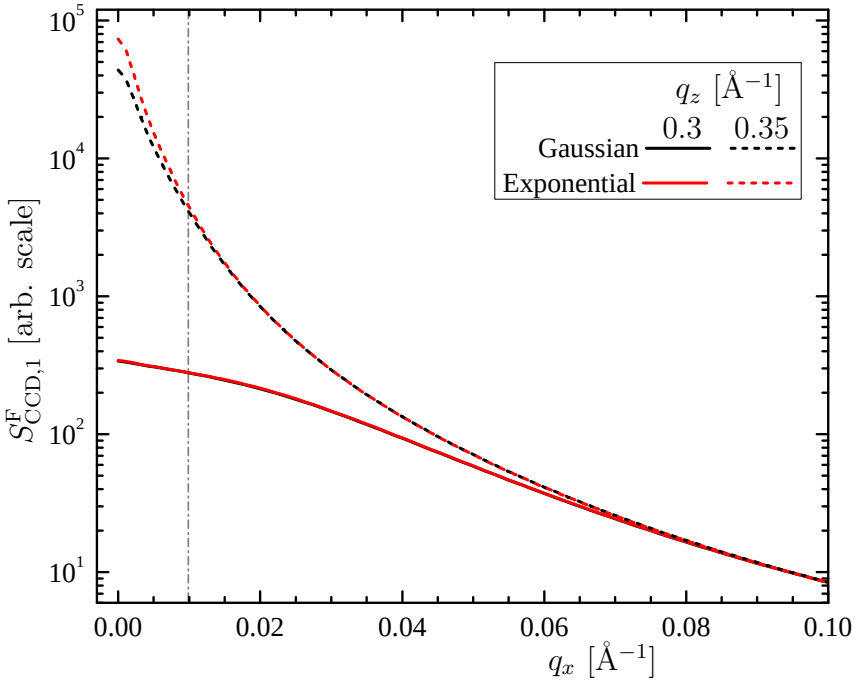


Figure 6.14: $S^{\mathrm{F}}_{\mathrm{CCD},1}(q_x, q_z)$ as a function of q_x is plotted for Gaussian and exponential subvolume distributions at $q_z = 0.3$ Å^{-1} and $q_z = 0.35$ Å^{-1}. The curves have been normalized at $q_x = 0.2$ Å^{-1}. Beyond $q_x \approx 0.1$ Å^{-1} the curves continue to converge. The vertical dashed-dotted gray line shows the minimum q_x-value typically analyzed.

boundary conditions, see Section 3.3.3 Eq. (3.71). The infinite domain and periodic boundary assumptions make the height-height correlation function more analytically tractable and therefore less computationally costly to evaluate. Below, it is shown that height-height correlations of sufficiently large domains are well-approximated by the correlations in the deep interior of an infinite domain.

Returning to an intermediate equation in the derivation of the height-height correlation function Eq. (3.71) and substituting $\omega = Q_z D$ and $v = \xi^2 Q_r^2/2$,

$$h_j(\rho, \ell, \tau) = \frac{k_{\mathrm{B}}T}{2\pi^2 B\xi^2} \int_0^{\tau} \mathrm{d}v \int_0^{\pi} \mathrm{d}\omega \, \frac{1 - J_0\left(\sqrt{2v}\rho\right)\cos(\omega j)}{\frac{v^2}{1+v\ell} + \sin^2(\omega/2)}. \tag{6.3}$$

Assuming that periodic boundary conditions are appropriate for finite-sized domains, $h_j(\rho, \ell, \tau)$ Eq. (6.3) is extended to be a function of the domain's diameter L_r and the domain's number of layers J,

$$h_j^{\mathrm{f}}(\rho, \ell, \tau; L_r, J) \equiv \frac{k_{\mathrm{B}}T}{2\pi^2 B\xi^2} \int_{\left(\frac{a}{L_r}\right)^2 \tau}^{\tau} \mathrm{d}v \int_{\pi/J}^{\pi} \mathrm{d}\omega \, \frac{1 - J_0\left(\sqrt{2v}\rho\right)\cos(\omega j)}{\frac{v^2}{1+v\ell} + \sin^2(\omega/2)}. \tag{6.4}$$

The integrals in h_j^{f} Eq. (6.4) are approximations for sums, and therefore, for decreasing L_r or J, Eq. (6.4) is increasingly approximate. Nevertheless, to compare the finite and infinite domain cases,

$$\Delta h_j^{\mathrm{f}}(\rho, \ell, \tau; L_r, J) \equiv \left| 1 - \frac{h_j^{\mathrm{f}}(\rho, \ell, \tau; L_r, J)}{h_j(\rho, \ell, \tau)} \right| \tag{6.5}$$

is considered. In Fig. 6.15, Eq. (6.5) for $J \to \infty$ is plotted as a function of ρ for several L_r/a, and in Fig. 6.16, Eq. (6.5) for $L_r \to \infty$ is plotted as a function of ρ for several J.

As expected for increasing ρ, h_j^{f} is an increasingly poor approximation of h_j. However, since the scattering intensity is dominated by short length scale correlations ($\rho \lesssim 10$), $h_j(\rho, \ell, \tau)$ is a reasonable approximation for domains with finite L_r and J. The physical domains will be assumed to be large enough ($L_r/a \gg 10^2$ and $J \gg 10$ layers) such that using h_j is accurate.

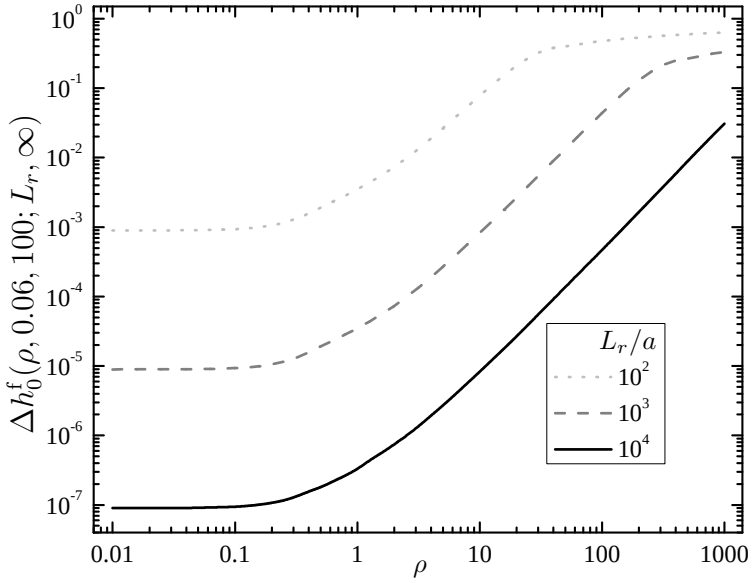


Figure 6.15: Relative difference Δh_j^{f} Eq. (6.5) is plotted as a function of ρ for several L_r/a with $j = 0$, $\ell = 0.06$, $\tau = 100$, and $J \to \infty$. Recall that $\rho = r/\xi$, and typically, $\xi \approx 50$ Å. The $j = 0$ case was chosen since it makes the dominant contribution to the predicted X-ray scattering intensity.

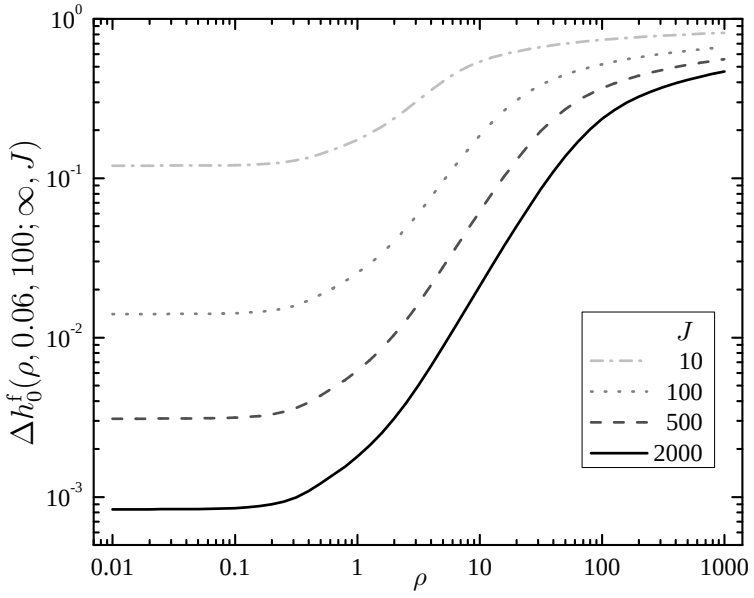


Figure 6.16: Relative difference Δh_j^{f} Eq. (6.5) is plotted as a function of ρ for several J with $j = 0$, $\ell = 0.06$, $\tau = 100$, and $L_r \to \infty$.

6.4 Second Experimental Structure Factor

In Chapter 5, two experimental structure factors were derived, $S^{\mathrm{F}}_{\mathrm{CCD},1}$ and $S^{\mathrm{F}}_{\mathrm{CCD},2}$, and the predicted intensity, see Section 5.4, is

$$\begin{aligned} I^{\mathrm{F}}_{\mathrm{CCD}}(q_x,q_z) &= I^{\mathrm{F}}_{\mathrm{CCD},1}(q_x,q_z) + I^{\mathrm{F}}_{\mathrm{CCD},2}(q_x,q_z) \\ &= \frac{|F(q_z)|^2}{q_z} S^{\mathrm{F}}_{\mathrm{CCD},1}(q_x,q_z) + \frac{F_\Delta(q_z)}{q_z} S^{\mathrm{F}}_{\mathrm{CCD},2}(q_x,q_z) \qquad (6.6) \\ &\equiv I^{\mathrm{F}}_{\mathrm{c}}(q_x,q_z) + I^{\mathrm{F}}_{\mathrm{bf}}(q_x,q_z). \qquad (6.7) \end{aligned}$$

Prior work recognized that the intensity from hydrated bilayer stacks could be written as the sum of two terms [38], but the term proportional to F_Δ was neglected, assuming $F_\Delta \ll |F|^2$. The structure factor / form factor separation derived in Section 3.2.2 is original to the current work, and therefore, $I^{\mathrm{F}}_{\mathrm{bf}} \equiv F_\Delta S^{\mathrm{F}}_{\mathrm{CCD},2}$ has never previously been considered.

$S^{\mathrm{F}}_{\mathrm{CCD},1}$ is the experimental structure factor of the bilayer stack, whereas $S^{\mathrm{F}}_{\mathrm{CCD},2}$ is for a single bilayer in a stack. Fig. 6.17 shows $S^{\mathrm{F}}_{\mathrm{CCD},1}(q_x,q_z)$ (left-hand side) and $S^{\mathrm{F}}_{\mathrm{CCD},2}(q_x,q_z)$ (right-hand side). Only $S^{\mathrm{F}}_{\mathrm{CCD},1}$ has peaks along the meridian, the characteristic scattering feature corresponding to a repeat out-of-plane distance. Both functions decay for increasing q_x at constant q_z. $S^{\mathrm{F}}_{\mathrm{CCD},1}$ and $S^{\mathrm{F}}_{\mathrm{CCD},2}$ are plotted as functions of q_z in Fig. 6.18 and as functions of q_x in Fig. 6.19. For sufficiently large q_x or q_z, $S^{\mathrm{F}}_{\mathrm{CCD},1} \approx S^{\mathrm{F}}_{\mathrm{CCD},2}$.

As was emphasized at the end of Section 5.4, $S^{\mathrm{F}}_{\mathrm{CCD},1}$ and $S^{\mathrm{F}}_{\mathrm{CCD},2}$ have similar functional forms. They differ in their sums over out-of-plane index values, compare f_1 Eq. (5.145) and f_1' (5.150) reproduced below for convenience,

$$f_1(\rho,q_z) = \sum_{j=0}^{\infty}{}' \frac{H_z(jD,q_z)}{\sqrt{1+h_j\tilde{\sigma}_z^{*2}}} \exp\left\{-\frac{q_z^2 h_j + j^2D^2\tilde{\sigma}_z^{*2}}{2\left(1+h_j\tilde{\sigma}_z^{*2}\right)}\right\} \cos\left(\frac{q_z jD}{1+h_j\tilde{\sigma}_z^{*2}}\right) \qquad (6.8)$$

$$\begin{aligned} f_1'(\rho,q_z) &= \sum_{j=0}^{\infty}{}' \delta_{j,0} \frac{H_z(jD,q_z)}{\sqrt{1+h_j\tilde{\sigma}_z^{*2}}} \exp\left\{-\frac{q_z^2 h_j + j^2D^2\tilde{\sigma}_z^{*2}}{2\left(1+h_j\tilde{\sigma}_z^{*2}\right)}\right\} \cos\left(\frac{q_z jD}{1+h_j\tilde{\sigma}_z^{*2}}\right) \qquad (6.9) \\ &= \frac{H_z(0,q_z)}{\sqrt{1+h_0\tilde{\sigma}_z^{*2}}} \exp\left\{-\frac{q_z^2 h_0}{2\left(1+h_0\tilde{\sigma}_z^{*2}\right)}\right\}. \qquad (6.10) \end{aligned}$$

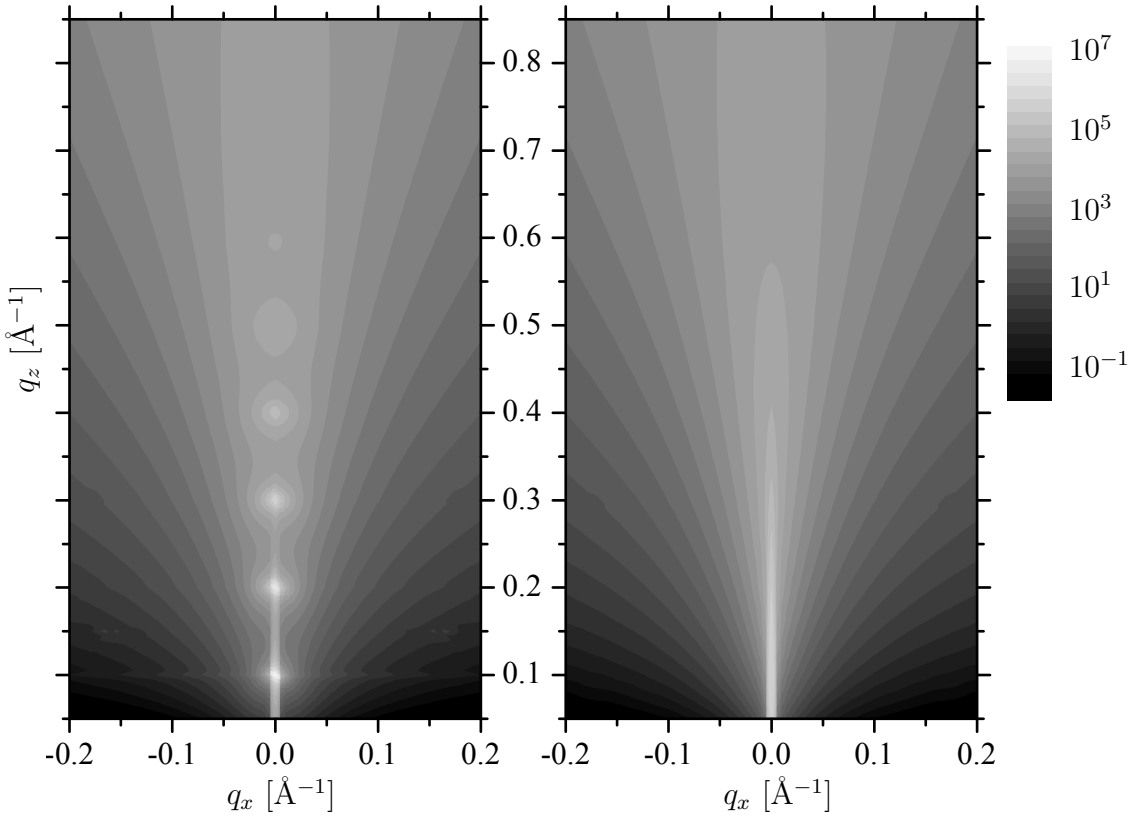


Figure 6.17: $S^{\mathrm{F}}_{\mathrm{CCD},1}$ (left-hand side) and $S^{\mathrm{F}}_{\mathrm{CCD},2}$ (right-hand side) are shown using the same logarithmic grayscale for the parameter values in Table 6.1.

Note, the dependences of several functions were not written explicitly in Eqs. (6.8)-(6.10): $h_j(\rho,\ell,\tau)$ and $\tilde{\sigma}^*_z(q_z)$. For all q_z-values, the largest contribution to f_1 is the $j=0$ term, and for small q_z the many $j\neq 0$ terms dominate. For sufficiently large q_z-values, the exponential in Eq. (6.8) rapidly decays, and the $j=0$ term becomes dominant, $f_1(\rho, q_z \gg 0) \approx f_1'(\rho, q_z \gg 0)$. The q_x-dependence of $S^{\mathrm{F}}_{\mathrm{CCD},1}$ and $S^{\mathrm{F}}_{\mathrm{CCD},2}$ are primarily determined by $f_2(q_x,q_y,q_z)$ Eq. (5.146),

$$f_2(q_x,q_y,q_z) = \int_0^\infty \mathrm{d}r\ rH_r(r) J_{\mathrm{m}}\left(\sqrt{q_x^2+q_y^2}\ r\right) f_1(\rho,q_z). \tag{6.11}$$

For large q_x-values, only smaller $\rho = r/\xi$ significantly contribute to f_2 because its integrand becomes increasingly oscillatory for increasing q_x. Since $h_0 \ll h_{j\neq 0}$ for small ρ (see Fig. 4.1 for a plot of $h_j(\rho,\ell,\tau)$), the $j=0$ term in Eq. (6.8) dominates for sufficiently large q_x regardless of the q_z-value.

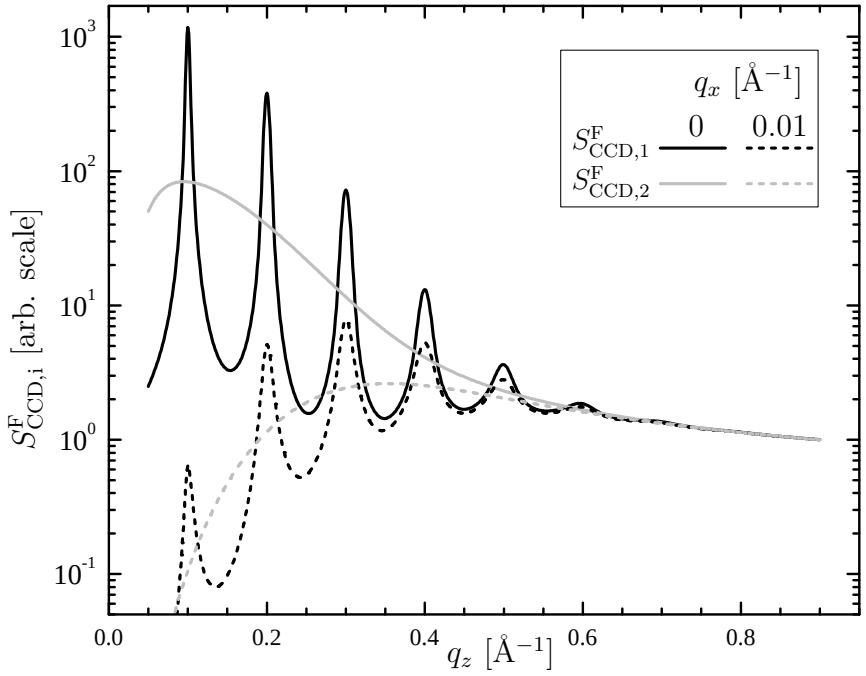


Figure 6.18: $S^{\mathrm{F}}_{\mathrm{CCD},1}$ and $S^{\mathrm{F}}_{\mathrm{CCD},2}$ are plotted as functions of q_z for q_x-values of 0 Å^{-1} and 0.01 Å^{-1}. The curves are normalized at $q_z = 0.9$ Å^{-1}.

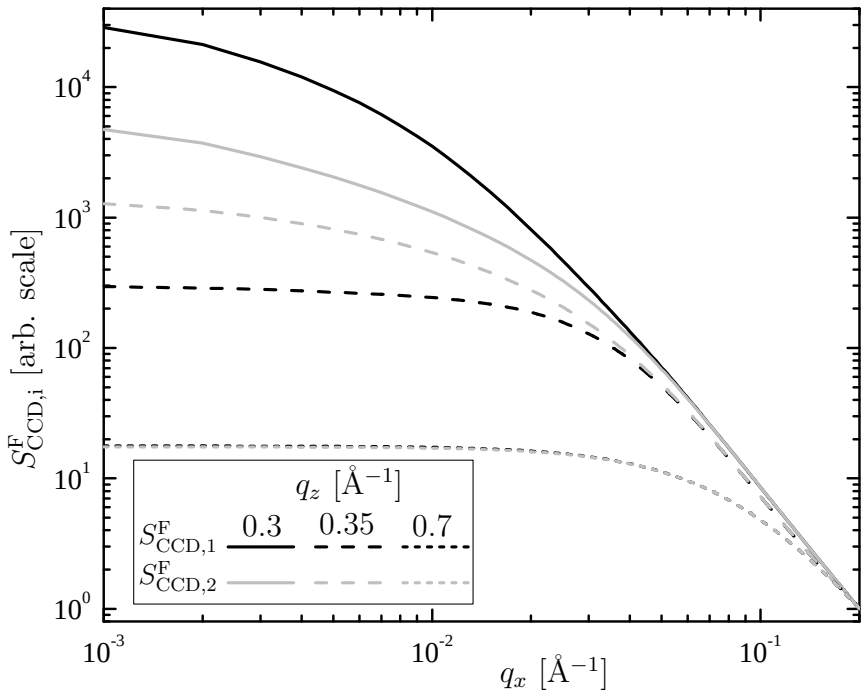


Figure 6.19: $S^{\mathrm{F}}_{\mathrm{CCD},1}$ and $S^{\mathrm{F}}_{\mathrm{CCD},2}$ are plotted as functions of q_x for q_z-values of 0.3 Å^{-1}, 0.35 Å^{-1}, and 0.7 Å^{-1}. The curves are normalized at $q_x = 0.2$ Å^{-1}.

The predicted X-ray scattering intensity $I^{\mathrm{F}}_{\mathrm{CCD}}$ Eq. (6.7) is dependent on the sum of $I^{\mathrm{F}}_{\mathrm{c}} \propto |F|^2 S^{\mathrm{F}}_{\mathrm{CCD},1}$ and $I^{\mathrm{F}}_{\mathrm{bf}} \propto F_{\Delta} S^{\mathrm{F}}_{\mathrm{CCD},2}$. In Sections 7.4.1 and 7.4.2, it is shown that typically $F_{\Delta} \ll |F|^2$, based on a model for bilayer thickness fluctuations and fitting measured scattering from stacks of DOPC bilayers. Therefore, even though $S^{\mathrm{F}}_{\mathrm{CCD},1}$ and $S^{\mathrm{F}}_{\mathrm{CCD},2}$ are of similar magnitude, $I^{\mathrm{F}}_{\mathrm{c}} \gg I^{\mathrm{F}}_{\mathrm{bf}}$ for most q_z-values.

Chapter 7

Data Analysis

Reiterating Eqs. (5.152) and (5.153), the theoretical intensity $I^{\mathrm{F}}_{\mathrm{CCD}}\left[q_x(p_x), q_z(p_z)\right]$ and measured intensity $I_{\mathrm{m}}(p_x, p_z)$ are related by

$$I^{\mathrm{F}}_{\mathrm{CCD}}\left[q_x(p_x), q_z(p_z)\right] \equiv \Phi(q_z) S^{\mathrm{F}}_{\mathrm{CCD},1}(q_x, q_z) + \Phi_{\Delta}(q_z) S^{\mathrm{F}}_{\mathrm{CCD},2}(q_x, q_z) \tag{7.1}$$

$$= I_{\mathrm{m}}\left(p_x, p_z\right) - c(p_z), \tag{7.2}$$

where for notational convenience

$$\Phi(q_z) \equiv \frac{|F(q_z)|^2}{q_z}, \tag{7.3}$$

$$\Phi_{\Delta}(q_z) \equiv \frac{F_{\Delta}(q_z)}{q_z}, \tag{7.4}$$

and $c(p_z)$ models remaining background scattering. If the background subtraction is satisfactory, then $c(p_z) = 0$ can be enforced, the case used here. The approximate relations between **q**-space and CCD-space were presented earlier, see Eq. (5.133) and Eq. (5.128). The measured data are fitted following the same protocol as for the tilt-independent analysis [48]. First, initial guesses are used to evaluate $S^{\mathrm{F}}_{\mathrm{CCD},1}$ and $S^{\mathrm{F}}_{\mathrm{CCD},2}$. Next, $\Phi(q_z)$, $\Phi_{\Delta}(q_z)$, and $c(q_z)$ are determined by a linear fit to $I_{\mathrm{m}}(p_x, p_z)$ for each p_z-value. Given the values of Φ, Φ_{Δ}, and c, parameters of the experimental structure factors are varied to minimize

$$\chi^2 \equiv \sum_{q_x,q_z} \mathcal{R}^2(q_x, q_z) \tag{7.5}$$

where $\mathcal{R}$ are the scaled residuals,

$$\mathcal{R}(q_x, q_z) \equiv \frac{I_{\rm m}(q_x, q_z) - I^{\rm F}_{\rm CCD}(q_x, q_z)}{\sigma_{\rm e}\left[I_{\rm m}(q_x, q_z)\right]}, \tag{7.6}$$

and $\sigma_{\rm e}$ is the estimated standard deviation of the measured intensity. The resulting structure factor parameter values are used as new initial guesses, and the process repeats until either a minimum in χ^2-space is found or the desired number of iterations have been completed. [19]

Following common convention to compare models with different numbers of degrees of freedom, the χ^2-values are normalized by the degrees of freedom $\mathcal{K}$, yielding reduced χ^2-values

$$\chi^2_{\rm red} \equiv \frac{\chi^2}{\mathcal{K}} \tag{7.7}$$

where

$$\mathcal{K} \equiv \mathcal{N} - \mathcal{P}. \tag{7.8}$$

$\mathcal{N}$ is the number of CCD pixels within the fitted region (typically about 4×10^4), and $\mathcal{P}$ is the number of parameters. For a typical fit, there are about 200 linear scaling parameters $\mathcal{P}_{\rm L}$ that correspond to $\Phi(q_z)$ (one for every row of the fitted region of the CCD) and as many as 6 nonlinear parameters $\mathcal{P}_{\rm NL}$ associated with the experimental structure factor $\{K_c,\, B,\, K_\theta,\, \mathscr{L}_r,\, \mathscr{L}_z,\, a\}$. [20] Considering $\Phi_\Delta(q_z)$ adds 200 more linear parameters. Even though there are many linear parameters, determining their values

[19] Given typical initial parameter values, a minimum in χ^2-space is often located in much less than 20 iterations and takes a total computation time of about 3 hours on a modern 4-core processor.

[20] $\mathcal{P}_{\rm NL}$ may be less than the number of fitted parameters. For instance if $\mathscr{L}_r \gg \mathcal{L}_x$ and $\mathscr{L}_z \gg \mathcal{L}_z$, then the experimental structure factor is independent of $\mathscr{L}_r$ and $\mathscr{L}_z$, even if they are "free" parameters. Since $\mathcal{P}_{\rm NL} \ll \mathcal{P}_{\rm L} \ll \mathcal{N}$, the ambiguity in $\mathcal{P}_{\rm NL}$ is of little concern.

is computationally trivial because there is a simple analytic relation for their best values [80]. A modified version of the Levenberg-Marquardt algorithm is used to determine the values of the nonlinear parameters [48]. [21]

The estimated measurement errors σ_{e} are the combination of statistical noise inherent to the CCD (σ_{back}) and the counting statistics associated with X-ray scattering (σ_{s}),

$$\sigma_{\mathrm{e}}^2 = \sigma_{\mathrm{back}}^2 + \sigma_{\mathrm{s}}^2. \tag{7.9}$$

σ_{back}^2 is determined using a region of a sample exposure with no discernible sample scattering, see Fig. 7.1. Following the previous tilt independent analysis [48], the variance of the sample X-ray scattering σ_{s}^2 is modeled as $a_{\mathrm{F}} I_{\mathrm{m}}$ where $a_{\mathrm{F}} = 0.25$ is typical. Poisson statistics alone suggest $\sigma_{\mathrm{s}}^2 = I_{\mathrm{m}}$; however, the intensity reported by the CCD is related to the number of incident photons by an unknown multiplicative factor (electronic gain). Therefore, the value of a_{F} is empirically determined. In principal, the same volume of the stacked bilayer sample could be exposed to X-rays many times, thereby quantifying the uncertainty of the measured intensity. In practice, the hydration of the sample is time-dependent, and the same part of a sample can only be X-rayed for a limited duration before suffering beam damage. The sample width (15 mm) is much greater than the beam width (about 0.2 mm). Therefore, scattering from many different parts of the same sample can be measured and compared. However, even different parts of the same sample are not statistically equivalent, having different D-spacings which makes combining them impossible.

A detailed analysis of the scattering from a DOPC sample is discussed in Sections 7.1 - 7.4. Fig. 7.1 shows the relevant region of a background subtracted DOPC exposure. Table 7.1 lists the values of the important sample, experimental, and coherence parameters. Anticipating later results, $\Phi_{\Delta} S_{\mathrm{CCD},2}^{\mathrm{F}}$ is neglected in fits presented in Sections 7.1 - 7.3. First, in Section 7.1, the measured scattering is fitted by both the tilt-dependent and tilt-independent models, and the tilt-dependent model is shown to better account for the data than the tilt-independent model. Next, the degree to which the measured data are sensitive to the values of $\mathscr{L}_r$ and $\mathscr{L}_z$ is evaluated in

[21] Most of the computational time fitting data is spent evaluating $S_{\mathrm{CCD},1}^{\mathrm{F}}$ since it requires the calculation of several nested integrals, see Section 5.4.

Section 7.2. $\mathscr{L}_r$ and $\mathscr{L}_z$ insignificantly influence fits to the data, and therefore, they will often be eliminated as model parameters in favor of using coherence lengths to limit long length scale correlations. Then in Section 7.3, several different q_x, q_z-regions are fitted to assess the uncertainty in the values of $\{K_c,\ B,\ K_\theta,\ \mathscr{L}_r,\ \mathscr{L}_z,\ a\}$ due to choosing a fitting region. Finally, the complete model in Eq. (7.1) is evaluated in Section 7.4. It is shown that for most q_z-values $\Phi S^{\mathrm{F}}_{\mathrm{CCD},1} \gg \Phi_\Delta S^{\mathrm{F}}_{\mathrm{CCD},2}$. In Section 7.6, the uncertainty of fitted parameter values is determined. The uncertainty is related to the curvature of χ^2-space in the vicinity of the minimum χ^2-value located by the nonlinear fitting algorithm. Table 7.11 lists the determined uncertainties of the fitted K_c-, B-, K_θ-, and a-values, and to summarize, the uncertainties are $\lesssim 1.5\%$ of the fitted parameter values.

Table 7.1: Sample and experimental parameter values for 2015 DOPC exposure.

	parameter	[units]	value	description
sample	D	[Å]	63.8	out-of-plane repeat distance
	T	[°C]	30	temperature
	L_{s}	[mm]	5	sample length along the beam
	t_{s}	[μm]	10	sample thickness
	γ_{m}	[°]	0	FWHM of mosaicity distribution
	μ	[mm]	3.08	$1/e$ X-ray absorption length in sample
	ϵ		0.999998	index of refraction
experimental	λ	[Å]	1.108	X-ray wavelength
	$\mathcal{S}$	[mm]	387.2	sample to detector distance
	p_{s}	[mm/pixel]	0.07113	pixel size
	b_x	[pixels]	2.3	beam width on CCD in x-direction
	$\Delta\lambda/\lambda$		0.012	energy dispersion
	$\Delta\gamma_x$		5×10^{-5}	beam angular divergence in x-direction
	$\Delta\gamma_z$		1×10^{-4}	beam angular divergence in z-direction
coherence	$\xi_{\mathrm{T}x}$	[Å]	11000	transverse beam coherence along $\hat{\mathbf{x}}$
	$\xi_{\mathrm{T}z}$	[Å]	5500	transverse beam coherence along $\hat{\mathbf{z}}$
	ξ_{L}	[Å]	46	longitudinal beam coherence

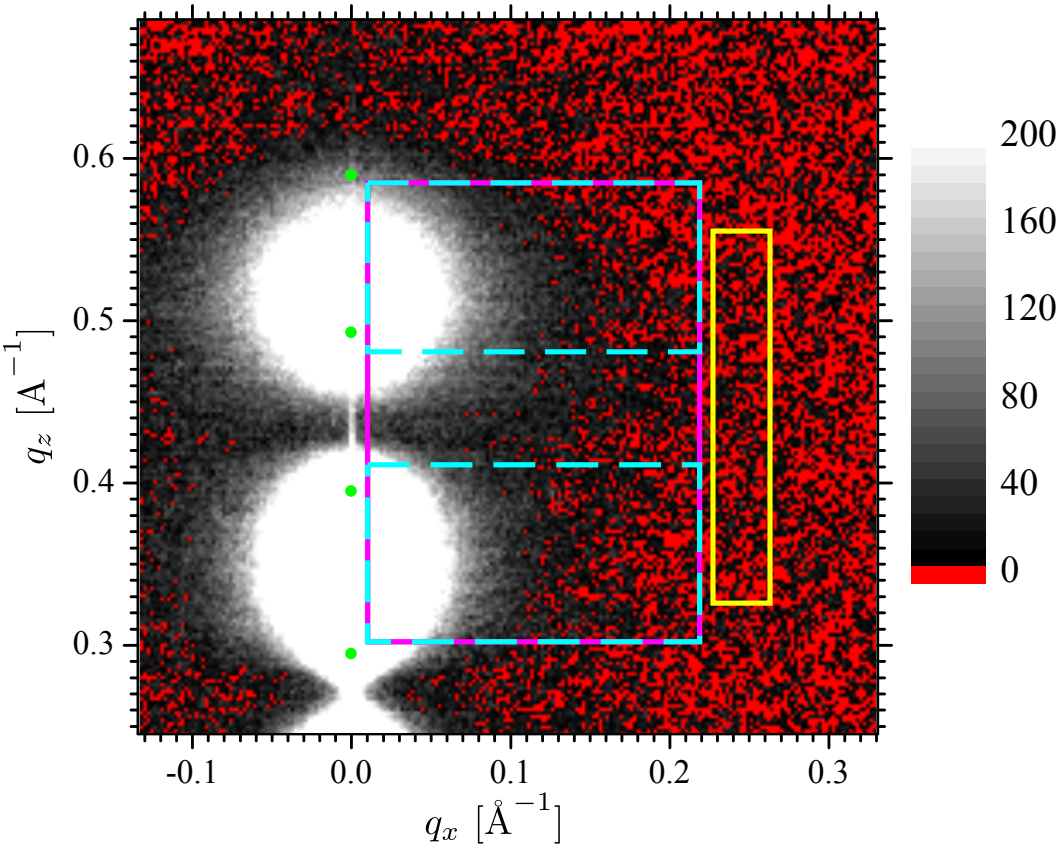


Figure 7.1: The background subtracted scattering intensity from a stack of DOPC bilayers is shown. Intensity is expressed by a linear grayscale except that red pixels indicate intensity less than zero and white indicates intensity greater than 200. The predicted theoretical intensity is compared to the measured data within either the two cyan dashed rectangles or within the solid magenta rectangle. σ^2_{back} is the mean square intensity within the yellow rectangle where the mean is essentially zero. The green circles show the positions of the Caillé peaks for $D = 63.8$ Å.

7.1 Comparing Tilt-dependent and -independent Models

The DOPC exposure shown in Fig. 7.1 was fit using both tilt-dependent and tilt-independent models. Anticipating later results, $\Phi_\Delta S^{\mathrm{F}}_{\mathrm{CCD},2}$ is neglected, and only the data within the dashed cyan rectangles are fitted. The tilt-independent model is a special case of the tilt-dependent one in which $K_\theta \to \infty$ and $a \to 0$; in practice, $K_\theta = 5000$ mN/m and $a = 4$ Å are sufficient. The measured intensity and model fits are plotted in Fig. 7.2 for several values of q_z. The fitted values of the experimental structure factor and χ^2_{red} are listed in Table 7.2. For $q_x \lesssim 0.06$ Å^{-1}, the tilt-dependent and -independent models yield visually similar fits. For greater q_x, the tilt-independent prediction deviates systematically from the measurements. As expected, the tilt-dependent model predicts increased scattering at greater q_x as compared to the tilt-independent model, see Section 6.1.1. To emphasize the model predictions as a function of q_x, the measured data and models are averaged over the fitted q_z-values and plotted in Fig. 7.3 along with the associated scaled residuals $\mathcal{R}$ Eq. (7.6). A slight dip in the measured intensity is visible at $q_x \approx 0.18$ Å^{-1}, consistent with $a \approx 17$ Å (see Section 6.1.4).

Table 7.2: Parameter values for tilt-dependent and tilt-independent models.

Parameter [units]		Tilt-dependent	Tilt-independent
K_c	[$\times 10^{-13}$ ergs]	8.5	7.4
B	[$\times 10^{12}$ ergs/cm^4]	7.0	7.2
K_θ	[mN/m]	107	5000*
a	[Å]	18	4*
χ^2_{red}		1.471	1.660

* indicates a fixed parameter value.

The differences between the tilt-dependent and -independent model fits are accentuated by comparing χ^2_{red}-values limited to subsets of the total analyzed region. The analyzed q_x, q_z-region is divided into subregions 0.02 Å^{-1} wide in the q_x-direction, including all relevant q_z-values, and Fig. 7.4 plots χ^2_{red}-values for these q_x-dependent subregions. For all subregions except the region centered at $q_x = 0.2$ Å^{-1}, the tilt-dependent χ^2_{red}-value is less than the tilt-independent χ^2_{red}-value. Also, the χ^2_{red}-values

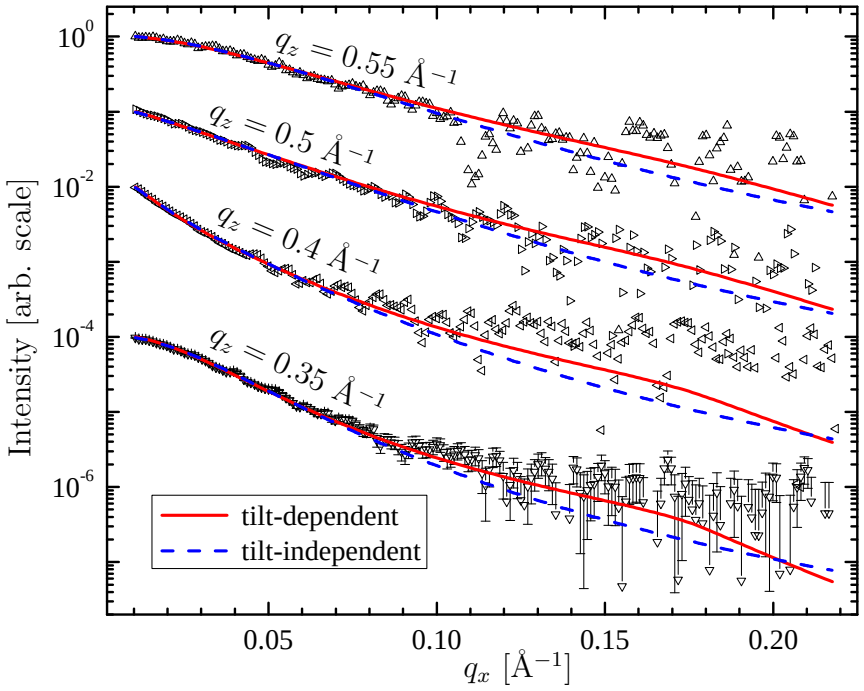


Figure 7.2: Measured data and tilt-dependent and -independent fits are plotted as functions of q_x for several q_z-values. Representative error bars for $q_z = 0.35$ Å^{-1} correspond to $\pm\sigma_e$. The curves have been vertically offset to improve visibility. Note, due to the logarithmic vertical axis, negative intensity values are not plotted.

tend to decrease for increasing q_x, suggesting that both models better account for the scattering at greater q_x (smaller I_m) as compared to lesser q_x (greater I_m).

Tilt-dependent and -independent models are further compared by inspecting the residuals between the fits and the data. The scaled residuals $\mathcal{R}(q_x, q_z)$ are shown for both models in Fig. 7.5. As expected since the χ^2_{red}-values in Fig. 7.4 are significantly greater than 1 [81], there are q_x, q_z-regions where $|\mathcal{R}(q_x, q_z)|$ tends to be much greater than 0 (correlated residuals). Since tilt-dependent and -independent $\mathcal{R}(q_x, q_z)$ are visually similar, the scaled residuals are examined using a different method.

The scaled residuals from tilt-dependent and -independent fits are quantitatively assessed using $\mathcal{R}$ distributions. The scaled residuals are divided into two groups based on q_x-value; $\mathcal{R}$ from lesser q_x (q_x^L: $0.01 \lesssim q_x \lesssim 0.06$ Å^{-1}) and $\mathcal{R}$ from greater q_x (q_x^G: $0.06 \lesssim q_x \lesssim 0.18$ Å^{-1}). The resulting $\mathcal{R}$ distributions are plotted in Fig. 7.6 with corresponding Gaussian fits, see Table 7.3 for Gaussian fit parameter values. The intermediate q_x-value of 0.06 Å^{-1} was chosen because the tilt-dependent and -independent models appear to significantly differ for $q_x \gtrsim 0.06$ Å^{-1}, see Fig. 7.3.

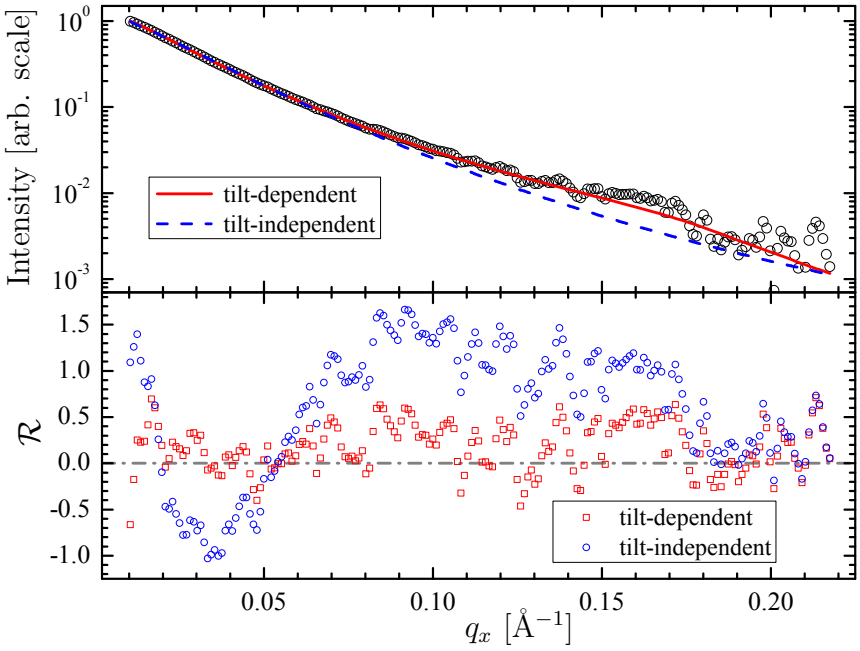


Figure 7.3: After averaging over all fitted q_z-values, the measured data and tilt-dependent and -independent fits are plotted as functions of q_x. Also, the scaled residuals $\mathcal{R}$ for both fits are plotted as functions of q_x. The dashed-dotted gray line is a guide to the eye.

q_x-values greater than 0.18 Å^{-1} are not considered in order to minimize the influence of the a parameter on the $\mathcal{R}$ distributions because a is treated differently for the tilt-dependent and -independent fits. In the case of a statistically ideal fit, the mean μ and standard deviation (SD) σ of a scaled residual distribution are consistent with 0 and 1, respectively. For both q_x^{L} and q_x^{G}, $|\mu|$ of the tilt-dependent distribution is smaller than $|\mu|$ of the tilt-independent distribution, consistent with the diminished χ^2_{red}-values in Fig. 7.4. For q_x^{G} the tilt-independent model systematically predicts less intensity than is measured, and therefore the mean is significantly shifted from 0.

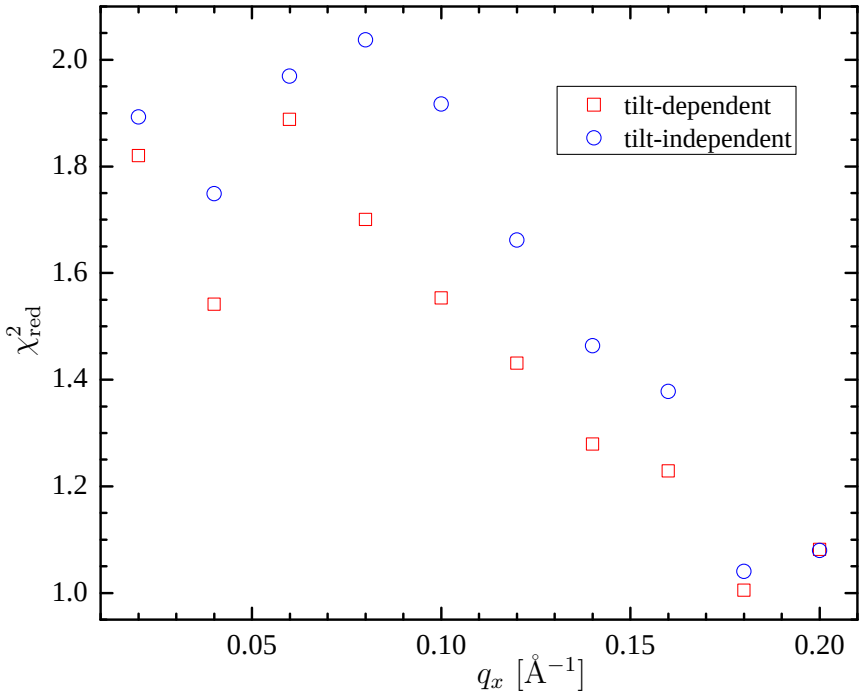


Figure 7.4: χ^2_{red}-values from tilt-dependent and -independent fits are plotted for 0.02 Å^{-1} wide q_x-ranges.

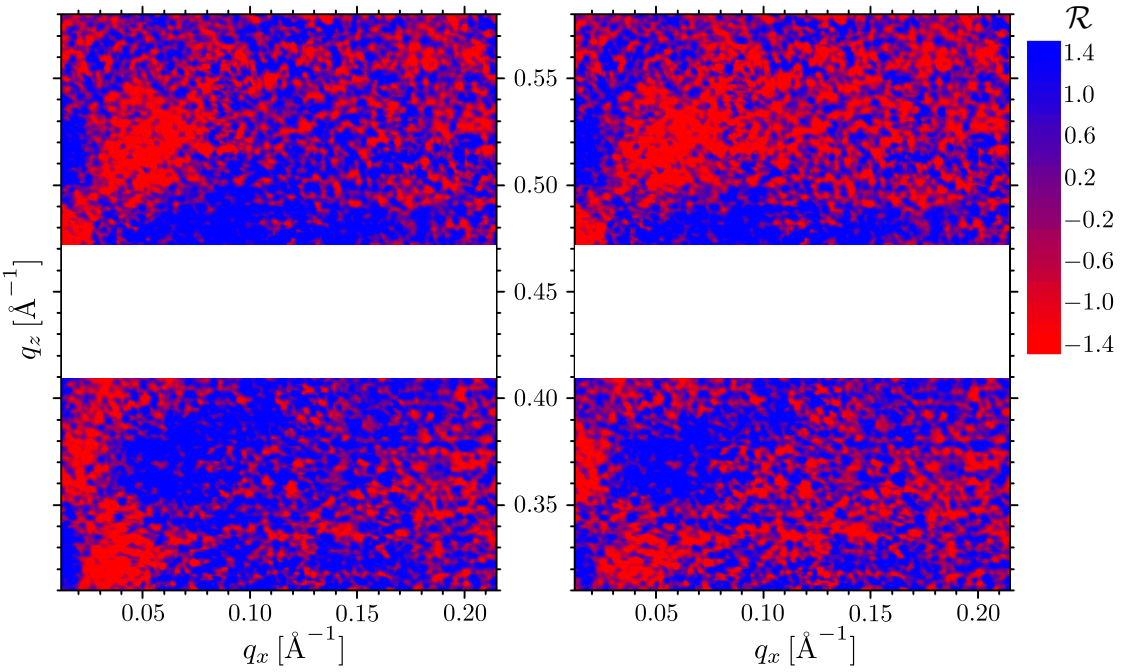


Figure 7.5: Scaled residuals $\mathcal{R}$ Eq. (7.6) of tilt-independent (left-hand side) and tilt-dependent (right-hand side) model fits.

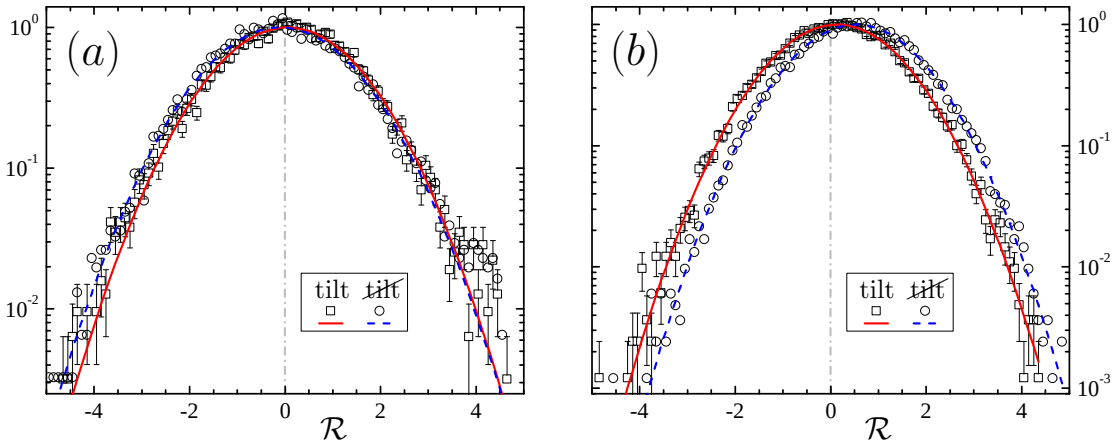


Figure 7.6: Tilt-dependent and -independent (~~tilt~~) $\mathcal{R}$ distributions for (*a*) $0.01 \lesssim q_x \lesssim 0.06$ Å^{-1} and (*b*) $0.06 \lesssim q_x \lesssim 0.18$ Å^{-1}. The red and blue lines are Gaussian fits to the distributions, and Table 7.3 summarizes the fitted parameter values. The distributions have been normalized by the fitted Gaussian amplitudes. Representative error bars for the tilt-dependent distribution are the square root of the number of pixels whose $\mathcal{R}$-value is within a given $\mathcal{R}$-bin of size 0.1. The dashed-dotted gray lines are guides to the eye.

Table 7.3: Parameter values for scaled residual distributions plotted in Fig. 7.6.

parameter	$0.01 \lesssim q_x \lesssim 0.06$ Å^{-1}		$0.06 \lesssim q_x \lesssim 0.18$ Å^{-1}	
	tilt	~~tilt~~	tilt	~~tilt~~
μ (mean)	0.052	-0.11	0.13	0.53
$\Delta\mu$	0.013	0.013	0.0076	0.0075
σ (SD)	1.3	1.3	1.2	1.2
$\Delta\sigma$	0.0096	0.0098	0.0054	0.0054

7.2 Limiting Long Length Scale Correlations

Long length scale correlations are limited by the smaller of the sample coherence volume and the domain size, see Sections 5.1 and 5.3.2 for many details. Most importantly from a data fitting perspective, the sample coherence volume is determined by measured beam properties, while the domain characteristic diameter $\mathscr{L}_r$ and height $\mathscr{L}_z$ are unknown. Previously in Sections 6.1.2 and 6.1.3, the experimental structure factor $S^{\mathrm{F}}_{\mathrm{CCD},1}$ was shown to be fairly insensitive to $\mathscr{L}_r$ and $\mathscr{L}_z$ within the typically analyzed q_x, q_z-region, and therefore, to minimize the number of parameters participating in the nonlinear least squares fit, it was suggested that $\mathscr{L}_r$ and $\mathscr{L}_z$ be eliminated in favor of using the sample coherence volume to limit long length scale correlations.

The insensitivity of $S^{\mathrm{F}}_{\mathrm{CCD},1}$ to $\mathscr{L}_r$ and $\mathscr{L}_z$ is further assessed by fitting measured data. Two fitting procedures are compared. In the first procedure, $\mathscr{L}_r$ and $\mathscr{L}_z$ are fixed to sufficiently large values such that sample coherence always limits long length scale correlations. In the second procedure, $\mathscr{L}_r$ and $\mathscr{L}_z$ are free parameters whose values are determined by the nonlinear fitting routine. Given the experimental beam divergence and energy spread, see Table 7.1, coherence lengths dominate for $\mathscr{L}_r > \xi_{\mathrm{T}z} \approx 5500$ Å and $\mathscr{L}_z > 2\pi\xi_{\mathrm{L}}/(\lambda q_{z,\min}) \approx 900$ Å, where $q_{z,\min}$ is the smallest q_z-value in the fitted q_x, q_z-region. Table 7.4 summarizes the relevant fitted parameter values of the experimental structure factor as well as χ^2_{red} for several pairs of different initial values for $\mathscr{L}_r$ and $\mathscr{L}_z$. Consistent with Sections 6.1.2 and 6.1.3, different values of $\mathscr{L}_r$ and $\mathscr{L}_z$ only modestly affect χ^2_{red}. Table 7.4 shows that the fitted values of $\mathscr{L}_r$ and $\mathscr{L}_z$ are initial value dependent. If the initial value of $\mathscr{J}$ or $\mathscr{L}_r$ is greater than 14 or 5500 Å, respectively, then the fitted and initial values are about the same.[22]

In Table 7.4, the red and blue χ^2_{red}-values are the best fits that correspond to suppressing $\mathscr{L}_r$ and $\mathscr{L}_z$ ($\not{\mathscr{L}}_i$) and fitting $\mathscr{L}_r$ and $\mathscr{L}_z$, respectively. The residuals of the two aforementioned fits are compared as a function of q_x by calculating χ^2_{red}-values limited to subsets of the total analyzed region. The analyzed q_x, q_z-region is divided into subregions 0.02 Å^{-1} wide in the q_x-direction, including all relevant q_z-values, and Fig. 7.7 plots χ^2_{red}-values for these q_x-dependent subregions. For $q_x \lesssim 0.1$ Å^{-1} using $\not{\mathscr{L}}_i$

[22]Since the nonlinear space is searched using a modified Levenberg Marquardt (mLM) algorithm which is a local minimization routine, a certain degree of initial value dependence in the fitted values is to be expected. Additionally, for $\mathscr{J} \gtrsim 14$ and $\mathscr{L}_r \gtrsim 5500$ Å, the fitted values are dependent on the detailed implementation of the mLM algorithm. If only a narrow range of values are sampled in the vicinity of an initial parameter value, the mLM algorithm may not modify the values of $\mathscr{J}$ and $\mathscr{L}_r$ because the χ^2_{red}-space is flat along the $\mathscr{J}$- and $\mathscr{L}_r$-directions for $\mathscr{J} > 14$ and $\mathscr{L}_r > 5500$ Å.

Table 7.4: Fitted parameter values for different initial values of $\mathscr{L}_r$ and $\mathscr{J} \equiv \mathscr{L}_z/D$ ($D = 63.8$ Å).

	parameter [units]		fits					
initial values	$\mathscr{L}_r$	[$\times 10^3$ Å]	∞^*	2.5	5	5	5	10
	$\mathscr{J}$	[$\mathscr{L}_z/D$]	∞^*	10	5	10	20	10
fitted values	$\mathscr{L}_r$	[$\times 10^3$ Å]	∞^*	2.7	5.2	5.0	4.5	10.
	$\mathscr{J}$	[$\mathscr{L}_z/D$]	∞^*	9	6	8	20.	9
	K_c	[$\times 10^{-13}$ ergs]	8.5	8.4	8.0	8.3	8.5	8.3
	B	[$\times 10^{12}$ ergs/cm^4]	7.0	7.2	8.0	7.3	7.0	7.3
	K_θ	[mN/m]	107	115	126	112	105	113
	a	[Å]	18	17	17	18	18	17
	χ^2_{red}		1.471	1.464	1.468	1.468	1.470	1.469

* indicates a fixed parameter value.

as free parameters slightly diminishes χ^2_{red}-values, consistent with expectations from Sections 6.1.2 and 6.1.3. To further quantify the differences between the red and blue fits, corresponding $\mathcal{R}$ distributions are plotted in Fig 7.8. The scaled residual are divided into two groups; $\mathcal{R}$ from lesser q_x-values (q_x^{L}: $0.01 \lesssim q_x \lesssim 0.1$ Å^{-1}) and $\mathcal{R}$ from greater q_x (q_x^{G}: $0.1 \lesssim q_x \lesssim 0.22$ Å^{-1}). The $\mathcal{R}$ distributions are fit by Gaussians, and the fitted parameter values are summarized in Table 7.5. Using $\mathscr{L}_r$ and $\mathscr{L}_z$ as free parameters, does not yield a statistically improved $\mathcal{R}$ distribution. Therefore, unless otherwise stated, $\mathscr{L}_r$ and $\mathscr{L}_z$ are fixed to sufficiently large values such that coherence considerations limit long length scale correlations.

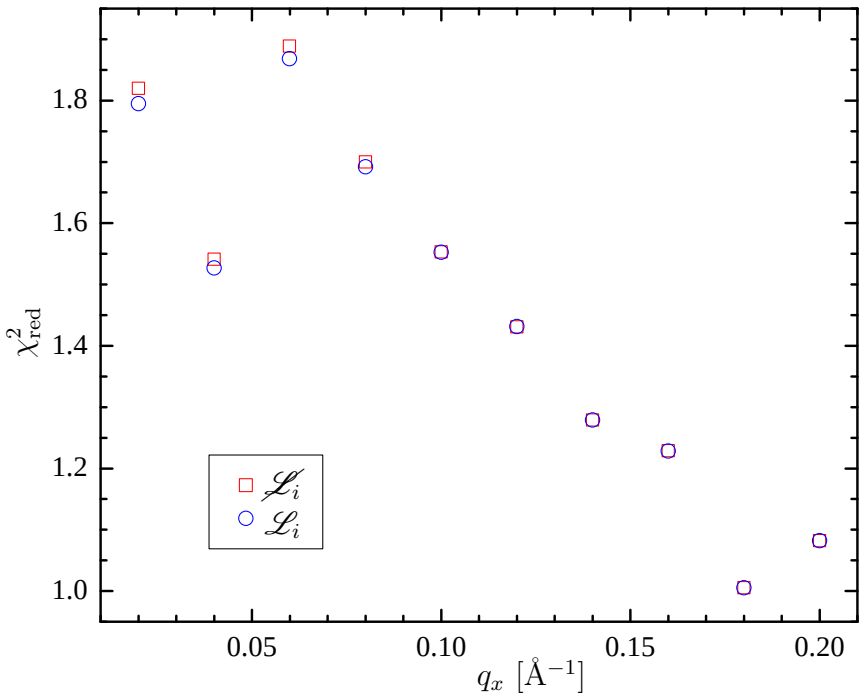


Figure 7.7: χ^2_{red}-values from suppressing $\mathscr{L}_i$ ($\not\mathscr{L}_i$) and fitting to determine $\mathscr{L}_i$-values are plotted for 0.02 Å^{-1} wide q_x-ranges.

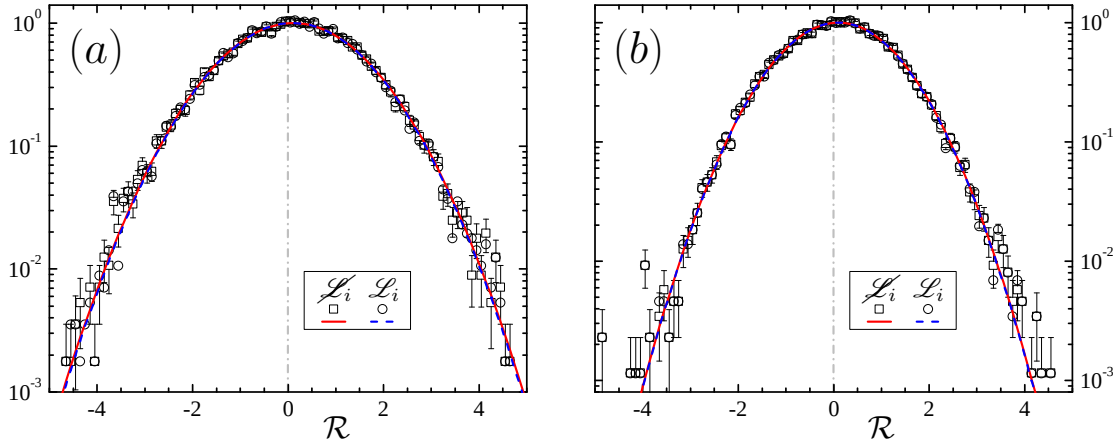


Figure 7.8: $\mathcal{R}$ distributions corresponding to suppressed ($\mathscr{L}_i$) and fitted $\mathscr{L}_i$ for (a) $0.01 \lesssim q_x \lesssim 0.1$ Å^{-1} and (b) $0.1 \lesssim q_x \lesssim 0.22$ Å^{-1}. The lines are Gaussian fits to the distributions, and Table 7.5 summarizes the fitted parameter values. The distributions have been normalized by the fitted Gaussian amplitudes. Representative error bars for fitted $\mathscr{L}_i$ are the square root of the number of pixels whose $\mathcal{R}$-value is within a given $\mathcal{R}$-bin of size 0.1. The dashed-dotted gray lines are guides to the eye.

Table 7.5: Parameter values for scaled residual distributions plotted in Fig. 7.8.

parameter	$0.01 \lesssim q_x \lesssim 0.1$ Å^{-1}		$0.1 \lesssim q_x \lesssim 0.22$ Å^{-1}	
	$\mathscr{L}_i$	$\mathscr{L}_i$	$\mathscr{L}_i$	$\mathscr{L}_i$
μ (mean)	0.10	0.10	0.094	0.092
$\Delta\mu$	0.0096	0.0096	0.0069	0.0069
σ (SD)	1.3	1.3	1.1	1.1
$\Delta\sigma$	0.0069	0.0069	0.0051	0.0050

7.3 Fitted q_x, q_z-Region

In Section 6.1.1, it is established that $S^{\mathrm{F}}_{\mathrm{CCD},1}$ is sensitive to varying $\{K_c,\ B,\ K_\theta\}$ in the q_x, q_z-region within the magenta rectangle in Fig. 7.1. For the analyses in Sections 7.1 and 7.2, only the data within the two cyan rectangles are fitted. In Section 7.3.1, the reason for neglecting the region within the magenta rectangle but between the two cyan rectangles is discussed. The chosen minimum and maximum q_x-values ($q_{x,\mathrm{min}}$ and $q_{x,\mathrm{max}}$, respectively) of the fitted region are compromises between several competing issues. Therefore, in Section 7.3.2, the aforementioned competing issues are summarized, and the dependence of $\{K_c,\ B,\ K_\theta,\ \mathscr{L}_r,\ \mathscr{L}_z,\ a\}$-values on different choices for $q_{x,\mathrm{min}}$ and $q_{x,\mathrm{max}}$ is demonstrated.

7.3.1 q_z-Range

Data within the magenta rectangle in Fig. 7.1 are fitted using the tilt-dependent and -independent models. Fitted parameter values are listed in Table 7.6 for both cyan and magenta bounded regions of data. Fitting the cyan and magenta regions results in similar fitted parameter values, however, the χ^2_{red}-values associated with the magenta region are significantly larger than χ^2_{red}-values fitting the cyan region. The scaled residuals map for the tilt-dependent fit of the magenta bounded region is shown in Fig. 7.9. For $0.41 \lesssim q_z \lesssim 0.47$ Å^{-1}, the residuals are large for most of the q_x-range. Fig. 7.10 plots the data and tilt-dependent and -independent model fits, averaging $0.41 \leq q_z \leq 0.47$ Å^{-1}. For $q_x \gtrsim 0.04$ Å^{-1}, both models systematically predict less intensity than is experimentally observed. The data and models appear more consistent for $q_x \lesssim 0.04$ Å^{-1}; however, the scaled residuals are large within the aforementioned q_x-range. Since both tilt-dependent and -independent models systematically deviate from the measured scattering for $0.41 \lesssim q_z \lesssim 0.47$ Å^{-1}, this q_z-range is neglected for the majority of the analyses.

The q_z-range 0.41 - 0.47 Å^{-1} is unremarkable from the perspective of the experimental structure factors, see Fig. 6.17 for typical $S^{\mathrm{F}}_{\mathrm{CCD},1}$ and $S^{\mathrm{F}}_{\mathrm{CCD},2}$. In Fig. 7.1, the measured scattering intensity is less intense for $0.41 \lesssim q_z \lesssim 0.47$ Å^{-1} due to $|F(q_z)|^2$. Therefore, the discrepancy between data and models may be attributable to unaccounted for mixing between $|F|^2$ and $S^{\mathrm{F}}_{\mathrm{CCD},1}$, for instance mosaicity (see Section 5.2) or **q**-resolution (see Section 5.3.2). Alternatively, the systematic deviations between data and models may involve F_Δ. This hypothesis is tested in Section 7.4.2, and it is shown

Table 7.6: Parameter values for cyan and magenta bounded fitting regions in Fig. 7.1 ($D = 63.8$ Å).

Parameter [units]		tilt-dependent		tilt-independent	
		cyan	magenta	cyan	magenta
K_c	[$\times 10^{-13}$ ergs]	8.5	8.6	7.4	7.3
B	[$\times 10^{12}$ ergs/cm^4]	7.0	7.0	7.2	7.3
K_θ	[mN/m]	107	95	5000*	5000*
a	[Å]	18	17	4*	4*
χ^2_{red}		1.471	1.656	1.660	1.843

* indicates a fixed parameter value.

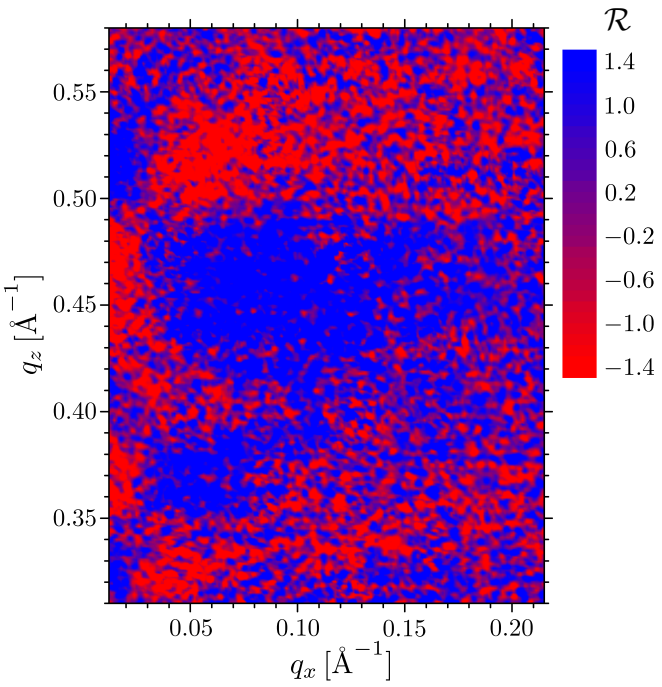


Figure 7.9: Scaled residuals $\mathcal{R}$ of tilt-dependent model fit for q_x, q_z-region within the magenta rectangle in Fig. 7.1.

that including the term $F_\Delta S^{\text{F}}_{\text{CCD},2}$ does not improve the fit for $0.41 \lesssim q_z \lesssim 0.47$ Å^{-1}. Previously, the unfavorable comparison between measured intensity near minima of $|F|^2$ and the tilt-independent theory was discussed in the context of the scattering from hydrated stacks of DMPC bilayers [82]. Empirically, poor fits near apparent $|F|^2$ minima are typical.

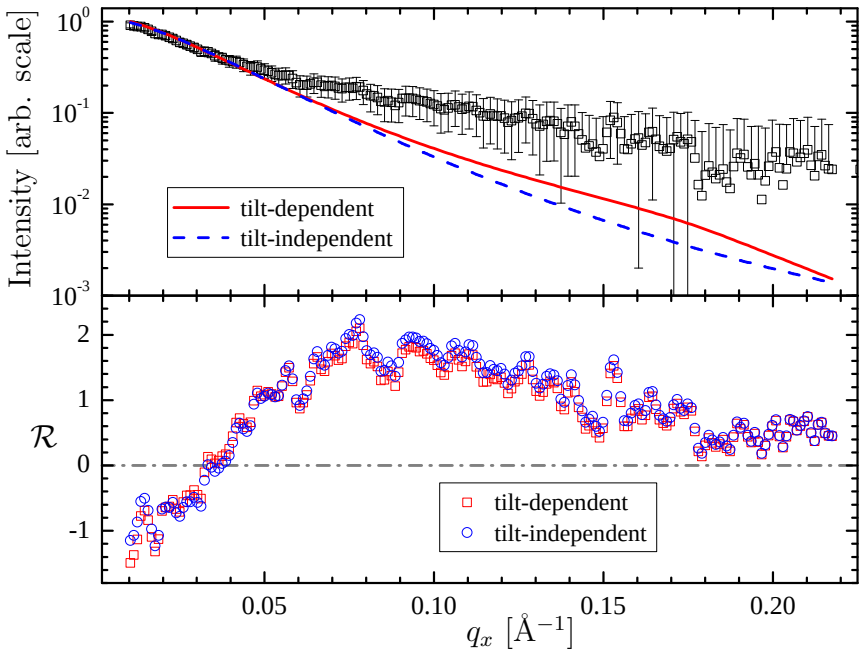


Figure 7.10: Measured data and tilt-dependent and -independent model fits are plotted as functions of q_x, after averaging $0.41 \leq q_z \leq 0.47$ Å^{-1}. Representative error bars indicate 1 standard deviation. Also, the scaled residuals $\mathcal{R}$ for both fits are plotted as functions of q_x. The dashed-dotted gray line is a guide to the eye.

7.3.2 q_x-Range

$q_{x,\min}$ for Analysis

The minimum q_x-value of the fitting range $q_{x,\min}$ is a compromise between several competing issues. Two issues advocate for a larger $q_{x,\min}$. The predicted scattering intensity neglects the scattering from the Si substrate which is known to be concentrated around $q_x = 0$, typically within $|q_x| \approx 0.003$ Å^{-1}. Also, $S^{\mathrm{F}}_{\mathrm{CCD},1}$ is increasingly insensitive to $\mathscr{L}_r$ and $\mathscr{L}_z$ for increasing q_x, see Sections 6.1.2 and 6.1.3. Since $\mathscr{L}_r$ and $\mathscr{L}_z$ are of secondary importance compared to $\{K_c,\, B,\, K_\theta\}$, a greater $q_{x,\min}$-value is chosen to reduce the dependence of $S^{\mathrm{F}}_{\mathrm{CCD},1}$ on $\mathscr{L}_r$ and $\mathscr{L}_z$. On the other hand, the measured data at smaller q_x tend to be the most intense and are more sensitive to the the long length scale predictions of the model as compared to larger q_x. Consequently, a compromise $q_{x,\min}$-value has been chosen to be 0.01 Å^{-1} in this lab.

To assess the dependence of fitted parameter values on $q_{x,\min}$, q_x, q_z-regions with different $q_{x,\min}$-values are fitted. Table 7.7 lists the resulting fitted parameter values. Based on Sections 6.1.2 and 6.1.3, $S^{\mathrm{F}}_{\mathrm{CCD},1}$ is known to be increasingly sensitive to the values of $\mathscr{L}_r$ and $\mathscr{L}_z$ for decreasing q_x. The fitted parameter values are similar for all case in which $\mathscr{L}_i$ were suppressed. For both $q_{x,\min} = 0.005$ Å^{-1} and 0.016 Å^{-1}, the fitted values of $\mathscr{L}_r$ are unreasonably small. In the $q_{x,\min} = 0.005$ Å^{-1} case, the model may not adequately predict long length scale phenomena, or the specular scattering from the substrate is non-negligible. For $q_{x,\min} = 0.016$ Å^{-1}, there may be insufficient data to reliably determine $\mathscr{L}_r$. If $\mathscr{L}_i$ are suppressed, it may by advantageous to use $q_{x,\min} = 0.016$ Å^{-1} as compared to $q_{x,\min} = 0.01$ Å^{-1}because the moduli values are not too dissimilar and a larger $q_{x,\min}$-value makes $S^{\mathrm{F}}_{\mathrm{CCD},1}$ less sensitive to the secondary parameters $\mathscr{L}_i$. Although, fitting data at smaller q_x exposes the deficiencies of the current modeling, potentially motivating future improvements.

$q_{x,\max}$ for Analysis

The $q_{x,\max}$-value for the typical fitting region, see Fig. 7.1, was chosen to include all pixels for which the average of the measured intensity over a small q_x region is greater than 0. In other words, $q_{x,\max} \approx 0.22$ Å^{-1} is the intersection of $I_{\mathrm{m}}(p_x)$ and the line $I = 0$. Alternatively, a more conservative $q_{x,\max}$-value of 0.17 Å^{-1} is the intersection

Table 7.7: Parameter values for various $q_{x,\min}$-values of the fitting range.

		$q_{x,\min}$ [Å^{-1}]					
Parameter [units]		0.005		0.01		0.016	
K_c	[$\times 10^{-13}$ ergs]	9.7	8.3	8.4	8.5	10.1	8.6
B	[$\times 10^{12}$ ergs/cm^4]	6.5	6.6	7.2	7.0	6.2	7.2
K_θ	[mN/m]	105	130	115	107	92	100
a	[Å]	18	17	17	18	18	18
$\mathscr{L}_r$	[Å]	300	∞^*	2700	∞^*	300	∞^*
$\mathscr{J}$	[$\mathscr{L}_z/D$]	9	∞^*	9	∞^*	14	∞^*
χ^2_{red}		1.569	1.633	1.464	1.471	1.356	1.380

* indicates a fixed parameter value.

of $I_{\text{m}}(p_x)$ and $I = \sigma_{\text{back}}$.[23] To an extent, a larger $q_{x,\max}$-value is useful because the scattering at larger q_x-values is more sensitive to the short length scale predictions of the model as compared to scattering at smaller q_x-values. However, the analysis is based on a continuum model (see Section 3.1), which is only physically reasonable for sufficiently small q_x, so fitting measured scattering at large q_x may yield spurious results. Table 7.8 lists potential $q_{x,\max}$-values based on length scales of the current continuum model.

Table 7.8: Possible $q_{x,\max}$-values based on length scales of the continuum model.

		$q_{x,\max}$ [Å^{-1}]
Parameter	value [Å]	π/parameter
D	63.8	0.05
ξ	58	0.05
a	17	0.18
ξ_θ	8.6	0.37

The value of $q_{x,\max}$ is evaluated using fitted parameter values and the scaled residuals from the fits. Table 7.9 lists fitted parameter values for several $q_{x,\max}$-values. Several fixed values of a were sampled since a is expected to be the parameter most sensitive to $q_{x,\max}$. The value of a has little effect on fitted K_c and B values. However,

[23] Currently, the fitting software does not support a q_z-dependent $q_{x,\max}$, and therefore, the most intense regions at large q_x have been used to set $q_{x,\max}$.

fixing the value of a to be less than 17 Å significantly increases the fitted value of K_θ. When a is fitted, similar K_θ-values are determined. For $q_{x,\max} = 0.11$ Å^{-1}, the fitted a-value of 24 Å is unreasonable because the measured data do not precipitously decrease for $q_x > \pi/24$ Å ≈ 0.13 Å^{-1}. The scaled residuals corresponding to the $q_{x,\max} = 0.22$ Å^{-1} fit are plotted in Fig. 7.3, after averaging over all fitted q_z-values. If the continuum approximation were to be a progressively worse approximation for scattering at increasing q_x-values within the fitted range, the scaled residuals might increase as a function of q_x. However, the tilt-dependent model tends to better account for the measured scattering for increasing q_x, see Fig. 7.4.

Table 7.9: Parameter values for cyan bounded fitting region in Fig. 7.1 ($D = 63.8$ Å).

		$q_{x,\max}$ [Å^{-1}]											
Parameter [units]		0.11				0.17				0.22			
K_c	[$\times 10^{-13}$ ergs]	8.5	8.5	8.5	8.6	8.4	8.4	8.4	8.6	8.3	8.3	8.4	8.5
B	[$\times 10^{12}$ ergs/cm^4]	7.0	7.0	7.0	7.0	7.0	7.0	7.0	7.0	7.0	7.0	7.0	7.0
K_θ	[mN/m]	112	112	111	97	120	121	117	102	128	127	123	107
a	[Å]	4*	8*	12*	24	4*	8*	12*	19	4*	8*	12*	18
χ^2_{red}		1.765	1.764	1.763	1.735	1.619	1.617	1.614	1.606	1.487	1.486	1.483	1.471

* indicates a fixed parameter value.

7.4 Comparing $I^{\mathrm{F}}_{\mathrm{CCD},1}$ and $I^{\mathrm{F}}_{\mathrm{CCD},2}$

$I^{\mathrm{F}}_{\mathrm{CCD},1} \propto |F|^2 S^{\mathrm{F}}_{\mathrm{CCD},1}$ and $I^{\mathrm{F}}_{\mathrm{CCD},2} \propto F_\Delta S^{\mathrm{F}}_{\mathrm{CCD},2}$ were derived in Section 5.4, see Eqs. (5.149) and (5.151), respectively. Previously in Section 6.4, $S^{\mathrm{F}}_{\mathrm{CCD},1}$ and $S^{\mathrm{F}}_{\mathrm{CCD},2}$ were shown to be of similar magnitude, yet $S^{\mathrm{F}}_{\mathrm{CCD},2}$ was neglected for the rest of Chapter 6, assuming that $|F|^2 \gg F_\Delta$. Additionally when fitting data, $F_\Delta S^{\mathrm{F}}_{\mathrm{CCD},2}$ is neglected in all Sections in this chapter besides the current one. Recall,

$$\begin{aligned} F_\Delta(q_z) &\equiv \left[\overline{\left\langle |F_0(\mathbf{r}, q_z)|^2 \right\rangle} - \left| \overline{\langle F_0(\mathbf{r}, q_z) \rangle} \right|^2 \right] \\ &\geq 0 \end{aligned} \tag{7.10}$$

and $F(q_z) \equiv \overline{\langle F_0(\mathbf{r}, q_z) \rangle}$, see F_Δ in Eq. (3.36) and $F(q_z)$ in Eq. (3.34). First in Section 7.4.1, the relationship between $|F|^2$ and F_Δ is evaluated by hypothesizing a model for fluctuations in the electron density profile. Then, fits to measured X-ray scattering intensity from a hydrated stack of DOPC bilayers are presented in Section 7.4.2. Both Subsections conclude that the contribution to the measured intensity due to $F_\Delta S^{\mathrm{F}}_{\mathrm{CCD},2}$ Eq. (5.151) is negligible, and therefore, $I^{\mathrm{F}}_{\mathrm{CCD}} \approx |F|^2 S^{\mathrm{F}}_{\mathrm{CCD},1}/q_z$.

7.4.1 Modeling F_Δ

The relationship between $|F|^2$ and F_Δ can be evaluated theoretically, assuming a model for the fluctuations of the electron density profile (EDP). The modeling and corresponding results are briefly summarized below, see Appendix C.1 for details and further discussion. The fluctuations in question are due to the peristaltic modes which are treated *en masse* in the modeling of the stacked bilayer EDP in Section 3.2.1. The EDP fluctuations are hypothesized to be independent out-of-plane extensions and compressions of the monolayers (L) with the associated energy given by Eq. (C.25)

$$E^{\mathrm{L}}_{\mathrm{A}}(\Delta D) = K_A A_o \left(\frac{\Delta D}{D_c} \right)^2, \tag{7.11}$$

where K_A is the compression modulus of the whole bilayer, A_o is the reference area, ΔD is the change in thickness, and D_c is the hydrocarbon thickness. The relevant peri-

staltic fluctuations are assumed to involve the collective motion of several molecules;[24] an approximate lower bound on the A_o-value of 2000 Å^2 (about 30 molecules) is used. The effective modulus in $E_{\mathrm{A}}^{\mathrm{L}}$ Eq. (7.11) is $K_A A_0$, and consequently, choosing a small A_0-value is equivalent to reducing the energetic cost to modify the thickness of a leaflet. Therefore, the smearing of the EDP described below is intended to be an approximate upper bound on the effect of thermal thickness fluctuations. Additionally, since the values of K_A are not strongly dependent on lipid membrane composition [83], the presented argument is interpreted as a general case.

Using the model in Eq. (7.11) and an input EDP from a simulation [84], the ensemble averaged quantities $\left\langle \left| F^{\mathrm{L}}(q_z) \right|^2 \right\rangle$ and $\left| \left\langle F^{\mathrm{L}}(q_z) \right\rangle \right|^2$ are calculated and plotted in Fig. 7.11. The most relevant comparison is between

$$F_{\Delta}^{\mathrm{L}}(q_z) \equiv \left\langle \left| F^{\mathrm{L}}(q_z) \right|^2 \right\rangle - \left| \left\langle F^{\mathrm{L}}(q_z) \right\rangle \right|^2 \tag{7.12}$$

and $\left| \left\langle F^{\mathrm{L}} \right\rangle \right|^2$. For all q_z except near $\left| \left\langle F^{\mathrm{L}}(q_z) \right\rangle \right|^2 \approx 0$, $\left| \left\langle F^{\mathrm{L}} \right\rangle \right|^2 \gg F_{\Delta}^{\mathrm{L}}$. Therefore, it is expected that $F_{\Delta} S_{\mathrm{CCD},2}^{\mathrm{F}}$ is negligible compared to $|F|^2 S_{\mathrm{CCD},1}^{\mathrm{F}}$ except possibly near minima of $|F(q_z)|^2$.

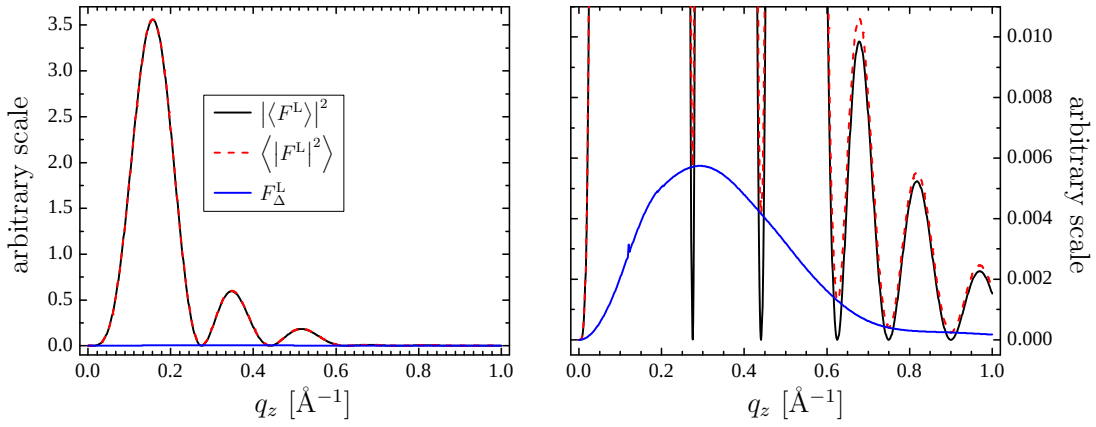


Figure 7.11: $\left\langle \left| F^{\mathrm{L}} \right|^2 \right\rangle$, $\left| \left\langle F^{\mathrm{L}} \right\rangle \right|^2$, and F_{Δ}^{L} are plotted for $K_A = 2.75 \times 10^{-21}$ J/Å^2, $A_o = 2000$ Å^2, and $D_c = 30$ Å. In the right-hand panel, the vertical axis is expanded as compared to the left-hand panel to highlight F_{Δ}^{L}.

[24] In Section 3.2.1, the single bilayer reference electron density ρ_{s} is assumed to be inherently broadened by protrusion modes.

7.4.2 Fitting Measured Intensity

Scattering intensity from fully hydrated DOPC bilayers is fit using two methodologies. One procedure concurrently determines $|F|^2$ and F_Δ and therefore is termed the parallel method. The parallel fitting procedure was previously outlined at the beginning of this chapter. Summarizing the most important points, initial guesses are used to evaluate $S^{\mathrm{F}}_{\mathrm{CCD},1}$ and $S^{\mathrm{F}}_{\mathrm{CCD},2}$. Then, $|F|^2$ and F_Δ are determined by a linear fit to $I_{\mathrm{m}}(p_x, p_z)$ for each p_z-value. Given the values of $|F|^2$ and F_Δ, structure factor parameters are updated using a nonlinear fit. The updated structure factor parameters are used as new initial guesses and the process iterates.

The second fitting procedure leverages known attributes of $S^{\mathrm{F}}_{\mathrm{CCD},1}$ and $S^{\mathrm{F}}_{\mathrm{CCD},2}$ to separate the intensity contributions of $|F|^2 S^{\mathrm{F}}_{\mathrm{CCD},1}$ and $F_\Delta S^{\mathrm{F}}_{\mathrm{CCD},2}$ and is called the series method. In Section 6.4, it was shown that for $q_x > q_x^{\mathrm{c}}(p_z)$ $S^{\mathrm{F}}_{\mathrm{CCD},1}(q_x, q_z) \approx S^{\mathrm{F}}_{\mathrm{CCD},2}(q_x, q_z)$, and therefore, $I^{\mathrm{F}}_{\mathrm{CCD}}$ Eq. (7.1) can be simplified,

$$I^{\mathrm{F}}_{\mathrm{CCD}}\left[q_x > q_x^{\mathrm{c}}(p_z), q_z(p_z)\right] \approx \frac{|F(q_z)|^2 + F_\Delta(q_z)}{q_z} S^{\mathrm{F}}_{\mathrm{CCD},1}\left[q_x > q_x^{\mathrm{c}}(p_z), q_z\right] \tag{7.13}$$

$$= I_{\mathrm{m}}\left(p_x > p_x^{\mathrm{c}}, p_z\right). \tag{7.14}$$

Using Eq. (7.13), it is possible that the sum $|F(q_z)|^2 + F_\Delta(q_z) \equiv F^*(q_z)$ is more robustly determined than the parallel method's determination of $|F|^2$ and F_Δ.

First in the series fitting methodology, $S^{\mathrm{F}}_{\mathrm{CCD},1}$ and $S^{\mathrm{F}}_{\mathrm{CCD},2}$ are calculated using initial guesses for their parameter values. Then for each p_z-value, q_x^{c} is determined by comparing $S^{\mathrm{F}}_{\mathrm{CCD},1}$ and $S^{\mathrm{F}}_{\mathrm{CCD},2}$. $F^*(q_z)$ is determined using Eq. (7.13) and a linear least squares fit. Next, the difference of the total intensity and $F^*(q_z) S^{\mathrm{F}}_{\mathrm{CCD},1}/q_z$,

$$I_{\mathrm{m}}(p_x, p_z) - \frac{F^*(q_z)}{q_z} S^{\mathrm{F}}_{\mathrm{CCD},1}(q_x, q_z) = \frac{F_\Delta(q_z)}{q_z}\left(S^{\mathrm{F}}_{\mathrm{CCD},2} - S^{\mathrm{F}}_{\mathrm{CCD},1}\right), \tag{7.15}$$

is used to determine F_Δ using a second linear least squares fit. Finally, the structure factor parameters are refined using a nonlinear least squares fit.

The parallel and series fitting methods were applied to the measured data within the magenta rectangle shown in Fig. 7.1. The resulting $|F|^2$ and F_Δ are plotted in Fig. 7.12. Since by definition $F_\Delta \geq 0$, much of the fitted F_Δ-regions are unreasonable.

Also, $|F(q_z)|^2$ is inconsistent with previous experiments and simulations [16] with the caveat that the cited experimental work effectively assumed $F_\Delta \ll |F|^2$. Correlations in the fitted $|F|^2$ and F_Δ suggest that the measured scattering is insensitive to $|F|^2$ and F_Δ individually; overwhelming positive or negative values of F_Δ are matched by corresponding deviations in $|F|^2$. F^* is plotted in Fig. 7.13 and is much smoother than $|F|^2$ and F_Δ. F^* is similar to both $\left|\left\langle F^{\mathrm{L}}\right\rangle\right|^2$ and $\left\langle\left|F^{\mathrm{L}}\right|^2\right\rangle$ plotted in Fig. 7.11. Results from both the parallel and series fitting procedures suggest that the data do not support inclusion of the term $F_\Delta S^{\mathrm{F}}_{\mathrm{CCD},2}$.

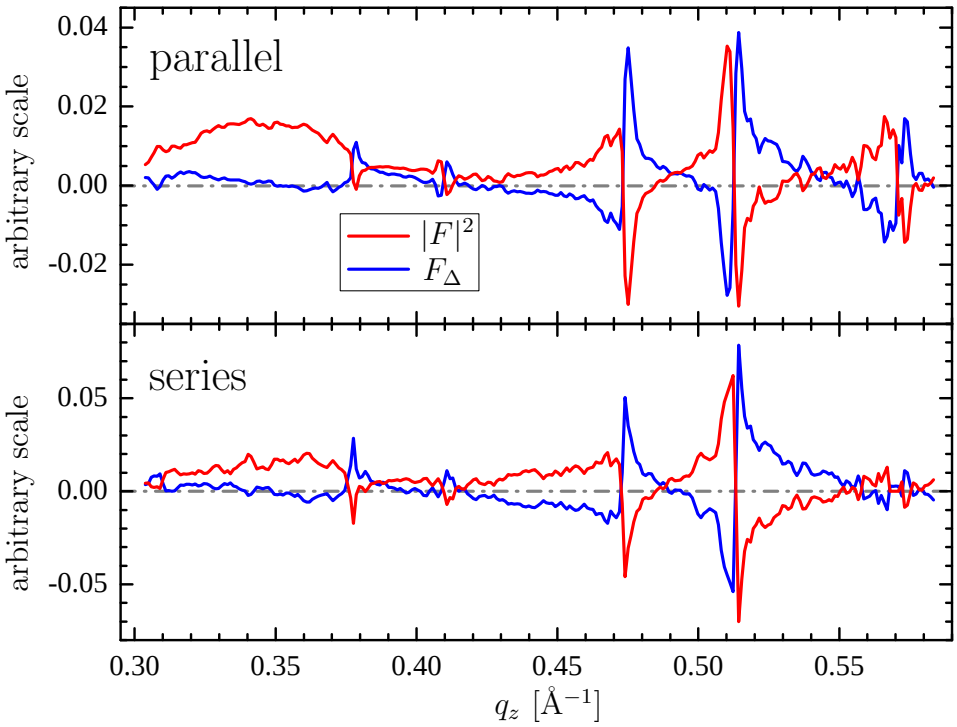


Figure 7.12: The determined $|F(q_z)|^2$ and $F_\Delta(q_z)$ are plotted from both the parallel (top) and series (bottom) fitting methods on the same arbitrary scale. The dashed-dotted gray lines are guides to the eye.

In Section 7.4.1, it was shown that $F^{\mathrm{L}}_\Delta \ll \left|\left\langle F^{\mathrm{L}}\right\rangle\right|^2$ for all q_z except near $\left|\left\langle F^{\mathrm{L}}(q_z)\right\rangle\right|^2 \approx 0$. Therefore, it is worth considering whether the contribution of $F_\Delta S^{\mathrm{F}}_{\mathrm{CCD},2}$ to the measured intensity may be significant near minima in I_{m} along the q_z-direction (for example near $q_z = 0.44$ Å^{-1} in Fig. 7.1). Fig. 7.14 shows parallel and series fits and measured data centered at $q_z = 0.44$ Å^{-1}, averaging $0.41 \lesssim q_z \lesssim 0.47$ Å^{-1}. Neither fit satisfactorily describes the measurement, and therefore, there is no conclusive experimental evidence supporting a significant contribution from $F_\Delta S^{\mathrm{F}}_{\mathrm{CCD},2}$. From an

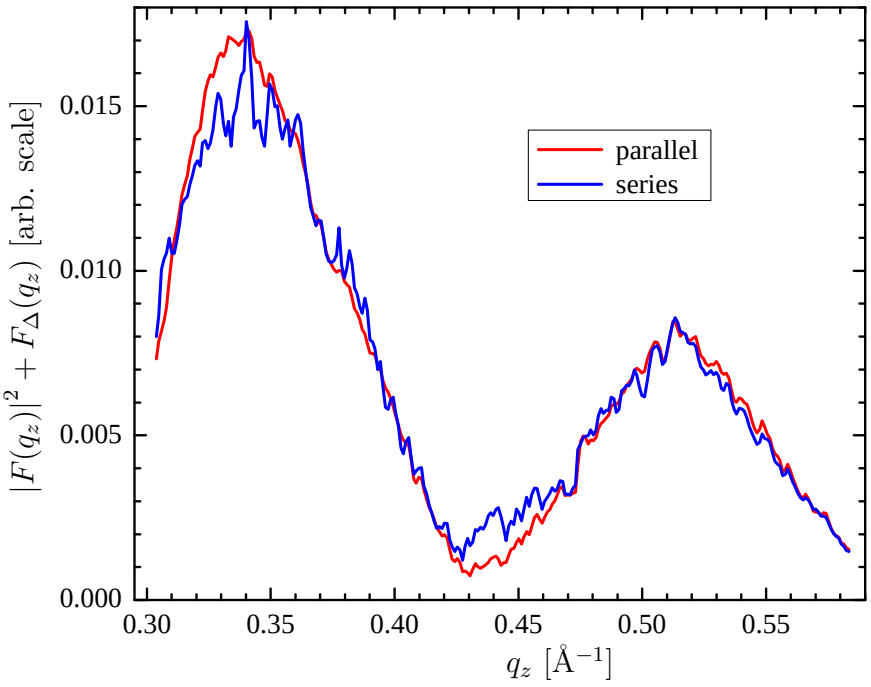


Figure 7.13: $|F(q_z)|^2 + F_\Delta(q_z)$ is plotted from both the parallel and series fitting methods.

electron density modeling perspective (see Section 3.2.1), the fluctuations attributed to the peristaltic modes are inconsequential for predicting the X-ray scattering in the typical q_x, q_z-region.

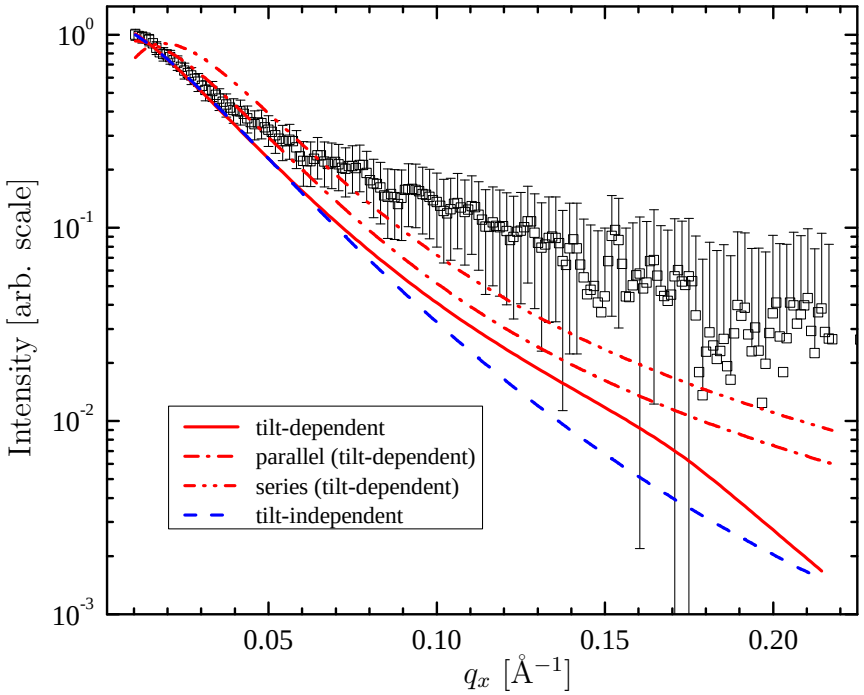


Figure 7.14: Measured data and the tilt-dependent, parallel, series, and tilt-independent fits are plotted as functions of q_x, averaging $0.41 \lesssim q_z \lesssim 0.47$ Å^{-1}. Representative error bars indicate 1 standard deviation.

7.5 Form Factor

Besides parameter values of the experimental structure factor, the scaling factor $\Phi(q_z) = |F(q_z)|^2/q_z$ is also determined by fitting the measured scattering intensity. [25] Following the Nagle lab protocol, $\Phi(q_z)$ is evaluated using the data within the q_x, q_z-region bounded by a yellow rectangle in Fig. 7.15 along with $S^{\mathrm{F}}_{\mathrm{CCD},1}$ parameter values listed in Tables 7.10. Since Φ is a fitted parameter with an associated uncertainty, there is a significant chance that $\Phi < 0$ for small Φ. Consequently, to show this in graphs, $|F(q_z)|$ has commonly been plotted as [85]

$$|F(q_z)| \equiv \mathrm{sgn}\left[\Phi(q_z)\right] \sqrt{|\Phi(q_z)|\ q_z}, \tag{7.16}$$

where sgn[...] returns the sign of its argument. Ignoring the negative values of Φ unduly biases fits of $|F|$ to larger positive values.

Table 7.10: Sets of fitted parameter values used to determine $\Phi(q_z)$.

Parameter [units]		tilt	tilt and $\mathscr{L}_i$	~~tilt~~
K_c	[$\times 10^{-13}$ ergs]	8.5	8.4	7.4
B	[$\times 10^{12}$ ergs/cm^4]	7.0	7.2	7.2
K_θ	[mN/m]	107	115	5000*
a	[Å]	18	17	4*
$\mathscr{L}_r$	[Å]	∞*	2700	∞*
$\mathscr{J}$	[$\mathscr{L}_z/D$]	∞*	9	∞*

* indicates a fixed parameter value.

$|F(q_z)|$ are plotted in Fig. 7.16 corresponding to the three sets of fitted parameter values in Table 7.10. Consistent $|F|$ are determined for both tilt-dependent and -independent models as well as for fitting $\mathscr{L}_i$ (see Section 7.2) within the tilt-dependent model. However, the interpretation of $|F(q_z)|^2$ in terms of the single membrane electron density ρ_{s} is different for the tilt-dependent and -independent models. In Section 3.2.2, Eqs. (3.19) and (3.34) define the tilt-dependent form factor,

[25] In previous Nagle lab software, the determined scaling factors were not absorption corrected, see Section 6.2 in [48]. In the current software, the experimental structure factor is absorption corrected because the absorption correction is dependent on the incident angle [50]. Consequently, $\Phi(q_z)$ are absorption corrected.

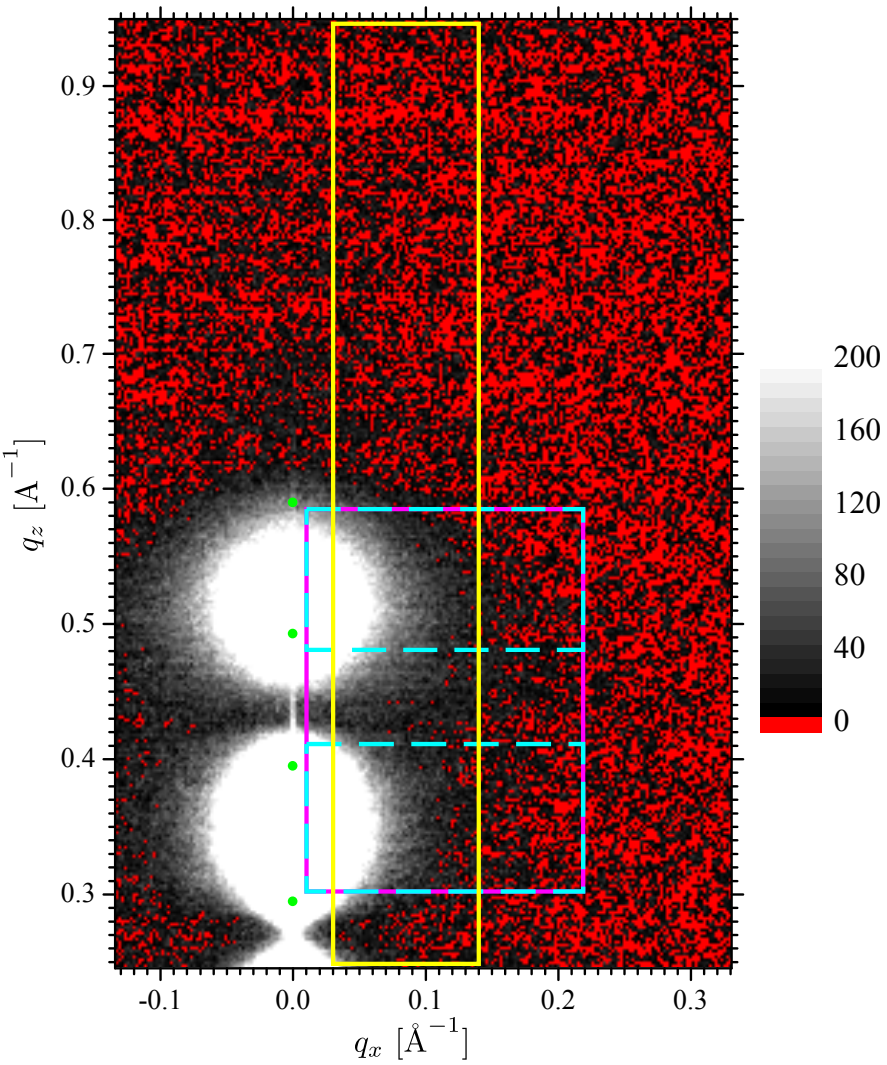


Figure 7.15: The background subtracted intensity from a stack of DOPC bilayers is shown. Intensity is expressed by a linear grayscale except that red pixels indicate intensity less than zero and white indicates intensity greater than 200. $\Phi(q_z)$ is determined using the fitted $S^{\mathrm{F}}_{\mathrm{CCD},1}$ parameter values in Table 7.10 and the data within the yellow rectangle. The green circles indicate positions of Caillé peaks.

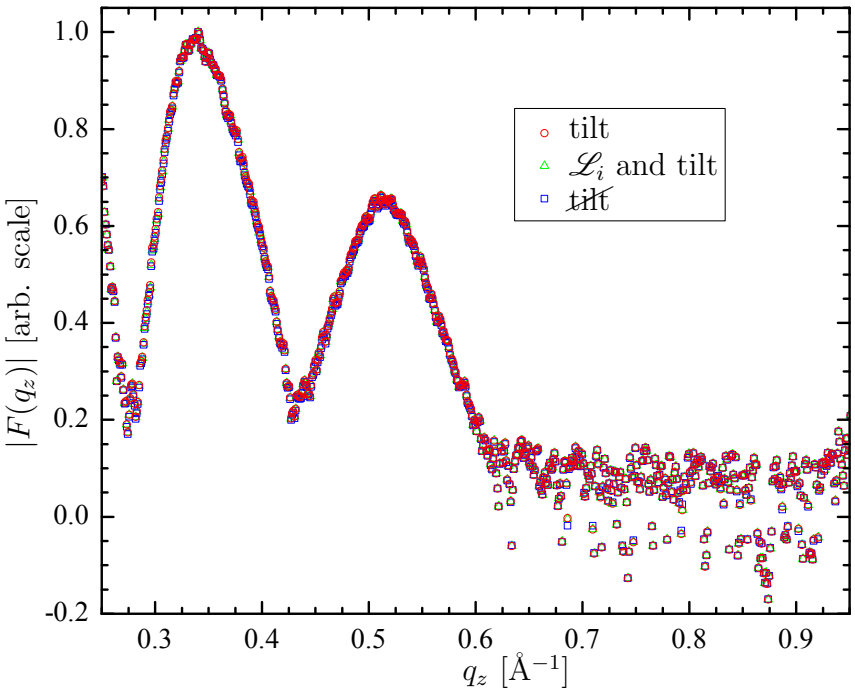


Figure 7.16: The determined $|F(q_z)|$ Eq. (7.16) are plotted for fitted $S^{\mathrm{F}}_{\mathrm{CCD},1}$ parameter values listed in Table 7.10. Commonly, a smooth baseline is subtracted from $\Phi(q_z)$ such that $|F(q_z)|$ is zero at apparent minima (for example $q_z \approx 0.28$ Å^{-1} and ≈ 0.42 Å^{-1}). The aforementioned subtraction was not performed.

$$F(q_z) \equiv \frac{1}{A}\int_A \mathrm{d}^2\mathbf{r} \int_{-D/2}^{D/2} \mathrm{d}\tilde{z}\, \frac{\langle \rho_\mathrm{s}[\tilde{z}, P_o(\mathbf{r})]\rangle}{\langle \Psi_0 \rangle} e^{iq_z \tilde{z}/\langle \Psi_0 \rangle}. \tag{7.17}$$

Substituting $z = \tilde{z}/\langle \Psi_0 \rangle$ into Eq. (7.17),

$$F(q_z) \approx \frac{1}{A}\int_A \mathrm{d}^2\mathbf{r} \int \mathrm{d}z \left\langle \rho_\mathrm{s}\Big[z\langle \Psi_0 \rangle, P_0(\mathbf{r})\Big]\right\rangle e^{iq_z z}. \tag{7.18}$$

Finally, the undulation correction (UC) [39] is recognized,

$$\Psi_\mathrm{UC} \equiv \langle \Psi_0 \rangle, \tag{7.19}$$

and $F(q_z)$ is concisely expressed as

$$F(q_z) \approx \int \mathrm{d}z\ \rho(z) e^{iq_z z} \tag{7.20}$$

where

$$\rho(z) \equiv \overline{\left\langle \rho_\mathrm{s}\Big[z\Psi_\mathrm{UC}, P_0(\mathbf{r})\Big]\right\rangle}. \tag{7.21}$$

In comparison, the tilt-independent form factor was previously defined in [48] as

$$F'(q_z) \equiv \int \mathrm{d}z\ \rho'(z) e^{iq_z z}, \tag{7.22}$$

where $\rho'(z)$ is conceptually similar to $\overline{\langle \rho_\mathrm{s}[z, P_0(\mathbf{r})]\rangle}$ given the discussion in Section 3.2 of [48]. Eq. (7.21) emphasizes the effect of Ψ_UC; it stretches or contracts the electron density in the z-direction. A term similar to Ψ_UC would be present in $F'(q_z)$ Eq. (7.22) if $\cos\alpha_b$ had not been neglected, see Section 3.2 in [48] and compare Eqs. (3.1) and (3.2). Prior work has operationally recognized the influence of a UC [39, 48, 85], but the above derivation clearly derives the relations between the hypothesized single membrane electron density, Ψ_UC, and the result of an X-ray scattering measurement. Most importantly, Ψ_UC is different for tilt-dependent and -independent models. Therefore, even if the measured $|F(q_z)|$ for tilt-dependent and -independent models are consistent, the interpretation in terms of electron density differ. Ψ_UC is further discussed in Appendix C.2.

7.6 Uncertainty in Primary Fitted Parameters

As suggested in Sections 7.2 and 7.3, the fitted parameter values depend on the details of the fitting procedure. Consequently, the uncertainty of the determined parameter values could reflect the aforementioned fitted parameter value variation. However, the various fitting methodologies are not equally reasonable. Therefore, the present section focuses on the uncertainty of fitted parameters given a particular choice of fitting protocol.

The fitted q_x, q_z-region is shown in Fig. 7.1, and $\mathscr{L}_r$ and $\mathscr{L}_z$ are suppressed by fixing their values such that coherence considerations limit long length scale correlations, see Section 7.2. Fitted parameter values have associated uncertainty reflecting the curvature of the χ^2-space in the vicinity of the minimum located by the nonlinear least-squares algorithm. Following the common precedent [81], the uncertainty of a fitted parameter value is quantified by how much its value must be modified to increase the χ^2-value by 1, allowing all other parameter values to be determined by the fitting algorithm. The change in the χ^2 value from the χ^2 value of the best tilt-dependent analysis is called $\Delta\chi^2$. For $\{K_c, B, K_\theta, a\}$, the aforementioned procedure was used, fixing each parameter value to $\Delta\% = \{-5\%, -2\%, -1\%, 1\%, 2\%, 5\%\}$ of its best tilt-dependent fitted value, see Table 7.11. The resulting $\Delta\chi^2$-values are listed in Table 7.11. For a given parameter, uncertainty values were determined by fitting the associated $\Delta\chi^2$-values (a row in Table 7.11) to

$$\Delta\chi^2(\Delta\%) = a(\Delta\%)^2 + b(\Delta\%)^3, \tag{7.23}$$

where a and b are constants determined by a linear least squares fit. From the fit Eq. (7.23), parameter values corresponding to $\Delta\chi^2 = 1$ were determined and thereby, uncertainties on the best fitted parameter values. In Fig. 7.17, the $\Delta\chi^2$-values associated with K_c in Table 7.11 are plotted as a function of the percent change in the fixed K_c-value to illustrate the aforementioned uncertainty analysis.

The best tilt-dependent parameter values and associated uncertainties are also listed in Table 7.11. $\Delta\chi^2$ increases more rapidly for changes in K_c- and B-values as compared to changes in K_θ- and a-values. This may in part be due to the fact that K_θ and a are primarily determined by the weaker measured intensity at larger q_x as compared to K_c and B which are determined by the stronger measured intensity at

Table 7.11: Parameter values and associated uncertainties based on a $\Delta\chi^2$-value of 1.

	$\Delta\chi^2$						
Parameter	-5%	-2%	-1%	1%	2%	5%	final value
K_c	706.0	122.7	29.6	10.3	68.2	495.9	8.5 ± 0.017
B	215.6	19.2	-2.7	15.0	40.6	119.3	7.0 ± 0.027
K_θ	13.4	1.1	0.9	-9.3	3.5	16.6	107 ± 1.4
a	24.0	10.6	-1.7	7.1	16.2	38.9	$18^{+0.15}_{-0.16}$

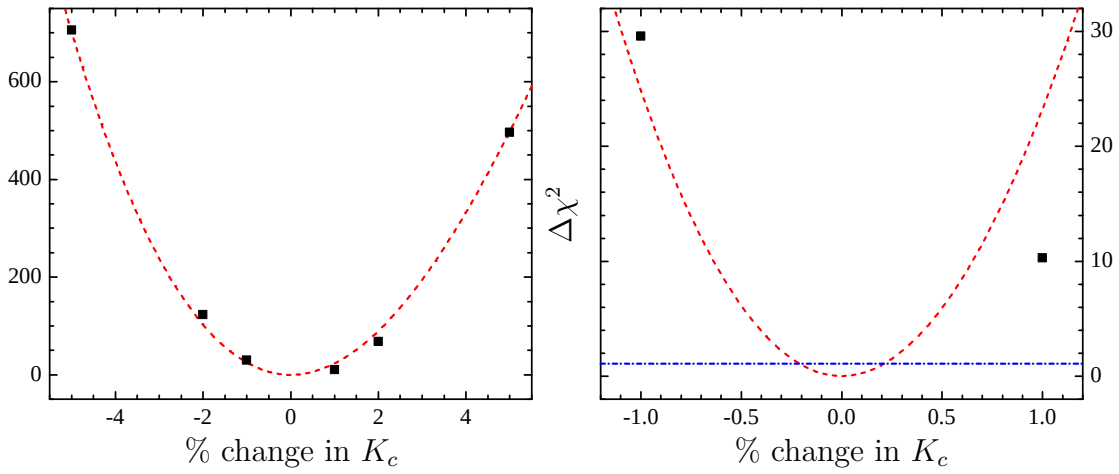


Figure 7.17: $\Delta\chi^2$-values listed in Table 7.11 corresponding to K_c are plotted as a function of the % change in the best tilt-dependent K_c-value (8.5×10^{-13} ergs). The red dashed line is the best fit of Eq. (7.23). The right-hand plot emphasizes the small $\Delta\chi^2$-range, and the blue dotted-dashed line shows $\Delta\chi^2 = 1$.

smaller q_x. Since the ratio of signal to noise typically increases for increasing q_x, the χ^2-value is less sensitive to changes in the values of K_θ and a as compared to K_c and B. The uncertainty values in Table 7.11 are all less than about 1.3%. The small uncertainty values are primarily due to the large number of CCD pixels in the fitted q_x, q_z-region (typically about 4×10^4). Consequently, a χ^2_{red}-value of 1.5 (typical for Table 7.11) corresponds to a χ^2-value of about 6×10^4. Therefore, $\Delta\chi^2 = 1$ is only a change in χ^2 of about 0.002%. [26]

[26]It is possible that the intensity measured in different pixels is correlated. In the case of correlated pixels, χ^2 and χ^2_{red} are related by a number less than the number of pixels within the fitted region. Consequently, the change in a parameter value corresponding to a $\Delta\chi^2$-value of 1 will likely be larger than the values listed in Table 7.11. From this perspective, the uncertainties listed in Table 7.11 are lower bounds on the precision of the fitted parameters.

As indicated previously, the uncertainty values in Table 7.11 indicate the precision of the fitted parameter values given the large data set. These uncertainty values do not reflect other sources of uncertainty (such as experimental and sample preparation) that influence the typically determined parameter values. In Chapter 8, determined parameter values for several exposures of three different DOPC samples are listed and discussed. Fitted parameter values determined from exposures corresponding to different parts of the same sample are shown to vary by more than the uncertainties listed in Table 7.11. Therefore, the uncertainty associated with the precision of the nonlinear fitting is neglected subsequently.

Three $\Delta\chi^2$-values are negative in Table 7.11. In other words, the corresponding fit resulted in a fit with a smaller χ^2-value than the tilt-dependent fit listed in Table 7.2. The parameter values associated with the negative $\Delta\chi^2$-values in Table 7.11 are listed in Table 7.12. The fitted parameter values are negligibly different. The slightly smaller χ^2-values are likely due to fitting 3 free parameters (the case for the values in the first 3 columns in Table 7.12) as opposed to fitting 4 free parameters (the case for the final column in Table 7.12). The difficulty of finding a minimum of a highly nonlinear space increases rapidly with increasing dimension of the search space. Additionally, the nonlinear least squares algorithm (Levenberg-Marquardt) is known to be a local minimizer, and the aforementioned four fits had different initial parameter values.

Table 7.12: Fitted parameter values for fits in Table 7.11 for which $\Delta\chi^2 < 0$.

Parameter [units]		B -1%	K_θ 1%	a -1%	tilt-dependent †
K_c	[$\times 10^{-13}$ ergs]	8.5	8.5	8.5	8.5
B	[$\times 10^{12}$ ergs/cm^4]	6.9 ‡	7.0	7.0	7.0
K_θ	[mN/m]	106.6	107.8 ‡	106.8	106.7
a	[Å]	17.5	17.7	17.5 ‡	17.7

† values from Table 7.2

‡ indicates a fixed parameter value.

Chapter 8

Results for Many DOPC Samples

Many CCD exposures of the scattering from DOPC samples were analyzed, following the analysis methodology described in Section 7.1. First, a kLB was substracted from the measured scattering intensity (see Section 2.5.1), and then, the 2 box method was used to remove residual background intensity (see Section 2.5.2). A similar fitting q_x, q_z-fitting region was chosen for all of the exposures, see Fig. 6.1 specifically the regions within the dashed cyan rectangles. $\mathscr{L}_r$ and $\mathscr{L}_z$ were fixed to sufficiently large values to suppress their influence on $S^{\mathrm{F}}_{\mathrm{CCD},1}$, and $F_\Delta S^{\mathrm{F}}_{\mathrm{CCD},2}$ is neglected, as previously argued in Section 7.4. Table 8.1 lists experimental parameter values, and Table 8.2 lists the fitted parameter values for DOPC exposures from 2013 - 2015. Each column in a given year corresponds to a different part of the same DOPC sample. The final row of Table 8.2 lists $\left(\chi^{2,\cancel{\mathrm{tilt}}}_{\mathrm{red}}/\chi^{2,\mathrm{tilt}}_{\mathrm{red}}\right)$; the tilt-dependent χ^2_{red} is about 20% smaller than the tilt-indepedent χ^2_{red}. Section 8.1 discusses the measured values of K_c and K_θ and their associated uncertainties. Final values of $K_c = 8.3 \pm 0.6 \times 10^{-13}$ ergs and $K_\theta = 91 \pm 7$ mN/m are determined. In Section 8.2 the determined B-values are further analyzed in order to evaluate the Hamaker parameter which mediates the van der Waals interaction between bilayers.

Table 8.1: Experimental parameter values for 2013 - 2015 DOPC exposures.

parameter	[units]	2013	2014	2015	description
μ	[mm]	2.60	2.60	3.08	$1/e$ X-ray absorption length in sample
λ	[Å]	1.175	1.177	1.108	X-ray wavelength
$\mathcal{S}$	[mm]	359.3	373	387.2	sample to detector distance
b_x	[pixels]	2.3	2.5	2.3	beam width on CCD in x-direction
$\Delta\lambda/\lambda$		0.012	0.012	0.012	energy dispersion
$\Delta\gamma_x$		5×10^{-5}	5×10^{-5}	5×10^{-5}	beam angular divergence in x-direction
$\Delta\gamma_z$		1×10^{-4}	2×10^{-4}	1×10^{-4}	beam angular divergence in z-direction

Table 8.2: Tilt-dependent and -independent fitted parameter values for DOPC exposures measured between 2013 and 2015. ⋆

	Parameter [units]	2013					2014			2015			
	D † [Å]	59.9	60.7	62.9	63.0	63.8	61.1	63.3	63.4	58.9	62.3	63.8	63.8
tilt	K_c [$\times 10^{-13}$ ergs]	9.4	8.4	7.9	7.7	8.0	8.2	7.7	7.9	8.2	9.6	8.5	8.7
	B [$\times 10^{12}$ ergs/cm^4]	46	25	9.0	8.6	7.7	13	7.2	7.3	30	13	7.0	6.9
	K_θ [mN/m]	94	98	92	91	90	80	85	85	85	83	107	91
	a [Å]	11	14	15	15	15	16	17	16	15	15	18	16
	χ^2_{red}	2.777	2.828	2.445	2.278	2.484	2.544	1.665	2.192	6.018	9.933	1.471	1.695
~~tilt~~ ‡	K_c [$\times 10^{-13}$ ergs]	9.3	6.8	6.5	6.4	6.6	6.5	6.3	6.5	6.5	7.5	7.4	7.3
	B [$\times 10^{12}$ ergs/cm^4]	46	25	9.6	9.0	8.0	14	7.8	7.8	30	13	7.2	7.1
	χ^2_{red}	4.451	3.814	3.012	2.740	2.901	3.079	2.073	2.721	6.631	12.073	1.660	2.031
	ratio $\left(\chi^{2,\sout{\text{tilt}}}_{\text{red}}/\chi^{2,\text{tilt}}_{\text{red}}\right)$	1.60	1.35	1.23	1.20	1.17	1.21	1.25	1.24	1.10	1.22	1.13	1.20

⋆ Parameter values are listed without their negligible uncertainties due to the analysis, see Section 7.6.

† The D-spacing is the same for tilt-dependent and -independent.

‡ The K_θ- and a-values were fixed to 5000 mN/m and 4 Å, respectively.

8.1 K_c and K_θ

Both the values of K_c and K_θ listed in Table 8.2 are plotted as a function of year in Fig. 8.1. Besides experimental concerns, the year an exposure was taken is of little interest. The more important consideration is that DOPC samples from different years are different DOPC samples. Therefore, the year to year differences of the average K_c- and K_θ-values (weighted by $1/\chi^2_{\text{red}}$) and their spreads are listed in Table 8.3 and interpreted as sample variation. The uncertainty values in Table 8.3 are much greater than the uncertainty of the individual fitted parameter values due to the curvature of the χ^2-space, see Section 7.6. Therefore, the "intrinsic" uncertainty of the parameter values was neglected. The 2013 and 2015 DOPC samples appear consistent with each other but inconsistent with the 2014 sample; however, all averages and uncertainties were calculated using fewer than 6 values. More statistically robust estimates of $K_c = 8.4 \pm 0.6 \times 10^{-13}$ ergs and $K_\theta = 90 \pm 7$ mN/m are determined by averaging all fitted values. The final averages and associated uncertainties are likely to have both statistical and systematic contributions from both the X-ray scattering analysis and the sample preparation.

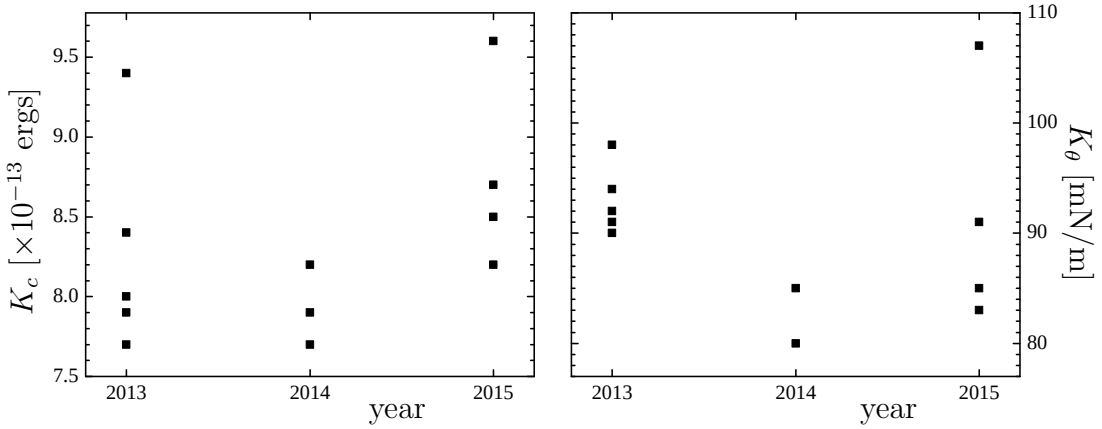


Figure 8.1: The tilt-dependent values of K_c and K_θ listed in Table 8.2 are plotted as a function of year. In 2014, there were two exposures, both with fitted K_θ-value of 85 mN/m.

In principal, K_c and K_θ are mechanical properties of single membranes, and only B is an attribute of the bilayer stack. However, all three moduli might function as effective parameters in describing the bilayer stack height-height correlation function, and therefore, the determined K_c- and K_θ-values could reflect a mixture of single

Table 8.3: Average K_c- and K_θ-values for DOPC samples from 2013 - 2015.

	Parameter [units]		2013	2014	2015	All
tilt	K_c	[$\times 10^{-13}$ ergs]	8.2 ± 0.7	7.9 ± 0.3	8.6 ± 0.6	8.3 ± 0.6
	K_θ	[mN/m]	93 ± 3	84 ± 3	97 ± 11	91 ± 7
~~tilt~~	K_c	[$\times 10^{-13}$ ergs]	7.0 ± 1.2	6.4 ± 0.1	7.3 ± 0.5	6.9 ± 0.8

and stacked bilayer properties. To assess this concern, the K_c- and K_θ-values listed in Table 8.2 are plotted as functions of D in Fig. 8.2. The determined K_c- and K_θ-values appear independent of the repeat distance perpendicular to the bilayer planes, and therefore, they appear to be single membrane attributes consistent with their theoretical definitions in Section 3.1.

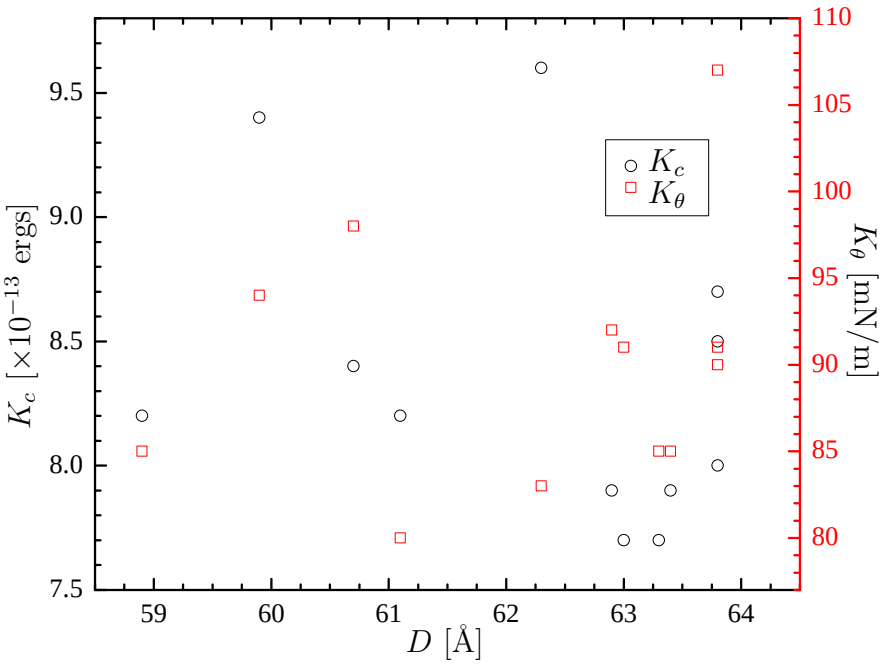


Figure 8.2: Tilt-dependent values of K_c and K_θ listed in Table 8.2 are plotted as functions of D.

The tilt-dependent and tilt-independent K_c-values are listed in Table 8.3. The tilt-dependent K_c-value is on average about 20% larger than the tilt-independent value. This is understandable because the total softness of the membrane was formerly modeled just by a K_c "spring constant"; adding another softening degree of freedom requires K_c to increase for the same degree of overall softness. However, the system

is more complex than two ideal springs in series since the system's response to K_c and K_θ is Q_r-dependent. Furthermore, the inclusion of tilt should not greatly modify the determined K_c-value compared to the tilt-independent analysis because the tilt-dependent height spectrum is only inconsistent with the tilt-independent spectrum for large Q_r (short real space length scales), see Fig. 3.4.

Comparing to Literature Values

The composite tilt-dependent and -independent determined value of $K_c/(k_\mathrm{B}T)$ from all three years is compared to some literature experimental and simulation values listed in Table 8.4. The values listed above the single horizontal line were previously summarized and reported [16]. The first "X-ray stacks" value is a literature average using a tilt-independent analysis [48] on data taken before 2013. Red values were determined in this thesis, and blue values were reported earlier by me using a tilt-dependent analysis and DOPC exposures from 2013 [32]. [27] The 2013 - 2015 composite tilt-independent $K_c/(k_\mathrm{B}T)$-value of 16.5 ± 1.9 is consistent with the corresponding value of 18.2 ± 2.7 determined by others using DOPC data prior to 2013.

The K_c-values determined by the tilt-dependent analysis are more consistent with the K_c-values determined by shape fluctuation analysis and molecular dynamics (MD) simulations than the K_c-values determined by the tilt-independent analysis. However, even the tilt-dependent "X-ray stacks" K_c-values are less than the values determined by shape fluctuation analysis and most results from MD simulation. All five values from MD simulations were determined using the same all-atom CHARMM simulation but using different methodologies to extract a K_c-value. For the first three K_c-values, different real space interpretations of the lipid director were used;

[27] The 2014 [32] and current X-ray scattering analysis software are slightly different. The 2014 analysis followed previous analyses [48] except that it used a structure factor expressed in cylindrical coordinates, see Section 5.1, and q_y-dependent integration limits for the CCD integral, see Section 5.3.5. Other modifications to the experimental structure factor detailed in Chapter 5 were implemented after the submission of [32]. Both the current and the 2014 versions of the analysis software were used to analyze DOPC exposures from 2013 and determined similar values of K_c and K_θ; $8.2 \pm 0.7 \times 10^{-13}$ ergs vs $8.3 \pm 0.6 \times 10^{-13}$ ergs and 93 ± 3 mN/m vs 95 ± 7 mN/m for now and 2014, respectively.

Table 8.4: Values of $K_c/(k_BT)$ determined from various experimental procedures and molecular dynamics simulation. Values were adjusted to 30 °C.

X-ray stacks	MM GUV[a]	tethers[b] GUV	Shapes[c] GUV	MD Simulation
18.2 ± 2.7 [16] ▷	19.1 ± 2.2 [87]	16 ± 2 [88]	26.5 ± 2.7 [89]	
15.1 ± 1.6 [47] ▷	23 ± 2.2 [90]	23 ± 5 [91]	24 ± 2 [90]	
16.5 ± 0.7 [32] ▷				26.6 ± 0.7 [25] 1
19.8 ± 1.4 [32] ◁				27.0 [25] 2
16.5 ± 1.9 ▷				25.4 [25] 3
19.8 ± 1.4 ◁				24.5 [25] 1
				22.1 ± 1.1 [25] ◇

[a] micromechanical manipulation of giant unilamellar vesicles (GUV)
[b] pulling cylindrical tethers
[c] analysis of shapes
▷ tilt-independent analysis
◁ tilt-dependent analysis
1 2 3 See [25] Supporting Information; number corresponds to tilt definition in thesis text
◇ See [25] Supporting Information; used method described in [86]

1. unit vector which points from the midpoint between a lipid phosphorous atom and glycerol C2 atom to the midpoint between the terminal methyl atoms on the lipid tail

2. unit vector which points from phosphorous atom to the mean point between terminal tail methyl atoms

3. unit vector which points from the glycerol backbone C2 atom to the mean point between terminal tail methyl atoms,

and the spectrum associated with the longitudinal component of the director field was analyzed, conceptually following [22]. The fourth K_c-value used Definition 1 for tilt, and the height spectrum was analyzed. The fifth K_c-value was determined using a real space analysis method first described by Khelashvili *et al.* [86]. Clearly, the K_c-value determined from MD simulation is dependent on the details of the analysis method [21], and for at least one of the methods the determined K_c-value is consistent with the most recent tilt-dependent "X-ray stacks" value.

The determined value of K_θ is compared to literature values in Table 8.5. The red value was determined in this thesis, and the blue value was reported earlier by me using a slightly different tilt-dependent analysis and DOPC exposures only

from 2013 [32]. The first two "Generic" K_θ-values are estimates based on relations between a tilted lipid and its interfacial area or chain length, respectively. Both models hypothesize that $K_\theta \approx 2\gamma_{ow}$, where γ_{ow} is the oil-water surface tension. [28]

Table 8.5: Values of K_θ determined from experiments and MD simulations.

Lipid	K_θ [mN/m]	Temp. [°C]	Method	Ref.
DOPC	90 ± 7	30	LAXS	
	95 ± 7	30	LAXS	[32]
	24 (48 *)	30	wide angle X-ray scattering	[93]
	$\sim$80 †‡	30	united atom	[23]
	66 ± 2 ^{1}	24.9	all-atom CHARMM	[25]
	75 ^{2}	24.9	all-atom CHARMM	[25]
	56 ^{3}	24.9	all-atom CHARMM	[25]
Generic	100	NA	coarse estimate	[31]
	100		coarse estimate	[93]
	160 †		mean-field theory	[94]

† 2× reported monolayer value
‡ assuming area is 70 Å^2
* assuming basic unit is chains (molecules)
$^{1\,2\,3}$ See Supporting Information; number corresponds to director definition in text

Similarly to the K_c-values determined from MD simulations, the determined K_θ-values are sensitive to the definition of tilt; depending on the tilt definition, the K_θ-values extracted from the simulation vary by about ±15%. The value reported in [23] and the largest K_θ-value from [25] are only about 10 and 20% smaller than the experimental K_θ-values, respectively. Yet another interpretation of the lipid director may yield better agreement between the experimental K_θ-value and analysis of the spectrum associated with the transverse component of the director spectrum [25]. Finally, the fields of molecular models could simply give different values even if the analysis is perfect.

The inconsistency of the X-ray and MD simulation determined values of K_c and K_θ is further evaluated by fitting measured X-ray data, fixing the value of K_θ to

[28] γ_{ow} decreases by only ~0.3%/°C [92], suggesting that temperature differences between MD and LAXS are insignificant in Table 8.5.

be the MD simulation determined value of 66 mN/m. Table 8.6 lists the results of fitting two exposures where K_θ was fixed. In both cases the determined K_c-value increases but not by enough to agree with the K_c-value determined via MD simulation ($11.1 \pm 0.3 \times 10^{-13}$ ergs). Also, while χ^2_{red} only increases modestly, the increase in χ^2 is more than 1000.

Table 8.6: Fitted parameter values for K_θ fixed to MD simulation determined value of 66 mN/m.

Parameter [units]		2014		2015	
D	[Å]	61.1		63.8	
K_c	[$\times 10^{-13}$ ergs]	8.5	8.2	9.3	8.5
B	[$\times 10^{12}$ ergs/cm^4]	13	13	7	7
K_θ	[mN/m]	66 †	80	66 †	107
a	[Å]	18	16	23	18
χ^2_{red}		2.574	2.544	1.512	1.471

† indicates a fixed parameter value.

Besides the X-ray scattering analysis detailed in this thesis, no other experimental technique has measured K_θ. Both mechanical manipulation [15] and shape fluctuation analysis [14, 17] of giant unilamellar vesicles are unlikely experimental candidates for determining K_θ because they primarily probe long length scales for which K_θ only marginally affects membrane mechanics [93]. Since K_θ most significantly influences short length scales, measuring its value in real space may be experimentally impractical. In contrast, it is plausible that the far-field elastic scattering from single bilayers could be analyzed to determine K_θ, see the second Subsection in Section 8.1.1. Alternatively, the value of K_θ may be assessable by experimental techniques that investigate membrane dynamics. However, complementary theoretical work remains outstanding, not altogether unexpected given that theoretical and experimental work on tilt-dependent membrane mechanics is rather recent.

8.1.1 Future Work

Remarks Regarding Stacked Bilayers

Overall, the values of K_c and K_θ determined by the tilt-dependent analysis of X-ray scattering from stacked lipid bilayers compare favorably with other experimental methodologies as well as with simulations. Still, there remain inconsistencies worth investigating. There are many possible reasons for the discrepancy between K_c and K_θ-values determined by various methods as compared to the X-ray method detailed in this thesis. Unlike all other methods in Table 8.4 which investigate single bilayers, the samples in the X-ray scattering analysis are multilamellar, and in part, this difference may account for differences in the K_c-values listed in Table 8.4. Although, the difference in determined K_c-values for single membrane techniques is at least as large as the difference between X-ray stacks and shape analysis of GUVs. Additionally, the K_c and K_θ-values determined by the tilt-dependent analysis of X-ray scattering from stacked bilayers are not obviously corrupted by intermembrane interactions since they do not appear to depend on D, see Fig. 8.2 and the associated discussion in the second paragraph of Section 8.1.

The "X-ray stacks" tilt-dependent K_c-value may be inconsistent with K_c-values determined by shape fluctuation analysis and simulations because the modeling of the X-ray scattering from stacked bilayers remains inadequate, even after the implementation of a tilt-dependent model. In Section 7.1, it is shown that the tilt-dependent model systematically deviates from the measured intensity, see Fig. 7.5. Critically, the scaled residuals are larger for smaller q_x. In other words, the tilt-dependent predictions are more accurate for shorter length scales as compared to longer length scales. Both sample-dependent details and theoretical shortcomings could yield the aforementioned long length scale discrepancies.

Long length scale correlations in the sample are sensitive to several sample-dependent factors such as the domain distributions, the supporting substrate, the sample's free upper surface, and defects. Neglecting the scattering specific to the aforementioned features and focusing on their effects on the stacked bilayers, the primary effect of all these possibilities is to alter the boundary conditions for the calculation of the height-height correlation function. In general, boundary conditions more significantly affect long length scale correlations as compared to short length scale correlations, possibly explaining the increased scaled residuals at smaller q_x

as compared to larger q_x. Height-height correlation functions can be calculated for boundary conditions other than periodic ones, and the corresponding X-ray scattering predictions can be compared to measurements. Such theoretical and numerical endeavors are likely to be quite laborious because most boundary condition choices lead to a less analytically tractable theory compared to periodic boundary conditions, see Section 3.3.3. Additionally, the aforementioned increased scaled residuals occur at $0.01 \lesssim q_x \lesssim 0.1$ Å^{-1} which correspond to in-plane lengths between about 60 and 600 Å. The current analysis suggests that the in-plane size of sample domains are much greater than 600 Å (see Section 7.2), and therefore, boundary conditions are unlikely to be the most significant source of deviations between the current analysis and the X-ray scattering measurements.

The deviations between the tilt-dependent X-ray predictions and the measured intensity at $0.01 \lesssim q_x \lesssim 0.1$ Å^{-1} may be attributable to deficiencies of the bilayer stack free energy functional, see Section 3.1 specifically Eq. (3.4). Conceptually, the stacked bilayer free energy can be decomposed into terms dependent on fluctuations within a given membrane (intramembrane terms) and terms dependent on fluctuations that explicitly couple different membranes (intermembrane terms). $\mathcal{F}_\mathrm{u}$ Eq. (3.4) is reproduced and the intramembrane and intermembrane terms are indicated by red and blue underlines, respectively,

$$\mathcal{F}_\mathrm{u} = \frac{1}{2}\sum_j \int_{A_\mathrm{P}} \mathrm{d}^2\mathbf{r} \ \left[\underline{K_c\left(\nabla^2 z_j^+ + \boldsymbol{\nabla}\cdot\hat{\mathbf{m}}_j\right)^2 + K_\theta|\hat{\mathbf{m}}_j|^2} + \underline{B\left(z_{j+1}^+ - z_j^+\right)^2}\right]. \tag{8.1}$$

Within the complete Watson *et al.* model [1], there are several more terms than in Eq. (8.1), but the majority of additional terms describe the peristaltic contributions to the single membrane free energy. Since the deviations between the current theory and X-ray measurements occur for $q_x \lesssim 0.1$ Å^{-1} (in-plane lengths greater than about 60 Å), the peristaltic modes which correspond to thickness fluctuations are unlikely to be significant for in-plane lengths much greater than the bilayer thickness (about 45 Å).

Alternatively, the intermembrane term could be extended to be a function of fields besides the bilayer midplane field z_j^+. Fully hydrated bilayers in a stack are far enough apart that fields involved in the peristaltic part of the complete Watson model are unlikely to be significantly correlated between different membranes. Still, neglecting

protrusions, there are two fields besides z_j^+ involved in the undulation part of the Watson model to consider; $\hat{\mathbf{m}}_j(\mathbf{r})$ and $\varepsilon_j(\mathbf{r})$, where ε_j describes the deviations of the surface separating the two monolayer leaflets from z_j^+ [1]. Possible new harmonic intermembrane terms include

$$\frac{1}{2}B'\left(\varepsilon_{j+1}^+ - \varepsilon_j^+\right)^2 \tag{8.2}$$

and

$$\frac{1}{2}B''\left|\hat{\mathbf{m}}_j\right|\left(z_{j+1}^+ - z_j^+\right), \tag{8.3}$$

where B' and B'' are new bulk moduli and the $\hat{\mathbf{m}}$-dependent term follows from symmetry arguments [40] (see pp. 337-339). However, these new terms may be less significant than known anharmonic intermembrane interactions dependent on z_j^+ [95].

The deviations between the tilt-dependent X-ray predictions and the measured intensity may be related to inadequacies of the model bilayer electron density, see Section 3.2.1 specifically Eq. (3.7) reproduced below,

$$\rho_j(\mathbf{r}, z) = \rho_{\mathrm{s}}\Big(\left[z - jD - z_j^+(\mathbf{r})\right]\Psi_j(\mathbf{r}), P_j(\mathbf{r})\Big). \tag{8.4}$$

The current electron density $\rho_j(\mathbf{r}, z)$ Eq. (8.4) is a minor extension of the classic smectic A electron density [40]. $\rho_j(\mathbf{r}, z) \neq \rho_{\mathrm{s}}(z)$ primarily because of fluctuations in $z_j^+(\mathbf{r})$, where $\rho_{\mathrm{s}}(z)$ is the electron density of a single static membrane inherently broadened by protrusion modes, see Section 3.2.1; the geometric factor $\psi_j(\mathbf{r})$ and the *en masse* peristaltic field $P_j(\mathbf{r})$ are of secondary importance. To predict the X-ray scattering for $0.01 \lesssim q_x \lesssim 0.1$ Å^{-1} (in-plane lengths between 60 and 600 Å), it may be necessary to express the bilayer electron density explicitly respecting internal degrees of freedom. For example, the bilayer electron density could be expressed as the sum of monolayer or lipid molecule electron densities. Either of the aforementioned perspectives is likely to yield a bilayer electron density in which fields other than z_j^+ start to become relevant.

Complementary Single Membrane X-ray Experiment and Analysis

In principal, the X-ray scattering from single lipid bilayers could be measured and analyzed to determine K_c and K_θ, thereby probing the extent to which the values determined using the X-ray stacks methodology deviate from single membrane values. Instead of a stacked bilayer free energy functional, a single (s) membrane model, like $\mathcal{F}_\mathrm{s}$ Eq. (3.3), could be used. The predicted X-ray scattering would be of a form similar to Eq. (3.20) except that the subscript zeros and sum over out-of-plane index values are discarded,

$$I_\mathrm{s}(\mathbf{q}) \equiv \int\int \mathrm{d}^2\mathbf{r}\ \mathrm{d}^2\mathbf{r}'\ e^{i\mathbf{q}_\mathbf{r}\cdot(\mathbf{r}-\mathbf{r}')}\exp\left\{-\frac{q_z^2}{2}\left\langle\left[z^+(\mathbf{r})-z^+(\mathbf{r}')\right]^2\right\rangle\right\}\left\langle|F(\mathbf{r},q_z)|^2\right\rangle, \quad (8.5)$$

where

$$F(\mathbf{r},q_z) \approx \int_{-\infty}^{\infty}\mathrm{d}\tilde{z}\ \frac{\rho_\mathrm{s}[\tilde{z},P(\mathbf{r})]}{\langle\Psi\rangle}\exp\left\{iq_z\tilde{z}/\langle\Psi\rangle\right\}. \quad (8.6)$$

The single membrane height-height correlation function $\left\langle\left[z^+(\mathbf{r})-z^+(\mathbf{r}')\right]^2\right\rangle$ can be derived using $\mathcal{F}_\mathrm{s}$ Eq. (3.3). The analysis of the described scattering experiment is straightforward; however, the scattering experiment is quite challenging. To reach most single membrane samples, the incident X-rays must travel a significant distance through bulk water, greatly attenuating both the incident X-ray intensity and scattering intensity. Additionally, since scattering intensity is proportional to the amount of material in the X-ray beam, the scattering intensity from a single membrane is likely much weaker than the scattering from stacked bilayers. The aforementioned experimental issues can be mitigated by using high energy X-rays (longer $1/e$-length in water) and large surface area membranes. Already, the X-ray scattering from single solid supported and "floating" bilayers at the solid-water interface have been measured and analyzed [96, 97, 98, 99, 100, 101]. Removing the supporting substrate entirely such as in vesicles has the advantage that the free energy model does not contain a term describing the bilayer-substrate interaction [101]. A single GUV could be held at the end of a pipette while X-rays scatter from the opposite end of the vesicle. Further, the vesicle's surface tension could be modified *in situ* between X-ray exposures.

8.2 B

In Table 8.2, the value of the bulk modulus B decreases as a function of increasing D, a previously described effect [102]. The tilt-independent B-values are often larger than the values of B determined by the tilt-dependent analysis. The variation in the value of B is related to the increased K_c-value determined by the tilt-dependent analysis, and the different roles of K_c and B in the relation for the height-height correlation function $h_j(r/\xi, \ell, \tau)$,

$$h_j(r/\xi, \ell, \tau) = \frac{D^2\eta}{2\pi^2} \int_0^\tau \mathrm{d}v \, \frac{1 - J_0\left(\sqrt{2v}\frac{r}{\xi}\right)\left(\sqrt{1+\frac{v^2}{1+v\ell}} - \frac{v}{\sqrt{1+v\ell}}\right)^{2j}}{\frac{v}{\sqrt{1+v\ell}}\sqrt{1+\frac{v^2}{1+v\ell}}}, \tag{8.7}$$

where

$$\xi = \sqrt[4]{K_c/B} \tag{8.8}$$

and

$$\eta = \frac{\pi k_\mathrm{B} T}{2D^2\sqrt{K_c B}}, \tag{8.9}$$

(originally from Eqs. (3.81), (3.59), and (3.79), respectively). ξ is an in-plane bending dependent length scale, whereas η is a multiplicative factor. For small r, the value of $h_j(r/\xi, \ell, \tau)$ is proportional to η and the integrand is independent of ξ. [29] $h_j(r/\xi, \ell, \tau)$ Eq. (8.7) is plotted in Fig. 8.3 using the last 2014 column in Table 8.2. The tilt-dependent and -independent correlation functions are similar for small r ($r \lesssim \xi$, where $\xi \approx 35$ Å is typical) and j, but are increasingly dissimilar for increasing r and j. Intuitively, the best tilt-independent parameter values are the ones that yield a height-height correlation function $h_j(r/\xi, 0, \infty)$ that mimics $h_j(r/\xi, \ell, \tau)$ calculated using the tilt-dependent parameter values. Since the tilt-independent K_c-value is less than the tilt-dependent K_c, the tilt-independent B-value must be greater than

[29] However, τ is dependent on ξ. For large v, the integrand of Eq. (8.7) decays like v^{-1}. Therefore, for small r, Eq. (8.7) is approximately independent of ξ.

the tilt-dependent B for the tilt-dependent and -independent η-values to not be too dissimilar. If the η-values significantly differ, the tilt-dependent and -independent $h_j(r/\xi, \ell, \tau)$ will disagree for small r.

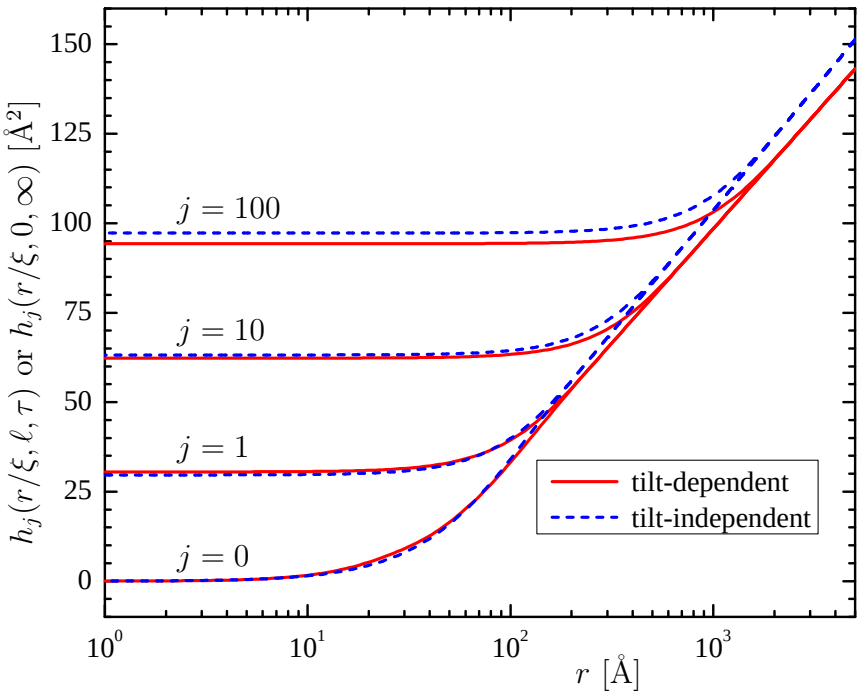


Figure 8.3: Tilt-dependent and -independent height-height correlation functions $h_j(r/\xi, \ell, \tau)$ and $h_j(r/\xi, 0, \infty)$, see Eq. (8.7), are plotted as functions of r using the red parameter values in Table 8.2.

Using the values of B and D in Table 8.2, the Hamaker parameter mediating the van der waals interaction between bilayers is determined. First in Section 8.2.1, following the derivation using the discrete smectic A model [58], the fluctuation free energy per unit area $\mathcal{F}_{\text{fl}}$ is derived using the tilt-dependent model. Then in Section 8.2.2, the values of B and D in Table 8.2 and $\mathcal{F}_{\text{fl}}$ are used to determine the fluctuation pressure, and subsequently, the Hamaker parameter is evaluated.

8.2.1 Fluctuation Free Energy: $\Delta\mathcal{F}_{\text{fl}}$

In Appendix D.4, the tilt-dependent fluctuation free energy per unit area of one bilayer $\Delta\widetilde{\mathcal{F}}_{\text{fl}}$ is derived. Quoting the final result Eq. (D.29),

$$\Delta\widetilde{\mathcal{F}}_{\text{fl}} = \frac{k_{\text{B}}TD}{8\pi^2}\int_{-\pi/D}^{\pi/D}\mathrm{d}Q_z\ \int_0^{\pi/a}\mathrm{d}Q_r\ Q_r \ln\left(1+\frac{4\sin^2\left(Q_zD/2\right)}{\xi^4Q_r^4}\left(1+\xi_\theta^2Q_r^2\right)\right). \tag{8.10}$$

In the limit $\xi_\theta \to 0$ and $a \to 0$,

$$\lim_{\substack{\xi_\theta\to 0\\ a\to\infty}} \Delta\widetilde{\mathcal{F}}_{\text{fl}} \equiv \Delta\widetilde{\mathcal{F}}_{\text{fl}}^{\cancel{\text{tilt}}} \tag{8.11}$$

$$= \frac{k_{\text{B}}TD}{8\pi^2}\int_{-\pi/D}^{\pi/D}\mathrm{d}Q_z\ \int_0^{\infty}\mathrm{d}Q_r\ Q_r \ln\left(1+\frac{4\sin^2\left(Q_zD/2\right)}{\xi^4Q_r^4}\right) \tag{8.12}$$

$$= \frac{k_{\text{B}}T}{2\pi}\sqrt{\frac{B}{K_c}}, \tag{8.13}$$

where $\Delta\widetilde{\mathcal{F}}_{\text{fl}}^{\cancel{\text{tilt}}}$ is the tilt-independent fluctuation free energy per unit area of one bilayer and was previously derived [58].

8.2.2 Hamaker Parameter

The D-spacing is hypothesized to be determined by a competition between several pressures [58, 102]: the osmotic pressure P_{osm}, the fluctuation pressure P_{fl}, the repulsive hydration pressure P_{hyd}, and the van der Waals pressure P_{vdW},

$$0 = -P_{\text{osm}}(D'_{\text{w}}) + P_{\text{fl}}(D'_{\text{w}}) + P_{\text{hyd}}(D'_{\text{w}}) - P_{\text{vdW}}(D'_{\text{w}}), \tag{8.14}$$

where D'_{w} is the interbilayer water spacing,

$$P_{\rm hyd}(D'_{\rm w}) = P_{\rm h}\exp\left\{-D'_{\rm w}/\lambda_{\rm h}\right\}, \tag{8.15}$$

$$P_{\rm vdW}(D'_{\rm w}) = \frac{H}{6\pi}\left(\frac{1}{D'^{3}_{\rm w}} - \frac{2}{\left(D'_{\rm w}+D'_{\rm B}\right)^{3}} + \frac{1}{\left(D'_{\rm w}+2D'_{\rm B}\right)^{3}}\right), \tag{8.16}$$

H is the Hamaker parameter, and $D'_{\rm B} = 44.8$ Å [102] is the steric bilayer thickness,

$$D'_{\rm w} \equiv D - D'_{\rm B}. \tag{8.17}$$

$P_{\rm h} = 0.55\times10^{8}$ J/m^3 and $\lambda_{\rm h} = 2.2$ Å are well-determined from previous work [103]. At full hydration $P_{\rm osm} = 0$, and therefore, if $P_{\rm fl}$ is known, the only unknown in Eq. (8.14) is H the Hamaker parameter.

Using the fitted parameter values from Table 8.2, $P_{\rm fl}$ is determined. Only the tilt-dependent quantities are significantly discussed, but the corresponding tilt-independent analysis is also completed to compare the results. First, $\Delta\mathcal{F}_{\rm fl}$ Eq. (8.10) is evaluated and plotted as a function of $D'_{\rm w}$ in Fig. 8.4. The dashed lines are exponential fits to the data, suggesting that

$$\Delta\widetilde{\mathcal{F}}_{\rm fl} \sim \exp\left\{-D'_{\rm w}/\lambda_{\rm fl}\right\}, \tag{8.18}$$

where $\lambda_{\rm fl} = 5.3\pm0.5$ Å ($\lambda_{\rm fl}^{\cancel{\rm tilt}} = 5.9\pm0.4$ Å). Of note, the analytical theories that predict the exponential dependence of $\Delta\widetilde{\mathcal{F}}_{\rm fl}$ on $D'_{\rm w}$, see Eq. (8.18), also predict that $\lambda_{\rm fl} = 2\lambda_{\rm h}$ [103]. For both the tilt-dependent and -independent models, $\lambda_{\rm fl} > 2\lambda_{\rm h} = 4.4$ Å, consistent with previous experimental work, see Table 8.7. Using Eq. (8.18), the fluctuation pressure is

$$P_{\rm fl} \equiv -\left(\frac{\partial\,\Delta\widetilde{\mathcal{F}}_{\rm fl}}{\partial D'_{\rm w}}\right)_{T} = \frac{\Delta\widetilde{\mathcal{F}}_{\rm fl}}{\lambda_{\rm fl}}. \tag{8.19}$$

At full hydration (FH) Eq. (8.14) simplifies,

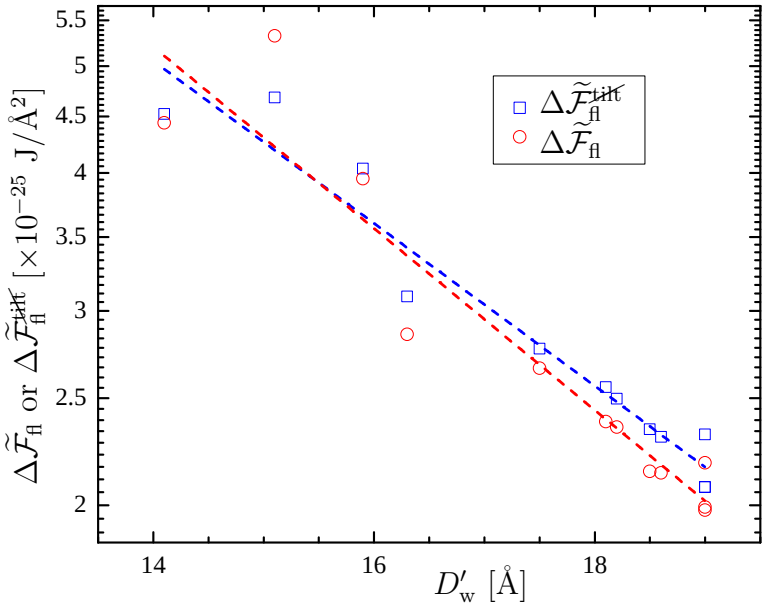


Figure 8.4: $\Delta\widetilde{\mathcal{F}}_{fl}^{\not{tilt}}$ and $\Delta\widetilde{\mathcal{F}}_{fl}$ are plotted as functions of D'_w. The dashed lines are exponential fits to the correspondingly colored data.

Table 8.7: Tilt-dependent and -independent values of λ_{fl} and H.

Parameter [units]	tilt	~~tilt~~		
λ_{fl} [Å]	5.3 ± 0.5	5.9 ± 0.4	5.8 [102]	5.9 [103]
H [$\times 10^{-21}$ J]	6.4 ± 0.4	6.1 ± 0.4	5.4 [102]	

$$0 = P_{\mathrm{fl}}(D'_{\mathrm{w}}) + P_{\mathrm{hyd}}(D'_{\mathrm{w}}) - P_{\mathrm{vdW}}(D'_{\mathrm{w}}). \tag{8.20}$$

Using P_{fl} Eq. (8.19), $\Delta\widetilde{\mathcal{F}}_{\mathrm{fl}}$ Eq. (D.29), and $D_{\mathrm{FH}} = 63.8$ Å, the Hamaker parameter is $H = 6.4 \pm 0.4 \times 10^{-21}$ J ($H^{\not{\mathrm{tilt}}} = 6.1 \pm 0.4 \times 10^{-21}$ J). $H^{\not{\mathrm{tilt}}}$ is slightly larger than the previously determined value of 5.4×10^{-21} J [102]. Unlike the current analysis, the previous work only considered data from a single DOPC sample. The tilt-dependent H is greater than $H^{\not{\mathrm{tilt}}}$ because P_{vdW} must increase to balance the increased P_{fl}.

Chapter 9

Conclusions

This thesis has reported experimental evidence supporting the enrichment of the classic Helfrich-Canham membrane model to include tilt-dependent terms. The current work has described a tilt-dependent analysis of the X-ray scattering from oriented stacks of fluid phase lipid bilayers. Several X-ray exposures from different DOPC samples have been analyzed, and final single membrane mechanical moduli values of $K_c = 8.4 \pm 0.6 \times 10^{-13}$ ergs and $K_\theta = 90 \pm 7$ mN/m were determined at 30 °C. The tilt-dependent K_c-value is more consistent with literature values than the K_c-value determined using a tilt-independent analysis. However, the determined tilt-dependent K_c-value is between 15 and 25% less than most values determined from MD simulations. The experimentally determined K_θ-value is between 10 and 20% greater than values reported from MD simulations. As of yet, there is no other experimental technique that has determined the value of K_θ.

The tilt-dependent X-ray scattering analysis is briefly summarized. First in Chapter 3, a tilt-dependent stacked bilayer free energy functional was hypothesized, based on a recent single membrane tilt-dependent free energy. Then, a tilt-dependent stacked bilayer electron density was posited, and a novel form factor / structure factor separation was derived. Within this analysis, the height-height correlation function remains the most important statistical quantity for predicting the X-ray scattering from stacked bilayers. The tilt-dependent height-height correlation function was derived, and in Chapter 4 an approximate analytic form for long in-plane length scales was derived. Like the tilt-independent theory, the tilt-dependent height-height correlation function logarithmicly diverges with increasing in-plane length scale, yielding quasi-long range order of the stacked bilayers. In Chapter 5 the theoretically pre-

dicted intensity was modified by several sample concerns including domain sizes and mosaicity and several experimental issues such as X-ray beam coherence, geometric broadening, and absorption of the incident and scattered X-rays. In Chapter 6, it was shown that all three mechanical moduli K_c, B (bulk modulus that mediates intermembrane interactions), and K_θ are plausibly determined by the new tilt-dependent X-ray scattering analysis. In Chapter 7 measured scattering intensity from a single X-ray exposure of stacked DOPC bilayers was analyzed using both tilt-dependent and -independent models. The tilt-dependent model was shown to better account for the measurements, supporting the extension of the classic Helfrich-Canham model to include a tilt degree of freedom. Finally in Chapter 8, many exposures from three different DOPC samples were analyzed yielding the average K_c- and K_θ-values and associated uncertainties quoted above.

Much theoretical and experimental work relies upon the Helfrich-Canham model of membrane mechanics. It is unlikely that the recent tilt-dependent models will quantitatively influence all previous membrane-related work; however, the tilt-dependent perspective in which internal degrees of freedom are quantitatively considered may eventually be pervasive in the membrane research community. As mentioned in the Introduction, the relatively recent tilt-dependent models should motivate new and exciting future work, especially now that they are experimentally supported.

Appendices

Appendix A

Chapter 3: Some Details in Theoretical Derivations

A.1 Free Energy Involving a Hermitian Matrix

In Section 3.3.1, the stacked membrane free energy functional $\mathcal{F}_{\rm u}$ Eq. (3.39) is expressed in Fourier space in terms of a matrix equation involving a Hermitian matrix, see Eq (3.51). Below, the relation between a Hermitian matrix and various thermal averages is derived.

If orthonormal eigenvectors of a Hermitian matrix $\mathbb{H}$ are chosen and written as the columns of an orthogonal matrix, $\mathbb{O}$, then $\mathbb{H}$ can be expressed as

$$\mathbb{H} = \mathbb{O}\mathbb{D}\mathbb{O}^T = \mathbb{O}\mathbb{D}\mathbb{O}^{-1}, \tag{A.1}$$

where $\mathbb{D}$ is a diagonal matrix whose elements are the eigenvalues of $\mathbb{H}$, λ_i. The spectral theorem ensures that such a decomposition always exists for a Hermitian matrix. Additionally, the fact the $\mathbb{O}^T = \mathbb{O}^{-1}$ for an orthogonal matrix was utilized. Substituting Eq. (A.1) into the general form for a free energy functional written in matrix form, see Eq. (3.51) for an example,

$$\mathcal{F} = \frac{1}{2}\sum_{\mathbf{Q}} \langle f(-\mathbf{Q})|\mathbb{H}|f(\mathbf{Q})\rangle \tag{A.2}$$

$$= \frac{1}{2}\sum_{\mathbf{Q}} \left\langle f(-\mathbf{Q})|\mathbb{O}\mathbb{D}\mathbb{O}^{-1}|f(\mathbf{Q})\right\rangle \tag{A.3}$$

$$= \frac{1}{2}\sum_{\mathbf{Q}} \langle g(-\mathbf{Q})|\mathbb{D}|g(\mathbf{Q})\rangle \tag{A.4}$$

$$= \frac{1}{2}\sum_{\mathbf{Q}}\sum_{i} \lambda_i \langle g(-\mathbf{Q})|g(\mathbf{Q})\rangle\,, \tag{A.5}$$

where normal coordinates, $|g\rangle = \mathbb{O}^{-1}|f\rangle$, were introduced. Applying the equipartition theorm to the normal coordinates, $g_i(\mathbf{Q})$,

$$\lambda_i \frac{\left\langle g_i(\mathbf{Q})g_j(\mathbf{Q}')\right\rangle_{\text{th}}}{2} = \frac{k_{\text{B}}T}{2}\delta_{i,j}\delta_{\mathbf{Q},-\mathbf{Q}'} \tag{A.6}$$

where $\langle\rangle_{\text{th}}$ denotes a thermal average. Rewriting Eq. (A.6) as a matrix equation,

$$\left\langle |g(\mathbf{Q})\rangle\langle g(\mathbf{Q}')|\right\rangle_{\text{th}} = k_{\text{B}}T\mathbb{D}^{-1}\delta_{\mathbf{Q},-\mathbf{Q}'}. \tag{A.7}$$

Working towards an equation in terms of $|f(\mathbf{Q})\rangle$ by rewriting Eq. (A.7),

$$\left\langle \mathbb{O}|g(\mathbf{Q})\rangle\langle g(\mathbf{Q}')|\mathbb{O}^{-1}\right\rangle_{\text{th}} = k_{\text{B}}T\mathbb{O}\mathbb{D}^{-1}\mathbb{O}^{-1}\delta_{\mathbf{Q},-\mathbf{Q}'} \tag{A.8}$$

$$\left\langle |f(\mathbf{Q})\rangle\langle f(\mathbf{Q}')|\right\rangle_{\text{th}} = k_{\text{B}}T\mathbb{H}^{-1}\delta_{\mathbf{Q},-\mathbf{Q}'}. \tag{A.9}$$

Various thermal averages involving $|f(\mathbf{Q})\rangle$ can be expressed in terms of $\mathbb{H}^{-1}$.

A.2 $\Psi_j(\mathbf{r})$

In Section 3.2.2 the small variance of $\Psi_0(\mathbf{r})$ was used to justify a simplification of $I_j(\mathbf{q})$ in Eq. (3.17). The following several subsections validate the aforementioned claim regarding $\Psi_0(\mathbf{r})$. In Subsection A.2.1, $\Psi_j(\mathbf{r})$ is expressed in terms of more analytically useful fields. Then, in Subsection A.2.2 the variance of $\Psi_0(\mathbf{r})$ is shown

to be small. Finally, the transition from $I_j^{\mathrm{a}}(\mathbf{q})$ Eq. (3.17) to $I_j^{\mathrm{b}}(\mathbf{q})$ Eq. (3.20) is established in Subsection A.2.3.

A.2.1 Reformulation

Using the definition of Ψ_j, Eq. (3.7),

$$\Psi_0 = \frac{-\mathbf{N}_0^{(1)} \cdot \hat{\mathbf{z}} - \mathbf{N}_0^{(2)} \cdot \hat{\mathbf{z}}}{\mathbf{N}_0^{(1)} \cdot \mathbf{n}_0^{(1)} + \mathbf{N}_0^{(2)} \cdot \mathbf{n}_0^{(2)}} \tag{A.10}$$

$$= \frac{\cos \alpha_{\mathrm{b}}^{(1)} + \cos \alpha_{\mathrm{b}}^{(2)}}{\cos \alpha_{\mathrm{t}}^{(1)} + \cos \alpha_{\mathrm{t}}^{(2)}}, \tag{A.11}$$

where $\alpha_{\mathrm{b}}^{(\beta)}$ is the angle between the local bilayer normal $-\mathbf{N}^{(\beta)}$ and $\hat{\mathbf{z}}$ and $\alpha_{\mathrm{t}}^{(\beta)}$ is the angle between the local lipid director $\mathbf{n}^{(\beta)}$ and $\mathbf{N}^{(\beta)}$. β identifies the upper (1) or lower (2) monolayer leaflet. Assuming that $\alpha_{\mathrm{b}}^{(\beta)}$ and $\alpha_{\mathrm{t}}^{(\beta)}$ are small, Ψ_0 Eq. (A.11) is approximated,

$$\Psi_0 \approx \frac{2 + \frac{\left(\alpha_{\mathrm{b}}^{(1)}\right)^2 + \left(\alpha_{\mathrm{b}}^{(2)}\right)^2}{2}}{2 + \frac{\tan^2 \alpha_{\mathrm{t}}^{(1)} + \tan^2 \alpha_{\mathrm{t}}^{(2)}}{2}} \tag{A.12}$$

$$\approx \left(1 + \frac{\left(\alpha_{\mathrm{b}}^{(1)}\right)^2 + \left(\alpha_{\mathrm{b}}^{(2)}\right)^2}{4}\right)\left(1 - \frac{\tan^2 \alpha_{\mathrm{t}}^{(1)} + \tan^2 \alpha_{\mathrm{t}}^{(2)}}{4}\right). \tag{A.13}$$

$\alpha_{\mathrm{b}}^{(\beta)} \approx \boldsymbol{\nabla} z^{(\beta)}$ for small amplitude out-of-plane fluctuations, and from the definition of $\mathbf{m}$, it follows that

$$\left|\mathbf{m}^{(\beta)}\right|^2 = \tan^2 \alpha_{\mathrm{t}}^{(\beta)} \approx \left|\mathbf{m}_{xy}^{(\beta)}\right|^2. \tag{A.14}$$

Substituting into Ψ_0 Eq. (A.13),

$$\Psi_0 \approx \left(1 + \frac{\left(\boldsymbol{\nabla} z_0^{(1)}\right)^2 + \left(\boldsymbol{\nabla} z_0^{(2)}\right)^2}{4}\right)\left(1 - \frac{\left|\mathbf{m}_{0,xy}^{(1)}\right|^2 + \left|\mathbf{m}_{0,xy}^{(2)}\right|^2}{4}\right). \tag{A.15}$$

Using the definitions [1],

$$z^+ \equiv \frac{z^{(1)} + z^{(2)}}{2}, \tag{A.16}$$

$$z^- \equiv \frac{z^{(1)} - z^{(2)} - 2b_0}{2}, \tag{A.17}$$

$$\bar{\mathbf{m}} \equiv \frac{\mathbf{m}_{xy}^{(1)} + \mathbf{m}_{xy}^{(2)}}{2}, \tag{A.18}$$

$$\tag{A.19}$$

and

$$\hat{\mathbf{m}} \equiv \frac{\mathbf{m}_{xy}^{(1)} - \mathbf{m}_{xy}^{(2)}}{2}, \tag{A.20}$$

Ψ_0 Eq. (A.15) is rewritten in terms of fluctuation fields expressly involved in the complete Watson Model [1],

$$\Psi_0 \approx 1 + \frac{1}{2}\left(\left|\boldsymbol{\nabla} z_0^+\right|^2 + \left|\boldsymbol{\nabla} z_0^-\right|^2 - |\hat{\mathbf{m}}_0|^2 - |\bar{\mathbf{m}}_0|^2\right), \tag{A.21}$$

where terms of higher order than the free energy functional (quartic vs quadratic) were neglected.

A.2.2 Variance

The variance of Ψ_0,

$$\mathrm{Var}\left[\Psi_0(\mathbf{r})\right] = \left\langle |\Psi_0|^2 \right\rangle - \left|\langle \Psi_0 \rangle\right|^2, \tag{A.22}$$

is written in terms of known fluctuation fields using Ψ_0 Eq. (A.21),

$$\Psi_0 \approx 1 + \frac{1}{2}\left(\left|\boldsymbol{\nabla} z_0^+\right|^2 + \left|\boldsymbol{\nabla} z_0^-\right|^2 - |\hat{\mathbf{m}}_0|^2 - |\bar{\mathbf{m}}_0|^2\right) \tag{A.23}$$

$$\equiv 1 + \sum_{i=1}^{4} \psi_i. \tag{A.24}$$

Later sums in this section will appear without explicit limits. Substituting Ψ_0 Eq. (A.24) into $\mathrm{Var}\left[\Psi_0(\mathbf{r})\right]$ Eq. (A.22) and simplifying,

$$\mathrm{Var}\left[\Psi_0\right] \approx \left\langle \left| 1 + \sum \psi_i \right|^2 \right\rangle - \left| 1 + \sum \langle \psi_i \rangle \right|^2 \tag{A.25}$$

$$= 1 + 2\sum \langle \psi_i \rangle + \left\langle \left| \sum \psi_i \right|^2 \right\rangle - \left[1 + 2\sum \langle \psi_i \rangle + \left| \left\langle \sum \psi_i \right\rangle \right|^2 \right] \tag{A.26}$$

$$= \left\langle \left| \sum \psi_i \right|^2 \right\rangle - \left| \left\langle \sum \psi_i \right\rangle \right|^2. \tag{A.27}$$

$\mathrm{Var}\left[\Psi_0\right]$ Eq. (A.27) is necessarily small since it involves quantities less than one and raised to the fourth power. While some of the terms in $\mathrm{Var}\left[\Psi_0\right]$ Eq. (A.27) can be evaluated, many terms involve a thermal average of a quartic quantity which is beyond the order of the free energy functional.

A.2.3 Implications

In Section 3.2.2 the small variance of $\Psi_0(\mathbf{r})$ was utilized to simplify an ensemble average, compare I_j^{a} Eq. (3.17) and I_j^{b} (3.20),

$$\left\langle e^{iq_z\left[z_0^+(\mathbf{r}) - z_0^+(\mathbf{r}')\right]} \left|F_0(\mathbf{r}, q_z)\right|^2 \right\rangle \approx \left\langle e^{iq_z\left[z_0^+(\mathbf{r}) - z_0^+(\mathbf{r}')\right]} \right\rangle \left\langle \left|F_0(\mathbf{r}, q_z)\right|^2 \right\rangle. \tag{A.28}$$

The approximation made in Eq. (A.28) is quantitatively evaluated by investigating the difference of the two sides,

$$\left\langle e^{iq_z\left[z_0^+(\mathbf{r}) - z_0^+(\mathbf{r}')\right]} \left(\left|F_0(\mathbf{r}, q_z)\right|^2 - \left\langle \left|F_0(\mathbf{r}, q_z)\right|^2 \right\rangle \right) \right\rangle. \tag{A.29}$$

Specifically, it will be shown that

$$\left(|F_0(\mathbf{r},q_z)|^2 - \left\langle |F_0(\mathbf{r},q_z)|^2 \right\rangle\right) \approx 0. \tag{A.30}$$

Neglecting, the z_j^+-dependent part of Eq. (A.29) and using the defintion of $F_0(\mathbf{r},q_z)$ Eq. (3.18),

$$\int\int \mathrm{d}z\ \mathrm{d}z'\ \rho_\mathrm{s}[z,P_0(\mathbf{r})]\rho_\mathrm{s}[z',P_0(\mathbf{r})]\left[\frac{e^{iq_z\left(\frac{z}{\Psi_0(\mathbf{r})}+\frac{z'}{\Psi_0(\mathbf{r}')}\right)}}{\Psi_0(\mathbf{r})\Psi_0(\mathbf{r}')} - \frac{e^{iq_z\frac{z+z'}{\langle\Psi_0\rangle}}}{\langle\Psi_0(\mathbf{r})\rangle^2}\right]. \tag{A.31}$$

Using $\Psi_0(\mathbf{r}) \equiv 1-\delta(\mathbf{r})$ and δ' as shorthand for $\delta(\mathbf{r}')$,

$$\frac{1}{\Psi_0(\mathbf{r})} \equiv \frac{1}{1-\delta} = \sum_{n=0}^{\infty}\delta^n \tag{A.32}$$

and

$$\exp\left\{iq_z\left(\frac{z}{\Psi_0(\mathbf{r})}+\frac{z'}{\Psi_0(\mathbf{r}')}\right)\right\} \approx e^{iq_z(z+z')}e^{iq_z(z\delta+z'\delta')} \tag{A.33}$$

$$= e^{iq_z(z+z')}\sum_{n=0}^{\infty}\frac{[iq_z(z\delta+z'\delta')]^n}{n!} \tag{A.34}$$

since $\delta \ll 1$. Using Eqs. (A.32) and (A.34), the Ψ_0-dependent part of Eq. (A.31) is rewritten,

$$\frac{e^{iq_z\left(\frac{z}{\Psi_0(\mathbf{r})}+\frac{z'}{\Psi_0(\mathbf{r}')}\right)}}{\Psi_0(\mathbf{r})\Psi_0(\mathbf{r}')}-\frac{e^{iq_z\frac{z+z'}{\langle\Psi_0\rangle}}}{\langle\Psi_0\rangle^2} \tag{A.35}$$

$$\approx e^{iq_z(z+z')}\cdot$$

$$\left[\sum_{n=0}^{\infty}\delta^n\sum_{m=0}^{\infty}\delta'^m\sum_{j=0}^{\infty}\frac{\left[iq_z\left(z\delta+z'\delta'\right)\right]^j}{j!}-\sum_{n=0}^{\infty}\langle\delta\rangle^n\sum_{m=0}^{\infty}\langle\delta\rangle^m\sum_{j=0}^{\infty}\frac{\left[iq_z\left(z+z'\right)\langle\delta\rangle\right]^j}{j!}\right]$$

$$\propto\sum_{n=0}^{\infty}\sum_{m=0}^{\infty}\sum_{j=0}^{\infty}\frac{(iq_z)^j}{j!}\left[\delta^n\delta'^m\left[\left(z\delta+z'\delta'\right)\right]^j-\langle\delta\rangle^n\langle\delta\rangle^m\left[\left(z+z'\right)\langle\delta\rangle\right]^j\right]. \tag{A.36}$$

Using the binomial formula

$$(x+y)^j=\sum_{k=0}^{j}\binom{j}{k}x^{j-k}y^k, \tag{A.37}$$

Eq. (A.36) is further rewritten,

$$\propto\sum_{n=0}^{\infty}\sum_{m=0}^{\infty}\sum_{j=0}^{\infty}\sum_{k=0}^{j}\binom{j}{k}\frac{(iq_z)^j}{j!}\langle\delta\rangle^n\langle\delta\rangle^m\left(z\langle\delta\rangle\right)^{j-k}\left(z'\langle\delta\rangle\right)^k\cdot$$

$$\left[\frac{\delta^n\delta^m(z\delta)^{j-k}(z'\delta')^k}{\langle\delta\rangle^n\langle\delta\rangle^m\left(z\langle\delta\rangle\right)^{j-k}\left(z'\langle\delta\rangle\right)^k}-1\right] \tag{A.38}$$

$$\propto\sum_{n=0}^{\infty}\sum_{m=0}^{\infty}\sum_{j=0}^{\infty}\sum_{k=0}^{j}\binom{j}{k}\frac{(iq_z)^j}{j!}\langle\delta\rangle^n\langle\delta\rangle^m\left(z\langle\delta\rangle\right)^{j-k}\left(z'\langle\delta\rangle\right)^k\cdot \tag{A.39}$$

$$\left[\left(\frac{\delta}{\langle\delta\rangle}\right)^{n+j-k}\left(\frac{\delta'}{\langle\delta\rangle}\right)^{m+k}-1\right]. \tag{A.40}$$

Given $\mathrm{Var}\left[\Psi_0\right]$ is small (see Section A.2.2), $\mathrm{Var}\left[\delta\right]$ is also small. Therefore, $\langle\delta\rangle\approx\delta$, and consequently, the term in square brackets in Eq. (A.40) is approximately zero. Since Eq. (A.40) is proportional to the error in the approximation in Eq. (A.28), it has been shown that

$$\left\langle e^{iq_z\left[z_0^+(\mathbf{r})-z_0^+(\mathbf{r}')\right]}\left|F_0(\mathbf{r},q_z)\right|^2\right\rangle \approx \left\langle e^{iq_z\left[z_0^+(\mathbf{r})-z_0^+(\mathbf{r}')\right]}\right\rangle \left\langle\left|F_0(\mathbf{r},q_z)\right|^2\right\rangle, \tag{A.41}$$

the original assertion in Section 3.2.2, compare Eqs. (3.18) and (3.19).

Appendix B

Cartesian Structure Factor

In Section 5.1, the stacked membrane sample is assumed to be composed of cylindrical domains. Previously, the domains were assumed to be rectangular cuboids [44, 48], partially motivated by considering the effect of X-ray coherence [48]. Assuming rectangular domains the structure factor was expressed in Cartesian coordinates, simplifying many subsequent calculations (see Chapter 4 [48]). It will be shown that the Cartesian structure factor predicts X-ray scattering features that are not observed.

The cylindrical coordinate many domain (MD) structure factor has been previously presented, see Eq. (5.9),

$$S_{\mathrm{MD}}(q_r, q_z) = {\sum_{j=0}^{\infty}}' H_z(jD)\cos(q_z jD)\int_0^{\infty} \mathrm{d}r\ rH_r(r)J_0(q_r r)G(r, j, q_z). \tag{B.1}$$

For comparison, the Cartesian (c) structure factor, Eq. (4.5) in [48], is reproduced,

$$\begin{aligned} &S^{\mathrm{c}}_{\mathrm{MD}}(q_x, q_y, q_z) \\ &= {\sum_{j=0}^{\infty}}' H_z(jD)\cos(q_z jD)\int_0^{\infty} \mathrm{d}x\ H_x(x)\cos(q_x x)\int_0^{\infty} \mathrm{d}y\ H_y(y)\cos(q_y y)G(r, j, q_z), \end{aligned} \tag{B.2}$$

where Eq. (B.2) has been written to emphasize its similarities to Eq. (B.1). Independent of specific choices regarding the scattering pair correlation function $G(r, j, q_z)$

or finite size effects (H_r, H_z, H_x, H_y), several general features of the structure factors can be discussed. S_{MD} and $S^{\mathrm{c}}_{\mathrm{MD}}$ will be large for $q_z = 2\pi h/D$ because of the factors of $\cos(q_z jD)$ where $h \in \mathbb{N}$. S_{MD} will also be large for $q_r = 0$ because of the Bessel function, and similarly, $S^{\mathrm{c}}_{\mathrm{MD}}$ will be large for $q_x = 0$ or $q_y = 0$.

S_{MD} Eqs. (B.1) and $S^{\mathrm{c}}_{\mathrm{MD}}$ Eq. (B.2) are shown in Fig. B.1 for $q_z = 2\pi/D$ as functions of q_x and q_y. The cylindrical and Cartesian symmetries are apparent in the left-hand and right-hand sides, respectively. In the Cartesian contour plot (right-hand side), the ridges of large intensity along $q_x = 0$ and $q_y = 0$ are related to the features previously referred to as "spikes", see pp. 66 [48]. The "spikes" could be referred to as Caillé sheets since they emanate from Caillé peaks [104].

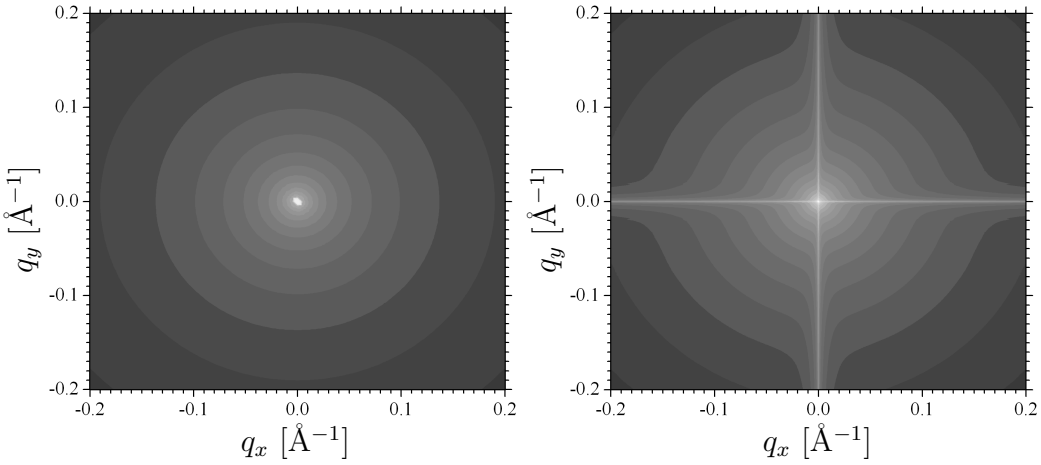


Figure B.1: Contour plots of $S_{\mathrm{MD}}\left(\sqrt{q_x^2 + q_y^2}, 2\pi/D\right)$, left-hand side, and $S^{\mathrm{c}}_{\mathrm{MD}}(q_x, q_y, 2\pi/D)$, right-hand side, are shown. A logarithmic grayscale indicates the value, where white corresponds to most intense. Typical parameter value were used to calculate S_{MD} and $S^{\mathrm{c}}_{\mathrm{MD}}$.

To calculate the X-ray scattering intensity corresponding to an exposure in which the bilayer stack was continuously rotated, the structure factor must be integrated over all sampled incident angles, see Section 5.3.5,

$$I^{\mathrm{F}}_{\mathrm{CCD}}(q_x, q_z) \sim \int_{q_{y,\mathrm{lb}}}^{q_{y,\mathrm{ub}}} \mathrm{d}q_y \; S_{\mathrm{MD}}(q_x, q_y, q_z). \tag{B.3}$$

Previously, the integration range was approximated by a q_x-independent range, see Fig. 4.5 pp. 60 in Ref. [48]. In Section 5.3.5, q_x-dependent integration limits were derived. Examples of the q_x-independent and q_x-dependent integration ranges are shown in Fig. B.2. The solid and dashed lines indicate the range of q_y values which are

summed to determine $I^{\mathrm{F}}_{\mathrm{CCD}}(q_x, q_z)$. The q_x-independent limits always include $q_y = 0$. However, only $S^{\mathrm{c}}_{\mathrm{MD}}$ (not S_{MD}) has a ridge of intensity along $q_y = 0$. Therefore, using q_x-independent limits for the CCD integral is a worse approximation in the $S^{\mathrm{c}}_{\mathrm{MD}}$ case as compared to the S_{MD} case. If q_x-independent limits are used along with $S^{\mathrm{c}}_{\mathrm{MD}}$, the Caillé sheets are predicted at larger q_x in $I^{\mathrm{F}}_{\mathrm{CCD}}(q_x, 2\pi h/D)$ than in the q_x-dependent integration limits case because the q_x-independent limits always include the ridge of intensity centered at $q_y = 0$.

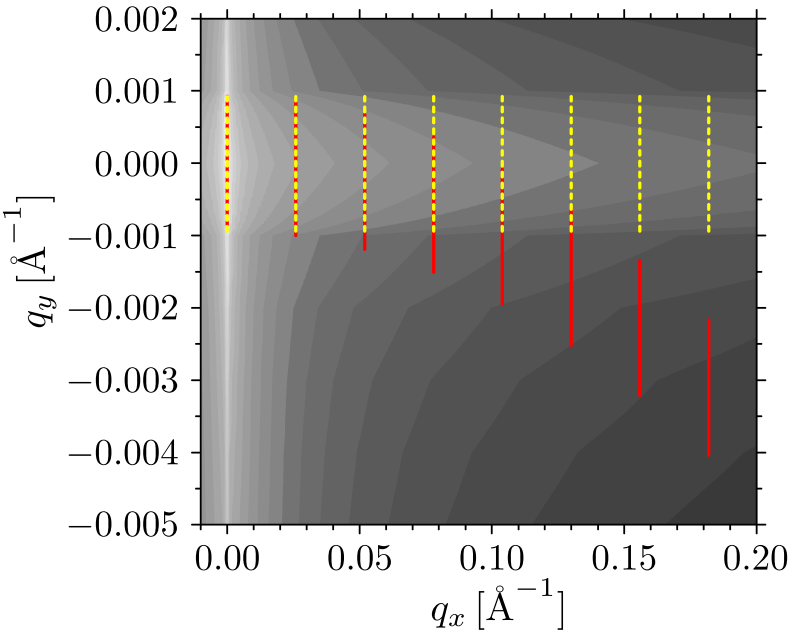


Figure B.2: A subregion of the q_x, q_y-region in the right-hand plot of Fig. B.1 is shown. Note, the q_x- and q_y-axes show different ranges. The yellow dashed lines and red solid lines indicate the range of integrated q_y-values for several q_x-values for the q_x-independent and q_x-dependent integration limits, respectively.

The Cartesian structure factor $S^{\mathrm{c}}_{\mathrm{MD}}$ in Fig. B.1 predicts a feature in the X-ray scattering that is not experimentally observed. For a fixed incident angle exposure, a row of CCD pixels (running p_x) corresponds to a trajectory in **q**-space. The q_z-value for each pixel in a row is nearly constant, and therefore, the **q**-space trajectory is approximately q_z-independent (q_x, q_y-trajectory). In Fig. B.3, $S^{\mathrm{c}}_{\mathrm{MD}}$ is shown as a function of q_x and q_y for $q_z = 2\pi/D$, and q_x, q_y-trajectories are plotted for various incident angles, ω. For $\omega = \sin^{-1}\left(\frac{h\lambda}{2D}\right)$, a trajectory includes the point $(q_x, q_y) = (0, 0)$. The depicted ω-values were chosen to sample a range of ω about the Bragg angle corrresponding to $D = 62.8$ Å, $\lambda = 1.1775$ Å and $h = 1$ ($\omega^{\mathrm{B}}_1 \approx 0.54°$).

In Fig. B.4 the intensity along the q_x, q_y-trajectories depicted in Fig. B.3 is plotted as a function of q_x. The q_x-axis is approximately a linear function of p_x. For $\omega > \omega_1^{\mathrm{B}}$, the intensity does not monotonically decay for increasing q_x. Instead, a peak-like feature sharpens for increasing $\omega - \omega_1^{\mathrm{B}}$. The feature is due to the trajectories starting on the $q_y > 0$ side of the intensity ridge and ending on the $q_y < 0$ side. The peak-like feature is predicted for all $q_z = 2\pi h/D$ at q_x-values dependent on ω. For comparison, the intensity of S_{MD} along the same q_x, q_y-trajectories depicted in Fig. B.3 never show a peak-like feature because S_{MD} does not have ridges of large intensity along $q_x = 0$ and $q_y = 0$, see for example the left-hand side of Fig. B.1. The peak-like feature is not observed experimentally, and therefore, S_{MD} is favored as compared to $S_{\mathrm{MD}}^{\mathrm{c}}$.

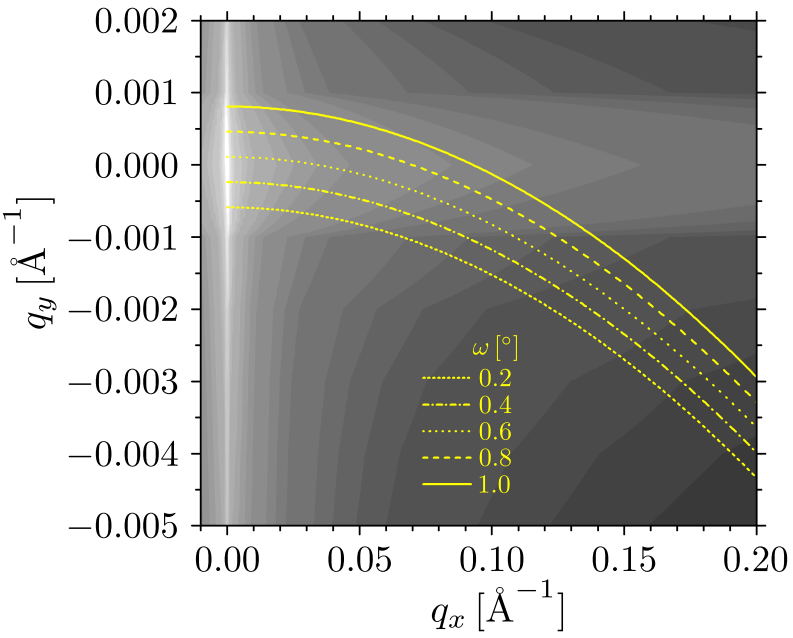


Figure B.3: A subregion of the q_x, q_y-region in the right-hand plot of Fig. B.1 is shown. Note, the q_x- and q_y-axes show different ranges. The yellow solid and dashed lines indicate the q_x, q_y-trajectories probed by a row of CCD pixels during a fixed angle exposure. The $h = 1$ Bragg angle is $\omega_1^{\mathrm{B}} \approx 0.54°$.

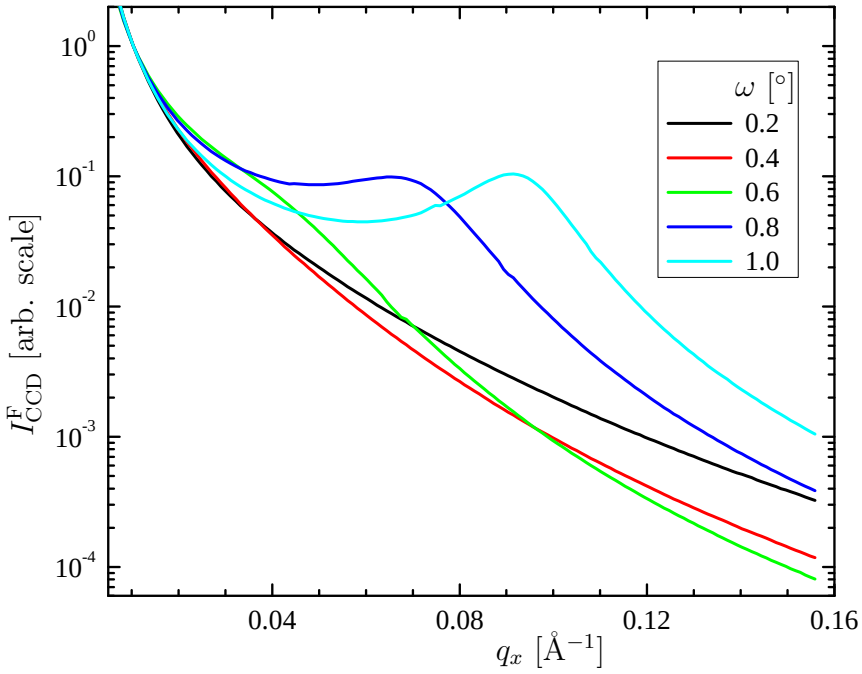


Figure B.4: The predicted intensity along the solid and dashed yellow lines involving $S^{\mathrm{c}}_{\mathrm{MD}}$ in Fig. B.3 is plotted as a function of q_x for $q_z = 2\pi/D$; the intensity is normalized at $q_x = 0.01$ Å^{-1}. For increasing ω beyond $\omega^{\mathrm{B}}_1 \approx 0.54°$, a peak in intensity develops, and its center shifts to greater q_x.

Appendix C

Form Factor Details

C.1 Fluctuations in Electron Density

In Section 3.2.2 the scattering intensity was decomposed into the sum of two terms,

$$I(\mathbf{q}) \approx \left|\overline{\langle F_0(\mathbf{r}, q_z)\rangle}\right|^2 S(\mathbf{q}) + F_\Delta(q_z) S_0(\mathbf{q}), \tag{C.1}$$

where

$$F_\Delta(q_z) \equiv \left[\overline{\left\langle |F_0(\mathbf{r}, q_z)|^2 \right\rangle} - \left|\overline{\langle F_0(\mathbf{r}, q_z)\rangle}\right|^2\right]. \tag{C.2}$$

The overline indicates an in-plane spatial average. Commonly, the second term in Eq. (C.1) is assumed to be negligible compared to the first term; however, the relative magnitude of the terms is unknown. Retaining both terms, $I(\mathbf{q})$ Eq. (C.1) is further developed in Chapter 5, considering various theoretical and experimental issues

$$I^{\mathrm{F}}_{\mathrm{CCD}}(q_x, q_z) = \frac{\left|\overline{\langle F_0(\mathbf{r}, q_z)\rangle}\right|^2}{q_z} S_{\mathrm{CCD}}(q_x, q_z) + \frac{F_\Delta(q_z)}{q_z} S_{0,\mathrm{CCD}}(q_x, q_z). \tag{C.3}$$

In Section 6.4, $S^{\mathrm{F}}_{\mathrm{CCD},1}$ and $S^{\mathrm{F}}_{\mathrm{CCD},2}$ were calculated and found to have similar magnitudes. Therefore, the outstanding comparison is between $\left|\overline{\langle F_0(\mathbf{r}, q_z)\rangle}\right|^2$ and $F_\Delta(q_z)$.

$\overline{\left\langle |F_0(\mathbf{r}, q_z)|^2 \right\rangle}$ and $\left|\overline{\langle F_0(\mathbf{r}, q_z)\rangle}\right|^2$ are evaluated using two different models for the

fluctuations of the electron density profile (EDP). Assuming ergodicity, many snapshots from a molecular dynamics simulations at different times could be used to estimate $\overline{\left\langle |F_0(\mathbf{r}, q_z)|^2 \right\rangle}$ and $\left|\overline{\langle F_0(\mathbf{r}, q_z)\rangle}\right|^2$. As such snapshots are not readily available, the present analysis uses an in-plane and time averaged electron density of DOPC from simulation

$$\rho^*_{\text{sim}}(z) = \left\langle \overline{\rho_{\text{sim}}(\mathbf{r}, z)} \right\rangle \tag{C.4}$$

$$= \langle \rho_{\text{sim}}(z) \rangle \,. \tag{C.5}$$

To assess $\overline{\left\langle |F_0(\mathbf{r}, q_z)|^2 \right\rangle}$ and $\left|\overline{\langle F_0(\mathbf{r}, q_z)\rangle}\right|^2$, a three-dimensional EDP is required, but $\rho_{\text{sim}}(z)$ is one-dimensional. It is assumed that

$$\begin{aligned}
\overline{\left\langle |F_0(\mathbf{r}, q_z)|^2 \right\rangle} &\approx \left\langle \left|\overline{F_0(\mathbf{r}, q_z)}\right|^2 \right\rangle \\
&= \left\langle |F_0(q_z)|^2 \right\rangle \\
&= \left\langle \left| \int_{-D/2}^{D/2} \mathrm{d}z \; \rho_{\text{sim}}(z) e^{iq_z z} \right|^2 \right\rangle \qquad \text{(C.6)} \\
&= \left\langle |F(q_z)|^2 \right\rangle \qquad \text{(C.7)}
\end{aligned}$$

and

$$\begin{aligned}
\left|\overline{\langle F_0(\mathbf{r}, q_z)\rangle}\right|^2 &\approx \left|\left\langle \overline{F_0(\mathbf{r}, q_z)} \right\rangle\right|^2 \\
&= \left|\langle F_0(q_z)\rangle\right|^2 \\
&= \left| \left\langle \int_{-D/2}^{D/2} \mathrm{d}z \; \rho_{\text{sim}}(z) e^{iq_z z} \right\rangle \right|^2 \qquad \text{(C.8)} \\
&= \left|\langle F(q_z)\rangle\right|^2 . \qquad \text{(C.9)}
\end{aligned}$$

Fluctuations in $\rho_{\text{sim}}(z)$ are hypothesized to be out-of-plane extensions and compressions. The energy required to extend or compress the membrane laterally is related to the compression modulus K_A,

$$E_{\mathrm{A}}(A - A_o) = \frac{1}{2} K_A \frac{(A - A_o)^2}{A_o} \tag{C.10}$$

$$= \frac{1}{2} K_A \frac{(\Delta A)^2}{A_o} \tag{C.11}$$

where A_o is the reference area. With the standard assumption of constant volume, $D_c A_o \equiv V_c$, where D_c is the hydrocarbon thickness and V_c is the hydrocarbon volume, the change in area ΔA is rewritten in terms of a change in thickness ΔD,

$$(D_c + \Delta D)(A_o - \Delta A) \approx D_c A_o + \Delta D A_o - D_c \Delta A \tag{C.12}$$

$$= V_c = D_c A_o \tag{C.13}$$

$$\Rightarrow \Delta D A_o = D_c \Delta A \tag{C.14}$$

$$\rightarrow \Delta A = A_o \frac{\Delta D}{D_c}, \tag{C.15}$$

Substituting ΔA Eq. (C.15) into E_{A} Eq. (C.11), the compression energy is expressed in terms of a change in thickness

$$E_{\mathrm{A}}(\Delta D) = \frac{1}{2} K_A A_o \left(\frac{\Delta D}{D_c} \right)^2 . \tag{C.16}$$

For $K_A = 2.75 \times 10^{-21}$ J/Å^2, $A_o = 2000$ Å^2, and $E_{\mathrm{A}} = k_{\mathrm{B}}T/2$, $\Delta D / D_c = 0.028$.

C.1.1 Removing Fluctuations

The data from simulation, $\rho^*_{\mathrm{sim}}(z)$, have already been ensemble averaged. Preferably, $\overline{\left\langle |F_0(\mathbf{r}, q_z)|^2 \right\rangle}$ and $\left| \overline{\langle F_0(\mathbf{r}, q_z) \rangle^2} \right|$ would be calculated from $\rho_{\mathrm{sim}}(\mathbf{r}, z)$. While the in-plane dependence can not be easily recovered, the states of the ensemble can be determined given a model for the fluctuations,

$$\rho^*_{\mathrm{sim}}(z) = \langle \rho_{\mathrm{sim}}(z, \Delta D, \ldots) \rangle_{\Delta D, \ldots} \tag{C.17}$$

where $\{\Delta D, \ldots\}$ is the set of fluctuation parameters. In general $\rho_{\mathrm{sim}}(z, \Delta D \ldots)$ is not

unique. The possible $\rho_{\rm sim}(z, \Delta D \ldots)$ were constrained by requiring $\rho_{\rm sim}(z, \Delta D \ldots)$ to be of the form

$$\rho_{\rm sim}(z, \Delta D, \ldots) = \sum_n A_n \cos\left[\frac{2\pi n}{D} f(z, \Delta D, \ldots)\right], \tag{C.18}$$

where $f(z, \Delta D, \ldots)$ depends on the fluctuation model. $\rho_{\rm sim}(z, \Delta D, \ldots)$ was determined by substituting Eq. (C.18) into Eq. (C.17) and performing a nonlinear fit with fitting parameters $\{D, A_1, \ldots, A_n\}$.

C.1.2 Bilayer Model

Uniform extension and compression of the entire bilayer (B) is considered in this Subsection. Using $E_{\rm A}$ Eq. (C.16) and $\rho^*_{\rm sim}$ Eq. (C.17), $\rho_{\rm sim}(z)$ was determined. Both $\rho^*_{\rm sim}(z)$ and $\rho_{\rm sim}(z)$ are plotted in Fig. C.1. Using $\rho_{\rm sim}(z, \Delta D)$,

$$\rho_{\rm sim}(z, \Delta D) = \rho_{\rm sim}\left[\left(1 - \frac{\Delta D}{D_c}\right) z\right], \tag{C.19}$$

$\langle |F|^2 \rangle$ Eq. (C.6) and $|\langle F \rangle|^2$ (C.8) are expressed as

$$\left\langle \left| F^{\rm B}(q_z) \right|^2 \right\rangle \equiv \frac{1}{\mathcal{Z}^{\rm B}} \int_{-\infty}^{\infty} {\rm d}(\Delta D)\ e^{-\beta E_{\rm A}(\Delta D)} \left| \int_{-D/2}^{D/2} {\rm d}z\ \rho_{\rm sim}(z, \Delta D) e^{iq_z z} \right|^2 \tag{C.20}$$

and

$$\left| \left\langle F^{\rm B}(q_z) \right\rangle \right|^2 \equiv \left| \frac{1}{\mathcal{Z}^{\rm B}} \int_{-\infty}^{\infty} {\rm d}(\Delta D)\ e^{-\beta E_{\rm A}(\Delta D)} \int_{-D/2}^{D/2} {\rm d}z\ \rho_{\rm sim}(z, \Delta D) e^{iq_z z} \right|^2 \tag{C.21}$$

where $\beta = (k_{\rm B}T)^{-1}$ and $\mathcal{Z}^{\rm B}$ is the partition function,

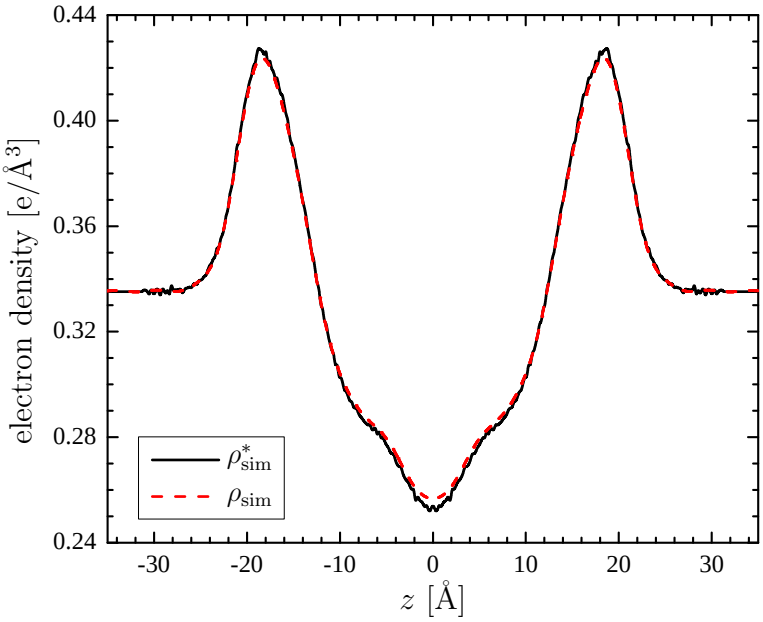


Figure C.1: The EDP from simulation $\rho^*_{\rm sim}(z)$ is plotted along with the corresponding EDP with fluctuations removed $\rho_{\rm sim}(z)$ as functions of the distance z from the bilayer midplane.

$$\mathcal{Z}^{\rm B} \equiv \int_{-\infty}^{\infty} {\rm d}(\Delta D)\; e^{-\beta E_{\rm A}(\Delta D)} \tag{C.22}$$

$$= \sqrt{\frac{2\pi D_c^2}{K_A A_o \beta}}. \tag{C.23}$$

$\left\langle \left| F^{\rm B} \right|^2 \right\rangle$ Eq. (C.20), $\left| \left\langle F^{\rm B} \right\rangle \right|^2$ Eq. (C.21), and their difference $F^{\rm B}_\Delta$ are plotted in Fig. C.2. Since $\rho_{\rm sim}(z)$ is an even function, $\rho_{\rm sim}(z, \Delta D)$ is also an even function, and therefore, $\left\langle \left| F^{\rm B} \right|^2 \right\rangle$ is similar to $\left| \left\langle F^{\rm B} \right\rangle \right|^2$ except that it is broadened in the q_z-direction. Consequently, $F^{\rm B}_\Delta$ is large where

$$\frac{\rm d}{{\rm d}q_z} \left| \left\langle F^{\rm B} \right\rangle \right|^2 \tag{C.24}$$

is large. $F^{\rm B}_\Delta$ tends to be most (least) significant near the minima (maxima) of $\left| \left\langle F^{\rm B} \right\rangle \right|^2$.

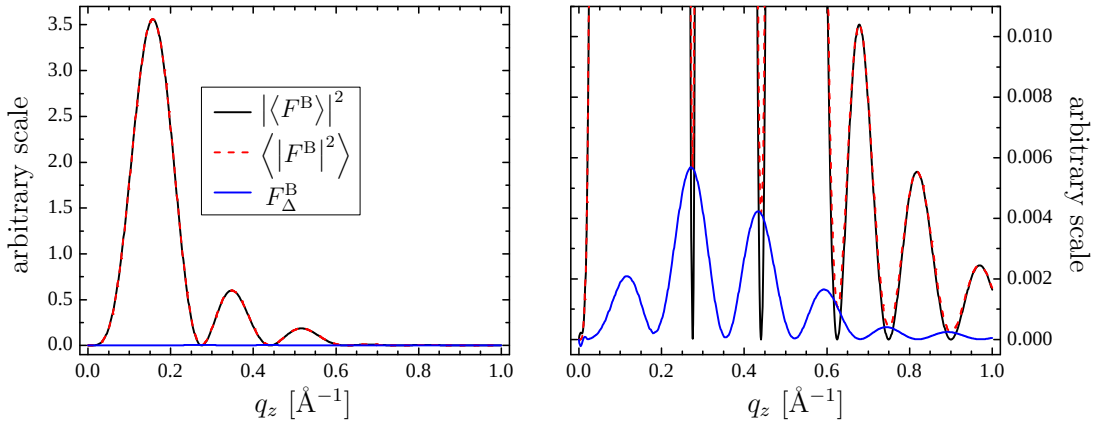


Figure C.2: $\left\langle \left|F^{\rm B}\right|^2 \right\rangle$ Eq. (C.20), $\left|\left\langle F^{\rm B}\right\rangle\right|^2$ Eq. (C.21), and their difference $F^{\rm B}_\Delta$ are plotted as functions of q_z. In the right panel, the vertical axis is expanded to highlight $F^{\rm B}_\Delta$. The arbitrary scale of the vertical axis is the same in the left and right panels.

C.1.3 Leaflets Model

In the leaflets model, the two bilayer leaflets are allowed to fluctuate independently. The leaflet compression modulus k_A and elastic thickness d_c are half of the corresponding bilayer values, $k_A \equiv K_A/2$ and $d_c \equiv D_c/2$. The compression energy for a leaflet (L) straightforwardly follows from the bilayer model $E_{\rm A}$ (C.16),

$$E^{\rm L}_{\rm A} = \frac{1}{2} k_A A_0 \left(\frac{\Delta D}{d_c}\right)^2 \tag{C.25}$$

$$= K_A A_0 \left(\frac{\Delta D}{D_c}\right)^2$$

$$= 2E_{\rm A}. \tag{C.26}$$

Using $E^{\rm L}_{\rm A}$ Eq. (C.26), $\rho^*_{\rm sim}$ Eq. (C.17), and Eq. (C.27), $\rho_{\rm sim}(z)$ is determined. $\rho^*_{\rm sim}(z)$ and $\rho_{\rm sim}(z)$ are plotted in Fig. C.3. Using $\rho_{\rm sim}(z, \Delta D, \Delta D')$,

$$\rho_{\rm sim}(z, \Delta D, \Delta D') = \begin{cases} \rho_{\rm sim}\left[\left(1 - \frac{\Delta D}{d_c}\right) z\right] & z \le 0 \\ \rho_{\rm sim}\left[\left(1 - \frac{\Delta D'}{d_c}\right) z\right] & z > 0. \end{cases} \tag{C.27}$$

$\langle |F|^2 \rangle$ Eq. (C.6) and $|\langle F \rangle|^2$ Eq. (C.8) are expressed as

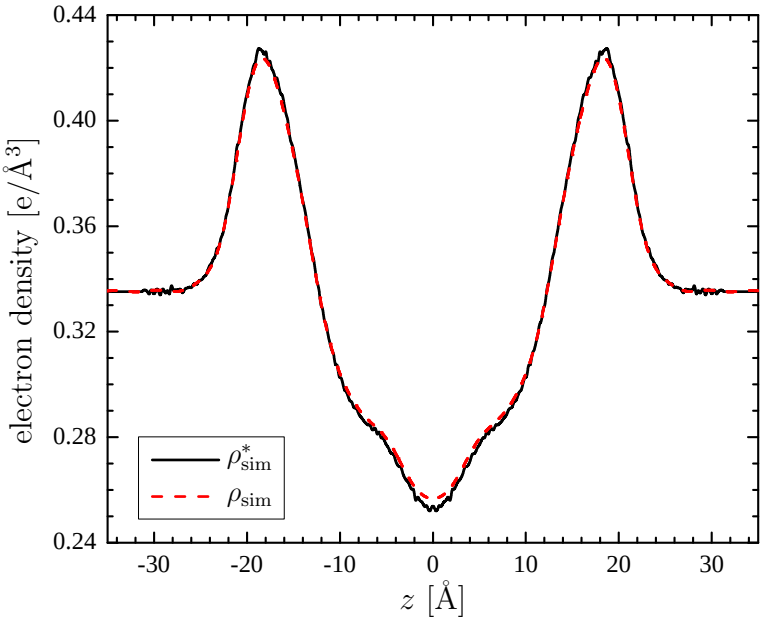


Figure C.3: The EDP from simulation $\rho^*_{\rm sim}(z)$ is plotted along with the corresponding EDP with fluctuations removed $\rho_{\rm sim}(z)$. The resulting EDP is nearly identical to the EDP plotted in Fig. C.1.

$$\left\langle \left| F^{\rm L}(q_z) \right|^2 \right\rangle \equiv \frac{1}{\mathcal{Z}^{\rm L}} \int_{-\infty}^{\infty} \int_{-\infty}^{\infty} {\rm d}(\Delta D){\rm d}(\Delta D')\; e^{-2\beta[E_{\rm A}(\Delta D)+E_{\rm A}(\Delta D')]} \left| \int_{-D/2}^{D/2} {\rm d}z\; \rho\left(z, \Delta D, \Delta D'\right) e^{iq_z z} \right|^2 , \tag{C.28}$$

and

$$\left| \left\langle F^{\rm L}(q_z) \right\rangle \right|^2 \equiv \left| \frac{1}{\mathcal{Z}^{\rm L}} \int_{-\infty}^{\infty} \int_{-\infty}^{\infty} {\rm d}(\Delta D){\rm d}(\Delta D')\; e^{-2\beta[E_{\rm A}(\Delta D)+E_{\rm A}(\Delta D')]} \int_{-D/2}^{D/2} {\rm d}z\; \rho\left(z, \Delta D, \Delta D'\right) e^{iq_z z} \right|^2 , \tag{C.29}$$

where $\mathcal{Z}^{\rm L}$ is the partition function,

$$\mathcal{Z}^{\mathrm{L}} \equiv \int_{-\infty}^{\infty}\int_{-\infty}^{\infty} \mathrm{d}(\Delta D)\mathrm{d}(\Delta D')\; e^{-\beta[E_{\mathrm{A}}(\Delta D)+E_{\mathrm{A}}(\Delta D')]} \tag{C.30}$$

$$= \frac{\pi D_c^2}{K_A A_o \beta}. \tag{C.31}$$

$\left\langle \left| F^{\mathrm{L}} \right|^2 \right\rangle$ Eq. (C.28), $\left| \left\langle F^{\mathrm{L}}(q_z) \right\rangle \right|^2$ Eq. (C.29), and their difference F_Δ^{L} are plotted in Fig. C.4.

Unlike the case of symmetric bilayer fluctuations in Section C.1.2, see the right panel of Fig. C.2, F_Δ^{L} has a single maximum and is significant at maxima of $\left| \left\langle F^{\mathrm{L}}(q_z) \right\rangle \right|^2$. For individual leaflet fluctuations, $\rho_{\mathrm{sim}}(z, \Delta D, \Delta D')$ is not in general an even function of z; both symmetric and asymmetric $\rho_{\mathrm{sim}}(z, \Delta D, \Delta D')$ with respect to $z = 0$ contribute to $\left\langle \left| F^{\mathrm{L}} \right|^2 \right\rangle$. Therefore, $\left\langle \left| F^{\mathrm{L}} \right|^2 \right\rangle$ is composed of the fluctuations that result in $\left\langle \left| F^{\mathrm{B}} \right|^2 \right\rangle$ in addition to asymmetric $\rho_{\mathrm{sim}}(z, \Delta D, \Delta D')$ states. Consequently, F_Δ^{L} to an extent is an envelope for F_Δ^{B}. It is plausible that a bilayer experiences both symmetric and asymmetric thickness fluctuations, and therefore, F_Δ^{L} is considered more realistic than F_Δ^{B}. Importantly, $F_\Delta^{\mathrm{L}}(q_z)$ is consistent with the use of a small, smooth background that is commonly drawn in this lab to give zeroes in $|\langle F(q_z)\rangle|^2$.

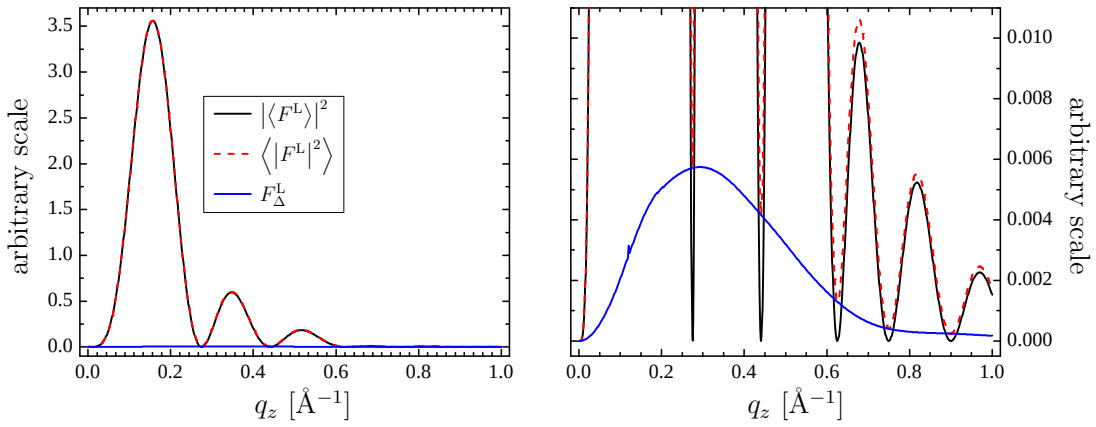


Figure C.4: $\left\langle \left| F^{\mathrm{L}} \right|^2 \right\rangle$ Eq. (C.28), $\left| \left\langle F^{\mathrm{L}} \right\rangle \right|^2$ Eq. (C.29), and their difference F_Δ^{L} are plotted. In the right panel, the vertical axis is expanded as compared to the left panel to highlight F_Δ^{L}. The arbitrary scale of the vertical axis is the same in the left and right panels and the same as used in Fig. C.2.

C.2 Undulation Correction

The undulation correction (UC) is a rescaling of the electron density profile normal to the bilayer plane, see Eq. (7.21). The influence of Ψ_{UC} on the electron density (or form factor) must be considered to compare various experimental, simulated, and theoretical results. The UC is akin to a normalization. As a common example, consider both an experiment and a simulation studying a single lipid bilayer. Because of computational limitations, the simulated membrane has a much smaller area than the experimental system, and that reduces the fluctuations compared to the experimental system. Indeed, only for simulations of very large area membranes is UC required [105]. Without employing a UC, the electron densities (or form factors) of the experimental and simulated systems may differ because of the difference in their allowed fluctuation modes. A similar argument could be made with regard to experimental results from unilamellar vesicles and oriented multilamellar arrays.

Utilizing a calculation completed by N. Lei [56, 106] and F. Auguste *et al.* [107], a correction for the fluctuating local bilayer normal $\boldsymbol{\nabla} z_j^+$ was previously suggested [39]. However, only the connection between the aforementioned fluctuations and the results for lipid area were made [48], although the connection to modifications of the form factor have been used routinely in this lab [85]. Section 7.5 clarifies the extent to which a UC affects the measured scattering. Below, a tilt-dependent UC will be derived with discussion relating to the tilt-independent UC. In Appendix A.2.1 Ψ_0 was decomposed in terms of more convenient fluctuation fields. Using Ψ_0 Eq. (A.21) and the definition of Ψ_{UC} Eq. (7.19),

$$\Psi_{\mathrm{UC}} \approx 1 + \frac{1}{2}\left(\left\langle \left|\boldsymbol{\nabla} z_0^+\right|^2 \right\rangle + \left\langle \left|\boldsymbol{\nabla} z_0^-\right|^2 \right\rangle - \left\langle |\hat{\mathbf{m}}_0|^2 \right\rangle - \left\langle |\bar{\mathbf{m}}_0|^2 \right\rangle\right) \tag{C.32}$$

$$\equiv 1 + \frac{1}{2}\sum_{i=1}^{4} \Psi_{\mathrm{UC}}^{(i)}. \tag{C.33}$$

Note, $z_0^-(\mathbf{r})$ and $\bar{\mathbf{m}}_0(\mathbf{r})$ are fields involved in the peristaltic part of the complete Watson *et al.* model [1]. Anticipating later results, Ψ_{UC} is derived only considering $\left\langle \left|\boldsymbol{\nabla} z_0^+\right|^2 \right\rangle$ in Section C.2.1. In Section C.2.2, it is shown that $\langle |\hat{\mathbf{m}}_0|^2 \rangle$, $\left\langle \left|\boldsymbol{\nabla} z_0^-\right| \right\rangle$, and $\langle |\bar{\mathbf{m}}_0|^2 \rangle$ are approximately system size independent. When comparing two systems with radii greater than $\sim$220 Å,

$$\Psi_{\mathrm{UC}}^{(2-4)} \equiv \sum_{i=2}^{4} \Psi_{\mathrm{UC}}^{(i)} \tag{C.34}$$

is the same for both systems. Therefore, after correcting each system using the appropriate $\left\langle \left| \boldsymbol{\nabla} z_0^+ \right|^2 \right\rangle$, the remaining short length scale fluctuations of the systems are consistent. This is an important point since $\Psi_{\mathrm{UC}}^{(2-4)}$ depends on many moduli that are currently unassessable by experiments. Previewing the main conclusions of Sections C.2.1 through C.2.2, the values of Ψ_{UC} are listed in Table C.1 using parameter values listed in Table C.2.

Table C.1: Contributions to Ψ_{UC} and Ψ_{UC} using values from Table C.2.

	value (Eq. #)		
	Watson†	Tilt‡	~~Tilt~~‡
$\left\langle \left\| \boldsymbol{\nabla} z_0^+ \right\|^2 \right\rangle$	0.022 (C.40)	0.030 (C.46)	0.019 (C.46)
$\left\langle \left\| \hat{\mathbf{m}}_0 \right\|^2 \right\rangle$	0.019 (C.66)		
$\left\langle \left\| \boldsymbol{\nabla} z_0^- \right\|^2 \right\rangle$	0.007 (C.71)		
$\left\langle \left\| \bar{\mathbf{m}}_0 \right\|^2 \right\rangle$	0.015 (C.72)		
Ψ_{UC}	0.998 (C.33)	1.015 (C.48)	1.010 (C.48)

† using parameter values from [1], B, and a; see Table C.2

‡ using parameter values from Section 7.1; see Table C.2

Table C.2: Parameter values from [1] and Section 7.1.

	parameter	[units]	value	description
[1]†	b_0	[nm]	1.8	average monolayer thickness
	κ_θ	[J/nm^2]	5.4×10^{-20}	tilt modulus
	k_c^b	[J]	7.7×10^{-20}	bending modulus at constant chain length
	k_A	[J/nm^2]	2.6×10^{-19}	compressibility modulus
	Ω	[J/nm]	1×10^{-19}	cross-term modulus
	κ_{tw}	[J]	7.7×10^{-21}	twist modulus
	k_c	[J]	6.7×10^{-20}	bending modulus at neutral surface
Sec. 7.1	K_c	[J]	8.5×10^{-20}	bilayer bending modulus
	B	[J/nm^4]	7×10^{-23}	bilayer bulk modulus
	K_θ	[J/nm^2]	10.7×10^{-20}	bilayer tilt modulus
	a	[nm]	1.7	short in-plane length scale cutoff

† reported monolayer values for DPPC from MD simulation using MARTINI

C.2.1 Ψ_{UC} Evaluated

For comparison of sufficiently large systems, see Section C.2.2,

$$\Psi_{\mathrm{UC}} \approx 1 + \frac{\left\langle \left| \boldsymbol{\nabla} z_0^+ \right|^2 \right\rangle}{2}. \tag{C.35}$$

$\left\langle \left| \boldsymbol{\nabla} z_0^+ \right|^2 \right\rangle$ is proportional to a sum over all allowed Fourier modes weighted by the appropriate spectrum. Using the definition of a Fourier transform Eq. (3.41),

$$\left\langle \left| \boldsymbol{\nabla} z_0^+(\mathbf{r}) \right|^2 \right\rangle = \left\langle \left| \frac{1}{\sqrt{A_{\mathrm{p}} J}} \sum_{\mathbf{Q}} i Q_r z_{\mathbf{Q}}^+ e^{i\mathbf{Q}_{\mathbf{r}} \cdot \mathbf{r}} \right|^2 \right\rangle \tag{C.36}$$

$$= \frac{1}{A_{\mathrm{p}} J} \sum_{\mathbf{Q}} \sum_{\mathbf{Q}'} Q_r Q_r' \left\langle \left| z_{\mathbf{Q}}^+ \right|^2 \right\rangle e^{i(\mathbf{Q}_{\mathbf{r}} + \mathbf{Q}_{\mathbf{r}}') \cdot \mathbf{r}}. \tag{C.37}$$

Substituting $\left\langle \left| z_{\mathbf{Q}}^+ \right|^2 \right\rangle$ Eq. (3.57) into Eq. (C.37),

$$\left\langle \left| \boldsymbol{\nabla} z_0^+ \right|^2 \right\rangle = \frac{k_{\mathrm{B}} T}{4 B A_{\mathrm{p}} J} \sum_{\mathbf{Q}} Q_r^2 \frac{1}{\aleph^2 + \sin^2(Q_z D/2)}. \tag{C.38}$$

Following methods similar to Section 3.3.3, $\left\langle \left| \boldsymbol{\nabla} z_0^+ \right|^2 \right\rangle$ Eq. (C.38) is further rewritten,

$$\left\langle \left| \boldsymbol{\nabla} z_0^+ \right|^2 \right\rangle = \frac{k_{\mathrm{B}} T}{2\pi B \xi^2} \int_{\pi/\tilde{a}}^{\pi/a} \mathrm{d}Q_r \; \frac{Q_r \left(1 + \xi_\theta^2 Q_r^2\right)}{\sqrt{4 + 4\xi_\theta^2 Q_r^2 + \xi^4 Q_r^4}} \tag{C.39}$$

$$= \frac{k_{\mathrm{B}} T}{4\pi K_c} \left[\left(1 - 2\frac{\xi_\theta^4}{\xi^4} \right) \ln\left(v + \sqrt{1 + v^2} \right) \Big|_\alpha^\beta + 2\frac{\xi_\theta^2}{\xi^2} \sqrt{1 - \frac{\xi_\theta^4}{\xi^4}} \sqrt{1 + v^2} \Big|_\alpha^\beta \right] \tag{C.40}$$

where $\pi/\tilde{a}$ is the short wavevector cutoff,

$$\alpha = \frac{\left(\frac{\xi\pi}{\tilde{a}}\right)^2 + 2\frac{\xi_\theta^2}{\xi^2}}{2\sqrt{1 - \frac{\xi_\theta^4}{\xi^4}}}, \tag{C.41}$$

and

$$\beta = \frac{\left(\frac{\xi\pi}{a}\right)^2 + 2\frac{\xi_\theta^2}{\xi^2}}{2\sqrt{1-\frac{\xi_\theta^4}{\xi^4}}}. \tag{C.42}$$

Since the tilt-associated length scale $\xi_\theta = \sqrt{K_c/K_\theta}$ (typically $\sim$10 Å) is less than $\xi = \sqrt[4]{K_c/B}$ (typically 40 - 60 Å),

$$\alpha \to \frac{1}{2}\left(\frac{\pi\xi}{\tilde{a}}\right)^2 \equiv \tilde{\tau} \tag{C.43}$$

$$\beta \to \frac{1}{2}\left(\frac{\pi\xi}{a}\right)^2 \equiv \tau. \tag{C.44}$$

Since $\xi > a$ and assuming $\xi \ll \tilde{a}$ which is related to the system size, $\tau \gg 1 \gg \tilde{\tau}$. Consequently, $\left\langle \left|\boldsymbol{\nabla} z_0^+\right|^2 \right\rangle$ Eq. (C.40) is significantly simplified

$$\left\langle \left|\boldsymbol{\nabla} z_0^+\right|^2 \right\rangle \approx \frac{k_\mathrm{B}T}{4\pi K_c}\left(\ln\left(v+\sqrt{1+v^2}\right)\Big|_0^\tau + 2\frac{\xi_\theta^2}{\xi^2}\sqrt{1+v^2}\Big|_0^\tau\right) \tag{C.45}$$

$$= \frac{k_\mathrm{B}T}{4\pi K_c}\left(2\ln\left(\frac{\pi\xi}{a}\right) + \left(\frac{\pi\xi_\theta}{a}\right)^2\right). \tag{C.46}$$

Substituting $\left\langle \left|\boldsymbol{\nabla} z_0^+\right|^2 \right\rangle$ Eq. (C.46) into Ψ_UC Eq. (C.35), the tilt-dependent UC is

$$\Psi_\mathrm{UC} \approx 1 + \frac{k_\mathrm{B}T}{4\pi K_c}\left(\ln\left(\frac{\pi\xi}{a}\right) + \frac{1}{2}\left(\frac{\pi\xi_\theta}{a}\right)^2\right) \tag{C.47}$$

$$= \Psi_\mathrm{UC}^{\cancel{\mathrm{tilt}}} + \frac{k_\mathrm{B}T}{8\pi K_c}\left(\frac{\pi\xi_\theta}{a}\right)^2, \tag{C.48}$$

where $\Psi_\mathrm{UC}^{\cancel{\mathrm{tilt}}}$ is the UC without considering tilt. Using the fitted parameter values from Section 7.1 ($a = 17$ Å, $\xi = 59$ Å, $\xi_\theta = 8.9$ Å, and $K_c/(k_\mathrm{B}T) \approx 20$; see Table C.2), Ψ_UC Eq. (C.48) is approximately 1.015 and 1.01 with and without tilt, respectively. Including the tilt degree of freedom increases the height spectrum at larger Q_r as compared to the tilt-independent model. Therefore as expected, the average angle

between $\hat{\mathbf{z}}$ and the local bilayer normal is larger in the tilt-dependent model.

C.2.2 Averages of Quantities Dominated by Short Length Scales

In Section C.2, the undulation correction Ψ_{UC} was shown to depend on $\left\langle \left| \boldsymbol{\nabla} z_0^+ \right|^2 \right\rangle$, $\langle |\hat{\mathbf{m}}_0|^2 \rangle$, $\left\langle \left| \boldsymbol{\nabla} z_0^- \right|^2 \right\rangle$, and $\langle |\bar{\mathbf{m}}_0|^2 \rangle$. However, the latter three thermal averages were neglected in Section C.2.1. $\langle |\hat{\mathbf{m}}_0|^2 \rangle$, $\left\langle \left| \boldsymbol{\nabla} z_0^- \right|^2 \right\rangle$, and $\langle |\bar{\mathbf{m}}_0|^2 \rangle$ are derived, and it is argued that these averages are dominated by short length scale fluctuations. When comparing two systems with sufficiently large areas, $\Psi_{\mathrm{UC}}^{(2-4)}$ Eq. (C.34) is the same for both systems, and therefore, it is unnecessary to include $\Psi_{\mathrm{UC}}^{(2-4)}$ in Ψ_{UC}.

To calculate the ensemble averages $\langle |\hat{\mathbf{m}}_0|^2 \rangle$, $\left\langle \left| \boldsymbol{\nabla} z_0^- \right|^2 \right\rangle$, and $\langle |\bar{\mathbf{m}}_0|^2 \rangle$, the complete Watson *et al.* model [1] is required. The Watson model is extended to describe bilayer stacks by adding the bilayer interaction term

$$\frac{B}{2} \left[z_{j+1}^+(\mathbf{r}) - z_j^+(\mathbf{r}) \right]^2, \tag{C.49}$$

and rewriting the fields as functions of the stacked bilayer index j. Following Watson *et al.* [1], the microscopic surface tension is neglected ($\gamma_\lambda = 0$), see Section IIIB [1]. Additionally, protrusion fluctuations are also neglected because they are not coupled to either the bending or peristaltic modes for vanishing microscopic surface tension. The resulting free energy functional is expressed in Fourier space as a sum of undulation (u) and peristaltic (p) contributions

$$\tilde{\mathcal{F}}_{\mathrm{u}} \equiv \sum_{\mathbf{Q}} \tilde{\mathbf{f}}_{\mathrm{u}}(-\mathbf{Q}) \, \mathbb{A} \, \tilde{\mathbf{f}}_{\mathrm{u}}^T(\mathbf{Q}) \tag{C.50}$$

and

$$\tilde{\mathcal{F}}_{\mathrm{p}} \equiv \sum_{\mathbf{Q}_\mathbf{r}} \tilde{\mathbf{f}}_{\mathrm{p}}(-\mathbf{Q}_\mathbf{r}) \, \mathbb{B} \, \tilde{\mathbf{f}}_{\mathrm{p}}^T(\mathbf{Q}_\mathbf{r}), \tag{C.51}$$

respectively, where

$$\tilde{\mathbf{f}}_{\mathrm{u}}(\mathbf{Q}) \equiv (z^{+}_{\mathbf{Q}},\, \hat{m}^{\parallel}_{\mathbf{Q}},\, \hat{m}^{\perp}_{\mathbf{Q}},\, \varepsilon_{\mathbf{Q}}), \tag{C.52}$$

$$\tilde{\mathbf{f}}_{\mathrm{p}}(\mathbf{Q}_{\mathbf{r}}) \equiv (z^{-}_{\mathbf{Q}_{\mathbf{r}}},\, \bar{m}^{\parallel}_{\mathbf{Q}_{\mathbf{r}}},\, \bar{m}^{\perp}_{\mathbf{Q}_{\mathbf{r}}}), \tag{C.53}$$

$$\mathbb{A} \equiv \begin{pmatrix} k_c^b Q_r^4 + 2B\sin^2(Q_z D/2) & -ik_c^b Q_r^3 & 0 & Q_r^2\Omega/(2b_0) \\ ik_c^b Q_r^3 & \kappa_\theta + k_c^b Q_r^2 & 0 & iQ_r\Omega/(2b_0) \\ 0 & 0 & \kappa_\theta + \kappa_{\mathrm{tw}} Q_r^2 & 0 \\ Q_r^2\Omega/(2b_0) & -iQ_r\Omega/(2b_0) & 0 & k_A/b_0^2 \end{pmatrix}, \tag{C.54}$$

and

$$\mathbb{B} \equiv \begin{pmatrix} \frac{k_A}{b_0^2} - \frac{Q_r^2\Omega}{b_0} + k_c^b Q_r^4 & \frac{iQ_r\Omega}{2b_0} - ik_c^b Q_r^3 & 0 \\ -\frac{iQ_r\Omega}{2b_0} + ik_c^b Q_r^3 & \kappa_\theta + k_c^b Q_r^2 & 0 \\ 0 & 0 & \kappa_\theta + \kappa_{\mathrm{tw}} Q_r^2 \end{pmatrix}. \tag{C.55}$$

The peristaltic contribution $\tilde{\mathcal{F}}_{\mathrm{p}}$ Eq. (C.51) is only a function of $\mathbf{Q}_{\mathbf{r}} = (Q_x, Q_y)$ because peristaltic fluctuations of different bilayers are not coupled by the bilayer interation term in Eq. (C.49). Intuitively, fully hydrated bilayers in a stack are far enough apart that peristaltic modes in different bilayers are unlikely to be significantly correlated. First, $\langle|\hat{\mathbf{m}}_0|^2\rangle$, $\left\langle\left|\boldsymbol{\nabla} z_0^-\right|^2\right\rangle$, and $\langle|\bar{\mathbf{m}}_0|^2\rangle$ are derived, and then, it is shown that $\langle|\hat{\mathbf{m}}_0|^2\rangle$, $\left\langle\left|\boldsymbol{\nabla} z_0^-\right|^2\right\rangle$, and $\langle|\bar{\mathbf{m}}_0|^2\rangle$ are primarily determined by short length scale fluctuations.

Deriving $\left\langle|\hat{\mathbf{m}}_0|^2\right\rangle$

Using the definition of a Fourier transform Eq. (3.41),

$$\left\langle|\hat{\mathbf{m}}_0|^2\right\rangle = \frac{1}{A_{\mathrm{p}} J} \sum_{\mathbf{Q},\mathbf{Q}'} \left[\left\langle\left|\hat{m}^{\perp}_{\mathbf{Q}}\right|^2\right\rangle + \left\langle\left|\hat{m}^{\parallel}_{\mathbf{Q}}\right|^2\right\rangle\right] e^{i(\mathbf{Q}_{\mathbf{r}}+\mathbf{Q}'_{\mathbf{r}})\cdot\mathbf{r}}. \tag{C.56}$$

The thermal averages in Eq. (C.56) are evaluated using 𝔸 Eq. (C.54) and the relation between a Hermitian matrix and a thermal average, see Appendix A.1. Note, $\tilde{\mathcal{F}}_{\mathrm{u}}$ Eq. (C.54) and $\tilde{\mathcal{F}}_{\mathrm{p}}$ Eq. (C.55) do not have a multiplicative $1/2$ prefactor, and therefore,

$$\left\langle |\tilde{f}(\mathbf{Q})\rangle\langle\tilde{f}(\mathbf{Q}')| \right\rangle_{\mathrm{th}} = \frac{k_{\mathrm{B}}T}{2}\mathbb{H}^{-1}\,\delta_{\mathbf{Q},-\mathbf{Q}'}, \tag{C.57}$$

where $\mathbb{H}$ is a Hermitian matrix. Simplifying the thermal average dependent part of Eq. (C.56),

$$\begin{aligned}
&\left\langle \left|\hat{m}^{\perp}_{\mathbf{Q}}\right|^2 \right\rangle + \left\langle \left|\hat{m}^{\parallel}_{\mathbf{Q}}\right|^2 \right\rangle \\
&= \frac{k_{\mathrm{B}}T}{2}\left(\mathbb{A}^{-1}_{3,3} + \mathbb{A}^{-1}_{2,2}\right)\,\delta_{\mathbf{Q},-\mathbf{Q}'} && \text{(C.58)}\\
&= \frac{k_{\mathrm{B}}T}{2}\left(\frac{1}{\kappa_\theta + \kappa_{\mathrm{tw}}Q_r^2} + \frac{k_c Q_r^4 + 2B\sin^2(Q_z D/2)}{\kappa_\theta\left[k_c Q_r^4 + 2B\sin^2(Q_z D/2)\right]}\right)\,\delta_{\mathbf{Q},-\mathbf{Q}'} && \text{(C.59)}\\
&= \frac{k_{\mathrm{B}}T}{2\kappa_\theta(1+\tilde{\xi}^2_{\mathrm{tw}}Q_r^2)}\left(1 + \frac{\left[\tilde{\xi}^4 Q_r^4 + 2\sin^2(QzD/2)\right](1+\tilde{\xi}^2_{\mathrm{tw}}Q_r^2)}{\tilde{\xi}^4 Q_r^4 + 2\sin^2(QzD/2)(1+\tilde{\xi}^2_\theta Q_r^2)}\right)\,\delta_{\mathbf{Q},-\mathbf{Q}'}, && \text{(C.60)}
\end{aligned}$$

where

$$k_c \equiv k_c^b - \frac{\Omega^2}{4k_A}, \tag{C.61}$$

$$\tilde{\xi}^4 \equiv k_c/B, \tag{C.62}$$

$$\tilde{\xi}^2_\theta \equiv k_c/\kappa_\theta, \tag{C.63}$$

and

$$\tilde{\xi}^2_{\mathrm{tw}} \equiv \kappa_{\mathrm{tw}}/\kappa_\theta. \tag{C.64}$$

Substituting Eq. (C.60) into $\left\langle |\hat{\mathbf{m}}_0|^2 \right\rangle$ Eq. (C.56) and following methods similar to Section 3.3.3,

$$\sum_{\mathbf{Q}} \to \frac{A_\mathrm{p} J}{(2\pi)^3} \int_{\pi/\tilde{a}}^{\pi/a} \mathrm{d}Q_r \, Q_r \int_0^{2\pi} \mathrm{d}\theta \int_{-\pi}^{\pi} \mathrm{d}\omega, \tag{C.65}$$

$$\begin{aligned} &\left\langle |\hat{\mathbf{m}}_0|^2 \right\rangle \\ &\approx \frac{k_\mathrm{B}T}{8\pi^2\kappa_\theta} \int_{\pi/\tilde{a}}^{\pi/a} \mathrm{d}Q_r \, \frac{Q_r}{1+\tilde{\xi}_\mathrm{tw}^2 Q_r^2} \int_{-\pi}^{\pi} \mathrm{d}\omega \left(1 + \frac{\left[\tilde{\xi}^4 Q_r^4 + 2\sin^2(\omega/2)\right](1+\tilde{\xi}_\mathrm{tw}^2 Q_r^2)}{\tilde{\xi}^4 Q_r^4 + 2\sin^2(\omega/2)(1+\tilde{\xi}_\theta^2 Q_r^2)} \right). \end{aligned} \tag{C.66}$$

Deriving $\left\langle \left| \boldsymbol{\nabla} z_0^- \right|^2 \right\rangle$

Using the definition of a Fourier transform Eq. (3.41), and $\mathbb{B}$ Eq. (C.55),

$$\begin{aligned} \left\langle \left| \boldsymbol{\nabla} z_0^-(\mathbf{r}) \right|^2 \right\rangle &= \left\langle \left| \frac{1}{\sqrt{A_\mathrm{p}}} \sum_{\mathbf{Q_r}} i Q_r z_{\mathbf{Q_r}}^- e^{i\mathbf{Q_r}\cdot\mathbf{r}} \right|^2 \right\rangle && \text{(C.67)} \\ &= \frac{1}{A_\mathrm{p}} \sum_{\mathbf{Q_r},\mathbf{Q_r'}} -Q_r Q_r' \left\langle \left| z_{\mathbf{Q_r}}^- \right|^2 \right\rangle e^{i(\mathbf{Q_r}+\mathbf{Q_r'})\cdot\mathbf{r}} \\ &= \frac{k_\mathrm{B}T}{2A_\mathrm{p}} \sum_{\mathbf{Q_r},\mathbf{Q_r'}} -Q_r Q_r' \, \mathbb{B}_{1,1}^{-1} \, e^{i(\mathbf{Q_r}+\mathbf{Q_r'})\cdot\mathbf{r}} \, \delta_{\mathbf{Q_r},-\mathbf{Q_r'}} \\ &= \frac{k_\mathrm{B}T}{2A_\mathrm{p}} \sum_{\mathbf{Q_r}} Q_r^2 \, \mathbb{B}_{1,1}^{-1}, && \text{(C.68)} \end{aligned}$$

where

$$\mathbb{B}_{1,1}^{-1}(Q_r) = \frac{k_c^b Q_r^2 + \kappa_\theta}{k_c^b \kappa_\theta Q_r^4 + Q_r^2 \left(\frac{k_A k_c^b}{b_0^2} - \frac{\kappa_\theta \Omega}{b_0} - \frac{\Omega^2}{4b_0^2} \right) + \frac{k_A \kappa_\theta}{b_0^2}}. \tag{C.69}$$

Following a similar methodology to Section 3.3.3,

$$\sum_{\mathbf{Q_r}} \to \frac{A_\mathrm{p}}{(2\pi)^2} \int_{\pi/\tilde{a}}^{\pi/a} \mathrm{d}Q_r \; Q_r \int_0^{2\pi} \mathrm{d}\theta, \tag{C.70}$$

and $\left\langle \left| \boldsymbol{\nabla} z_0^- \right|^2 \right\rangle$ Eq. (C.68) is further rewritten,

$$\left\langle \left| \boldsymbol{\nabla} z_0^- \right|^2 \right\rangle \approx \frac{k_\mathrm{B}T}{4\pi} \int_{\pi/\tilde{a}}^{\pi/a} \mathrm{d}Q_r \; Q_r^3 \, \mathbb{B}_{1,1}^{-1}(Q_r). \tag{C.71}$$

Deriving $\langle |\bar{\mathbf{m}}_0|^2 \rangle$

Using the definition of a Fourier transform Eq. (3.41) and $\mathbb{B}$ Eq. (C.55),

$$\begin{aligned} \left\langle |\bar{\mathbf{m}}_0|^2 \right\rangle &= \frac{1}{A_\mathrm{p}} \sum_{\mathbf{Q},\mathbf{Q}'} \left[\left\langle |\bar{m}_{\mathbf{Q}}^{\parallel}|^2 \right\rangle + \left\langle \left| \bar{m}_{\mathbf{Q}}^{\perp} \right|^2 \right\rangle \right] e^{i(\mathbf{Q_r}+\mathbf{Q}'_\mathbf{r})\cdot\mathbf{r}} \\ &\approx \frac{k_\mathrm{B}T}{4\pi} \int_{\pi/\tilde{a}}^{\pi/a} \mathrm{d}Q_r \; Q_r \left(\mathbb{B}_{2,2}^{-1} + \mathbb{B}_{3,3}^{-1} \right), \end{aligned} \tag{C.72}$$

where

$$\mathbb{B}_{2,2}^{-1}(Q_r) = \frac{k_c^b Q_r^4 - \frac{\Omega Q_r^2}{b_0} + \frac{k_A}{b_0^2}}{k_c^b \kappa_\theta Q_r^4 + Q_r^2 \left(\frac{k_A k_c^b}{b_0^2} - \frac{\kappa_\theta \Omega}{b_0} - \frac{\Omega^2}{4 b_0^2} \right) + \frac{k_A \kappa_\theta}{b_0^2}} \tag{C.73}$$

$$\mathbb{B}_{3,3}^{-1}(Q_r) = \frac{1}{\kappa_\theta + \kappa_\mathrm{tw} Q_r^2}. \tag{C.74}$$

System Size Dependence

The critical issue for comparing systems of different lateral size is the extent to which $\left\langle \left| \boldsymbol{\nabla} z_0^+ \right| \right\rangle$, $\langle |\hat{\mathbf{m}}_0|^2 \rangle$, $\left\langle \left| \boldsymbol{\nabla} z_0^- \right| \right\rangle$, and $\langle |\bar{\mathbf{m}}_0|^2 \rangle$ are sensitive to long length scale fluctuations. Therefore, the $\tilde{a}$-dependence ($\tilde{a}$ is the long length scale cutoff) of $\Psi_\mathrm{UC}^{(i)}$ – Eqs. (C.40), (C.66), (C.71), and (C.72), respectively – are investigated numerically,

$$\Delta\Psi_\mathrm{UC}^{(i)}(\tilde{a}) \equiv 1 - \frac{\Psi_\mathrm{UC}^{(i)}(\tilde{a})}{\Psi_\mathrm{UC}^{(i)}(\tilde{a}=\infty)}. \tag{C.75}$$

If $\Psi_{\mathrm{UC}}^{(i)}$ is dominated by short length scale fluctuations, then it is expected that $\Psi_{\mathrm{UC}}^{(i)}(\tilde{a})$ decays rapidly for increasing $\tilde{a}$. Since some of the $\Psi_{\mathrm{UC}}^{(i)}$ depend on parameter values not yet experimentally assessable, parameter values from MD simulations are used [1], see Table C.2. $\Delta\Psi_{\mathrm{UC}}^{(i)}$ Eq. (C.75) are plotted in Fig. C.5. $\left\langle \left| \boldsymbol{\nabla} z_0^+ \right| \right\rangle$ decays slowest and therefore is most system size dependent. For a system with radius ~ 200 Å, the other three averages are within 1% of their value for an infinite system. Therefore, it will often be unnecessary to include their contributions to Ψ_{UC} because most experimental and simulated systems have radii greater than 200 Å. To compare most experimental and simulated systems, the UC derived in Section C.2.1 which only considers $\left\langle \left| \boldsymbol{\nabla} z_0^+ \right|^2 \right\rangle$ is sufficient.

Moreover, $\langle |\hat{\mathbf{m}}_0|^2 \rangle$, $\left\langle \left| \boldsymbol{\nabla} z_0^- \right| \right\rangle$, and $\langle |\bar{\mathbf{m}}_0|^2 \rangle$ depend on moduli values that are not currently determinable by experiment (Ω, κ_{tw}, and k_c^b; see Table C.2 for definitions). Therefore, the aforementioned averages can only be evaluated using moduli values determined from simulations. Using values in Table C.2, the contributions from all four averages for $\tilde{a} = \infty$ are summarized in Table C.1. Using the values in Table C.1 and Eq. (C.33), $\Psi_{\mathrm{UC}} \approx 0.998$.

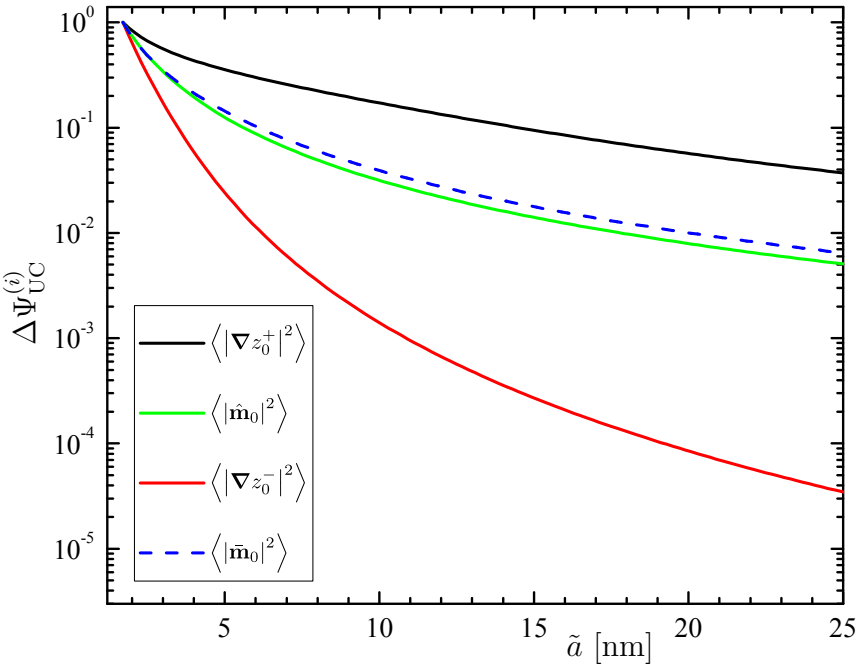


Figure C.5: $\left\langle \left| \boldsymbol{\nabla} z_0^+ \right| \right\rangle$, $\langle |\hat{\mathbf{m}}_0|^2 \rangle$, $\left\langle \left| \boldsymbol{\nabla} z_0^- \right| \right\rangle$, and $\langle |\bar{\mathbf{m}}_0|^2 \rangle$ – Eqs. (C.40), (C.66), (C.71), and (C.72), respectively – are plotted as functions of $\tilde{a}$. The relevant material parameter values are summarized in Table C.2. The curves are normalized at $\tilde{a} = 2$ nm.

Appendix D

Miscellaneous

D.1 a-Dependence of Structure Factor

In Section 6.1.4, it was established that varying the value of a only affects $S^{\mathrm{F}}_{\mathrm{CCD},1}(q_x, q_z)$ at greater q_x-values ($q_x \gtrsim \pi/a$). Fixing K_c, K_θ, and B, the structure factor as a function of a is explored. Restating S_{SD} Eq. (5.9), the structure factor for a single domain is expressed as

$$S_{\mathrm{SD}}(q_r, q_z; \tau') = \pi L_r^2 \sum_{j=0}^{J-1}{}' (J-j)\cos(q_z j D) \int_0^{L_r} \mathrm{d}r \; r F_r\left(\frac{r}{L_r}\right) J_0(q_r r) G(r, j, q_z; \tau'), \tag{D.1}$$

where the τ'-dependence in

$$G(r, j, q_z; \tau') = \exp\left\{-\frac{q_z^2}{2} h_j\left(r/\xi, \ell, \tau'\right)\right\} \tag{D.2}$$

has been stressed. As discussed in Section 4.1, changing the height-height function's upper integration limit approximately adds a constant to the height-height function, see Eq. (4.9),

$$h_j(\rho, \ell, \tau') \approx h_j(\rho, \ell, \tau) + \frac{D^2\eta}{2\pi^2} C^{\dagger}(\tau, \tau', \ell), \tag{D.3}$$

where

$$\tau = \frac{1}{2}\left(\frac{\pi\xi}{a}\right)^2. \tag{D.4}$$

Therefore, in the present context, τ' and τ only differ because of different a values. Substituting $h_j(\rho,\ell,\tau')$ Eq. (D.3) into S_{SD} Eq. (D.1),

$$\begin{aligned}
&S_{\mathrm{SD}}(q_r,q_z;\tau') \\
&= \pi L_r^2 {\sum_{j=0}^{J-1}}'(J-j)\cos(q_z jD)\int_0^{L_r}\mathrm{d}r\; rF_r\left(\frac{r}{L_r}\right)J_0(q_r r)e^{-\frac{q_z^2}{2}h_j(\rho,\ell,\tau')} \qquad \text{(D.5)}\\
&\approx e^{-\frac{q_z^2}{2}\frac{D^2\eta}{2\pi^2}C^\dagger(\tau,\tau',\ell)}\left[\pi L_r^2 {\sum_{j=0}^{J-1}}'(J-j)\cos(q_z jD)\int_0^{L_r}\mathrm{d}r\; rF_r\left(\frac{r}{L_r}\right)J_0(q_r r)e^{-\frac{q_z^2}{2}h_j(\rho,\ell,\tau)}\right]\\
&= e^{-\frac{q_z^2}{2}\frac{D^2\eta}{2\pi^2}C^\dagger(\tau,\tau',\ell)}S_{\mathrm{SD}}(q_r,q_z;\tau). \qquad \text{(D.6)}
\end{aligned}$$

Eq. (D.6) suggests that structure factors with different values of τ and τ' because of different values of a have significant differences as a function of q_z due to the q_z-dependent multiplicative prefactor. Note, Eq. (D.3) is reasonable for $j > 1$ and $\rho > 20$, and therefore, it is expected that Eq. (D.6) is an increasingly poor approximation for increasing q_r. In Section 6.1.4, the a-dependence of S_{CCD} is presented, and Eq. (D.6) is shown to be reasonable.

The effect of a on the structure factor was demonstrated using S_{SD} Eq. (D.1). The various sample and experimental concerns relating S_{SD} and $S^{\mathrm{F}}_{\mathrm{CCD},1}$ discussed in Sections 5.2 and 5.3 only slightly influence the prefactor [30]

$$\exp\left\{-\frac{q_z^2}{2}\frac{D^2\eta}{2\pi^2}C^\dagger(\tau,\tau',\ell)\right\}. \tag{D.7}$$

If only an upper bound on the value of a is assessable, the presented a-dependence of the structure factor is particularly important in estimating the uncertainty of the determined $|F(q_z)|^2$ as discussed in Section 6.1.4 and shown in Fig. 6.12.

[30] The most significant modification to Eq. (D.7) is due to the geometric broadening in the p_z-direction.

D.2 Computational Precision of $S^{\mathbf{F}}_{\mathbf{CCD,1}}$

At the end of Section 5.4, Eqs. (5.145)-(5.148) describe a methodology for calculating the predicted scattering intensity. The first two equations are reproduced below for convenience,

$$f_1(\rho, q_z) \equiv \sum_{j=0}^{\infty}{}' \frac{H_z(jD, q_z)}{\sqrt{1 + h_j\tilde{\sigma}_z^{*2}}} \exp\left\{-\frac{q_z^2 h_j + j^2 D^2 \tilde{\sigma}_z^{*2}}{2\left(1 + h_j\tilde{\sigma}_z^{*2}\right)}\right\} \cos\left(\frac{q_z jD}{1 + h_j\tilde{\sigma}_z^{*2}}\right) \tag{D.8}$$

$$f_2(q_r, q_z) \equiv \int_0^{\infty} \mathrm{d}r\ rH_r(r)J_0(q_r r)f_1(\rho, q_z). \tag{D.9}$$

Since the integrand of f_2 is oscillatory about $r = 0$, the numerical evaluation of f_2 requires the summation of many positive and negative terms of similar magnitude.

Even though f_2 is theoretically positive definite, the numerical calculation of f_2 is negative for some parameter values and (q_r, q_z). $f_2 < 0$ is more common for larger q_r-values because $J_0(q_r r)$ is increasingly oscillatory. The negative f_2-values are the result of f_1 and H_r being tabled and interpolated to finite precision. If f_1 and H_r are more precisely calculated, the number of negative f_2-values is diminished, but the analysis program runs much more slowly. f_1 and H_r are calculated at sufficient precision so that the instances of $f_2 < 0$ is typically of order 1 in 1000. When a negative $f_2(q_r^*, q_z)$-value is calculated, f_2-values calculated at neighboring q_r-values are interpolated to determine a positive $f_2(q_r^*, q_z)$-value.

D.3 Numerical Integration Issue

It was found that for $\rho \ll 1$ the GNU Scientific Library numerical integration returns incorrect values for $h_0(\rho, \ell, \tau)$ when compared to Mathematica. For $\rho \ll 1$, $J_0(\sqrt{2v}\rho)$ can be replaced by the first two terms in its Taylor series about $\rho = 0$, substantially simplifying the integrand of Eq. (4.1) and leading to an analytic solution to the integral. Beginning with Eq. (4.1) and replacing $J_0(\sqrt{2v}\rho)$ with its truncated Taylor series,

$$h_0(\rho,\ell,\tau) = \frac{D^2\eta}{2\pi^2}\int_0^\tau \mathrm{d}v\ \frac{1-J_0\left(\sqrt{2v}\rho\right)}{\frac{v}{\sqrt{1+v\ell}}\sqrt{1+\frac{v^2}{1+v\ell}}} \tag{D.10}$$

$$\approx \frac{D^2\eta}{2\pi^2}\int_0^\tau \mathrm{d}v\ \frac{1-\left(1-\frac{v\rho^2}{2}\right)}{\frac{v}{\sqrt{1+v\ell}}\sqrt{1+\frac{v^2}{1+v\ell}}} \tag{D.11}$$

$$\Rightarrow h_0^{\mathrm{a}}(\rho,\ell,\tau) \equiv \frac{D^2\rho^2\eta}{4\pi^2}\left[\ell\left(f_c(\tau)-1\right)-\left(\frac{\ell^2-2}{2}\right)\ln\left(\frac{2\tau+\ell+2f_c(\tau)}{\ell+2}\right)\right], \tag{D.12}$$

where $\tau = \frac{1}{2}\left(\frac{\pi\xi}{a}\right)^2$ and $f_c(x) = \sqrt{1+x\ell+x^2}$. The difference between the exact Eq. (D.10) and approximate Eq. (D.12) forms is quantified by

$$\Delta h_0^{\mathrm{a}}(\rho,\ell,\tau) \equiv \left|1-\frac{h_0^{\mathrm{a}}(\rho,\ell,\tau)}{h_0(\rho,\ell,\tau)}\right|. \tag{D.13}$$

In Fig. D.1, Eq. (D.13) is plotted as a function of ρ for $\ell = 2$ and $\ell = 0$. For $\rho < 0.005$, $3.5\times10^{-5} \lesssim h_0^{\mathrm{a}}(\rho,\ell,\tau) \lesssim 8\times10^{-5}$, and therefore, Eq. (D.12) is used to calculate $h_j(\rho,\ell,\tau)$ for $\rho < 0.005$ and $j = 0$.

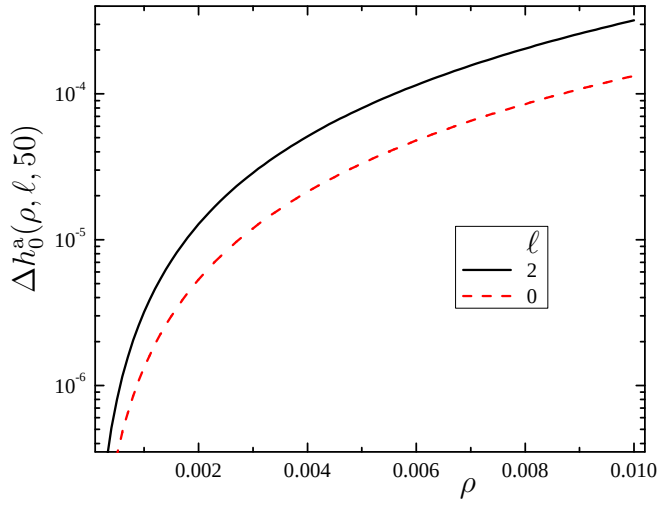


Figure D.1: The relative error of approximating the Bessel function with the first 2 terms in its Taylor series about 0 as a function of ρ for $\ell = 2$ (black solid line) and $\ell = 0$ (red dashed line). The solid and dashed lines are upper and lower bounds, respectively, for the relative error. A typical value of $\tau = 50$ was used.

D.4 Deriving Tilt-Dependent Fluctuation Free Energy: $\Delta\mathcal{F}_{\text{fl}}$

In Section 8.2.2, the tilt-dependent fluctuation free energy per unit area of one bilayer $\Delta\widetilde{\mathcal{F}}_{\text{fl}}$ is used to determine the Hamaker parameter H of a stack of DOPC bilayers. Below, $\Delta\widetilde{\mathcal{F}}_{\text{fl}}$ is derived.

The bilayer stack undulation free energy $\mathcal{F}_{\text{u}}$ Eq. (3.51) is treated as a Hamiltonian,

$$\mathcal{H}_{\text{u}} \equiv \mathcal{F}_{\text{u}} = \frac{1}{2}\sum_{\mathbf{Q}} \mathbf{f}_{\text{u}}(-\mathbf{Q})\,\mathbb{U}\,\mathbf{f}_{\text{u}}^{T}(\mathbf{Q}), \tag{D.14}$$

where

$$\mathbf{f}_{\text{u}}(\mathbf{Q}) = \left(z_{\mathbf{Q}}^{+},\, \hat{m}_{\mathbf{Q}}^{\parallel},\, \hat{m}_{\mathbf{Q}}^{\perp}\right), \tag{D.15}$$

and

$$\mathbb{U} = \begin{pmatrix} K_c Q_r^4 + 4B\sin^2(Q_z D/2) & -iK_c Q_r^3 & 0 \\ iK_c Q_r^3 & K_c Q_r^2 + K_\theta & 0 \\ 0 & 0 & K_\theta \end{pmatrix}. \tag{D.16}$$

$\mathcal{F}_{\text{fl}}$ is related to the partition function $\mathcal{Z}_{\text{fl}}$,

$$\mathcal{F}_{\text{fl}} \equiv -\frac{1}{\beta}\ln \mathcal{Z}_{\text{fl}}, \tag{D.17}$$

and therefore, the partition function is derived,

$$\mathcal{Z}_{\text{fl}} \equiv \int \mathrm{d}\left[\mathbf{f}_{\text{u}}(\mathbf{Q})\right]\, \exp\left\{-\beta\mathcal{H}_{\text{u}}\right\}. \tag{D.18}$$

Substituting $\mathcal{H}_{\text{u}}$ Eq. (D.14) into $\mathcal{Z}_{\text{fl}}$ Eq. (D.18),

$$\mathcal{Z}_{\text{fl}} = \prod_{\mathbf{Q}} \int \mathrm{d}\left[\mathbf{f}_{\text{u}}(\mathbf{Q})\right] \exp\left\{-\frac{\beta}{2}\mathbf{f}_{\text{u}}(-\mathbf{Q})\,\mathbb{U}\,\mathbf{f}_{\text{u}}^{T}(\mathbf{Q})\right\} \tag{D.19}$$

$$= \prod_{\mathbf{Q}} \left(\frac{\beta \det\left[\mathbb{U}\right]}{2\pi}\right)^{-1/2}. \tag{D.20}$$

$\mathcal{F}_{\text{fl}}$ Eq. (D.17) is evaluated using $\mathcal{Z}_{\text{fl}}$ Eq. (D.20),

$$\mathcal{F}_{\text{fl}} = \frac{1}{2\beta}\sum_{\mathbf{Q}} \ln\left(\frac{\beta \det\left[\mathbb{U}\right]}{2\pi}\right) \tag{D.21}$$

$$= \sum_{Q_z} \mathcal{F}_{\text{fl}}(Q_z), \tag{D.22}$$

where

$$\mathcal{F}_{\text{fl}}(Q_z) \equiv \frac{k_{\text{B}}T}{2}\frac{A_{\text{p}}}{(2\pi)^2}\int \mathrm{d}^2\mathbf{Q_r}\ \ln\left(\frac{\beta \det\left[\mathbb{U}\right]}{2\pi}\right). \tag{D.23}$$

The free energy of interest is the difference from a reference state with $B = 0$,

$$\Delta\mathcal{F}_{\text{fl}} = \mathcal{F}_{\text{fl}}(B \neq 0) - \mathcal{F}_{\text{fl}}(B = 0). \tag{D.24}$$

Using

$$\det\left[\mathbb{U}\right] = K_\theta^2\left[K_c Q_r^4 + 4B(1+\xi_\theta^2 Q_r^2)\sin^2\left(\frac{Q_z D}{2}\right)\right], \tag{D.25}$$

$\Delta\mathcal{F}_{\text{fl}}(Q_z)$ is expressed as

$$\Delta\mathcal{F}_{\text{fl}}(Q_z) = \frac{k_{\text{B}}TA_{\text{p}}}{8\pi^2}\int \mathrm{d}^2\mathbf{Q_r}\ \ln\left(1 + \frac{4\sin^2\left(Q_z D/2\right)}{\xi^4 Q_r^4}\left(1+\xi_\theta^2 Q_r^2\right)\right) \tag{D.26}$$

$$= \frac{k_{\text{B}}TA_{\text{p}}}{4\pi}\int_0^{\pi/a} \mathrm{d}Q_r\ Q_r \ln\left(1 + \frac{4\sin^2\left(Q_z D/2\right)}{\xi^4 Q_r^4}\left(1+\xi_\theta^2 Q_r^2\right)\right). \tag{D.27}$$

For $\xi_\theta \to 0$ $\Delta\mathcal{F}_{\rm fl}(Q_z)$ Eq. (D.27) reduces to the tilt-independent result; the tilt-dependence is significant for $Q_r \gtrsim 1/\xi_\theta$ (for reasonable estimates of $\xi_\theta \approx 9$ Å and $a \approx 16$ Å, $1/\xi_\theta < \pi/a$). Finally, using $\Delta\mathcal{F}_{\rm fl}(Q_z)$ Eq. (D.27) and Eq. (D.22), the fluctuation free energy per unit area of one bilayer is

$$\Delta\widetilde{\mathcal{F}}_{\rm fl} \equiv \frac{\Delta\mathcal{F}_{\rm fl}}{JA_{\rm p}} \tag{D.28}$$

$$= \frac{k_{\rm B}TD}{8\pi^2}\int_{-\pi/D}^{\pi/D}{\rm d}Q_z\ \int_0^{\pi/a}{\rm d}Q_r\ Q_r \ln\left(1+\frac{4\sin^2\left(Q_zD/2\right)}{\xi^4Q_r^4}\left(1+\xi_\theta^2Q_r^2\right)\right). \tag{D.29}$$

In the limit $\xi_\theta \to 0$ and $a \to \infty$,

$$\lim_{\substack{\xi_\theta\to 0\\ a\to\infty}} \Delta\widetilde{\mathcal{F}}_{\rm fl} \equiv \Delta\widetilde{\mathcal{F}}_{\rm fl}^{\cancel{\rm tilt}} \tag{D.30}$$

$$= \frac{k_{\rm B}TD}{8\pi^2}\int_{-\pi/D}^{\pi/D}{\rm d}Q_z\ \int_0^{\infty}{\rm d}Q_r\ Q_r \ln\left(1+\frac{4\sin^2\left(Q_zD/2\right)}{\xi^4Q_r^4}\right) \tag{D.31}$$

$$= \frac{k_{\rm B}TD}{8\pi\xi^2}\int_{-\pi/D}^{\pi/D}{\rm d}Q_z\,\left|\sin(Q_zD/2)\right| \tag{D.32}$$

$$= \frac{k_{\rm B}T}{2\pi}\sqrt{\frac{B}{K_c}}. \tag{D.33}$$

where $\Delta\widetilde{\mathcal{F}}_{\rm fl}^{\cancel{\rm tilt}}$ is the tilt-independent fluctuation free energy per unit area of one bilayer and was previously derived [58].

Appendix E

Vesicle Undulation Correction

Another method to measure the form factor $|F|$ uses scattering from so-called large unilamellar vesicles (ULVs) [85]. That method does not determine values of the mechanical moduli which is the primary focus of this thesis. In the past an undulation correction (UC), see Section C.2, has not been applied to $|F|$ determined using scattering from ULV. Previous researchers argued that a UC was unneccessary because "long wavelength undulations are suppressed by the vesicle size" [85]. Certainly, a vesicle's size limits the longest possible undulation wavelength, but for a quasi-spherical vesicle, undulations with wavelengths shorter than the vesicle's circumference are permitted. In principal, to compare ULV $|F|$ and $|F|$ determined using oriented stacked bilayers or $|F|$ determined from simulations, the ULV $|F|$ should be undulation corrected.

In Sections E.1 and E.2, a UC is derived for spherical and planar geometries, respectively. The spherical geometry is more appropriate for the description of vesicles, but the planar geometry is simpler and is used for comparison, see Section E.3. It is shown that the vesicle UC tends to be smaller than the planar membrane UC, see Fig. E.1, because of differences in their respective height spectra, see Fig. E.2. Additionally, the vesicle UC is reduced by finite effective surface tension ($\bar{\sigma}$), see Fig. E.3. For 250 Å radius ULV and $a = 17$ Å, the vesicle UC is calculated to be less than 1.005, significantly less than the typical UC for oriented bilayer stacks, see Table C.1 (specifically the "Tilt" and "~~Tilt~~" columns).

E.1 Spherical Geometry

The vesicle height fluctuation spectrum was first derived by Milner and Safran [108]. Since it is convenient for later derivations, the notation of Barbetta *et al.* [109] is followed. The quasi-spherical vesicle's shape is parameterized in spherical coordinates

$$\mathbf{r} = R[1 + u(\theta, \phi)]\hat{\mathbf{r}}, \tag{E.1}$$

where $u(\theta, \phi) \ll 1$ and descibes the vesicle's deviations from a sphere with radius R. The vesicle free energy will be described within the Helfrich model [10]

$$H = \int \mathrm{d}S \ (2K_c C^2 + \sigma), \tag{E.2}$$

where S is the surface of the vesicle and C is the local mean curvature, essentially $\nabla^2 z^+/2$. In the context of describing a quasi-spherical vesicle, σ is an effective surface tension since it was introduced as a Lagrange multiplier to approximately constrain the vesicle's surface area [108].

Decomposing $u(\theta, \phi)$ into spherical harmonics Y_ℓ^m,

$$u(\theta, \phi) = \frac{u_{0,0}}{\sqrt{4\pi}} + \sum_\omega u_{\ell,m} Y_\ell^m(\theta, \phi), \tag{E.3}$$

where

$$u_{\ell,-m} = (-1)^m u_{\ell,m}^* \tag{E.4}$$

and

$$\sum_\omega \equiv \sum_{\ell=2}^{L} \sum_{m=-\ell}^{\ell}. \tag{E.5}$$

L is a high wavevector cutoff. Note that the $\ell = 1$ modes are discarded since they correspond to translations. Barbetta *et al.* [109] expressed the vesicle height-height fluctuation spectrum as

$$\langle u_{\ell,m} u_{\ell',m'} \rangle = (-1)^m \frac{k_{\mathrm{B}} T}{\tilde{H}_\ell} \, \delta_{\ell,\ell'} \delta_{m,-m'} \tag{E.6}$$

where

$$\tilde{H}_\ell \equiv K_c(\ell - 1)(\ell + 2)(\ell^2 + \ell + \bar{\sigma}) \tag{E.7}$$

and

$$\bar{\sigma} \equiv \sigma R^2 / K_c. \tag{E.8}$$

The vesicle UC is proportional to $\left\langle |\boldsymbol{\nabla} u(\theta,\phi)|^2 \right\rangle$ where $\boldsymbol{\nabla}$ only acts along $\hat{\theta}$ and $\hat{\phi}$,

$$\left\langle |\boldsymbol{\nabla} u(\theta,\phi)|^2 \right\rangle = \left\langle \left| \frac{\partial u}{\partial \theta} \hat{\theta} + \frac{1}{\sin\theta} \frac{\partial u}{\partial \phi} \hat{\phi} \right|^2 \right\rangle \tag{E.9}$$

$$= \left\langle \left| \frac{\partial u}{\partial \theta} \right|^2 + \frac{1}{\sin^2\theta} \left| \frac{\partial u}{\partial \phi} \right|^2 \right\rangle$$

$$= \left\langle |u_\theta|^2 \right\rangle + \frac{1}{\sin^2\theta} \left\langle |u_\phi|^2 \right\rangle \tag{E.10}$$

where $u_i = \frac{\partial u}{\partial i}$. Relations for both $\left\langle |u_\theta|^2 \right\rangle$ and $\left\langle |u_\phi|^2 \right\rangle$ have been presented previously [109]. In the interest of completeness and to facilitate future tilt-dependent extensions, derivations of $\left\langle |u_\theta|^2 \right\rangle$ and $\left\langle |u_\phi|^2 \right\rangle$ are given below.

E.1.1 $\left\langle |u_\theta|^2 \right\rangle$

Using $u(\theta,\phi)$ Eq. (E.3), $\langle u_{\ell,m} u_{\ell',m'} \rangle$ Eq. (E.6), and $(-1)^m Y_\ell^{-m} = (Y_\ell^m)^*$,

$$\left\langle |u_\theta|^2 \right\rangle = \sum_{\omega,\omega'} \frac{\partial Y_\ell^m(\Omega)}{\partial\theta} \frac{\partial Y_{\ell'}^{m'}(\Omega)}{\partial\theta} \langle u_{\ell,m} u_{\ell',m'} \rangle \tag{E.11}$$

$$= \sum_{\omega,\omega'} (-1)^m \frac{k_\mathrm{B}T}{\tilde{H}_\ell} \frac{\partial Y_\ell^m}{\partial\theta} \frac{\partial Y_{\ell'}^{m'}}{\partial\theta} \delta_{\ell,\ell'} \delta_{m,-m'}$$

$$= \sum_{\omega} (-1)^m \frac{k_\mathrm{B}T}{\tilde{H}_\ell} \frac{\partial Y_\ell^m}{\partial\theta} \frac{\partial Y_\ell^{-m}}{\partial\theta}$$

$$= \sum_{\ell=2}^{L} \frac{k_\mathrm{B}T}{\tilde{H}_\ell} \sum_{m=-\ell}^{\ell} \frac{\partial Y_\ell^m}{\partial\theta} \frac{\partial (Y_\ell^m)^*}{\partial\theta}. \tag{E.12}$$

The m-dependent part of $\left\langle |u_\theta|^2 \right\rangle$ in Eq. (E.12) is further simplified using the addition theorem for spherical harmonics,

$$\sum_{m=-\ell}^{\ell} Y_\ell^m(\theta_1,\phi_1)[Y_\ell^m(\theta_2,\phi_2)]^* = \frac{2\ell+1}{4\pi} P_\ell[\cos(\gamma)], \tag{E.13}$$

where P_ℓ is the Legendre polynomial of order ℓ and

$$\cos\gamma = \cos\theta_1\cos\theta_2 + \sin\theta_1\sin\theta_2\cos(\phi_1-\phi_2). \tag{E.14}$$

Setting $\phi_1 = \phi_2 = \phi$ in $\cos\gamma$ leads to $\cos\gamma = \cos(\theta_1-\theta_2)$, and differentiating both sides of Eq. (E.13) with respect to θ_1 and θ_2,

$$\sum_{m=-\ell}^{\ell} \partial_{\theta_1} Y_\ell^m(\theta_1,\phi) \partial_{\theta_2} [Y_\ell^m(\theta_2,\phi)]^* = \frac{2\ell+1}{4\pi} \partial_{\theta_1}\partial_{\theta_2} P_\ell[\cos(\gamma)] \tag{E.15}$$

$$= \frac{2\ell+1}{4\pi} \frac{\partial}{\partial\theta_1} \left(\frac{\partial(\cos\gamma)}{\partial\theta_2} \frac{dP_\ell(\cos\gamma)}{d(\cos\gamma)} \right)$$

$$= \frac{2\ell+1}{4\pi} \frac{\partial}{\partial\theta_1} \left(\sin\gamma \frac{dP_\ell(\cos\gamma)}{d(\cos\gamma)} \right)$$

$$= \frac{2\ell+1}{4\pi} \left(-\sin^2\gamma \frac{d^2P_\ell(\cos\gamma)}{d(\cos\gamma)^2} + \cos\gamma \frac{dP_\ell(\cos\gamma)}{d(\cos\gamma)} \right), \tag{E.16}$$

where $\partial_i = \frac{\partial}{\partial i}$. Using the Legendre differential equation,

$$\sin^2\gamma \frac{d^2 P_\ell(\cos\gamma)}{d(\cos\gamma)^2} = -\ell(\ell+1)P_\ell(\cos\gamma) + 2\cos\gamma \frac{dP_\ell(\cos\gamma)}{d(\cos\gamma)} \tag{E.17}$$

and setting $\theta_1 = \theta_2 = \theta$, Eq. (E.16) is rewritten as

$$\sum_{m=-\ell}^{\ell} \partial_\theta Y_\ell^m(\theta,\phi)\partial_\theta [Y_\ell^m(\theta,\phi)]^* = \frac{2\ell+1}{4\pi}\left(\ell(\ell+1)P_\ell(0) - \cos(0)\left.\frac{dP_\ell(\cos\gamma)}{d(\cos\gamma)}\right|_{\gamma=0}\right) \tag{E.18}$$

$$= \frac{2\ell+1}{4\pi}\left(\ell(\ell+1) - \frac{\ell(\ell+1)}{2}\right)$$

$$= \frac{(2\ell+1)}{4\pi}\frac{\ell(\ell+1)}{2}, \tag{E.19}$$

where the Legendre polynomial property that a derivative evaluated at an end point is $P_\ell(1) = \frac{\ell(\ell+1)}{2}$ was used. Substituting Eq. (E.19) into $\left\langle |u_\theta|^2 \right\rangle$ Eq. (E.12) finishes the derivation of $\left\langle |u_\theta|^2 \right\rangle$,

$$\left\langle |u_\theta|^2 \right\rangle = \frac{k_\mathrm{B}T}{8\pi}\sum_{\ell=2}^{L} \frac{\ell(\ell+1)(2\ell+1)}{\tilde{H}_\ell}. \tag{E.20}$$

E.1.2 $\left\langle |u_\phi|^2 \right\rangle$

Using $u(\theta,\phi)$ Eq. (E.3),

$$\left\langle |u_\phi|^2 \right\rangle = \sum_{\omega,\omega'} \partial_\phi Y_\ell^m(\Omega)\partial_\phi Y_{\ell'}^{m'}(\Omega)\left\langle u_{\ell,m}u_{\ell',m'}\right\rangle \tag{E.21}$$

$$= \sum_{\omega}(-1)^m \frac{k_\mathrm{B}T}{\tilde{H}_\ell}\partial_\phi Y_\ell^m \partial_\phi Y_\ell^{-m}$$

$$= \sum_{\ell=2}^{L}\frac{k_\mathrm{B}T}{\tilde{H}_\ell}\sum_{m=-\ell}^{\ell}\partial_\phi Y_\ell^m \partial_\phi (Y_\ell^m)^*. \tag{E.22}$$

The m-dependent part of $\left\langle |u_\phi|^2 \right\rangle$ Eq. (E.22) is simplified utilizing the addition theorem for spherical harmonics, Eq. (E.13), but now $\theta_1 = \theta_2 = \theta \rightarrow \cos\gamma = \cos^2\theta + \sin^2\theta\cos(\phi_1 - \phi_2)$. Differentiating both sides of Eq. (E.13) with respect to ϕ_1 and ϕ_2

$$\sum_{m=-\ell}^{\ell} \partial_{\phi_1} Y_\ell^m(\theta,\phi_1)\partial_{\phi_2}[Y_\ell^m(\theta,\phi_2)]^* \tag{E.23}$$

$$\begin{aligned}
&= \frac{2\ell+1}{4\pi}\partial_{\phi_1,\phi_2} P_\ell[\cos(\gamma)] \\
&= \frac{2\ell+1}{4\pi}\frac{\partial}{\phi_1}\left(\frac{\partial\cos\gamma}{\phi_2}\frac{dP_\ell(\cos\gamma)}{d(\cos\gamma)}\right) \\
&= \frac{2\ell+1}{4\pi}\frac{\partial}{\phi_1}\left(\sin^2\theta\sin(\phi_1-\phi_2)\frac{dP_\ell(\cos\gamma)}{d(\cos\gamma)}\right) \\
&= \frac{2\ell+1}{4\pi}\left(-\sin^4\theta\sin^2(\phi_1-\phi_2)\frac{d^2P_\ell(\cos\gamma)}{d(\cos\gamma)^2} + \sin^2\theta\cos(\phi_1-\phi_2)\frac{dP_\ell(\cos\gamma)}{d(\cos\gamma)}\right).
\end{aligned} \tag{E.24}$$

Setting $\phi_1 = \phi_2 = \phi$ in Eq. (E.24),

$$\sum_{m=-\ell}^{\ell} \partial_{\phi} Y_\ell^m(\theta,\phi)\partial_{\phi}[Y_\ell^m(\theta,\phi)]^* = \frac{2\ell+1}{4\pi}\left(\sin^2\theta\frac{dP_\ell(\cos\gamma)}{d(\cos\gamma)}\right)\Bigg|_{\gamma=0} \tag{E.25}$$

$$= \frac{2\ell+1}{4\pi}\sin^2\theta\frac{\ell(\ell+1)}{2}. \tag{E.26}$$

Substituting Eq. (E.26) into $\left\langle |u_\phi|^2 \right\rangle$ Eq. (E.22),

$$\left\langle |u_\phi|^2 \right\rangle = \sin^2\theta\frac{k_\mathrm{B}T}{8\pi}\sum_{\ell=2}^{L}\frac{\ell(\ell+1)(2\ell+1)}{\tilde{H}_\ell} \tag{E.27}$$

$$= \sin^2\theta\left\langle |u_\theta|^2 \right\rangle. \tag{E.28}$$

E.1.3 Spherical UC

Finally, combining $\left\langle |u_\theta|^2 \right\rangle$ Eq. (E.20) and $\left\langle |u_\phi|^2 \right\rangle$ Eq. (E.28) the UC for a spherical (s) vesicle is

$$\Psi^{\mathrm{s}}_{\mathrm{UC}} \equiv 1 + \frac{1}{2}\left\langle |\boldsymbol{\nabla} u(\Omega)|^2 \right\rangle \tag{E.29}$$

$$= 1 + \frac{1}{2}\left(\left\langle |u_\theta|^2 \right\rangle + \frac{1}{\sin^2\theta}\left\langle |u_\phi|^2 \right\rangle \right) \tag{E.30}$$

$$= 1 + \frac{k_{\mathrm{B}}T}{16\pi K_c} \sum_{\ell=2}^{L} \frac{\ell(\ell+1)(2\ell+1)}{(\ell-1)(\ell+2)(\ell^2+\ell+\bar{\sigma})}, \tag{E.31}$$

where the definition of $\tilde{H}_\ell$ Eq. (E.7) was used. $\Psi^{\mathrm{s}}_{\mathrm{UC}}$ is a function of K_c, $\bar{\sigma}$, and the vesicle's size. Barbetta *et al.* argue that the largest appropriate spherical harmonic is

$$L = \lfloor \sqrt{4 + R^2/a^2} - 1 \rfloor, \tag{E.32}$$

where R is the vesicle radius, π/a is the longest considered wavevector, and $\lfloor x \rfloor$ returns the integer part of x. For $R/a \gg 1$, $L \approx \lfloor R/a \rfloor$. Also, Barbetta *et al.* conclude that σ ranges from -10^{-24} J/Å^2 for a vesicle with a radius of 50 nm to -10^{-26} J/Å^2 for a vesicle with a radius of $\sim 1\,\mu$m. Assuming $K_c \sim 10^{-19}$ J, then $\bar{\sigma}$ Eq. (E.8) is -0.9.

E.2 Planar Geometry

An approximate vesicle undulation correction can be derived using the single planar membrane height fluctuation spectrum,

$$\left\langle \left| z^+_{\mathbf{Q_r}} \right|^2 \right\rangle = \frac{k_{\mathrm{B}}T}{A_{\mathrm{p}}} \left(\frac{1}{K_c Q_r^4 + \sigma Q_r^2} \right) \delta_{\mathbf{Q_r},-\mathbf{Q'_r}}, \tag{E.33}$$

where σ is the membrane surface tension. In Appendix C.2.1 it was shown that the undulation correction is dependent on $\left\langle |\boldsymbol{\nabla} z^+|^2 \right\rangle$,

$$\left\langle \left| \boldsymbol{\nabla} z^+(\mathbf{r}) \right|^2 \right\rangle = \left\langle \left| \sum_{Q_x,Q_y} i(Q_x\hat{\mathbf{x}} + Q_y\hat{\mathbf{y}}) z_{\mathbf{Q_r}}(\mathbf{Q_r}) e^{i\mathbf{Q_r}\cdot\mathbf{r}} \right|^2 \right\rangle \tag{E.34}$$

$$= \frac{k_{\mathrm{B}}T}{A_{\mathrm{p}}} \sum_{\mathbf{Q_r}} \frac{1}{K_c Q_r^2 + \sigma}. \tag{E.35}$$

Assuming the step size in Q_r is sufficiently small, $\sum_{\mathbf{Q_r}}$ is replaced by $\frac{A_\mathrm{p}}{(2\pi)^2}\int \mathrm{d}\mathbf{Q_r}$. π/a and $\pi/\tilde{a}$ are the longest and shortest Q_r modes, respectively, and

$$\begin{aligned}\left\langle \left|\boldsymbol{\nabla} z^+(\mathbf{r})\right|^2 \right\rangle &= \frac{k_\mathrm{B}T}{4\pi^2}\int_{\pi/\tilde{a}}^{\pi/a} \mathrm{d}\mathbf{Q_r}\ \frac{1}{K_c Q_r^2+\sigma} \\ &= \frac{k_\mathrm{B}T}{4\pi K_c}\left[\ln\left(\frac{K_c\pi^2}{a^2}+\sigma\right)-\ln\left(\frac{K_c\pi^2}{\tilde{a}^2}+\sigma\right)\right].\end{aligned} \tag{E.36}$$

The single planar (p) membrane UC is

$$\Psi^\mathrm{p}_\mathrm{UC} \equiv 1+\frac{\left\langle \left|\boldsymbol{\nabla} z^+(\mathbf{r})\right|^2 \right\rangle}{2} \tag{E.37}$$

$$= 1+\frac{k_\mathrm{B}T}{4\pi K_c}\left[\ln\left(\frac{\tilde{a}}{a}\right)+\frac{1}{2}\ln\left(\frac{1+\frac{\sigma a^2}{K_c\pi^2}}{1+\frac{\sigma\tilde{a}^2}{K_c\pi^2}}\right)\right]. \tag{E.38}$$

E.3 Spherical and Planar UCs Compared

The spherical and planar UCs (Eqs. (E.31) and (E.38), respectively) are reproduced for convenience,

$$\Psi^\mathrm{s}_\mathrm{UC} \equiv 1+\frac{k_\mathrm{B}T}{16\pi K_c}\sum_{\ell=2}^{L}\frac{\ell(\ell+1)(2\ell+1)}{(\ell-1)(\ell+2)(\ell^2+\ell+\bar{\sigma})} \tag{E.39}$$

and

$$\Psi^\mathrm{p}_\mathrm{UC} \equiv 1+\frac{k_\mathrm{B}T}{4\pi K_c}\left[\ln\left(\frac{R}{a}\right)+\frac{1}{2}\ln\left(\frac{1+\frac{\sigma a^2}{K_c\pi^2}}{1+\frac{\sigma R^2}{K_c\pi^2}}\right)\right], \tag{E.40}$$

respectively, where $\tilde{a}$ was replaced by R in Eq. (E.40). In Fig. E.1, Eqs. (E.39) and (E.40) are plotted as functions of R/a for $\sigma = 0$ ($\Rightarrow \bar{\sigma} = 0$) and $K_c/(k_\mathrm{B}T) = 19$ (recall that $L = \lfloor\sqrt{4+R^2/a^2}-1\rfloor$). $\Psi^\mathrm{p}_\mathrm{UC}$ is consistently larger than $\Psi^\mathrm{s}_\mathrm{UC}$ because of differences in the planar and spherical height fluctuation spectra. The planar and spherical height spectra are plotted in Fig. E.2. While both spectra decay with the same exponent for large wavenumber, -4, the spherical spectrum decays slower at small wavenumber. In Fig. E.3 Eq. (E.39) is plotted as a function of $\bar{\sigma}$ for values of $R/a = \{10,\ 20,\ 40,\ 80\}$ and $K_c/(k_\mathrm{B}T) = 19$. Due to stability considerations,

the minimum value of $\bar{\sigma}$ is -6 [109], and the maximum value is approximately 100, assuming that $\sigma < 10$ mN/m. The value of $\bar{\sigma}$ is different for each vesicle, and typical values of $\bar{\sigma}$ are between 20 and 60 for GUVs [110]. The values of $\bar{\sigma}$ for ULVs are unknown. Assuming $\bar{\sigma} > 0$ and $a = 17$ Å, $\Psi^{\rm s}_{\rm UC} < 1.005$ for a 250 Å radius ULV, significantly less than typical $\Psi_{\rm UC}$ for stacked bilayers, see Table C.1 (specifically the "Tilt" and "~~Tilt~~" columns).

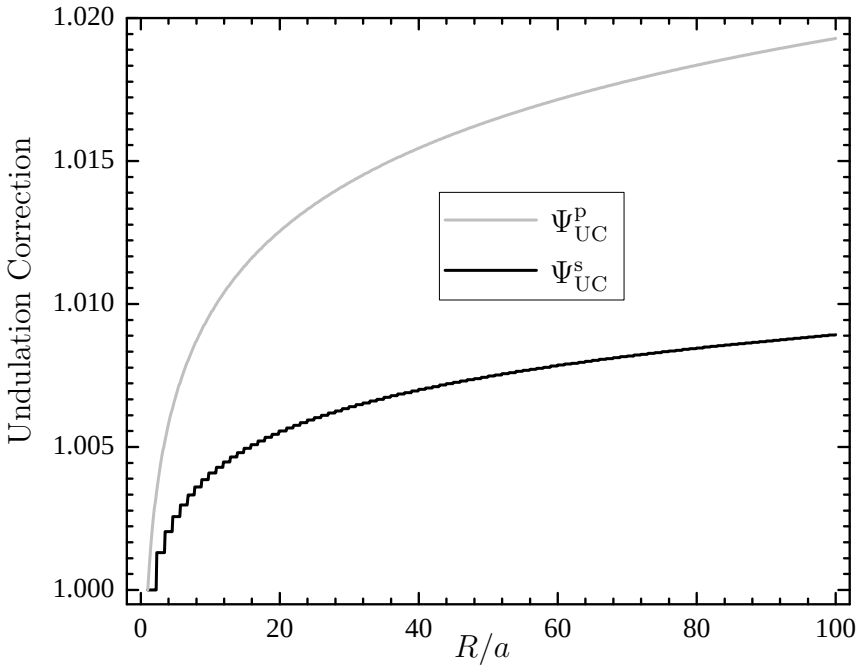


Figure E.1: The spherical and planar UC are plotted as functions of R/a for $\bar{\sigma} = 0$. The steplike features in $\Psi^{\rm s}_{\rm UC}$ are due to the discrete nature of L in Eq. (E.39).

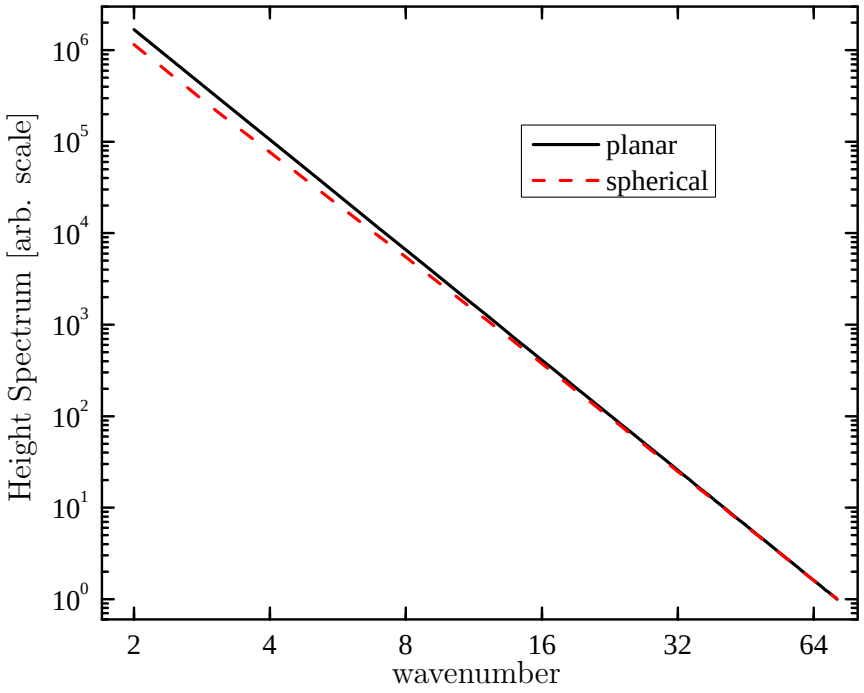


Figure E.2: The planar Eq. (E.33) and spherical Eq. (E.6) height spectra are plotted as functions of the wavenumber for $\sigma = 0$. The horizontal axis is log base 2.

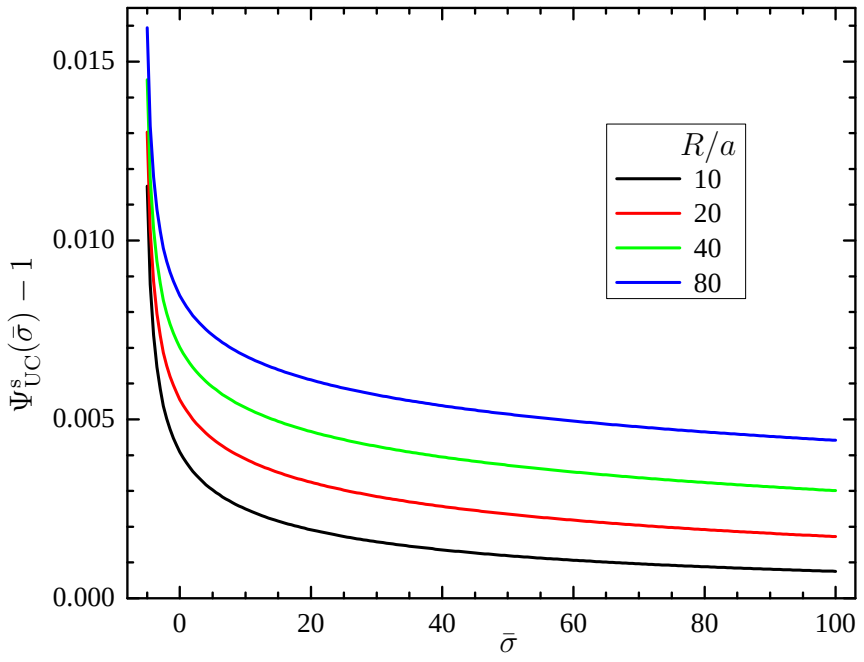


Figure E.3: Ψ^s_{UC} is plotted as a function of $\bar{\sigma}$ for several values of R/a.

Appendix F

Relating the Tilt Field and the Order Parameter

Recently, it has been suggested that molecular tilt makes a significant contribution to the membrane free energy [21, 32, 1, 22, 31]. In this appendix, predictions of a tilt-dependent model are related to attributes of fluid phase acyl chains. First in Section F.1, a single membrane free energy is introduced. Then in Section F.1.1, it is shown that the chain order parameter S_{mol} and the thermal average of the tilt field are related. In Section F.1.1, relations between S_{mol} and K_θ are derived, assuming either a continuum or a discrete set of in-plane wavevectors. Finally in Section F.2, it is shown that correlations between tilt fields of different bilayers are negligible, consistent with the common assumption in the analysis of wide angle X-ray scattering from stacked bilayers [53].

Tilt quantifies the deviation of a director of a lipid molecule from the local monolayer normal and is defined,

$$\mathbf{m} \equiv \frac{\mathbf{n}}{\mathbf{n}\cdot\mathbf{N}} - \mathbf{N}, \tag{F.1}$$

where $\mathbf{N}$ points along the monolayer normal, $\mathbf{n}$ is the lipid director, and $\mathbf{n}\cdot\mathbf{N} = \cos\theta$. $\mathbf{n}$ and $\mathbf{N}$ are unit vectors. Using the definition of $\mathbf{m}$ Eq. (F.1),

$$|\mathbf{m}|^2 = \frac{\mathbf{n}\cdot\mathbf{n}}{(\mathbf{n}\cdot\mathbf{N})^2} - 2\frac{\mathbf{n}\cdot\mathbf{N}}{\mathbf{n}\cdot\mathbf{N}} + (\mathbf{N}\cdot\mathbf{N}) \tag{F.2}$$

$$= \frac{1}{\cos^2\theta} - 1$$

$$= \tan^2\theta$$

$$\approx \theta^2. \tag{F.3}$$

F.1 Single Membrane Free Energy

Tilt-dependent predictions are derived using the complete Watson *et al.* model [1] but neglecting protrusions. Such a model was previously expressed in Appendix C.2.2, where it was augmented by an intermembrane interaction term. Here, only a single membrane is considered so the results from Appendix C.2.2 are used in the limit $B \to 0$.

F.1.1 Order Parameter Relations

Previously, a relation between the order parameter S_{mol} and K_θ was suggested [93],

$$K_\theta^{\mathrm{CPL}} = \frac{3k_{\mathrm{B}}T}{A_{\mathrm{c}}(1 - S_{\mathrm{mol}})}, \tag{F.4}$$

where A_{c} is the area of a lipid chain and K_θ is a bilayer modulus. Below, different relations between S_{mol} and K_θ are derived. Starting from the definition of the order parameter

$$S_{\mathrm{mol}} \equiv \left\langle \frac{3\cos^2\theta - 1}{2} \right\rangle \tag{F.5}$$

$$= \frac{3\left\langle\cos^2\theta\right\rangle - 1}{2}$$

$$\approx \frac{3\left\langle 1 - \theta^2/2\right\rangle - 1}{2}$$

$$= 1 - \frac{3}{4}\left\langle\theta^2\right\rangle$$

$$\Rightarrow \left\langle\theta^2\right\rangle \approx \frac{4}{3}\left(1 - S_{\mathrm{mol}}\right), \tag{F.6}$$

where θ is the angle between the local monolayer normal and the lipid director. Using Eq. (F.3), S_{mol} is related to the tilt field of a monolayer of a bilayer

$$\left\langle \left|\mathbf{m}^{(1)}\right|^2 \right\rangle = \left\langle \left|\mathbf{m}^{(2)}\right|^2 \right\rangle \tag{F.7}$$

$$\left\langle |\hat{\mathbf{m}} + \bar{\mathbf{m}}|^2 \right\rangle \approx \frac{4}{3}\left(1 - S_{\mathrm{mol}}\right), \tag{F.8}$$

where the definitions of $\hat{\mathbf{m}}$ and $\bar{\mathbf{m}}$ were used

$$\hat{\mathbf{m}} \equiv \frac{\mathbf{m}^{(1)} + \mathbf{m}^{(2)}}{2} \tag{F.9}$$

and

$$\bar{\mathbf{m}} \equiv \frac{\mathbf{m}^{(1)} - \mathbf{m}^{(2)}}{2}. \tag{F.10}$$

Additionally, $\langle \hat{\mathbf{m}}\bar{\mathbf{m}} \rangle = 0$ since $\hat{\mathbf{m}}$ and $\bar{\mathbf{m}}$ are not coupled in the complete Watson model [1], and therefore Eq. (F.8) is simplified

$$\left\langle |\hat{\mathbf{m}}|^2 \right\rangle + \left\langle |\bar{\mathbf{m}}|^2 \right\rangle \approx \frac{4}{3}\left(1 - S_{\mathrm{mol}}\right). \tag{F.11}$$

$\left\langle |\hat{\mathbf{m}}|^2 \right\rangle$ was also previously evaluated in Appendix C.2.2. Using Eq. (C.59) for $B = 0$,

$$\left\langle |\hat{\mathbf{m}}|^2 \right\rangle = \sum_{\mathbf{Q_r}} \frac{k_{\mathrm{B}}T}{2A_{\mathrm{p}}} \left(\frac{1}{\kappa_\theta + \kappa_{\mathrm{tw}} Q_r^2} + \frac{1}{\kappa_\theta} \right), \tag{F.12}$$

where the factor of A_{p} is from the definition of the Fourier transform, see Eq. (3.41). $\left\langle |\bar{\mathbf{m}}|^2 \right\rangle$ was previously evaluated in Appendix C.2.2. Using Eqs. (C.73) and (C.74),

$$\left\langle |\bar{\mathbf{m}}|^2 \right\rangle = \sum_{\mathbf{Q_r}} \frac{k_\mathrm{B}T}{2A_\mathrm{p}} \left(\frac{k_c^b Q_r^4 - \frac{\Omega Q_r^2}{b_0} + \frac{k_A}{b_0^2}}{k_c^b \kappa_\theta Q_r^4 + Q_r^2 \left(\frac{k_A k_c^b}{b_0^2} - \frac{\kappa_\theta \Omega}{b_0} - \frac{\Omega^2}{4b_0^2} \right) + \frac{k_A \kappa_\theta}{b_0^2}} + \frac{1}{\kappa_\theta + \kappa_\mathrm{tw} Q_r^2} \right) \tag{F.13}$$

$$= \sum_{\mathbf{Q_r}} \frac{k_\mathrm{B}T}{2A_\mathrm{p}} \left(\frac{1}{\kappa_\theta + \frac{4k_A k_c^b Q_r^2 - \Omega^2 Q_r^2}{4\left(k_c^b b_0^2 Q_r^4 - \Omega b_0 Q_r^2 + k_A\right)}} + \frac{1}{\kappa_\theta + \kappa_\mathrm{tw} Q_r^2} \right) \tag{F.14}$$

$$= \sum_{\mathbf{Q_r}} \frac{k_\mathrm{B}T}{2A_\mathrm{p}} \left(\frac{1}{\kappa_\theta f(Q_r)} + \frac{1}{\kappa_\theta + \kappa_\mathrm{tw} Q_r^2} \right), \tag{F.15}$$

where

$$f(Q_r) \equiv 1 + \frac{4k_A k_c^b Q_r^2 - \Omega^2 Q_r^2}{4\kappa_\theta \left(k_c^b b_0^2 Q_r^4 - \Omega b_0 Q_r^2 + k_A\right)}. \tag{F.16}$$

Using Eqs. (F.12) and (F.15), $\left\langle \left|\mathbf{m}^{(1)}\right|^2 \right\rangle$ is evaluated assuming either a continuum or discrete set of in-plane wavevectors.

Continuum of Tilt Modes

Assuming the step size in Q_r is sufficiently small, $\sum_{\mathbf{Q_r}}$ is approximated by $\frac{A_\mathrm{p}}{(2\pi)^2} \int \mathrm{d}\mathbf{Q_r}$,

$$\left\langle \left|\mathbf{m}^{(1)}\right|^2 \right\rangle \approx \frac{A_\mathrm{p}}{(2\pi)^2} \int_0^{\pi/a} \mathrm{d}\mathbf{Q_r} \, \frac{k_\mathrm{B}T}{2A_\mathrm{p}} \left[\frac{1}{\kappa_\theta} \left(1 + \frac{1}{f(Q_r)} \right) + \frac{2}{\kappa_\theta + \kappa_\mathrm{tw} Q_r^2} \right] \tag{F.17}$$

$$= \frac{k_\mathrm{B}T}{4\pi\kappa_\theta} \int_0^{\pi/a} \mathrm{d}Q_r \; Q_r \left[1 + \frac{1}{f(Q_r)} + \frac{2}{1 + \tilde{\xi}_\mathrm{tw}^2 Q_r^2} \right] \tag{F.18}$$

where

$$\tilde{\xi}_\mathrm{tw}^2 \equiv \kappa_\mathrm{tw}/\kappa_\theta. \tag{F.19}$$

For simplicity, let $f(Q_r) \to 1$. Note, however that

$$\int_0^{\pi/a} \mathrm{d}Q_r \, \frac{Q_r}{f(Q_r)} \approx 1.05 \tag{F.20}$$

$$< \frac{\pi^2}{2a^2} \approx 1.708, \tag{F.21}$$

using the monolayer moduli values in Table C.2 and $a = 1.7$ nm. Therefore, $f(Q_r) = 1$ overestimates $\left\langle \left| \mathbf{m}^{(1)} \right|^2 \right\rangle$. Using $f(Q_r) = 1$ to simplify Eq. (F.18),

$$\left\langle \left| \mathbf{m}^{(1)} \right|^2 \right\rangle = \frac{k_\mathrm{B}T}{2\pi\kappa_\theta} \left(\frac{\pi^2}{2a^2} + \frac{\ln\left[1 + \left(\tilde{\xi}_\mathrm{tw}^2 \pi/a\right)^2\right]}{2\tilde{\xi}_\mathrm{tw}^2} \right) \tag{F.22}$$

$$= \frac{\pi k_\mathrm{B}T}{2a^2 K_\theta} \left(1 + \frac{\ln(1+\tau'^2)}{\tau'^2} \right), \tag{F.23}$$

where

$$\tau' \equiv \tilde{\xi}_\mathrm{tw}\pi/a \tag{F.24}$$

$$= \frac{K_\mathrm{tw}}{K_\theta}\pi/a \tag{F.25}$$

$$= \xi_\mathrm{tw}\pi/a \tag{F.26}$$

and bilayer moduli were substituted for monolayer moduli assuming that they are related by a factor of 2.

Substituting $\left\langle \left| \mathbf{m}^{(1)} \right|^2 \right\rangle$ Eq. (F.23) into Eq. (F.11),

$$\frac{\pi k_\mathrm{B}T}{2a^2 K_\theta} \left(1 + \frac{\ln(1+\tau'^2)}{\tau'^2} \right) \approx \frac{4}{3}\left(1 - S_\mathrm{mol}\right) \tag{F.27}$$

$$\Rightarrow K_\theta \approx \frac{3\pi k_\mathrm{B}T}{8a^2\left(1 - S_\mathrm{mol}\right)} \left(1 + \frac{\ln(1+\tau'^2)}{\tau'^2} \right). \tag{F.28}$$

Literature values are $K_\mathrm{tw} = 0.9 \times 10^{-20}$ J and $K_\theta = 6.6 \times 10^{-20}$ J/nm^2 [25], giving $\xi_\mathrm{tw} = 3.7$ Å. If $\xi_\mathrm{tw} \ll a \approx 15$ Å, the τ'-dependent part of Eq. (F.28) can be simplified and

$$K_\theta \approx \frac{3\pi k_\mathrm{B}T}{4a^2\left(1-S_\mathrm{mol}\right)}. \tag{F.29}$$

Eq. (F.29) is similar to K_θ^CPL Eq. (F.4), identifying $4a^2/\pi \rightarrow A_\mathrm{c}$. However, $A_\mathrm{c} \approx 34$ Å^2 and $4a^2/\pi \gtrsim 80$ Å^2, assuming that $a > 8$ Å. Therefore, for DOPC at 30 °C, $A_\mathrm{c} = 34$ Å^2, $S_\mathrm{mol} = S_\mathrm{X\text{-}ray}/1.35 = 0.27/1.35 = 0.2$ [53], and $a = 8$ Å, Eq. (F.29) predicts a significantly smaller K_θ (19 mN/m) as compared to the prediction of K_θ^CPL Eq. (F.4) (46 mN/m). For increasing a, the disagreement between K_θ Eq. (F.29) and K_θ^CPL Eq. (F.4) increases. $K_\theta^\mathrm{CPL} = 46$ mN/m compares favorably to the value of 66 mN/m determined from an all-atom CHARMM simulation of DOPC [25]. Assuming a continuum of tilt modes does not yield a reasonable prediction for K_θ given experimental values of S_mol.

Discrete Tilt Modes

Instead of making the replacement $\sum_{\mathbf{Q_r}} \rightarrow \frac{A_\mathrm{p}}{(2\pi)^2}\int \mathrm{d}\mathbf{Q_r}$, $\sum_{\mathbf{Q_r}}$ is evaluated assuming a discrete set of in-plane wavevectors. There are N_c independent chains, and therefore, $A_\mathrm{p} = A_\mathrm{c}N_\mathrm{c}$. Using Eq. (F.12), Eq. (F.15) and $f(Q_r) = 1$,

$$\left\langle \left|\mathbf{m}^{(1)}\right|^2 \right\rangle = \sum_{\mathbf{Q_r}} \frac{k_\mathrm{B}T}{A_\mathrm{p}\kappa_\theta}\left(1+\frac{1}{1+\tilde{\xi}_\mathrm{tw}^2 Q_r^2}\right) \tag{F.30}$$

$$= \sum_{\mathbf{Q_r}} \frac{2k_\mathrm{B}T}{A_\mathrm{p}K_\theta}\left(1+\frac{1}{1+\xi_\mathrm{tw}^2 Q_r^2}\right) \tag{F.31}$$

$$= \frac{2k_\mathrm{B}T}{A_\mathrm{c}N_\mathrm{c}K_\theta}\sum_{Q_x=0}^{\pi/\sqrt{A_\mathrm{c}}}\sum_{Q_y=0}^{\pi/\sqrt{A_\mathrm{c}}}\left(1+\frac{1}{1+\xi_\mathrm{tw}^2 Q_r^2}\right) \tag{F.32}$$

$$= \frac{2k_\mathrm{B}T}{A_\mathrm{c}N_\mathrm{c}K_\theta}\sum_{i=0}^{\sqrt{N_\mathrm{c}}}\sum_{j=0}^{\sqrt{N_\mathrm{c}}}\left(1+\frac{1}{1+\frac{(\pi\xi_\mathrm{tw})^2}{A_\mathrm{c}N_\mathrm{c}}(i^2+j^2)}\right) \tag{F.33}$$

$$= \frac{2k_\mathrm{B}T}{A_\mathrm{c}K_\theta} f(A_\mathrm{c}, \xi_\mathrm{tw}), \tag{F.34}$$

where

$$f(A_{\mathrm{c}},\xi_{\mathrm{tw}}) \equiv \frac{1}{N_{\mathrm{c}}}\sum_{i=0}^{\sqrt{N_{\mathrm{c}}}}\sum_{j=0}^{\sqrt{N_{\mathrm{c}}}}\left(1+\frac{1}{1+\frac{(\pi\xi_{\mathrm{tw}})^2}{A_{\mathrm{c}}N_{\mathrm{c}}}(i^2+j^2)}\right). \tag{F.35}$$

Substituting $\left\langle\left|\mathbf{m}^{(1)}\right|^2\right\rangle$ Eq. (F.34) into Eq. (F.11),

$$\left\langle\left|\mathbf{m}^{(1)}\right|^2\right\rangle \approx f(A_{\mathrm{c}},\xi_{\mathrm{tw}})\frac{2k_{\mathrm{B}}T}{A_{\mathrm{c}}K_\theta} \approx \frac{4}{3}\left(1-S_{\mathrm{mol}}\right) \tag{F.36}$$

$$\Rightarrow K_\theta \approx f(A_{\mathrm{c}},\xi_{\mathrm{tw}})\frac{3k_{\mathrm{B}}T}{2A_{\mathrm{c}}\left(1-S_{\mathrm{mol}}\right)}. \tag{F.37}$$

Eq. (F.37) is similar to the relation derived in [93], see K_θ^{CPL} Eq. (F.4). For $A_{\mathrm{c}} = 34$ Å^2 (typical value for DOPC), the value of $f(A_{\mathrm{c}},\xi_{\mathrm{tw}})$ is between about 1 and 2 for 3.7 Å $\leq \xi_{\mathrm{tw}} \leq 0$ and 25 mN/m $\leq K_\theta \leq 50$ mN/m. For $\xi_{\mathrm{tw}} = 0$, K_θ Eq. (F.37) is equivalent to K_θ^{CPL} Eq. (F.4). The effect of twist is to decrease the power in $\left\langle\left|\hat{m}^{\perp}_{\mathbf{Q_r}}\right|^2\right\rangle$ and $\left\langle\left|\bar{m}^{\perp}_{\mathbf{Q_r}}\right|^2\right\rangle$ for $Q_r \gtrsim 1/\xi_{\mathrm{tw}}$, see Eqs. (C.59) and (C.74), respectively. Therefore, a nonzero K_{tw} diminishes $\left\langle\left|\mathbf{m}^{(1)}\right|^2\right\rangle$. Evaluating the sum over modes instead of using an integral approximation results in a K_θ-value that is more consistent with values determined from experiments and simulations. Similarly, it was previously argued by Lindahl and Edholm [19] that the mean square amplitude of the undulatory modes is different by a factor of about 2, depending on whether a sum over the modes or an integral approximation of the sum is evaluated.

F.2 $\left\langle\left|\hat{\mathbf{m}}_j\right|^2\right\rangle$ of Membrane Stack

In Section F.1, a single membrane free energy functional was used to predict the thermal average of the tilt field $\left\langle|\hat{\mathbf{m}}|^2\right\rangle$. Previously, the wide angle X-ray scattering from stacked bilayers has been analyzed to determine $S_{\text{X-ray}}$, assuming that fluctuations of chains in different bilayers are uncorrelated [53]. The aforementioned assumption is now examined by evaluating $\left\langle|\hat{\mathbf{m}}_j|^2\right\rangle$, using the stacked bilayer free energy $\mathcal{F}_{\mathrm{u}}$ Eq. (3.4).

Following the procedure described in Section 3.3.1, the tilt spectra are derived,

$$\left\langle \left| \hat{m}^{\parallel}_{\mathbf{Q}} \right|^2 \right\rangle = k_{\mathrm{B}}T\, \mathbb{U}^{-1}_{2,2}\, \delta_{\mathbf{Q},-\mathbf{Q}'} \tag{F.38}$$

$$= \frac{k_{\mathrm{B}}T}{K_\theta} \frac{K_c Q_r^4 + 4B \sin^2(Q_z D/2)}{K_c Q_r^4 + 4B\,(1+\xi_\theta^2 Q_r^2)\sin^2(Q_z D/2)}\, \delta_{\mathbf{Q},-\mathbf{Q}'} \tag{F.39}$$

$$\left\langle \left| \hat{m}^{\perp}_{\mathbf{Q}} \right|^2 \right\rangle = k_{\mathrm{B}}T\, \mathbb{U}^{-1}_{3,3}\, \delta_{\mathbf{Q},-\mathbf{Q}'} \tag{F.40}$$

$$= \frac{k_{\mathrm{B}}T}{K_\theta}\, \delta_{\mathbf{Q},-\mathbf{Q}'}. \tag{F.41}$$

Moving on to calculate $\left\langle |\hat{\mathbf{m}}_j|^2 \right\rangle$ using Eqs. (F.39) and (F.41),

$$\left\langle |\hat{\mathbf{m}}_j|^2 \right\rangle = \frac{1}{A_{\mathrm{p}} J} \sum_{\mathbf{Q},\mathbf{Q}'} \left[\left\langle \left| \hat{m}^{\parallel}_{\mathbf{Q}} \right| \right\rangle + \left\langle \left| \hat{m}^{\perp}_{\mathbf{Q}} \right| \right\rangle \right] e^{i(\mathbf{Q}_{\mathbf{r}}+\mathbf{Q}'_{\mathbf{r}})\cdot\mathbf{r} + i(Q_z+Q'_z)jD} \tag{F.42}$$

$$= \frac{k_{\mathrm{B}}T}{A_{\mathrm{p}} J K_\theta} \sum_{\mathbf{Q}} \left(1 + \frac{K_c Q_r^4 + 4B \sin^2(Q_z D/2)}{K_c Q_r^4 + 4B\,(1+\xi_\theta^2 Q_r^2)\sin^2(Q_z D/2)} \right). \tag{F.43}$$

Substituting $\sum_{\mathbf{Q}} \to \frac{A_{\mathrm{p}}}{(2\pi)^2} \int \mathrm{d}\mathbf{Q}_{\mathbf{r}}\ \frac{JD}{2\pi} \int_{-\pi/D}^{\pi/D} \mathrm{d}Q_z$,

$$\begin{aligned}
&\left\langle |\hat{\mathbf{m}}_j|^2 \right\rangle \\
&= \frac{k_{\mathrm{B}}TD}{8\pi^3 K_\theta} \int \mathrm{d}\mathbf{Q}_{\mathbf{r}}\ \int_{-\pi/D}^{\pi/D} \mathrm{d}Q_z \left(1 + \frac{K_c Q_r^4 + 4B \sin^2(Q_z D/2)}{K_c Q_r^4 + 4B\,(1+\xi_\theta^2 Q_r^2)\sin^2(Q_z D/2)} \right) \qquad \text{(F.44)} \\
&= \frac{k_{\mathrm{B}}TD}{4\pi^2 K_\theta} \int \mathrm{d}Q_r\ Q_r\ \int_{-\pi/D}^{\pi/D} \mathrm{d}Q_z \left(1 + \frac{\xi^4 Q_r^4/4 + \sin^2(Q_z D/2)}{\xi^4 Q_r^4/4 + (1+\xi_\theta^2 Q_r^2)\sin^2(Q_z D/2)} \right) \\
&= \frac{k_{\mathrm{B}}T}{4\pi^2 K_\theta} \int \mathrm{d}Q_r\ Q_r\ \int_{-\pi}^{\pi} \mathrm{d}\omega \left(1 + \frac{\xi^4 Q_r^4/4 + \sin^2(\omega/2)}{\xi^4 Q_r^4/4 + (1+\xi_\theta^2 Q_r^2)\sin^2(\omega/2)} \right). \qquad \text{(F.45)}
\end{aligned}$$

Substituting $v = \xi^2 Q_r^2/2$ into Eq. (F.45),

$$
\begin{aligned}
&\left\langle |\hat{\mathbf{m}}_j|^2 \right\rangle \\
&= \frac{k_{\mathrm{B}}T}{4\pi^2\xi^2 K_\theta} \int_0^\tau \mathrm{d}v \int_{-\pi}^{\pi} \mathrm{d}\omega \left(1 + \frac{v^2 + \sin^2(\omega/2)}{v^2 + (1+v\ell)\sin^2(\omega/2)} \right) && \text{(F.46)} \\
&= \frac{k_{\mathrm{B}}T}{4\pi^2\xi^2 K_\theta} \int_0^\tau \mathrm{d}v \, \frac{1}{1+v\ell} \int_{-\pi}^{\pi} \mathrm{d}\omega \left(1 + v\ell + \frac{v^2 + \sin^2(\omega/2)}{v^2/(1+v\ell) + \sin^2(\omega/2)} \right) \\
&= \frac{k_{\mathrm{B}}T}{4\pi^2\xi^2 K_\theta} \int_0^\tau \mathrm{d}v \, \frac{1}{1+x\ell} \int_{-\pi}^{\pi} \mathrm{d}\omega \left(1 + v\ell + \frac{v^2 + \frac{1-\cos\omega}{2}}{v^2/(1+v\ell) + \sin^2(\omega/2)} \right) \\
&= \frac{k_{\mathrm{B}}T}{4\pi^2\xi^2 K_\theta} \int_0^\tau \mathrm{d}v \, \frac{1}{1+v\ell} \left(2\pi(1+v\ell) + 2\pi \frac{v^2 + 1/2}{\sqrt{\aleph^2 + \aleph^4}} - \frac{2\pi}{2} \frac{1 + 2\aleph^2 - 2\sqrt{\aleph^2 + \aleph^4}}{\sqrt{\aleph^2 + \aleph^4}} \right), && \text{(F.47)}
\end{aligned}
$$

where $\aleph^2 = \frac{v^2}{1+v\ell}$. Simplifying the above expression,

$$
\begin{aligned}
&\left\langle |\hat{\mathbf{m}}_j|^2 \right\rangle \\
&= \frac{k_{\mathrm{B}}T}{4\pi^2\xi^2 K_\theta} \int_0^\tau \mathrm{d}v \; 2\pi \left(1 + \frac{v^2\ell + \sqrt{1 + v\ell + v^2}}{(1+v\ell)\sqrt{1+v\ell+v^2}} \right) && \text{(F.48)} \\
&= \frac{k_{\mathrm{B}}T}{2\pi\xi^2 K_\theta} \Bigg[v + f_c(v) + \frac{1}{\ell} \ln \left(\frac{(1+v\ell)^2}{[\ell + 2v + 2f_c(v)][\ell - 2v + \ell^2 v + 2f_c(v)]} \right) \\
&\qquad\qquad - \frac{\ell}{2} \ln \left[\ell + 2v + 2f_c(v) \right] \Bigg] \Bigg|_0^\tau \\
&\approx \frac{k_{\mathrm{B}}T}{2\pi\xi^2 K_\theta} 2\tau && \text{(F.49)} \\
&= \frac{\pi k_{\mathrm{B}}T}{2a^2 K_\theta}, && \text{(F.50)}
\end{aligned}
$$

where $f_c(v) = \sqrt{1 + v\ell + v^2}$. $\left\langle |\hat{\mathbf{m}}_j|^2 \right\rangle$ Eq. (F.50) is the same as $\left\langle |\hat{\mathbf{m}}|^2 \right\rangle$ Eq. (F.23) in the limit $\xi_{\mathrm{tw}} \to 0$. Therefore, correlations in the tilt fields of different bilayers insignificantly contribute to $\left\langle |\hat{\mathbf{m}}_j|^2 \right\rangle$, and consequently, the common assumption used to analyze wide angle X-ray scattering from fluid phase acyl chains is supported.

Bibliography

[1] M. C. Watson, E. S. Penev, P. M. Welch, and F. L. H. Brown, "Thermal fluctuations in shape, thickness, and molecular orientation in lipid bilayers," The Journal of Chemical Physics, vol. 135, no. 24, 2011.

[2] F. O. Schmitt, R. S. Bear, and G. L. Clark, "X-ray diffraction studies on nerve," Radiology, vol. 25, no. 2, pp. 131–151, 1935.

[3] Y. Levine and M. Wilkins, "Structure of oriented lipid bilayers," Nature, vol. 230, no. 11, pp. 69–72, 1971.

[4] V. Luzzati and A. Tardieu, "Lipid phases: structure and structural transitions," Annual Review of Physical Chemistry, vol. 25, no. 1, pp. 79–94, 1974.

[5] J. N. Israelachvili, Intermolecular and surface forces: revised third edition. Academic press, 2011.

[6] S. J. Singer and G. L. Nicolson, "The fluid mosaic model of the structure of cell membranes," Science, vol. 175, no. 4023, pp. 720–731, 1972.

[7] Y.-H. M. Chan and S. G. Boxer, "Model membrane systems and their applications," Current opinion in chemical biology, vol. 11, no. 6, pp. 581–587, 2007.

[8] Y. Shibata, J. Hu, M. M. Kozlov, and T. A. Rapoport, "Mechanisms shaping the membranes of cellular organelles," Annual Review of Cell and Developmental, vol. 25, pp. 329–354, 2009.

[9] L. V. Chernomordik and M. M. Kozlov, "Protein-lipid interplay in fusion and fission of biological membranes," Annual review of biochemistry, vol. 72, no. 1, pp. 175–207, 2003.

[10] W. Helfrich, "Elastic properties of lipid bilayers: theory and possible experiments.," Zeitschrift für Naturforschung. Teil C: Biochemie, Biophysik, Biologie, Virologie, vol. 28, no. 11, p. 693, 1973.

[11] P. B. Canham, "The minimum energy of bending as a possible explanation of the biconcave shape of the human red blood cell," Journal of Theoretical Biology, vol. 26, no. 1, pp. 61–81, 1970.

[12] R. Courant and D. Hilbert, Methods of mathematical physics, vol. 1. CUP Archive, 1966.

[13] D. H. Boal, Mechanics of the Cell. Cambridge University Press, 2012.

[14] M. Schneider, J. Jenkins, and W. Webb, "Thermal fluctuations of large quasi-spherical bimolecular phospholipid vesicles," Journal de Physique, vol. 45, no. 9, pp. 1457–1472, 1984.

[15] E. Evans and W. Rawicz, "Entropy-driven tension and bending elasticity in condensed-fluid membranes," Phys. Rev. Lett., vol. 64, no. 17, p. 2094, 1990.

[16] J. F. Nagle, "Introductory lecture: Basic quantities in model biomembranes," Faraday Discuss., vol. 161, pp. 11–29, 2013.

[17] R. Dimova, "Recent developments in the field of bending rigidity measurements on membranes," Advances in colloid and interface science, vol. 208, pp. 225–234, 2014.

[18] R. Goetz, G. Gompper, and R. Lipowsky, "Mobility and elasticity of self-assembled membranes," Phys. Rev. Lett., vol. 82, pp. 221–224, Jan 1999.

[19] E. Lindahl and O. Edholm, "Mesoscopic undulations and thickness fluctuations in lipid bilayers from molecular dynamics simulations," Biophysical Journal, vol. 79, no. 1, pp. 426–433, 2000.

[20] S. J. Marrink and A. E. Mark, "Effect of undulations on surface tension in simulated bilayers," The Journal of Physical Chemistry B, vol. 105, no. 26, pp. 6122–6127, 2001.

[21] E. R. May, A. Narang, and D. I. Kopelevich, "Role of molecular tilt in thermal fluctuations of lipid membranes," Phys. Rev. E, vol. 76, p. 021913, Aug 2007.

[22] M. C. Watson, E. G. Brandt, P. M. Welch, and F. L. H. Brown, "Determining biomembrane bending rigidities from simulations of modest size," Phys. Rev. Lett., vol. 109, p. 028102, Jul 2012.

[23] G. Khelashvili and D. Harries, "How cholesterol tilt modulates the mechanical properties of saturated and unsaturated lipid membranes," The Journal of Physical Chemistry B, vol. 117, no. 8, pp. 2411–2421, 2013.

[24] M. C. Watson, A. Morriss-Andrews, P. M. Welch, and F. L. Brown, "Thermal fluctuations in shape, thickness, and molecular orientation in lipid bilayers. ii. finite surface tensions," The Journal of chemical physics, vol. 139, no. 8, p. 084706, 2013.

[25] Z. A. Levine, R. M. Venable, M. C. Watson, M. G. Lerner, J.-E. Shea, R. W. Pastor, and F. L. Brown, "Determination of biomembrane bending moduli in fully atomistic simulations," Journal of the American Chemical Society, vol. 136, no. 39, pp. 13582–13585, 2014.

[26] E. G. Brandt, A. R. Braun, J. N. Sachs, J. F. Nagle, and O. Edholm, "Interpretation of fluctuation spectra in lipid bilayer simulations," Biophysical journal, vol. 100, no. 9, pp. 2104–2111, 2011.

[27] J. C. Albert, L. T. Ray, and J. F. Nagle, "Testing procedures for extracting fluctuation spectra from lipid bilayer simulations," The Journal of chemical physics, vol. 141, no. 6, p. 064114, 2014.

[28] F. C. MacKintosh and T. C. Lubensky, "Orientational order, topology, and vesicle shapes," Phys. Rev. Lett., vol. 67, pp. 1169–1172, Aug 1991.

[29] T. C. Lubensky and F. C. MacKintosh, "Theory of ripple phases of lipid bilayers," Phys. Rev. Lett., vol. 71, pp. 1565–1568, Sep 1993.

[30] M. Hamm and M. M. Kozlov, "Tilt model of inverted amphiphilic mesophases," The European Physical Journal B-Condensed Matter and Complex Systems, vol. 6, no. 4, pp. 519–528, 1998.

[31] M. Hamm and M. M. Kozlov, "Elastic energy of tilt and bending of fluid membranes," The European Physical Journal E, vol. 3, no. 4, pp. 323–335, 2000.

[32] M. Jablin, K. Akabori, and J. Nagle, "Experimental support for tilt-dependent theory of biomembrane mechanics," Physical review letters, vol. 113, no. 24, p. 248102, 2014.

[33] I. Pascher, M. Lundmark, P.-G. Nyholm, and S. Sundell, "Crystal structures of membrane lipids," Biochimica et Biophysica Acta (BBA)-Reviews on Biomembranes, vol. 1113, no. 3, pp. 339–373, 1992.

[34] M. Wiener, R. Suter, and J. Nagle, "Structure of the fully hydrated gel phase of dipalmitoylphosphatidylcholine," Biophysical journal, vol. 55, no. 2, pp. 315–325, 1989.

[35] M. C. Wiener and S. H. White, "Fluid bilayer structure determination by the combined use of x-ray and neutron diffraction. i. fluid bilayer models and the limits of resolution.," Biophysical journal, vol. 59, no. 1, p. 162, 1991.

[36] D. Roux and C. Safinya, "A synchrotron x-ray study of competing undulation and electrostatic interlayer interactions in fluid multimembrane lyotropic phases," Journal de Physique, vol. 49, no. 2, pp. 307–318, 1988.

[37] D. C. Wack and W. W. Webb, "Measurement by x-ray diffraction methods of the layer compressional elastic constant b in the lyotropic smectic-a (l α) phase of the lecithin-water system," Physical Review A, vol. 40, no. 3, p. 1627, 1989.

[38] R. Zhang, R. M. Suter, and J. F. Nagle, "Theory of the structure factor of lipid bilayers," Phys. Rev. E, vol. 50, pp. 5047–5060, Dec 1994. (See appendix).

[39] J. F. Nagle and S. Tristram-Nagle, "Structure of lipid bilayers," Biochimica et Biophysica Acta (BBA)-Reviews on Biomembranes, vol. 1469, no. 3, pp. 159–195, 2000.

[40] J. Prost and P. G. De Gennes, The physics of liquid crystals. No. 83, Oxford university press, 1995.

[41] A. Caillé, "X-ray scattering by smectic-a crystals," CR Acad Sci Ser B, vol. 274, pp. 891–893, 1972.

[42] J. Als-Nielsen, J. D. Litster, R. J. Birgeneau, M. Kaplan, C. R. Safinya, A. Lindegaard-Andersen, and S. Mathiesen, "Observation of algebraic decay

of positional order in a smectic liquid crystal," Phys. Rev. B, vol. 22, pp. 312–320, Jul 1980.

[43] R. Zhang, S. Tristram-Nagle, W. Sun, R. Headrick, T. Irving, R. M. Suter, and J. F. Nagle, "Small-angle x-ray scattering from lipid bilayers is well described by modified caillé theory but not by paracrystalline theory.," Biophysical journal, vol. 70, no. 1, p. 349, 1996.

[44] Y. Lyatskaya, Y. Liu, S. Tristram-Nagle, J. Katsaras, and J. F. Nagle, "Method for obtaining structure and interactions from oriented lipid bilayers," Phys. Rev. E, vol. 63, p. 011907, Dec 2000.

[45] T. Salditt, M. Vogel, and W. Fenzl, "Thermal fluctuations and positional correlations in oriented lipid membranes," Phys. Rev. Lett., vol. 90, p. 178101, Apr 2003.

[46] Y. Liu and J. F. Nagle, "Diffuse scattering provides material parameters and electron density profiles of biomembranes," Phys. Rev. E, vol. 69, p. 040901, Apr 2004.

[47] D.-P. Li, S.-X. Hu, and M. Li, "Full q-space analysis of x-ray scattering of multilamellar membranes at liquid-solid interfaces," Phys. Rev. E, vol. 73, p. 031916, Mar 2006.

[48] Y. Liu, Synchrotron x-ray scattering studies of the interactions and undulations of surfactant fluid multilayer membranes. Ph.D. thesis, Carnegie Mellon University, 2003.

[49] J. Pan, Supramolecular Organization of the Antimicrobial Peptide Alamethicin in Fluid Membranes. Ph.D. thesis, Carnegie Mellon University, 2009.

[50] K. Akabori, Structure determination of HIV-1 Tat/fuid phase membranes and DMPC ripple phase using X-ray scattering. Ph.D. thesis, Carnegie Mellon University, 2014.

[51] S. A. Tristram-Nagle, "Preparation of oriented, fully hydrated lipid samples for structure determination using x-ray scattering," in Methods in Membrane Lipids, pp. 63–75, Springer, 2007.

[52] S. Barna, M. Tate, S. Gruner, and E. Eikenberry, "Calibration procedures for charge-coupled device x-ray detectors," Review of Scientific Instruments, vol. 70, no. 7, pp. 2927–2934, 1999.

[53] T. T. Mills, G. E. Toombes, S. Tristram-Nagle, D.-M. Smilgies, G. W. Feigenson, and J. F. Nagle, "Order parameters and areas in fluid-phase oriented lipid membranes using wide angle x-ray scattering," Biophysical journal, vol. 95, no. 2, pp. 669–681, 2008.

[54] J.-B. Fournier, "Microscopic membrane elasticity and interactions among membrane inclusions: interplay between the shape, dilation, tilt and tilt-difference modes," The European Physical Journal B-Condensed Matter and Complex Systems, vol. 11, no. 2, pp. 261–272, 1999.

[55] N. Lei, C. Safinya, and R. Bruinsma, "Discrete harmonic model for stacked membranes: Theory and experiment," J. Phys. II France, vol. 5, no. 8, pp. 1155–1163, 1995.

[56] N. Lei, Synchrotron X-Ray Scattering Studies of the Interactions and Undulations of Surfactant Fluid Multilayer Membranes. Ph.D. thesis, Rutgers, 1993.

[57] R. Hołyst, "Landau-peierls instability, x-ray-diffraction patterns, and surface freezing in thin smectic films," Phys. Rev. A, vol. 44, pp. 3692–3709, Sep 1991.

[58] H. I. Petrache, N. Gouliaev, S. Tristram-Nagle, R. Zhang, R. M. Suter, and J. F. Nagle, "Interbilayer interactions from high-resolution x-ray scattering," Physical Review E, vol. 57, no. 6, pp. 7014–7024, 1998.

[59] D. Constantin, U. Mennicke, C. Li, and T. Salditt, "Solid-supported lipid multilayers: Structure factor and fluctuations," The European Physical Journal E, vol. 12, no. 2, pp. 283–290, 2003.

[60] T. Reusch, D. D. Mai, M. Osterhoff, D. Khakhulin, M. Wulff, and T. Salditt, "Nonequilibrium collective dynamics in photoexcited lipid multilayers by time resolved diffuse x-ray scattering," Phys. Rev. Lett., vol. 111, p. 268101, Dec 2013.

[61] C. Worthington, G. King, and T. McIntosh, "Direct structure determination of multilayered membrane-type systems which contain fluid layers," Biophysical journal, vol. 13, no. 5, pp. 480–494, 1973.

[62] J. Als-Nielsen and D. McMorrow, Elements of modern X-ray physics. John Wiley & Sons, 2011.

[63] M. Osipov and B. Ostrovskii, "Study of the orientational order in liquid crystals by x-ray scattering," Crystallography reviews, vol. 3, no. 2, pp. 113–152, 1992.

[64] J. Powles, "The structure of molecular liquids by neutron scattering," Advances in Physics, vol. 22, no. 1, pp. 1–56, 1973.

[65] A. Guinier, X-ray diffraction in crystals, imperfect crystals, and amorphous bodies. Courier Corporation, 1994.

[66] B. E. Warren, X-ray Diffraction. Courier Dover Publications, 1969.

[67] N. Gouliaev and J. F. Nagle, "Simulations of a single membrane between two walls using a monte carlo method," Phys. Rev. E, vol. 58, pp. 881–888, Jul 1998.

[68] A. Poniewierski and H. Robert, "Continuous-model description of layer fluctuations in finite smectic systems," Physical Review B, vol. 47, no. 15, p. 9840, 1993.

[69] V. Romanov and S. Ulyanov, "Dynamic and correlation properties of solid supported smectic-a films," Physical Review E, vol. 66, no. 6, p. 061701, 2002.

[70] D. K. de Boer, "X-ray scattering from smectic films on a substrate," Physical Review E, vol. 59, no. 2, p. 1880, 1999.

[71] M. Abramowitz and I. A. Stegun, Handbook of mathematical functions: with formulas, graphs, and mathematical tables. No. 55, Courier Dover Publications, 1972.

[72] F. F. Abraham and D. R. Nelson, "Fluctuations in the flat and collapsed phases of polymerized membranes," Journal de Physique, vol. 51, no. 23, pp. 2653–2672, 1990.

[73] H. Petrache, Structure and Interactions of Fluid Phospholipid Bilayers Measured by High Resolution X-ray Scattering. Ph.D. thesis, Carnegie Mellon University, 1998.

[74] S. K. Sinha, M. Tolan, and A. Gibaud, "Effects of partial coherence on the scattering of x rays by matter," Phys. Rev. B, vol. 57, pp. 2740–2758, Feb 1998.

[75] M. Tolan, "X-ray scattering from soft-matter thin films: Materials science and basic research," 1999.

[76] N. Kučerka, S. Tristram-Nagle, and J. F. Nagle, "Structure of fully hydrated fluid phase lipid bilayers with monounsaturated chains," The Journal of membrane biology, vol. 208, no. 3, pp. 193–202, 2006.

[77] S. K. Sinha, Z. Jiang, and L. B. Lurio, "X-ray photon correlation spectroscopy studies of surfaces and thin films," Advanced Materials, 2014.

[78] E. Mol, J. Shindler, A. Shalaginov, and W. De Jeu, "Correlations in the thermal fluctuations of free-standing smectic-a films as measured by x-ray scattering," Physical Review E, vol. 54, no. 1, p. 536, 1996.

[79] J. F. Nagle and J. Katsaras, "Absence of a vestigial vapor pressure paradox," Physical Review E, vol. 59, no. 6, p. 7018, 1999.

[80] W. H. Press, Numerical recipes 3rd edition: The art of scientific computing. Cambridge university press, 2007.

[81] P. R. Bevington, Data Reduction and Error Analysis for the Physical Sciences. McGraw Hill, first ed., 1969.

[82] N. Chu, N. Kučerka, Y. Liu, S. Tristram-Nagle, and J. F. Nagle, "Anomalous swelling of lipid bilayer stacks is caused by softening of the bending modulus," Physical review E, vol. 71, no. 4, p. 041904, 2005.

[83] E. Evans, W. Rawicz, and B. Smith, "Concluding remarks back to the future: mechanics and thermodynamics of lipid biomembranes," Faraday discussions, vol. 161, pp. 591–611, 2013.

[84] N. Kučerka, J. Katsaras, and J. F. Nagle, "Comparing membrane simulations to scattering experiments: introducing the simtoexp software," Journal of Membrane Biology, vol. 235, no. 1, pp. 43–50, 2010.

[85] N. Kučerka, Y. Liu, N. Chu, H. I. Petrache, S. Tristram-Nagle, and J. F. Nagle, "Structure of fully hydrated fluid phase dmpc and dlpc lipid bilayers using x-ray scattering from oriented multilamellar arrays and from unilamellar vesicles," Biophysical journal, vol. 88, no. 4, pp. 2626–2637, 2005.

[86] G. Khelashvili, B. Kollmitzer, P. Heftberger, G. Pabst, and D. Harries, "Calculating the bending modulus for multicomponent lipid membranes in different thermodynamic phases," Journal of chemical theory and computation, vol. 9, no. 9, pp. 3866–3871, 2013.

[87] W. Rawicz, K. Olbrich, T. McIntosh, D. Needham, and E. Evans, "Effect of chain length and unsaturation on elasticity of lipid bilayers," Biophysical journal, vol. 79, no. 1, pp. 328–339, 2000.

[88] B. Sorre, A. Callan-Jones, J.-B. Manneville, P. Nassoy, J.-F. Joanny, J. Prost, B. Goud, and P. Bassereau, "Curvature-driven lipid sorting needs proximity to a demixing point and is aided by proteins," Proceedings of the National Academy of Sciences, vol. 106, no. 14, pp. 5622–5626, 2009.

[89] R. S. Gracià, N. Bezlyepkina, R. L. Knorr, R. Lipowsky, and R. Dimova, "Effect of cholesterol on the rigidity of saturated and unsaturated membranes: fluctuation and electrodeformation analysis of giant vesicles," Soft Matter, vol. 6, no. 7, pp. 1472–1482, 2010.

[90] P. Shchelokovskyy, S. Tristram-Nagle, and R. Dimova, "Effect of the hiv-1 fusion peptide on the mechanical properties and leaflet coupling of lipid bilayers," New journal of physics, vol. 13, no. 2, p. 025004, 2011.

[91] A. Tian, B. R. Capraro, C. Esposito, and T. Baumgart, "Bending stiffness depends on curvature of ternary lipid mixture tubular membranes," Biophysical journal, vol. 97, no. 6, pp. 1636–1646, 2009.

[92] A. Georgiadis, G. Maitland, J. M. Trusler, and A. Bismarck, "Interfacial tension measurements of the (h2o+ n-decane+ co2) ternary system at elevated pressures

and temperatures," Journal of Chemical & Engineering Data, vol. 56, no. 12, pp. 4900–4908, 2011.

[93] J. F. Nagle, M. S. Jablin, S. Tristram-Nagle, and K. Akabori, "What are the true values of the bending modulus of simple lipid bilayers?," Chemistry and physics of lipids, vol. 185, pp. 3–10, 2015.

[94] S. May, Y. Kozlovsky, A. Ben-Shaul, and M. Kozlov, "Tilt modulus of a lipid monolayer," The European Physical Journal E, vol. 14, no. 3, pp. 299–308, 2004.

[95] N. Gouliaev and J. F. Nagle, "Simulations of interacting membranes in the soft confinement regime," Phys. Rev. Lett., vol. 81, pp. 2610–2613, Sep 1998.

[96] C. E. Miller, J. Majewski, T. Gog, and T. L. Kuhl, "Characterization of biological thin films at the solid-liquid interface by x-ray reflectivity," Physical review letters, vol. 94, no. 23, p. 238104, 2005.

[97] C. Reich, M. R. Horton, B. Krause, A. P. Gast, J. O. Rädler, and B. Nickel, "Asymmetric structural features in single supported lipid bilayers containing cholesterol and g m1 resolved with synchrotron x-ray reflectivity," Biophysical journal, vol. 95, no. 2, pp. 657–668, 2008.

[98] E. Novakova, K. Giewekemeyer, and T. Salditt, "Structure of two-component lipid membranes on solid support: An x-ray reflectivity study," Physical Review E, vol. 74, no. 5, p. 051911, 2006.

[99] C. Miller, J. Majewski, E. Watkins, D. Mulder, T. Gog, and T. Kuhl, "Probing the local order of single phospholipid membranes using grazing incidence x-ray diffraction," Physical review letters, vol. 100, no. 5, p. 058103, 2008.

[100] E. Watkins, C. Miller, D. Mulder, T. Kuhl, and J. Majewski, "Structure and orientational texture of self-organizing lipid bilayers," Physical review letters, vol. 102, no. 23, p. 238101, 2009.

[101] L. Malaquin, T. Charitat, and J. Daillant, "Supported bilayers: Combined specular and diffuse x-ray scattering," The European Physical Journal E: Soft Matter and Biological Physics, vol. 31, no. 3, pp. 285–301, 2010.

[102] J. Pan, S. Tristram-Nagle, N. Kučerka, and J. F. Nagle, "Temperature dependence of structure, bending rigidity, and bilayer interactions of dioleoylphosphatidylcholine bilayers," Biophysical journal, vol. 94, no. 1, pp. 117–124, 2008.

[103] S. Tristram-Nagle, H. I. Petrache, and J. F. Nagle, "Structure and interactions of fully hydrated dioleoylphosphatidylcholine bilayers," Biophysical journal, vol. 75, no. 2, pp. 917–925, 1998.

[104] Private communication with Dr. Kiyotaka Akabori during his graduate career at Carnegie Mellon University.

[105] A. R. Braun, E. G. Brandt, O. Edholm, J. F. Nagle, and J. N. Sachs, "Determination of electron density profiles and area from simulations of undulating membranes," Biophysical journal, vol. 100, no. 9, pp. 2112–2120, 2011.

[106] N. Lei and X. Lei, "Fluid membrane thermal fluctuations and bending curvature modulus determination," Langmuir, vol. 14, no. 8, pp. 2155–2159, 1998.

[107] F. Auguste, P. Barois, L. Fredon, B. Clin, E. Dufourc, and A. Bellocq, "Flexibility of molecular films as determined by deuterium solid state nmr," Journal de Physique II, vol. 4, no. 12, pp. 2197–2214, 1994.

[108] S. T. Milner and S. Safran, "Dynamical fluctuations of droplet microemulsions and vesicles," Physical Review A, vol. 36, no. 9, p. 4371, 1987.

[109] C. Barbetta, A. Imparato, and J. B. Fournier, "On the surface tension of fluctuating quasi-spherical vesicles," The European Physical Journal E: Soft Matter and Biological Physics, vol. 31, no. 3, pp. 333–342, 2010.

[110] J. Faucon, M. Mitov, P. Méléard, I. Bivas, and P. Bothorel, "Bending elasticity and thermal fluctuations of lipid membranes. theoretical and experimental requirements," Journal de Physique, vol. 50, no. 17, pp. 2389–2414, 1989.